UNIVERSITÀ
DEGLI STUDI
DI PADOVA

Head Office: Università degli Studi di Padova

Department of Chemical Sciences

Ph.D. COURSE IN: Molecular Sciences
CURRICULUM: Pharmaceutical Sciences
SERIES XXX

EXPLORING PROTEIN FLEXIBILITY DURING DOCKING TO INVESTIGATE LIGAND-TARGET RECOGNITION

Coordinator: Ch. mo Prof. Leonard Jan Prins
Supervisor : Ch. mo Prof. Stefano Moro

Ph.D. student : Veronica Salmaso

A mia mamma, mio papà e mia sorella

Abstract

Ligand-protein binding models have experienced an evolution during time: from the lock-key model to induced-fit and conformational selection, the role of protein flexibility has become more and more relevant. Understanding binding mechanism is of great importance in drug-discovery, because it could help to rationalize the activity of known binders and to optimize them. The application of computational techniques to drug-discovery has been reported since the 1980s, with the advent computer-aided drug design. During the years several techniques have been developed to address the protein flexibility issue.

The present work proposes a strategy to consider protein structure variability in molecular docking, through a ligand-based/structure-based integrated approach and through the development of a fully automatic cross-docking benchmark pipeline.

Moreover, a full exploration of protein flexibility during the binding process is proposed through the Supervised Molecular Dynamics. The application of a tabu-like algorithm to classical molecular dynamics accelerates the binding process from the micro-millisecond to the nanosecond timescales. In the present work, an implementation of this algorithm has been performed to study peptide-protein recognition processes.

Sommario

I modelli di riconoscimento ligando-proteina si sono evoluti nel corso degli anni: dal modello chiave-serratura a quello di *fit*-indotto e selezione conformazionale, il ruolo della flessibilità proteica è diventato via via più importante. Capire il meccanismo di riconoscimento è di grande importanza nella progettazione di nuovi farmaci, perchè può dare la possibilità di razionalizzare l'attività di ligandi noti e di ottimizzarli. L'applicazione di tecniche computazionali alla scoperta di nuovi farmaci risale agli anni '80, con l'avvento del cosiddetto "*Computer-Aided Drug Design*", o, tradotto, progettazione di farmaci aiutata dal computer. Negli anni sono state sviluppate molte tecniche che hanno affrontato il problema della flessibilità proteica.

Questo lavoro propone una strategia per considerare la variabilità delle strutture proteiche nel *docking*, attraverso un approccio combinato *ligand-based*/*structure-based* e attraverso lo sviluppo di una procedura completamente automatizzata di *docking* incrociato.

In aggiunta, viene proposta una piena esplorazione della flessibilità proteica durante il processo di legame attraverso la Dinamica Molecolare Supervisionata. L'applicazione di un algoritmo simil-tabu alla dinamica molecolare classica accelera il processo di riconoscimento dalla scala dei micro-millisecondi a quella dei nanosecondi. Nel presente lavoro è stata fatta un'implementazione di questa algoritmica per studiare il processo di riconoscimento peptide-proteina.

Introduction

1. Ligand-protein binding models

No protein is an island, but exerts its function through recognition with other molecular partners. Ligand-protein interactions are involved in many biological processes, so understanding binding mechanism has been occupying scientists for a long time. Several theories have been developed during the years, with an increasing emphasis on the degree of flexibility of the ligand and protein counterparts.

The first explanation of binding was provided by Emil Fischer in 1894 [1], who firstly proposed the "lock-key" model to explain enzyme specificity: in this model the ligand is natively complementary in shape to its protein binding site, which it recognizes and occupies rigidly as a key to its lock. However, this model could explain neither the behaviour of enzyme noncompetitive inhibition nor allosteric modulation. A modification of the "lock-key" theory was introduced by Koshland [2], who proposed the "induced-fit" theory starting from his observations on enzyme-substrate interactions: according to this binding model, the ligand is able to induce conformational changes to the protein, optimizing their interactions. Later works suggested that many conformational states of the same protein can exist before binding [3, 4], and a ligand can bind preferentially to one of these conformations; this laid the basis for the "conformational selection" model.

Protein-ligand binding is better explained in terms of protein energy landscape, a concept originated to explain protein folding. The free energy landscape model describes the whole conformational space accessible to a system: it consists of the free energy of the system as a function of its conformations (i. e. coordinates of its atoms), resulting in a hypersurface [5]. At a given instant, a protein exists as a single conformational state, but it explores different conformations in time. The probability to occupy a particular region of the phase space is correlated with the energy of that state. In other terms, the energy landscape is conceived as the probability distributions of all conformational states of a protein. The shape of the surface is made of hills and valleys, which respectively stands for low and high probability states. The global minimum and local minima respectively represents native state and metastable states, which are separated by energy barriers (transition states).

The folding energy surface answered to the Levinthal's paradox [6], which wondered about how protein could fold rapidly given the vastness of the search space. The folding landscape has the shape of a funnel, with the bottom occupied by the folded state; the funnel means that multiple parallel pathways could lead from the multitude of unfolded states to the stable native state [7–11]. The shape of the funnel bottom represents the flexibility of the folded protein: if it is smooth, the protein is rigid, while if it is rugged, with numerous valleys separated by low energy barriers, the protein is flexible.

On this basis, the binding process could be explained in terms of binding energy landscape [5, 12]. Binding can be interpreted as a folding without chain connectivity, and thus with a greater number of degrees of freedom; this makes the binding energy landscape even more complicated than the folding one. Starting from the simpler example, where both the binding counterparts are rigid (i. e. smooth folding-funnel), recognition process can be conceived as the search for the global minimum of the free energy surface described by the three translational and rotational degrees of freedom of the ligand and the protein. If the interacting counterparts are both flexible (i. e. rugged folding-funnel bottom), they exist as an ensemble of different conformations, and each conformation of the ligand may in principle interact with each conformation of the protein, making the binding landscape really complex [13].

The binding event can stabilize one of the conformations of the protein, either the native or a different one; in the second case, a shift is induced in the equilibrium of protein populations [14].

“Population-shift” (“conformational selection”) differs from “induced-fit” in the chronological sequence of events that bring to binding, and have different ranges of applicability [15–17]; according to the first, the ligand picks one of the already available conformations of the protein, while, according to the second, the ligand induces the conformational rearrangement on the protein. These two models can be used to explain the behaviour of agonists, partial-agonists, antagonists and inverse agonists of G-protein coupled receptors, with rhodopsin activation by all-trans retinal well approximated by “induced fit”, while “conformational selection” is suggested for binding of agonists to β2-adrenergic receptor [15–17].

However, new models are emerging, trying to merge the aforementioned models: an “extended conformational selection model”, for example, has proposed a “conformational selection” followed by conformational adjustment (“induced fit”) [18].

2. Computational methods to study ligand-protein binding

The study of binding mechanism, beyond its epistemological purpose, has concrete applications in modern medicinal chemistry and drug design.

Since 1980s, computer technologies have been applied to the drug discovery process [19], giving rise to Computer-Aided Drug Design (CADD). This technique earned great interest soon and deserved a cover article on October 5, 1981 Fortune magazine, entitled "Next Industrial Revolution: Designing Drugs by Computer at Merck" [19]. CADD techniques are used principally for three reasons: virtual screening, *hit*/*lead* optimization and design of novel compounds. In virtual screening a huge database of compounds is examined searching for binding capacity for a target and a subset of compounds is picked out and suggested for *in vitro* testing; the purpose is to increase the *hit* rate of novel drugs by reducing the number of compounds to test experimentally. The second application of CADD is the optimization of *hit/lead* compounds driven by the rationalization of structure-activity relationship. After the individuation of key elements to bind a target, design of new compounds may be attempted.

CADD methods may be classified as ligand-based (LB) and structure-based (SB), depending on the availability and employment of the target structure [20]. In the framework of CADD, structure-based drug design (SBDD) methods take advantage of the abundance of experimentally solved structures in the Protein Data Bank [21], which can possibly be used also as templates for homology models if the structure of interest is lacking. SBDD is based on the premise that the knowledge of the target structure can help to rationalize and optimize binding, since ligand-target interactions are mediated by their complementarity. With the evolution of the binding models it is clear that speaking of "target structure" is an approximation, given that proteins fluctuate among an ensemble of structures [12].

The possibility to predict ligand binding modes and to interpret binding processes is valuable to individuate, optimize and suggest novel ligands, and for this reason the scientific community has been putting great efforts in developing new computational techniques since the 1980s.

In the following paragraphs we will present an excursus of the main structure-based computational techniques employed in drug-discovery, making a parallelism between them and the aforementioned ligand-protein binding models. In fact, during years, molecular modeling techniques have been experiencing a progressive inclusion of flexibility features in conformational sampling, moving from a static to a dynamic view. The more the flexibility, the higher the number of degrees of freedom of the system, and consequently the computational effort, so this new dynamic view has been made possible by the improvement of hardware technologies. In any case, because of computational limitations, different techniques are used to maximize the balance between efficacy and efficiency, depending on the purpose of their application: for example, in a virtual screening speed is essential, while slower but higher accurate techniques can be used to *hit/lead* optimization.

2.1 Molecular Docking

The primary aim of molecular docking is the prediction of the best matching binding mode of a ligand to a macromolecular partner (here just proteins are considered). It consists of the generation of a number of possible conformations-orientations, i.e. poses, of the ligand within the protein binding-site. For this reason, the availability of the three-dimensional structure of the molecular target is a necessary condition; it can be an experimentally solved structure (such as by X-ray crystallography or NMR) or a structure obtained by computational techniques (such as homology modeling).

Molecular docking is composed mainly by two stages: an engine for orientational/conformational sampling and a scoring function, which associate a score to each predicted pose [22–24]. The sampling process should effectively search the conformational space described by the free energy landscape, where energy, in docking, is approximated by the scoring function. The scoring function should be able to associate the native bound-conformation to the global minimum of the energy hypersurface.

2.1.1 Scoring functions

Scoring functions play the role of poses selector, being used to discriminate putative correct binding modes and binders from non-binders in the pool of poses generated by the sampling engine.

There are essentially three types of scoring functions:

1. *Force-field based scoring functions*:

Force-field is a concept typical of molecular mechanics (see Box 1) which approximates the potential energy of a system through a combination of bonded (intramolecular) and nonbonded (intermolecular) components. In molecular docking generally the nonbonded components are taken into account, with possibly the ligand bonded terms, especially the torsional components. Intermolecular components include the van der Waals term, described by the Lennard-Jones potential, and the electrostatic potential, described by the Coulomb function, where a distance-dependent dielectric may be introduced to consider the solvent effect. However, additional terms have been added to the force-field scoring functions, such as solvation terms. [25]

Examples of force field based scoring functions are: GoldScore [26], AutoDock [27], GBVI/WSA [28].

2. *Empirical scoring functions*:

These functions are the sum of various empirical energy terms such as van der Waals, electrostatics, hydrogen bond, desolvation, entropy, hydrophobicity, *etc.*, which are weighted by coefficients optimized to reproduce binding affinity data of a training set by least squares fitting [22].

The LUDI [29] scoring function was the first example of an empirical one. Other empirical scoring functions are: GlideScore [30, 31], ChemScore [32], PLANTS$_{\text{CHEMPLP}}$ [33].

3. *Knowledge-based scoring functions*:

These methods assume that ligand-protein contacts statistically more observed are correlated with favorable interactions. Starting from a database of structures, the frequencies of ligand-protein atom pairs contacts are computed and converted into an energy component. When evaluating a pose, the aforementioned tabulated energy components are summed up for all ligand-protein atom pairs, giving the score of the pose.

DrugScore [34] [35] and GOLD/ASP [36] are examples of knowledge-based scoring functions.

4. *Consensus Scoring*:

This strategy consists of the combination of multiple scoring functions [37].

In addition, new scoring function have been developed; for example there are application of machine learning, interaction fingerprints, attempts with quantum mechanical scores [38].

Box1

Molecular mechanics is a method which approximates the treatment of molecules with the laws of classical mechanics, in order to limit the computational cost required for quantum mechanical calculations [131]. Atoms are considered as charged spheres connected by springs, neglecting the presence of electrons, in accordance with Born-Oppenheimer approximation [132]. The potential energy is approximated by a simple function, the force-field, which is the sum of bonded (intramolecular) and nonbonded energy terms. The basic form of the function comprises, in the bonded portion, bond stretching and bending described by harmonic potential, and torsional potential described by a trigonometric function. Nonbonded terms consist of van der Waals and Coulomb electrostatic interactions between couples of atoms.

As an example, the basic components of the CHARMM [76] force field are reported in the following equations

$$V = V_{bonded} + V_{nonbonded}$$

$$V_{bonded} = \sum_{bonds} K_b(b - b_0)^2 + \sum_{angles} K_\theta(\theta - \theta_0)^2 + \sum_{dihedrals} K_\chi(1 + \cos(n\chi - \delta))$$

$$V_{nonbonded} = \sum_{\substack{nonbonded \\ pairs\ ij}} \frac{q_i q_j}{\varepsilon r_{ij}} + \sum_{\substack{nonbonded \\ pairs\ ij}} \varepsilon_{ij}\left[\left(\frac{R_{min,ij}}{r_{ij}}\right)^{12} - 2\left(\frac{R_{min,ij}}{r_{ij}}\right)^{6}\right]$$

where K_b, K_θ and K_χ are the bond, angle and torsional force constants; b, θ and χ are bond length, bond angle and dihedral angle (0-subscript for the equilibrium values); n is the multiplicity and δ the phase of the torsional periodic function; r_{ij} is the distance between atoms i and j; q_i and q_j are the partial charges of atoms i and j; ε is the effective dielectric constant; ε_{ij} is the Lennard-Jones well depth and $R_{min,ij}$ is the distance between atoms i and j at Lennard-Jones minimum.

These terms may appear slightly different in different force-fields, and anharmonicity and cross-terms are generally added.

The parameters of the force field are obtained by fitting quantum mechanical or experimental values.

2.1.2 Sampling

The first molecular docking algorithm was developed in the 1980s by Kuntz et al. [39]; the receptor was approximated by a series of spheres filling its surface clefts, and the ligand by another set of spheres defining its volume. A search was made to find the best steric overlap between binding site and receptor spheres, neglecting any kind of conformational movement.

This method is a fully-rigid docking, according to the classification of docking techniques based on the degrees of flexibility of simulated molecules [40]:

1. *Rigid docking*:

both ligand and protein are considered as rigid entities, and just the three translational and three rotational degrees of freedom are considered during sampling. This approximation is analogous to the "lock-key" binding model and is mainly used for protein-protein docking, where the number of conformational degrees of freedom is too high to be sampled.

Generally in these methods the binding site and the ligand are approximated by "hot" points and the superposition of matching points is evaluated [41]. An example is the Triangle Matcher approach of MOE Dock [28].

2. *Semi-flexible docking*:

just one of the molecules, the ligand, is flexible, while the protein is rigid. Thus, the conformational degrees of freedom of the ligand are sampled, in addition to the six translational plus rotational ones. These methods assume that a fixed conformation of a protein may correspond to the one able to recognize the ligands to be docked. This assumption, as already reported, is not always verified.

3. *Flexible docking*:

it introduces the concept that a protein is not a passive rigid entity during binding, but considers both ligand and protein as flexible counterparts. Different methods have been introduced during years, some rested on the induced fit binding model and others on conformational selection.

The increase of flexibility describes a system with a great number of degrees of freedom, in other terms, the potential energy surface is function of numerous coordinates. Consequently, the computational effort required to perform a docking calculation is augmented. Both sampling and scoring should be optimized to give a good balance between accuracy and speed. In fact, the industry-friendly application of docking in virtual screening campaign of millions of compounds depends on the velocity of docking calculations. For this reason, more and more improvements are made in the development of new algorithms, able to deeply search the phase space, but not at the expense of velocity.

2.1.3 Semi-flexible docking

Several docking algorithms have been developed since the 1980s. Often it is difficult to classify clearly each docking software, because different algorithms may be integrated in a multi-phase approach. However, docking algorithms can be classified as follows [22, 24]:

1. *Systematic search techniques*:

In systematic search a set of discretized values is associated to each degree of freedom, and all the values of each coordinate are explored in a combinatorial way [25]. These methods are subdivided into:

a. *Exhaustive search:*

it is a systematic search in the strict sense, since all the rotable bonds of the ligands are examined in a systematic way. A number of constraints and termination criteria is generally established to limit the search space and avoid a combinatorial explosion. The docking pipeline of the software Glide [30, 42] involves a stage of exhaustive search.

b. *Fragmentation*:

the first implementation of ligand flexibility into docking was introduced by Desjarlais [43], who proposed a method made of fragmentation of the ligand, rigid docking of the fragments into the binding site, and subsequent linking of the fragments. In this way, partial flexibility is implemented at the joints between the fragments. Other methods, defined as incremental construction, dock one fragment first and then attach incrementally the others. Examples of methods utilizing fragmentation are FlexX [44] and Hammerhead [45].

c. *Conformational Ensemble*:

Rigid docking algorithms can be easily enriched by a sort of flexibility if an ensemble of previously generated conformers of the ligand is docked to the target, in a sort of conformational selection fashion on the ligand counterpart. Examples are offered by FLOG [46], EUDOC [47], MS-DOCK [48].

2. *Stochastic methods*:

Stochastic algorithms change randomly, instead of systematically, the values of the degrees of freedom of the system. The advantage of these techniques is the speed, so they could potentially find the optimal solution really fast. As a drawback, they do not ensure a full search of the conformational space, so the true solution may be missed. The lack of convergence is partially solved by increasing the number of iterations of the algorithm. The most famous stochastic algorithms are [22] :

a. *Monte Carlo (MC) methods*:

Monte Carlo methods are based on the Metropolis Monte Carlo algorithm, which introduces an acceptance criterion in the evolution of the docking search. In particular, at every iteration of the algorithm, a random modification of the ligand degrees of freedom is performed. Then, if the energy score of the pose is improved, the change is accepted, otherwise it is accepted according to the probability expressed in the following equation:

$$P \sim exp\left[\frac{-(E_1 - E_0)}{k_B T}\right]$$

where E_1 and E_0 are the energy score before and after the modification, k_B the Boltzmann constant, and T the temperature of the system.

This is the original form of Metropolis algorithm, but it is implemented in different variants within docking softwares. Some example are provided by the earlier versions of AutoDock [49, 50], ICM [51], QXP [52], MCDOCK [53], AutoDock Vina [54], ROSETTALIGAND [55].

b. *Tabu search methods*:

The aim of these algorithms is to prevent the exploration of already sampled zones of the conformational/positional space. Random modifications are performed on the degrees of freedom of the ligand at each iteration. The already sampled conformations are registered, and when a new pose is obtained, it is accepted only if not similar to any pose already explored. PRO_LEADS [56] and PSI-DOCK [57] are two examples of this category.

c. *Evolutionary Algorithms* (EA):

These algorithms are based on the idea of biological evolution, with the most famous ones coinciding with Genetic Algorithms (GAs). The concept of gene, chromosome, mutation and crossover are borrowed from biology. In particular, the degrees of freedom are encoded into genes, and each conformation of the ligand is described by a chromosome (collection of genes), which is assigned a fitness score. Mutations and crossovers occur within a population of chromosomes, and chromosomes with higher fitness survive and replace the worst ones. The most famous examples are GOLD [58, 59], AutoDock 3 & 4 (which implement a different version of GA, the Lamarckian GA) [27], PSI-DOCK [57], rDock [60].

d. *Swarm optimization (SO) methods*:

These methods take inspiration by swarm behaviour. The sampling of the degrees of freedom of a ligand is guided by the information deposited by good poses already sampled. For example, PLANTS [61] adopts an ACO (Ant Colony Optimization) algorithm mimicking the behaviour of ants, that communicate the easiest way to reach a source of food through the deposition of pheromone. Here, each degree of freedom is associated to a pheromone. Virtual ants choose conformations considering the values of pheromones, and successful ants contribute in pheromone deposition.

Other examples of SOs are: SODOCK [62], pso@autodock [63], PSOVina [64].

3. Simulation methods:

The most famous example of this category is Molecular Dynamics, a method that describes the time evolution of a system. A wider explanation will be given in the paragraph 2.2.1.

Energy minimization methods can be inserted in this category, but generally they are not used as stand-alone search engines [24]. Energy minimization is a local optimization technique, used to bring the system to the closest minimum on the potential energy surface.

2.1.4 Flexible docking

Some attempts have been made to introduce protein flexibility into docking calculations. These methods take advantage of different degrees of approximation and can be divided into approaches that consider single protein or multiple protein conformations [65].

1. *Single Protein Conformation*:

   a. *Soft docking:*

   This method, first described by Jiang and Kim [66], consists of an implicit and rough treatment of protein flexibility. The van der Waals repulsion term employed in force field scoring functions is reduced, allowing small clashes that permit a closer ligand-protein packing. In this way, a sort of induced-fit is simulated. As a drawback, this approach approximates just feeble protein movements, and could implicate unreal poses. [67, 68]

   b. *Sidechain flexibility*:

   This strategy introduces alternative conformations for some protein side chains [69]. This is generally done exploiting databases of rotamer libraries. Some docking methods, such as GOLD, sample some side chains degrees of freedom within their own search engine. Obviously, considering side chain flexibility, huge conformational variations of the protein are neglected by these methods.

2. *Multiple Protein Conformations*:

Multiple experimental structures may be available for the same target. Moreover, an ensemble of protein conformations can be obtained via computational techniques, such as Monte Carlo or Molecular Dynamics simulations. The idea of multiple protein conformations docking is to take into account all the diverse structures, following different possible strategies:

   a. *Average grid*:

   The structures of the ensemble are used to construct a single average-grid, which can be either a simple or weighted average combination of them [70].

   b. *United description of the protein*:

   In this case the structures do not collapse into an average grid, but are used to construct the best performing “chimera” protein. For example, FlexE [44] extracts the structurally conserved portions from the structures of the ensemble, and use them to construct an average rigid structure. This portion is fused to the flexible parts of the ensemble in a combinatorial fashion, giving a pool of “chimeras” that are used for docking.

c. *Individual conformations*:

The structures of the ensemble are considered as conformations that can possibly be bound by the ligand, so various docking run are performed, evaluating the ligands of interest on all the target conformations [71].

In light of the last considerations about multiple protein conformations docking, in the following section a deep insight will be given into Molecular Dynamics, firstly as a tool to generate ensemble of conformations, and secondly as a docking method itself.

2.2 Molecular Dynamics

Molecular dynamics (MD) is a computational technique that simulates the dynamic behaviour of molecular systems as a function of time, treating as flexible all the entities in the simulation box (ligand, protein, as well as water if explicit).

It was developed to simulate simple systems, with the first application to study collisions among hard spheres, in 1957 [72]. The first MD simulation of a biomolecule was accomplished in 1977 by McCammon et al. [73]; it was a 9.2 ps simulation of a 58-residues Bovine Pancreatic Trypsin Inhibitor (BPTI), carried out in vacuum with a crude molecular mechanics potential.

Molecular dynamics computes the movements of atoms along time by the integration of the Newton's equations of motions (classical mechanics), reported in the following equation [74, 75]:

$$\frac{\mathrm{d}^2 r_i(t)}{\mathrm{d}t^2} = \frac{F_i(t)}{m_i}$$

with *F_i(t)* force exterted on atom *i* at time *t*, *r_i(t)* vector position of atom *i* at time *t*, *m_i* mass of atom *i*.

In particular, time is partitioned into time steps (*δt*), which are used to propagate the system forward in time. Several integration algorithms are available, which derive Newton's equations by a discrete-time numerical approximation. The velocity-Verlet integrator is reported in the following equations as an example to compute position and velocity of an atom *i* at the time step *t+δt*, starting from step *t*.

$$r_i(t+\delta t) = r_i(t) + v_i(t)\delta t + \frac{1}{2}a_i(t)\delta t^2$$

$$v_i(t+\delta t) = v_i(t) + \frac{1}{2}\left[a_i(t) + a_i(t+\delta t)\right]\delta t$$

where *r_i(t)*, *v_i(t)* and *a_i(t)* are respectively position, velocity and acceleration of atom *i* at time *t*, and *r_i(t+δt)*, *v_i(t+δt)* and *a_i(t+δt)* are respectively position, velocity and acceleration of atom *i* at time *t+δt*.

Acceleration is calculated from the forces acting on atom *i* according to Newton's second law, and forces are computed from the force field, according to the following equation:

$$a_i(t) = \frac{\mathrm{d}^2 r_i(t)}{\mathrm{d}t^2} = \frac{F_i(t)}{m_i} = -\frac{\mathrm{d}V(r(t))}{\mathrm{d}r_i(t)}$$

where *V(r(t))* is the potential energy function retrieved by the force field (see box1).

The most used force field in molecular dynamics are CHARMM [76], AMBER [77], OPLS [78] and GROMOS [79].

2.2.1 Molecular Dynamics and exploration of the phase space

MD trajectories can be considered as sampling engines; in fact, they produce protein conformations usable for Multiple Protein Conformations docking applications. In particular, McCammon et al. developed the so called Relaxed-Complex Scheme (RCS): mini-libraries of compounds are docked by AutoDock [27] against a large ensemble of snapshots derived from unliganded protein MD trajectories [80–82]. This approach is founded on the conformational selection binding model.

Alternative conformers obtained through MD can also give insights into cryptic or allosteric binding sites [83]. For example, Schame et al. identified an alternative binding site, named “trench”, close to the active site of the HIV-1 integrase [84].

MD has further applications as a docking-coupled technique. In particular it can be used for the assessment of the stability and for the refinement of docking poses; incorrect poses are likely to be unstable and dissociate from the complex, while realistic ones will be stable [65].

Moreover, simulations in explicit solvent may enable to estimate the contribution of water during binding; for example, Klebe et al. developed a method to compute surface water networks that play a role in modulating binding affinities [85].

All the aforementioned applications of molecular dynamics are used as a complement to classic molecular docking techniques, but molecular dynamics itself can be interpreted as a docking method. In principle, the simulation of the complete binding process of a ligand, from the unbound state in bulk solvent to the bound state, would be a fully-flexible docking in explicit solvent. The possibility to investigate the whole binding process could give insights into: metastable states reached by the ligand during the simulation, alternative binding sites, the role of water during binding and conformational rearrangements preceding, concurrent or consecutive to binding.

However, the observation of a binding event during a classical MD simulation is very rare, raising the timescale problem. The timestep in molecular dynamics must be compatible with the fastest motion in the system; in particular, a timestep of 1-2 fs, corresponding to bond vibrations, has to be used. Thus, an high number of MD steps is required to simulate slow processes, such as large domains motions and binding (µs-ms) [86], making the computational effort really hard. In particular, slow timescales are linked to processes that require the overcoming of a high energy barrier [86], corresponding to low populated states in the conformational energy landscape; in this case the simulated system gets trapped in a local minimum, making classical MD inadequate to explore largely the conformational space.

2.2.2 Advances in classical MD simulations

In 1998 Duan and Kollman performed the first 1µs simulation of a protein in explicit solvent, observing the folding of a 36-residue villin headpiece subdomain from a fully unfolded state. This simulation was two orders of magnitude longer than a state-of-the-art simulation of that period, and it was made possible by advances in massively parallel supercomputers and efficient parallelized codes, but still required 2 months of CPU (Central Processing Units) time [87].

Specialized machines have also been designed specifically for MD calculations; for example, a supercomputer named Anton was conceived as a "computational microscope" and was developed with the idea to reach previously inaccessible simulation timescales within a reasonable computation time[88]. This machine has allowed Shaw et al. to characterize the folding of FiP35 WW domain from a fully extended state in a 100 µs simulation and, in addition, to reach the ms timescale in a single simulation of BPTI in the folded-state[89], followed recently by ubiquitin [90]. Moreover, with unbiased simulations in the order of ten µs, Shaw's group could simulate the complete binding process of beta blockers and agonists to β_2-adrenergic receptor [91] and kinase inhibitors to Src kinase [92].

As a drawback, the utilization of supercomputers is an expense that not many research groups can afford. The development of code able to exploit the speed of GPUs (Graphic Processing Units) has given access to long-timescale simulations at relatively low cost [93–95]. In fact, nowadays, simulations of hundreds of nanoseconds are easily performed, and reaching the microsecond timescale is an affordable issue on a GPU-equipped workstation [96].

Moreover, a paradigm shift seems to have been spreading, that is the possibility to simulate long processes using numerous trajectories shorter than the process itself instead of a single long trajectory. This idea has been exploited by the folding@home project, a worldwide distributed computing environment benefitting from the computers of private citizens, when not in use [97]. Since during a classical MD simulation the system is stuck in a minimum, waiting for the fortunate event that triggers the overcoming of an energy barrier, the simulation of many trajectories in parallel would increase the probability to meet the lucky event. Thus, numerous simulations are started from the same initial condition and run in parallel on different computers, and when one escapes from the energy minimum, all the simulations are stopped and started from the new productive configuration [98].

The new paradigm has found its best application in the use of Markov State Models (MSMs) and adaptive sampling. In fact, MSMs are based on an ensemble view of the dynamics, from which statistical properties, such as the probability to occupy a state and the probability to jump from one state to another, are computed. The construction of a Markov model is made of the discretization and projection of a trajectory into microstates, and of the computation of a transition probability matrix T(τ) at a given time, the lagtime τ, chosen in a way that the transition is memory-less (Markovian). Each element $T_{ij}(\tau)$ of the transition matrix represents the conditional probability to find the system in state *j* at time *t*+ τ while being in state *i* at time *t*. The transition matrix approximates the dynamic of the system, and enables to compute the free energy from the equilibrium probability distribution and to extrapolate the timescales of the slowest processes, even if they are not directly explored. On a qualitative fashion, the MSM may individuate diverse metastable states and construct multi-states models of the processes [99]. As an example, a MSM was constructed on an aggregate of nearly 500 100ns-trajectories describing benzamidine-trypsin binding (with 37% productive trajectories); this enabled to characterize the binding process individuating three transition states, and to estimate binding free energy with 1 kcal/mol difference from the experimental one (while a higher deviation from experiment was associated with the extrapolated k_{on} and k_{off}) [100]. Moreover, the computation of MSM on the collected data can give a feedback about undersampled zones of the phase space, suggesting where to focus further simulation, adapting the sampling (adaptive sampling methods) and increasing the efficiency of simulations [101, 102]. Currently, the major difficulties of this technique are related to the trajectories partition into discrete states, to the choice of the lagtime and to sufficient sampling able to guarantee statistical significance [103].

Several alternative techniques have been developed during the years to overcome the time limitation imposed by classical MD simulations. A first example consists in the Coarse Grained MD simulations, in which groups of atoms are condensed into spheres, reducing the degrees of freedom of the system [104]. This simplifies the conformational landscape of the system, but, as a drawback, the information on the all-atom simulations, that are precious for drug-discovery aim, are lost.

Additional strategies consist of enhanced sampling techniques that apply a bias to molecular dynamics simulations to increase the accessible timescale, enabling the simulation of slow processes like binding, unbinding and folding processes in reduced amount of time.

2.2.3 Enhanced sampling techniques

These methods add a bias force/potential to the system to increase the rate of escape from local minima, entailing an acceleration of conformational sampling. These methods have been conceived primarily to study either folding, binding or unbinding processes, sharing the underlying idea of sampling enhancement and overcoming high energy barriers.

Enhanced sampling techniques can be divided into methods that make use of collective variables to introduce the bias and methods that do not [105].

The employment of a collective variable (CV) is based on the idea that a complex system can be decomposed into one or a combination of reaction coordinates describing the process of interest. These coordinates are named collective variables since it is assumed they can summarize the behaviour of the entire system. After a careful choice of the CVs, the bias is added on these coordinates during the simulation enhancing sampling along the CVs. The phase space is reduced to the space of the collective variables, since the conformational space is projected to the selected CVs, with a consequent dimensional reduction of the free energy surface.

In the following paragraphs few representative enhanced sampling techniques are reported as an example.

2.2.3.1 Collective Variables-free methods

Replica Exchange Molecular Dynamics (REMD)

This method increases the temperature to accelerate the conformational sampling. The first formulation of Replica Exchange MD[106], also known as Parallel Tempering (PT), consists of the parallel simulation of a number of independent and simultaneous replicas of the same system, starting from the same configuration, but at different temperatures. At regular time intervals, two replicas characterized by neighbour temperatures are switched, or, in other terms, their temperatures are exchanged, with a probability determined by the energy (*E*) and temperature (*T*) of the system. In particular, the transition probability between simulations at temperatures T_1 and T_2 is determined by the Metropolis criterion:

$$P(T_1 \rightarrow T_2) = \begin{cases} 1 & for\ [\beta_2 - \beta_1](E_1 - E_2)\ \leq 0 \\ e^{-[\beta_2 - \beta_1](E_1 - E_2)} & for\ \ [\beta_2 - \beta_1](E_1 - E_2) > 0 \end{cases}$$

where $\beta=1/k_BT$ (with k_B the Boltzmann constant).

Temperatures are updated by rescaling the velocities of the parent simulations (v_1 and v_2 to v_1' and v_2') according to the following equation:

$$\begin{cases} v_1' = \sqrt{\dfrac{T_2}{T_1}} v_1 \\ v_2' = \sqrt{\dfrac{T_1}{T_2}} v_2 \end{cases}$$

The choice of the panel of temperatures is critical, and various strategies have been proposed to guide the selection [107].

REMD have been developed in several directions; for example in Hamiltonian Replica Exchange multiple Hamiltonians are used instead of temperatures [108]. REMD is mainly used to study protein folding, but applications to ligand binding can be found in literature [109].

Accelerated Molecular Dynamics (aMD)

Accelerated MD (aMD) facilitates the egress from a low energy basin by adding a bias potential function (*ΔV(r)*) when the system is entrapped in an energy minimum. In particular, when the potential energy (*V(r)*) is lower than a certain cutoff (*E*), the bias is added giving a modified potential (*V*(r)*=*V(r)*+ *ΔV(r)*); otherwise the simulation continues in the true-unbiased potential (*V*(r)*=*V(r)*).

The bias function is reported in the following equation:

$$\Delta V(r) = \frac{(E - V(r))^2}{\alpha + (E - V(r))}$$

where *E* is the potential energy cutoff and *α* is a tuning parameter determining the depth of the modified potential energy basin.

E has to be at least greater than V_{min} (the minimum potential energy, close to the starting configuration), while $\alpha = E - V_{min}$ will allow to maintain the underlying shape of the landscape [110]. A recent application of aMD has enabled the investigation of the significant conformational changes that P2Y1 receptor undergoes after activation [111].

2.2.3.2 Collective Variables-dependent methods

Steered Molecular Dynamics (SMD)

Taking inspiration from atomic force microscopy experiments, in Steered MD (SMD) an external force is applied to a ligand to drive it out of the target binding site [112]. In this way, SMD simulations can lead to the individuation of unbinding pathways, that can be used also to make inference on possible binding roots; in addition, the added force is assumed to be related to the binding strength.

The first implementations of SMD dealt with anchoring the ligand to a virtual spring, that can either have a constant stiffness and be pulled with constant speed on the free end [113], or have an increasing stiffness and be fixed on the free end at a distance larger than the unbinding pathway [114]. Other possibilities involve constant forces or application of forces on different CVs, such as nonlinear coordinates that can help to explore conformational rearrangement of protein domains [115]. SMD relies on an a priori definition of the applied force direction, which can be fixed (for example a simple straight line) or change during the simulation. The choice of the direction is not easy, because a ligand may bump into obstructions during its way out of the protein, but a method evaluating the minimal steric hindrance has been reported [116]. Moreover, integration with the targeted molecular dynamics (TMD) are reported: in TMD a bias force is applied to conduct the system from an initial to a desired final configuration [117], leading to the individuation of a path that can be used as set of directions for a SMD simulation [112].

Random Acceleration Molecular Dynamics (RAMD)

Random Acceleration MD (RAMD), also defined Random Expulsion MD, is an extension of SMD, and, like this, was developed to study the egress of a ligand from its target binding site. It consists in the application of an artificial randomly-directed force on a ligand to accelerate its unbinding. In this way, in comparison with SMD, RAMD avoids the preliminary choice of the force direction; consequently, if some obstructions are found during the exit pathway, the escape direction is switched.

In particular, the direction of the force is chosen stochastically and maintained for a number of MD steps. If during this time interval the average velocity of the ligand is lower than a specified cut-off (or, in other terms, if the distance covered by the ligand is lower than a cutoff distance, r_{min}), meaning that probably a rigid obstruction has been met, a new force direction is assigned to allow the ligand to search for alternative exit pathways [118].

Umbrella Sampling (US)

Umbrella Sampling (US) [119] consists in restraining the system along one or a combination of CVs. Commonly, the CV range of interest is divided into windows, each characterized by a CV reference value (ξ_{ref}). A bias potential enhances sampling in each window by forcing the system to stay close to the respective CV reference value. The bias is function of the reaction coordinate, and can have different shape, but generally consists in a simple harmonic, as in the following equation:

$$V(\xi) = \frac{k}{2}\,(\xi - \xi_{ref})^2$$

Where k is the strength of the potential and ξ is the value of the CV.

The strength of the bias must be high enough to let energy barriers crossing, but sufficiently low to let system distributions of different windows to overlap, which is required for post-processing analysis.

The aim of US is to force sampling in each window to collect sufficient statistics along the whole reaction coordinate. Then the distribution of the system along the CV is calculated, and from this the free energy along the CV [120]. Different post-processing methods can be used to perform combination and analysis of the data coming from the different US windows; the most famous are umbrella integration [121], the weighted histogram analysis method (WHAM) [122], and the more recent Dynamic Weighted Histogram Analysis (DHAM) [123], which can be used also to derive kinetic parameters.

Metadynamics

Metadynamics [124] introduces a bias potential to the Hamiltonian of the system in the form of a Gaussian-shaped function of one or more collective variables. In this case, the bias does not restrain or constrain the system, neither it forces the system along a preferable direction in the CV space. The bias is used to keep memory of the already explored zones of the phase space, and to discourage the system to visit them again [125].

At time t, the bias potential ($V_G(S,t)$) is reported in the following equation:

$$V_G(S,t) = \int_0^t \mathrm{d}t'\omega \exp\left(- \sum_{i=1}^{d} \frac{(S_i(R) - S_i\big(R(t')\big))^2}{2\sigma_i^2} \right)$$

where $S(R)=(S_1(R),...,S_d(R))$ is a set of d CVs (which ar functions of the coordinates R of the system), $S_i(R(t))$ is the value of the ith CV at time t, σ_i is the Gaussian width for the ith CV, and ω is the energy rate, given by:

$$\omega = \frac{W}{\tau_G}$$

with W the Gaussian height and τ_G the deposition rate.

Thus, the bias is “history-dependent”, because it is the sum of the Gaussians that have already been deposited in the CV space during time.

The free energy landscape is explored, starting from the bottom of a well, by a random walk; bias-Gaussians are deposited in the CV space with a given frequency, and at each iteration the bias is the sum of the already deposited Gaussians. As time goes by, the system, instead of being trapped in the bottom of a well, is pushed out by the hill of deposited Gaussians, and enters a new minimum. The process continues until all the minima are compensated by the bias potential[126].

In this way, metadynamics enables to enhance sampling and to reconstruct the free energy surface; this can be used to explore binding/unbinding processes [127], and, with the application of funnel metadynamics [128], to the estimation of binding free energy.

Unfortunately, it may occur that the free energy surface is overfilled, but this has been partially solved by well-tempered metadynamics, in which the height of the added Gaussian is rescaled by the already deposited bias [129]. Another issue with metadynamics is the choice of the CVs, which should describe the slowest motions of the system and the initial-final-relevant intermediates. Moreover, a small number of CVs must be used, so a good strategy is the combination with techniques able to enhance sampling along a great number of transverse coordinates[126], such as parallel tempering [130].

References

1. Fischer E (1894) Einfluss der Configuration auf die Wirkung der Enzyme. Berichte der deutschen chemischen Gesellschaft 27:2985–2993

2. Koshland DE (1958) Application of a Theory of Enzyme Specificity to Protein Synthesis. Proc Natl Acad Sci U S A 44:98–104

3. Austin RH, Beeson KW, Eisenstein L, Frauenfelder H, Gunsalus IC (1975) Dynamics of ligand binding to myoglobin. Biochemistry 14:5355–5373

4. Foote J, Milstein C (1994) Conformational isomerism and the diversity of antibodies. Proc Natl Acad Sci U S A 91:10370–10374

5. Frauenfelder H, Sligar SG, Wolynes PG (1991) The energy landscapes and motions of proteins. Science 254:1598–1603

6. Levinthal C (1968) Are there pathways for protein folding? Journal de chimie physique 65:44–45

7. Leopold PE, Montal M, Onuchic JN (1992) Protein folding funnels: a kinetic approach to the sequence-structure relationship. Proc Natl Acad Sci U S A 89:8721–8725

8. Onuchic JN, Socci ND, Luthey-Schulten Z, Wolynes PG (1996) Protein folding funnels: the nature of the transition state ensemble. Fold Des 1:441–450

9. Dill KA (1999) Polymer principles and protein folding. Protein Sci 8:1166–1180

10. Dill KA, Chan HS (1997) From Levinthal to pathways to funnels. Nat Struct Biol 4:10–19

11. Bryngelson JD, Wolynes PG (1989) Intermediates and barrier crossing in a random energy model (with applications to protein folding). J Phys Chem 93:6902–6915

12. Miller DW, Dill KA (1997) Ligand binding to proteins: the binding landscape model. Protein Sci 6:2166–2179

13. Tsai CJ, Kumar S, Ma B, Nussinov R (1999) Folding funnels, binding funnels, and protein function. Protein Sci 8:1181–1190

14. Kumar S, Ma B, Tsai CJ, Sinha N, Nussinov R (2000) Folding and binding cascades: dynamic landscapes and population shifts. Protein Sci 9:10–19

15. Okazaki K-I, Takada S (2008) Dynamic energy landscape view of coupled binding and protein conformational change: induced-fit versus population-shift mechanisms. Proc Natl Acad Sci U S A 105:11182–11187

16. Zhou H-X (2010) From induced fit to conformational selection: a continuum of binding mechanism controlled by the timescale of conformational transitions. Biophys J 98:L15–7

17. Deupi X, Kobilka BK (2010) Energy landscapes as a tool to integrate GPCR structure, dynamics, and function. Physiology (Bethesda) 25:293–303

18. Csermely P, Palotai R, Nussinov R (2010) Induced fit, conformational selection and independent dynamic segments: an extended view of binding events. Trends Biochem Sci 35:539–546

19. Van Drie JH (2007) Computer-aided drug design: the next 20 years. J Comput Aided Mol Des 21:591–601

20. Sliwoski G, Kothiwale S, Meiler J, Lowe EW (2014) Computational methods in drug discovery. Pharmacol Rev 66:334–395

21. Berman HM, Westbrook J, Feng Z, Gilliland G, Bhat TN, Weissig H, Shindyalov IN, Bourne PE (2000) The protein data bank. Nucleic Acids Res 28:235–242

22. Huang S-Y, Zou X (2010) Advances and challenges in protein-ligand docking. Int J Mol Sci 11:3016–3034

23. Abagyan R, Totrov M (2001) High-throughput docking for lead generation. Curr Opin Chem Biol 5:375–382

24. Kitchen DB, Decornez H, Furr JR, Bajorath J (2004) Docking and scoring in virtual screening for drug discovery: methods and applications. Nat Rev Drug Discov 3:935–949

25. Brooijmans N, Kuntz ID (2003) Molecular recognition and docking algorithms. Annu Rev Biophys Biomol Struct 32:335–373

26. Verdonk ML, Cole JC, Hartshorn MJ, Murray CW, Taylor RD (2003) Improved protein-ligand docking using GOLD. Proteins 52:609–623

27. Morris GM, Goodsell DS, Halliday RS, Huey R, Hart WE, Belew RK, Olson AJ (1998) Automated docking using a Lamarckian genetic algorithm and an empirical binding free energy function. J Comput Chem 19:1639–1662

28. Corbeil CR, Williams CI, Labute P (2012) Variability in docking success rates due to dataset preparation. J Comput Aided Mol Des 26:775–786

29. Böhm HJ (1994) The development of a simple empirical scoring function to estimate the binding constant for a protein-ligand complex of known three-dimensional structure. J Comput Aided Mol Des 8:243–256

30. Halgren TA, Murphy RB, Friesner RA, Beard HS, Frye LL, Pollard WT, Banks JL (2004) Glide: a new approach for rapid, accurate docking and scoring. 2. Enrichment factors in database screening. J Med Chem 47:1750–1759

31. Friesner RA, Murphy RB, Repasky MP, Frye LL, Greenwood JR, Halgren TA, Sanschagrin PC, Mainz DT (2006) Extra precision glide: docking and scoring incorporating a model of hydrophobic enclosure for protein-ligand complexes. J Med Chem 49:6177–6196

32. Eldridge MD, Murray CW, Auton TR, Paolini GV, Mee RP (1997) Empirical scoring functions: I. The development of a fast empirical scoring function to estimate the binding affinity of ligands in receptor complexes. J Comput Aided Mol Des 11:425–445

33. Korb O, Stützle T, Exner TE (2009) Empirical scoring functions for advanced protein-ligand docking with PLANTS. J Chem Inf Model 49:84–96

34. Gohlke H, Hendlich M, Klebe G (2000) Knowledge-based scoring function to predict protein-ligand interactions. J Mol Biol 295:337–356

35. Velec HFG, Gohlke H, Klebe G (2005) DrugScore(CSD)-knowledge-based scoring function derived from small molecule crystal data with superior recognition rate of near-native ligand poses and better affinity prediction. J Med Chem 48:6296–6303

36. Mooij WTM, Verdonk ML (2005) General and targeted statistical potentials for protein-ligand interactions. Proteins 61:272–287

37. Charifson PS, Corkery JJ, Murcko MA, Walters WP (1999) Consensus scoring: A method for obtaining improved hit rates from docking databases of three-dimensional structures into proteins. J Med Chem 42:5100–5109

38. Yuriev E, Holien J, Ramsland PA (2015) Improvements, trends, and new ideas in molecular docking: 2012-2013 in review. J Mol Recognit 28:581–604

39. Kuntz ID, Blaney JM, Oatley SJ, Langridge R, Ferrin TE (1982) A geometric approach to macromolecule-ligand interactions. J Mol Biol 161:269–288

40. Halperin I, Ma B, Wolfson H, Nussinov R (2002) Principles of docking: An overview of search algorithms and a guide to scoring functions. Proteins 47:409–443

41. Taylor RD, Jewsbury PJ, Essex JW (2002) A review of protein-small molecule docking methods. J Comput Aided Mol Des 16:151–166

42. Friesner RA, Banks JL, Murphy RB, et al (2004) Glide: a new approach for rapid, accurate docking and scoring. 1. Method and assessment of docking accuracy. J Med Chem 47:1739–1749

43. DesJarlais RL, Sheridan RP, Dixon JS, Kuntz ID, Venkataraghavan R (1986) Docking flexible ligands to macromolecular receptors by molecular shape. J Med Chem 29:2149–2153

44. Rarey M, Kramer B, Lengauer T, Klebe G (1996) A fast flexible docking method using an incremental construction algorithm. J Mol Biol 261:470–489

45. Welch W, Ruppert J, Jain AN (1996) Hammerhead: fast, fully automated docking of flexible ligands to protein binding sites. Chem Biol 3:449–462

46. Miller MD, Kearsley SK, Underwood DJ, Sheridan RP (1994) FLOG: a system to select “quasi-flexible” ligands complementary to a receptor of known three-dimensional structure. J Comput Aided Mol Des 8:153–174

47. Pang Y-P, Perola E, Xu K, Prendergast FG (2001) EUDOC: a computer program for identification of drug interaction sites in macromolecules and drug leads from chemical databases. Journal of computational chemistry 22:1750–1771

48. Sauton N, Lagorce D, Villoutreix BO, Miteva MA (2008) MS-DOCK: accurate multiple conformation generator and rigid docking protocol for multi-step virtual ligand screening. BMC Bioinformatics 9:184

49. Goodsell DS, Olson AJ (1990) Automated docking of substrates to proteins by simulated annealing. Proteins 8:195–202

50. Morris GM, Goodsell DS, Huey R, Olson AJ (1996) Distributed automated docking of flexible ligands to proteins: parallel applications of AutoDock 2.4. J Comput Aided Mol Des 10:293–304

51. Abagyan R, Totrov M, Kuznetsov D (1994) ICM?A new method for protein modeling and design: Applications to docking and structure prediction from the distorted native conformation. J Comput Chem 15:488–506

52. McMartin C, Bohacek RS (1997) QXP: powerful, rapid computer algorithms for structure-based drug design. J Comput Aided Mol Des 11:333–344

53. Liu M, Wang S (1999) MCDOCK: a Monte Carlo simulation approach to the molecular docking problem. J Comput Aided Mol Des 13:435–451

54. Trott O, Olson AJ (2010) AutoDock Vina: improving the speed and accuracy of docking with a new scoring function, efficient optimization, and multithreading. J Comput Chem 31:455–461

55. Meiler J, Baker D (2006) ROSETTALIGAND: protein-small molecule docking with full side-chain flexibility. Proteins 65:538–548

56. Baxter CA, Murray CW, Clark DE, Westhead DR, Eldridge MD (1998) Flexible docking using tabu search and an empirical estimate of binding affinity. Proteins 33:367–382

57. Pei J, Wang Q, Liu Z, Li Q, Yang K, Lai L (2006) PSI-DOCK: towards highly efficient and accurate flexible ligand docking. Proteins 62:934–946

58. Jones G, Willett P, Glen RC, Leach AR, Taylor R (1997) Development and validation of a genetic algorithm for flexible docking. J Mol Biol 267:727–748

59. Jones G, Willett P, Glen RC (1995) Molecular recognition of receptor sites using a genetic algorithm with a description of desolvation. J Mol Biol 245:43–53

60. Ruiz-Carmona S, Alvarez-Garcia D, Foloppe N, Garmendia-Doval AB, Juhos S, Schmidtke P, Barril X, Hubbard RE, Morley SD (2014) rDock: a fast, versatile and open source program for docking ligands to proteins and nucleic acids. PLoS Comput Biol 10:e1003571

61. Korb O, Stützle T, Exner TE (2006) PLANTS: Application of Ant Colony Optimization to Structure-Based Drug Design. In: Dorigo M, Gambardella LM, Birattari M, Martinoli A, Poli R, Stützle T (eds) Ant Colony Optimization and Swarm Intelligence. Springer Berlin Heidelberg, pp 247–258

62. Chen H-M, Liu B-F, Huang H-L, Hwang S-F, Ho S-Y (2007) SODOCK: swarm optimization for highly flexible protein-ligand docking. J Comput Chem 28:612–623

63. Namasivayam V, Günther R (2007) pso@autodock: a fast flexible molecular docking program based on Swarm intelligence. Chem Biol Drug Des 70:475–484

64. Ng MCK, Fong S, Siu SWI (2015) PSOVina: The hybrid particle swarm optimization algorithm for protein-ligand docking. J Bioinform Comput Biol 13:1541007

65. Alonso H, Bliznyuk AA, Gready JE (2006) Combining docking and molecular dynamic simulations in drug design. Med Res Rev 26:531–568

66. Jiang F, Kim SH (1991) Soft docking": matching of molecular surface cubes. J Mol Biol 219:79–102

67. Vieth M, Hirst JD, Koliński A, Brooks III CL (1999) Assessing energy functions for flexible docking. J Comput Chem 19:

68. Apostolakis J, Plückthun A, Caflisch A (1998) Docking small ligands in flexible binding sites. J Comput Chem 19:21–37

69. Leach AR (1994) Ligand docking to proteins with discrete side-chain flexibility. J Mol Biol 235:345–356

70. Knegtel RM, Kuntz ID, Oshiro CM (1997) Molecular docking to ensembles of protein structures. J Mol Biol 266:424–440

71. Huang S-Y, Zou X (2007) Ensemble docking of multiple protein structures: considering protein structural variations in molecular docking. Proteins 66:399–421

72. Alder BJ, Wainwright TE (1957) Phase transition for a hard sphere system. J Chem Phys 27:1208–1209

73. McCammon JA, Gelin BR, Karplus M (1977) Dynamics of folded proteins. Nature 267:585–590

74. Adcock SA, McCammon JA (2006) Molecular dynamics: survey of methods for simulating the activity of proteins. Chem Rev 106:1589–1615

75. Leach AR (2001) Molecular Modelling: Principles and Applications, illustrated. Pearson Education

76. MacKerell AD, Bashford D, Bellott M, et al (1998) All-atom empirical potential for molecular modeling and dynamics studies of proteins. J Phys Chem B 102:3586–3616

77. Cornell WD, Cieplak P, Bayly CI, Gould IR, Merz KM, Ferguson DM, Spellmeyer DC, Fox T, Caldwell JW, Kollman PA (1995) A Second Generation Force Field for the Simulation of Proteins, Nucleic Acids, and Organic Molecules. J Am Chem Soc 117:5179–5197

78. Jorgensen WL, Tirado-Rives J (1988) The OPLS [optimized potentials for liquid simulations] potential functions for proteins, energy minimizations for crystals of cyclic peptides and crambin. J Am Chem Soc 110:1657–1666

79. Oostenbrink C, Villa A, Mark AE, van Gunsteren WF (2004) A biomolecular force field based on the free enthalpy of hydration and solvation: the GROMOS force-field parameter sets 53A5 and 53A6. J Comput Chem 25:1656–1676

80. Lin J-H, Perryman AL, Schames JR, McCammon JA (2002) Computational drug design accommodating receptor flexibility: the relaxed complex scheme. J Am Chem Soc 124:5632–5633

81. Lin J-H, Perryman AL, Schames JR, McCammon JA (2003) The relaxed complex method: Accommodating receptor flexibility for drug design with an improved scoring scheme. Biopolymers 68:47–62

82. Amaro RE, Baron R, McCammon JA (2008) An improved relaxed complex scheme for receptor flexibility in computer-aided drug design. J Comput Aided Mol Des 22:693–705

83. Durrant JD, McCammon JA (2011) Molecular dynamics simulations and drug discovery. BMC Biol 9:71

84. Schames JR, Henchman RH, Siegel JS, Sotriffer CA, Ni H, McCammon JA (2004) Discovery of a novel binding trench in HIV integrase. J Med Chem 47:1879–1881

85. Betz M, Wulsdorf T, Krimmer SG, Klebe G (2016) Impact of Surface Water Layers on Protein--Ligand Binding: How Well Are Experimental Data Reproduced by Molecular Dynamics Simulations in a Thermolysin Test Case? J Chem Inf Model 56:223–233

86. Henzler-Wildman K, Kern D (2007) Dynamic personalities of proteins. Nature 450:964–972

87. Duan Y, Kollman PA (1998) Pathways to a protein folding intermediate observed in a 1-microsecond simulation in aqueous solution. Science 282:740–744

88. Shaw DE, Chao JC, Eastwood MP, et al (2008) Anton, a special-purpose machine for molecular dynamics simulation. Commun ACM 51:91

89. Shaw DE, Maragakis P, Lindorff-Larsen K, et al (2010) Atomic-level characterization of the structural dynamics of proteins. Science 330:341–346

90. Lindorff-Larsen K, Maragakis P, Piana S, Shaw DE (2016) Picosecond to millisecond structural dynamics in human ubiquitin. J Phys Chem B 120:8313–8320

91. Dror RO, Pan AC, Arlow DH, Borhani DW, Maragakis P, Shan Y, Xu H, Shaw DE (2011) Pathway and mechanism of drug binding to G-protein-coupled receptors. Proc Natl Acad Sci U S A 108:13118–13123

92. Shan Y, Kim ET, Eastwood MP, Dror RO, Seeliger MA, Shaw DE (2011) How does a drug molecule find its target binding site? J Am Chem Soc 133:9181–9183

93. Van Meel JA, Arnold A, Frenkel D, Portegies Zwart SF, Belleman RG (2008) Harvesting graphics power for MD simulations. Mol Simul 34:259–266

94. Friedrichs MS, Eastman P, Vaidyanathan V, Houston M, Legrand S, Beberg AL, Ensign DL, Bruns CM, Pande VS (2009) Accelerating molecular dynamic simulation on graphics processing units. J Comput Chem 30:864–872

95. Harvey MJ, Giupponi G, Fabritiis GD (2009) ACEMD: Accelerating Biomolecular Dynamics in the Microsecond Time Scale. J Chem Theory Comput 5:1632–1639

96. Harvey MJ, De Fabritiis G (2012) High-throughput molecular dynamics: the powerful new tool for drug discovery. Drug Discov Today 17:1059–1062

97. Shirts M, Pande VS (2000) COMPUTING: screen savers of the world unite! Science 290:1903–1904

98. Pande VS, Baker I, Chapman J, et al (2003) Atomistic protein folding simulations on the submillisecond time scale using worldwide distributed computing. Biopolymers 68:91–109

99. Prinz J-H, Wu H, Sarich M, Keller B, Senne M, Held M, Chodera JD, Schütte C, Noé F (2011) Markov models of molecular kinetics: generation and validation. J Chem Phys 134:174105

100. Buch I, Giorgino T, De Fabritiis G (2011) Complete reconstruction of an enzyme-inhibitor binding process by molecular dynamics simulations. Proc Natl Acad Sci U S A 108:10184–10189

101. Doerr S, De Fabritiis G (2014) On-the-Fly Learning and Sampling of Ligand Binding by High-Throughput Molecular Simulations. J Chem Theory Comput 10:2064–2069

102. Bowman GR, Ensign DL, Pande VS (2010) Enhanced modeling via network theory: Adaptive sampling of Markov state models. J Chem Theory Comput 6:787–794

103. Pande VS, Beauchamp K, Bowman GR (2010) Everything you wanted to know about Markov State Models but were afraid to ask. Methods 52:99–105

104. Kmiecik S, Gront D, Kolinski M, Wieteska L, Dawid AE, Kolinski A (2016) Coarse-Grained Protein Models and Their Applications. Chem Rev 116:7898–7936

105. De Vivo M, Masetti M, Bottegoni G, Cavalli A (2016) Role of molecular dynamics and related methods in drug discovery. J Med Chem 59:4035–4061

106. Sugita Y, Okamoto Y (1999) Replica-exchange molecular dynamics method for protein folding. Chem Phys Lett 314:141–151

107. Patriksson A, van der Spoel D (2008) A temperature predictor for parallel tempering simulations. Phys Chem Chem Phys 10:2073–2077

108. Fukunishi H, Watanabe O, Takada S (2002) On the Hamiltonian replica exchange method for efficient sampling of biomolecular systems: Application to protein structure prediction. J Chem Phys 116:9058

109. Wang K, Chodera JD, Yang Y, Shirts MR (2013) Identifying ligand binding sites and poses using GPU-accelerated Hamiltonian replica exchange molecular dynamics. J Comput Aided Mol Des 27:989–1007

110. Hamelberg D, Mongan J, McCammon JA (2004) Accelerated molecular dynamics: a promising and efficient simulation method for biomolecules. J Chem Phys 120:11919–11929

111. Li Y, Yin C, Liu P, Li D, Lin J (2017) Identification of a Different Agonist-Binding Site and Activation Mechanism of the Human P2Y1 Receptor. Sci Rep 7:13764

112. Isralewitz B, Gao M, Schulten K (2001) Steered molecular dynamics and mechanical functions of proteins. Curr Opin Struct Biol 11:224–230

113. Isralewitz B, Izrailev S, Schulten K (1997) Binding pathway of retinal to bacterio-opsin: a prediction by molecular dynamics simulations. Biophys J 73:2972–2979

114. Izrailev S, Stepaniants S, Balsera M, Oono Y, Schulten K (1997) Molecular dynamics study of unbinding of the avidin-biotin complex. Biophys J 72:1568–1581

115. Izrailev S, Crofts AR, Berry EA, Schulten K (1999) Steered molecular dynamics simulation of the Rieske subunit motion in the cytochrome bc(1) complex. Biophys J 77:1753–1768

116. Vuong QV, Nguyen TT, Li MS (2015) A New Method for Navigating Optimal Direction for Pulling Ligand from Binding Pocket: Application to Ranking Binding Affinity by Steered Molecular Dynamics. J Chem Inf Model 55:2731–2738

117. Schlitter J, Engels M, Krüger P, Jacoby E, Wollmer A (1993) Targeted Molecular Dynamics Simulation of Conformational Change-Application to the T ↔ R Transition in Insulin. Mol Simul 10:291–308

118. Lüdemann SK, Lounnas V, Wade RC (2000) How do substrates enter and products exit the buried active site of cytochrome P450cam? 1. Random expulsion molecular dynamics investigation of ligand access channels and mechanisms. J Mol Biol 303:797–811

119. Torrie GM, Valleau JP (1977) Nonphysical sampling distributions in Monte Carlo free-energy estimation: Umbrella sampling. J Comput Phys 23:187–199

120. Kästner J (2011) Umbrella sampling. Wiley Interdisciplinary Reviews: Computational Molecular Science 1:932–942

121. Kästner J, Thiel W (2005) Bridging the gap between thermodynamic integration and umbrella sampling provides a novel analysis method: "Umbrella integration". J Chem Phys 123:144104

122. Kumar S, Rosenberg JM, Bouzida D, Swendsen RH, Kollman PA (1992) THE weighted histogram analysis method for free-energy calculations on biomolecules. I. The method. J Comput Chem 13:1011–1021

123. Rosta E, Hummer G (2015) Free energies from dynamic weighted histogram analysis using unbiased Markov state model. J Chem Theory Comput 11:276–285

124. Laio A, Parrinello M (2002) Escaping free-energy minima. Proc Natl Acad Sci U S A 99:12562–12566

125. Laio A, Gervasio FL (2008) Metadynamics: a method to simulate rare events and reconstruct the free energy in biophysics, chemistry and material science. Reports on Progress in Physics 71:126601

126. Barducci A, Bonomi M, Parrinello M (2011) Metadynamics. Wiley Interdisciplinary Reviews: Computational Molecular Science 1:826–843

127. Gervasio FL, Laio A, Parrinello M (2005) Flexible docking in solution using metadynamics. J Am Chem Soc 127:2600–2607

128. Limongelli V, Bonomi M, Parrinello M (2013) Funnel metadynamics as accurate binding free-energy method. Proc Natl Acad Sci U S A 110:6358–6363

129. Barducci A, Bussi G, Parrinello M (2008) Well-tempered metadynamics: a smoothly converging and tunable free-energy method. Phys Rev Lett 100:020603

130. Bussi G, Gervasio FL, Laio A, Parrinello M (2006) Free-energy landscape for beta hairpin folding from combined parallel tempering and metadynamics. J Am Chem Soc 128:13435–13441

131. Vanommeslaeghe K, Guvench O, MacKerell AD (2014) Molecular mechanics. Curr Pharm Des 20:3281–3292

132. Born M, Oppenheimer R (1927) Zur Quantentheorie der Molekeln. Ann Phys 389:457–484

Aim of the work

As recalled in the introduction, protein flexibility plays a relevant role in ligand-protein recognition, thus it cannot be neglected in drug design. The excursus over the main molecular modeling techniques already available and currently in development has highlighted the urgency to work on new methods able to describe binding in an accessible timescale. The present work has been conceived in this framework, with the aim to contemplate the issue of protein conformational variability both in classical molecular docking and in molecular dynamics.

In the field of molecular docking, the question arises on how to deal with multiple conformations of the same protein. In fact, increasing numbers of structures are experimentally solved nowadays, and it is not uncommon to find tens to hundreds of crystallographic or NMR structures for the same macromolecule. As explained in the introduction, several possibilities have been experimented on how to exploit these data during docking, such as through the construction of average grids or chimera proteins, or using the whole ensemble of structures for different docking runs. Differently, our purpose is to investigate a docking benchmark strategy aimed to associate to each ligand of a database a custom structure chosen from the protein ensemble. The idea is to construct a completely automatic pipeline, able to reduce user intervention and to accelerate a virtual screening process.

Moreover, another part of the work is focused on the development and implementation of a new technique introduced by our research group in 2014*, the so called Supervised Molecular Dynamics, SuMD. SuMD is an algorithm that makes use of classical molecular dynamics (MD) to investigate ligand-protein binding processes. As reported in the introduction, the possibility to explore the recognition process is currently confined to extremely long classical MD simulations and biased MD simulations. Both these methods have drawbacks, linked to the length of the simulation in the first case, and to the introduction of the bias in the second. SuMD decreases the time scale of a binding process from micro-milliseconds to nanoseconds by introducing a tabu-like algorithm, but without biasing the potential. A classical MD simulation is divided into steps, where the distance between the centers of mass of the ligand and the binding site is monitored. The distance values are collected at regular intervals during a SuMD step and are fitted by a line; if the slope of the line is negative, a new SuMD step starts from the current velocities and configuration of the system, otherwise the simulation is restarted from the previous step.

Starting from this, the present work aims to further test and develop SuMD, exploring the pros and cons of this technique. Particular interest is put to broaden the applicability domain of this method, with major concern to peptide-protein binding, due to the pharmaceutical relevance of peptides.

***** *Sabbadin D, Moro S (2014) Supervised molecular dynamics (SuMD) as a helpful tool to depict GPCR-ligand recognition pathway in a nanosecond time scale. J Chem Inf Model 54:372–376*

Scientific Publications

Overview of the articles:

The scientific work has been divided into two main fields, one dedicated to molecular docking techniques and the other to molecular dynamics. The most important results are exposed in the current chapter through the scientific publications that have already been published.

1. Molecular Docking work

The first five articles deal with docking methods, and can be divided into two methodological works and three more applicative ones.

1.1 Methodological projects:

- *Salmaso V, Sturlese M, Cuzzolin A, Moro S (2016) DockBench as docking selector tool: the lesson learned from D3R Grand Challenge 2015. J Comput Aided Mol Des 30:773–789*

The participation to the docking challenge D3R Grand Challenge 2015 is described in this paper. The challenge required the pose prediction for a number of compounds towards heat shock protein 90 (Hsp90) and Mitogen activated protein kinase kinase kinase kinase 4 (MAP4K4). The availability of a high number of protein structures, particularly for Hsp90, raised the development of the present pipeline. Basically, compounds are associated to proteins on the basis of their chemical similarity with the co-crystallized ligand. Then, the DockBench tool is used to conduct a benchmark of different docking protocols and to perfom the screening.

- *Salmaso V, Sturlese M, Cuzzolin A, Moro S (2017) Combining self- and cross-docking as benchmark tools: the performance of DockBench in the D3R Grand Challenge 2. J Comput Aided Mol Des. doi: 10.1007/s10822-017-0051-4*

The participation to the next D3R Grand Challenge 2 is presented, with the optimization of the aforementioned procedure. In particular, a fully automatization of the pipeline is performed, integrating the preceding idea with a cross-docking benchmark.

1.2 Applicative projects:

- *Bertini S, Ghilardi E, Asso V, et al (2017) Sulfonamido-derivatives of unsubstituted carbazoles as BACE1 inhibitors. Bioorg Med Chem Lett 27:4812–4816*

In this work a structure-activity relationship study has been performed, rationalizing the binding mode of N-[3-(9H-carbazol-9-yl)-2-hydroxypropyl]-arylsulfonamides on β-Secretase (BACE1)

- *Carta D, Bortolozzi R, Sturlese M, et al (2017) Synthesis, structure-activity relationships and biological evaluation of 7-phenyl-pyrroloquinolinone 3-amide derivatives as potent antimitotic agents. Eur J Med Chem 127:643–660*

In this work the interactions of a series of 7-pyrrolo[3,2-*f*]quinolinones in the colchicine binding site of tubuline is rationalized.

- *Squarcialupi L, Betti M, Catarzi D, et al (2017) The role of 5-arylalkylamino- and 5-piperazino- moieties on the 7-aminopyrazolo[4,3-d]pyrimidine core in affecting adenosine A1 and A2A receptor affinity and selectivity profiles. J Enzyme Inhib Med Chem 32:248–263*

This article focuses on the rationalization of the selectivity profile of a series of 7-aminopyrazolo[4,3-d]pyrimidines on different adenosine receptor subtypes. A novel analysis method is proposed, which performs comparisons of the electrostatic and hydrophobic interaction fingerprints of the docked compounds with those of a known binder.

2. Molecular Dynamics Work

- *Cuzzolin A, Sturlese M, Deganutti G, Salmaso V, Sabbadin D, Ciancetta A, Moro S (2016) Deciphering the Complexity of Ligand-Protein Recognition Pathways Using Supervised Molecular Dynamics (SuMD) Simulations. J Chem Inf Model 56:687–705*

In this paper, the development and testing of SuMD are presented. The functionalities of the SuMD Analyzer tool are shown: a panel of geometric and energetic analysis can be automatically performed using this software.

- *Salmaso V, Sturlese M, Cuzzolin A, Moro S (2017) Combining self- and cross-docking as benchmark tools: the performance of DockBench in the D3R Grand Challenge 2. J Comput Aided Mol Des. doi: 10.1007/s10822-017-0051-4*

Here, the implementation of pepSuMD is reported, showing how the supervision can accelerate also the observation of a peptide-protein binding event. The analysis of the interactions on a per-residue scale can give insights into peptidic and proteic aminoacids that are relevant for the recognition.

In the end, a review is reported, summarizing some of the tools developed by our research group in the last years:

Ciancetta A, Cuzzolin A, Deganutti G, Sturlese M, Salmaso V, Cristiani A, Sabbadin D, Moro S (2016) New Trends in Inspecting GPCR-ligand Recognition Process: the Contribution of the Molecular Modeling Section (MMS) at the University of Padova. Mol Inform 35:440–448

DockBench as docking selector tool: the lesson learned from D3R Grand Challenge 2015

Veronica Salmaso, Mattia Sturlese, Alberto Cuzzolin, Stefano Moro

(2016) DockBench as docking selector tool: the lesson learned from D3R Grand Challenge 2015. J Comput Aided Mol Des 30:773–789

Abstract

Structure-based drug design (SBDD) has matured within the last two decades as a valuable tool for the optimization of low molecular weight lead compounds to highly potent drugs. The key step in SBDD requires knowledge of the three-dimensional structure of the target-ligand complex, which is usually determined by X-ray crystallography. In the absence of structural information for the complex, SBDD relies on the generation of plausible molecular docking models. However, molecular docking protocols suffer from inaccuracies in the description of the interaction energies between the ligand and the target molecule, and often fail in the prediction of the correct binding mode. In this context, the appropriate selection of the most accurate docking protocol is absolutely relevant for the final molecular docking result, even if addressing this point is absolutely not a trivial task. D3R Grand Challenge 2015 has represented a precious opportunity to test the performance of DockBench, an integrate informatics platform to automatically compare RMDS-based molecular docking performances of different docking/scoring methods. The overall performance resulted in the blind prediction are encouraging in particular for the pose prediction task, in which several complex were predicted with a sufficient accuracy for medicinal chemistry purposes.

1. Introduction

Molecular docking is widely adopted SBDD approach and its impact is clearly demonstrated by the plethora of software developed until now. In the Click2Drug directory [1] more than 50 software are listed, while more than 60 are catalogued on Wikipedia [2]. Considering that several docking algorithms can be coupled to different scoring functions, the number of different docking/scoring combinations is extremely vast.

The primary issue all docking programs try to address is what combination of orientation and conformation (pose) is the most favorable relative to all the other combinations sampled. When applied to screening, the process also requires a comparison of the best pose (or top best poses) of a given ligand with those of the other ligands such that a final ranking (or ordering) can be obtained. However, molecular docking protocols suffer from inaccuracies in the description of the interaction energies between the ligand and the target molecule, and often fail in the prediction of the correct binding mode. In this context, the appropriate selection of the most accurate docking protocol is absolutely relevant for the final molecular docking performance, even if addressing this point is absolutely not a trivial task for several reasons: (a) each docking protocol has its peculiar input and output file formats, making their managing really tedious when different software are used; (b) input docking parameters can be very different among diverse programs strongly limiting their use in parallel; (c) more and more frequently it is possible that a molecular target was crystallized in more than one form, and it is then necessary to determine which of these is the most suitable for the docking procedure, in particular, when applied to a virtual screening study; and d) last but not least, the fundamental role played by water molecules during the molecular docking simulations.

To overcome these critical issues, we recently developed a tool to support the molecular modeler in identifying the most accurate protocol by an automated and simultaneous comparison of 17 docking/scoring combinations using a self-docking benchmark procedure [3]. In particular, DockBench is an integrate informatics platform to automatically compare RMDS-based molecular docking performances of different docking/scoring methods. An intuitive graphical analysis can help docking users, including non-expert ones, to identify the best docking/scoring combination to perform a docking-based virtual screening campaign. In this contest, D3R Grand Challenge 2015 has represented a precious opportunity to test the performance of DockBench tool in a blind exercise and using high quality ligand–protein complex structures. In particular, D3R Grand Challenge 2015 was organized allowing participants to compete, in a two-stage process, in the prediction of ligand pose and ligand ranking using two very well known therapeutic targets: heat shock protein 90 (Hsp90) and Mitogen activated protein kinase kinase kinase kinase 4 (MAP4K4). Hsp90 is a chaperone protein which has been deeply investigated over the past decades for its crucial role in cancer cells [4], and MAP4K4 is a serine/threonine kinase that has emerged as such a potential therapeutic target for several disorders, in particular for metabolic and cardiovascular diseases [5].

Considering the peculiarity of the DockBench tool in facilitating the prediction of the ligand poses, we decided to concentrate our efforts in determining the best docking method able to reproduce the most accurate pose geometries. The results obtained in the D3R Grand Challenge 2015 (GC2015) revealed a promising capability of our pipeline in pose prediction task. In particular, the mean RMSD obtained in the Hsp90-complexes was 0.86 Å, while for MAP4K4-complexes the mean RMSD showed less accurate value (3.34 Å). The complete pipeline of DockBench used during the two-stage process of the D3R Grand Challenge 2015 GC2015 and a retrospective analysis of its performance will be described in the present study.

2. Experimental section

2.1 Overview of the workflow

The key concept of the workflow adopted in the GC2015 was the identification of the best protocol available in our laboratory in reproducing the crystallographic poses of selected ligands. In detail, given the target and a set of blind ligands, the workflow was articulated into four steps:

(1) Collection of a training set of complexes containing the target from the protein data bank;

(2) Comparing the performance in a self-docking procedure of 17 different docking protocol on the training set;

(3) Selection of one or more suitable protocols according the RMSD;

(4) Evaluation of the similarity of the blind set and the training set of ligands. If significant similarity was found, it drove the selection of the protein conformation;

(5) Docking of the blind ligands;

(6) Selection of the poses using scoring procedures and visual inspection for ambiguous conformations.

In the ranking predictions the protocol was mostly derived from the pose prediction workflow with a further implementation of rescoring procedures.

The procedure of each pose and rank prediction follows all the points depicted above, but tailoring few of them according the set of blind ligands and the protein target (detailed workflow in Figs. 1, 5) and is commented along the results and discussions.

2.2 Hardware

All computational studies were performed on a 200 cores cluster based on Ubuntu operating system (distribution 14.04, 64 bit) under the network file system (NFS) service. MD simulations were carried out by using Acemd [6] on a GPU cluster of 20 NVIDIA GTX graphics cards.

2.3 Ligands preparation

All ligands were prepared following an in-house pipeline previously reported [7]. Briefly, Corina 3.4 was used to generate three-dimensional structures, as well as to neutralize and deprive them of potential counterions [8]. For each compound, the most favorable ionic state was selected by using the ‘‘Protonate’’ tool implemented in MOE suite and based on Generalized Born electrostatics model [9]. MOE was also used to generate the possible tautomeric states, to energy minimize, and to assign the partial charges of each candidate using MMFF94x force field [10]

2.4 Preparation of ligand–protein complexes

The complexes provided by the organizers as well as those retrieved from the Protein Data Bank (PDB) [11] were subjected to the Structure Preparation and ‘‘Protonate-3D’’ tools implemented in MOE2015.10 suite [9], including water molecules if present.

2.5 Molecular docking

Molecular docking calculations were carried out using the following software: AutoDock 4.2.5.1 [12], AutoDock Vina1.1.2 [13], Glide 6.5 [14, 15], GOLD 5.2 [16], MOE 2015.10 [17], PLANTS 1.2 [18], rDock [19]. DockBench 1.0 [3] was used to perform and analyze molecular docking benchmarks. DockBench default parameters have been set for all docking protocols. MOE 2015.10 was used for docking rescoring procedure, using the following scoring function: pKi, GBVI/WSA, Affinity dG [20].

2.6 Chemical similarity and docking analysis

In house bash or python scripts were used for determining Tanimoto’s similarity using OpenBabel [21] and for calculating root mean square deviations (RMSD) using OpenEye [22], respectively. Visual inspection was performed on MOE 2015.10 and Chimera UCSF [23]. ChEMBL database [24] was queried to obtain experimental affinities using a substructure search tool as implemented in MOE.

2.7 Molecular dynamics simulations

Ligand-Hsp90 complexes selected among docking poses were prepared with AmberTool14 [25] for Molecular Dynamics (MD) simulations as follows.

Each system was solvated with explicit waters (TIP3P model) resulting in a box with boundaries at least 11Å far from any atom of the complex. The simulation box was neutralized with Na^+/Cl^- ions to a final concentration of 0.1 M. Consequently, the prepared systems were simulated by using AMBER14 [26] Force Field [27] and periodic boundary conditions. General Amber Force Field (GAFF) [28] parameters were used for the ligands, along with RESP partial charges [29], which were obtained with Antechamber [25] by fitting electrostatic potential points calculated with Gaussian [30].

The system equilibration was performed through a stepwise procedure that begins with a conjugate-gradient minimization of 300 steps in order to reduce the steric clashes of the prepared system. The equilibration phase was performed through two consecutive steps, with different ensembles and atom positional restrains. In the first protocol, the MD simulation was performed in a NVE ensemble for 100 ps, with a force constant of 1 kcal mol^{-1} $Å^{-2}$ applied to all protein atoms in order to allow the equilibration of the water molecules. Thereafter, a MD simulation of 500 ps in the NPT ensemble was performed by keeping the alpha-carbons of the protein restrained with the same force magnitude of the previous step. During this step, the temperature was maintained at 310 K by a Langevin thermostat and the pressure at 1 atm by a Berendsen barostat. Subsequently, all MD simulations were conducted in the NVT ensemble, maintaining the temperature at 310 K.

In all MD simulations, the non-bonded long-range Coulomb interactions were handled by using the particle mesh Ewald summation method (PME) [31] with a cutoff distance of 9 Å and a switching distance of 7.5 Å. All the poses were simultaneously compared in a knockout tournament framework.

Each MD simulation was carried out for 10 ns during which a modified dynamic scoring function (DSF) [32] was computed. This scoring is defined as the cumulative sum of the ligand–protein interaction energy (IE): it includes electrostatic (IEele) and van der Waals (IEvdw) contributions.

The wIE are plotted against the simulation time and linearly fitted to the collected data to obtain the slope coefficient that provides an estimation of the strength of the interaction and the stability of the binding mode.

2.8 Electrostatic energy fingerprints

Electrostatic interactions in MAP4K4-ligand complexes were studied by calculating the Electrostatic Energy Fingerprints (EEF). Amber99 partial charges were computed for the proteins and PM3 partial charges were computed for the ligands using MOE. Per residue electrostatic energy interactions were computed thanks to a in-house SVL script used in MOE. Interactions of the residues within 10 Å from each ligand were plotted in a heat map. This graph, reporting on the X-axis the protein residues of the binding site and on the Y-axis the ligands, attributes a color to the strength of the interactions: in particular, electrostatic energy diminishes going from red to blue. Gnuplot4.5 [33] was used to draw the plots.

3. Results and discussion

D3R Grand Challenge 2015 was organized as a two-stage process applied to Hsp90 and MAP4K4 datasets. In both cases, stage 1 was subdivided in two tasks: the first consisting of a ‘‘pose prediction’’ phase, and the second of a ‘‘ranking prediction’’ phase. Stage 2 had the same aim of stage 1 ‘‘ranking prediction’’ phase, with, as an advantage, the disclosure of the crystallographic structures object of phase 1 ‘‘pose prediction’’ phase.

As anticipated in the Introduction, our computational work was mainly devoted to ‘‘pose prediction’’ following the mantra concept in SBDD that the identification/selection of the most accurate docking protocol is the key step in the prediction of the correct binding mode. For this purpose, we have compared the ability of different docking/scoring combinations in reproducing crystallographic poses, taking advantage of the DockBench software.

3.1 Hsp90

3.1.1 Stage 1: Pose prediction phase

The challenge of Hsp90 Stage 1-‘‘Pose prediction’’ phase was to predict the coordinates of six protein–ligand complexes and to rank the affinities of 180 compounds, referred to as ‘‘*ligand test set*’’ in this paper. The workflow used for the pose prediction is reported in Fig. 1 (on the left), and it is divided into four tasks: Hsp90 complexes selection, selection of docking protocol, docking calculations and, finally, best pose selection.

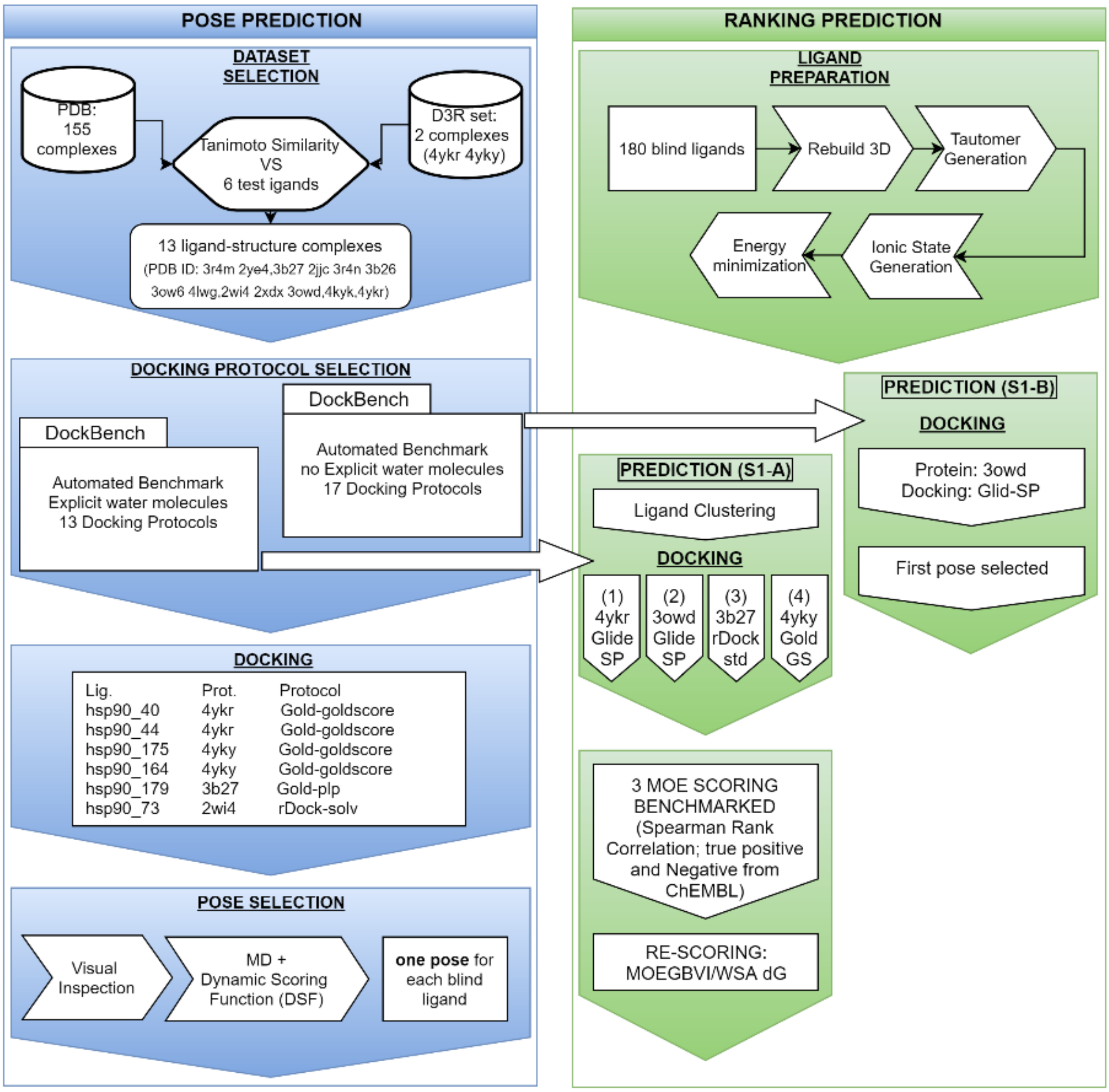
POSE PREDICTION
DATASET SELECTION
PDB: 155 complexes
Tanimoto Similarity VS 6 test igands
D3R set: 2 complexes (4ykr 4yky)
13 ligand-structure complexes (PDB ID: 3r4m 2ye4,3b27 2jjc 3r4n 3b26 3ow6 4lwg,2wi4 2xdx 3owd,4kyk,4ykr)
DOCKING PROTOCOL SELECTION
DockBench
Automated Benchmark Explicit water molecules 13 Docking Protocols
DockBench
Automated Benchmark no Explicit water molecules 17 Docking Protocols
DOCKING
Lig. Prot. Protocol
hsp90_40 4ykr Gold-goldscore
hsp90_44 4ykr Gold-goldscore
hsp90_175 4yky Gold-goldscore
hsp90_164 4yky Gold-goldscore
hsp90_179 3b27 Gold-plp
hsp90_73 2wi4 rDock-solv
POSE SELECTION
Visual Inspection
MD + Dynamic Scoring Function (DSF)
one pose for each blind ligand
RANKING PREDICTION
LIGAND PREPARATION
180 blind ligands
Rebuild 3D
Tautomer Generation
Ionic State Generation
Energy minimization
PREDICTION (S1-B)
DOCKING
Protein: 3owd Docking: Glid-SP
First pose selected
PREDICTION (S1-A)
Ligand Clustering
DOCKING
(1) 4ykr Glide SP
(2) 3owd Glide SP
(3) 3b27 rDock std
(4) 4yky Gold GS
3 MOE SCORING BENCHMARKED (Spearman Rank Correlation; true positive and Negative from ChEMBL)
RE-SCORING: MOEGBVI/WSA dG

Fig. 1 Workflow for Posing and Scoring predictions designed for the challenge on Hsp90. In *blue panel* is reported the procedure used in the docking stage divided in four main tasks as reported in the discussion section: Database selection, Docking Protocol Selection, Docking Calculation, and Pose Selection. The Scoring Prediction pipeline is schematized on the *green panel*. The Scoring Procedure consists in a first ligand preparation step, then two different prediction are sketched (Prediction S1-A and S1-B)

Hsp90 complexes selection Hsp90 is a well-known target in medicinal chemistry which has been deeply investigated in the last two decades by structural biology. At the time of the challenge, we identified in the Protein Data Bank [11] 155 Hsp90-ligand complexes, as listed in Supplementary Information. Two further complexes provided by the organizers (PDB ID: 4YKR, 4YKY) were added to the structures collected from the PDB. Due to the large amount of structural information, we decided to reduce the number of the crystallographic structures focusing our attention only to those complexes in which the co-crystallized ligands were structurally similar to those provided to us by the organizers. The selection was carried out using a filter based on Tanimoto's similarity (FP2 fingerprints): in particular similarity was evaluated for each of the 6 ligands to be docked against the 157 crystallographic ligands. We selected the Hsp90 crystallographic complexes in which the co-crystallized ligand showed a similarity index greater than 0.5, resulting in 13 structures: 3R4 M [34], 2YE4 [35], 3B27 [36], 2JJC [37], 3R4 N [34], 3B26 [36], 3OW6 [38], 4LWG [39], 2WI4 [40], 2XDX [41], 3OWD [38], 4YKR [42], 4YKY [43] (referred to as their PDB IB). Co-crystallized ligands of these 13 complexes will be called ''*ligand training set*'' from here on out in this manuscript. Crystallographic structures and ligand training set were prepared for molecular docking study according to the pipeline reported in the Experimental section.

Selection of docking protocol In the case of Hsp90 the selection of the docking protocol has been carried out taking into account the possible presence of water molecules as mediators of interactions between the ligand and the residues of the binding cavity. The criterion that has been used for the selection of the water molecules is based both on the assessment of their direct interaction with the ligand and the protein, and of the similarity of their B-factor with the average B-factor of the heavy atoms of the backbone of the protein. A list of the water molecules taken into account for each crystal structure is reported in Table SI1.

The *ligand training set* was subjected to two benchmark studies as reported in the workflow (Fig. 1): the first one, in which each ligand of the *training set* has been self-docked using 17 docking/scoring combinations in the absence of water molecules, and the second one in which the same ligands have been self-docked using 13 docking/scoring combinations protocols taking into account the selected water molecules.

In DockBench, to judge the performances of the different docking protocols, 20 poses were generated for each ligand of the *training set* and the RMSD values between predicted and crystallographic poses were calculated.

In order to evaluate the performances of the docking protocols, the lowest ($RMSD_{min}$) and average ($RMSD_{ave}$) RMSD values over the 20 poses, as well as the highest number of conformations with a RMSD value lower than the corresponding X-ray resolution (R), $N^{(RMSD<R)}$, were compared for all the docking protocols. For the specific purpose of the D3R Grand Challenge 2015, we have exploited DockBench ability in suggesting the most accurate docking protocols, that are the protocols able to predict the pose closest to the experimental

one. For this reason, we have focalized our attention on the docking protocols showing lowest RMSD$_{min}$ values. This resulted in different docking protocols in relation to different crystal structures, and sometimes in more than one successful docking protocol for the same crystal structure.

Interestingly, the results of DockBench indicated a significant improvement in reproducing the experimental crystallographic poses when the water molecules were included in the docking procedure, as reported in Fig. 2a. Indeed, including water molecules several protocols were able to reproduce the experimental coordinates with RMSD below 2.0 Å. Following these computational evidences, we decided to include the same crystallographic water molecules also during the docking simulations of the *ligand test set*.

Finally, for each ligand of the test set we have selected the crystallographic structure of Hsp90 in which the co-crystallized ligand was structurally more similar to the docked ligand.

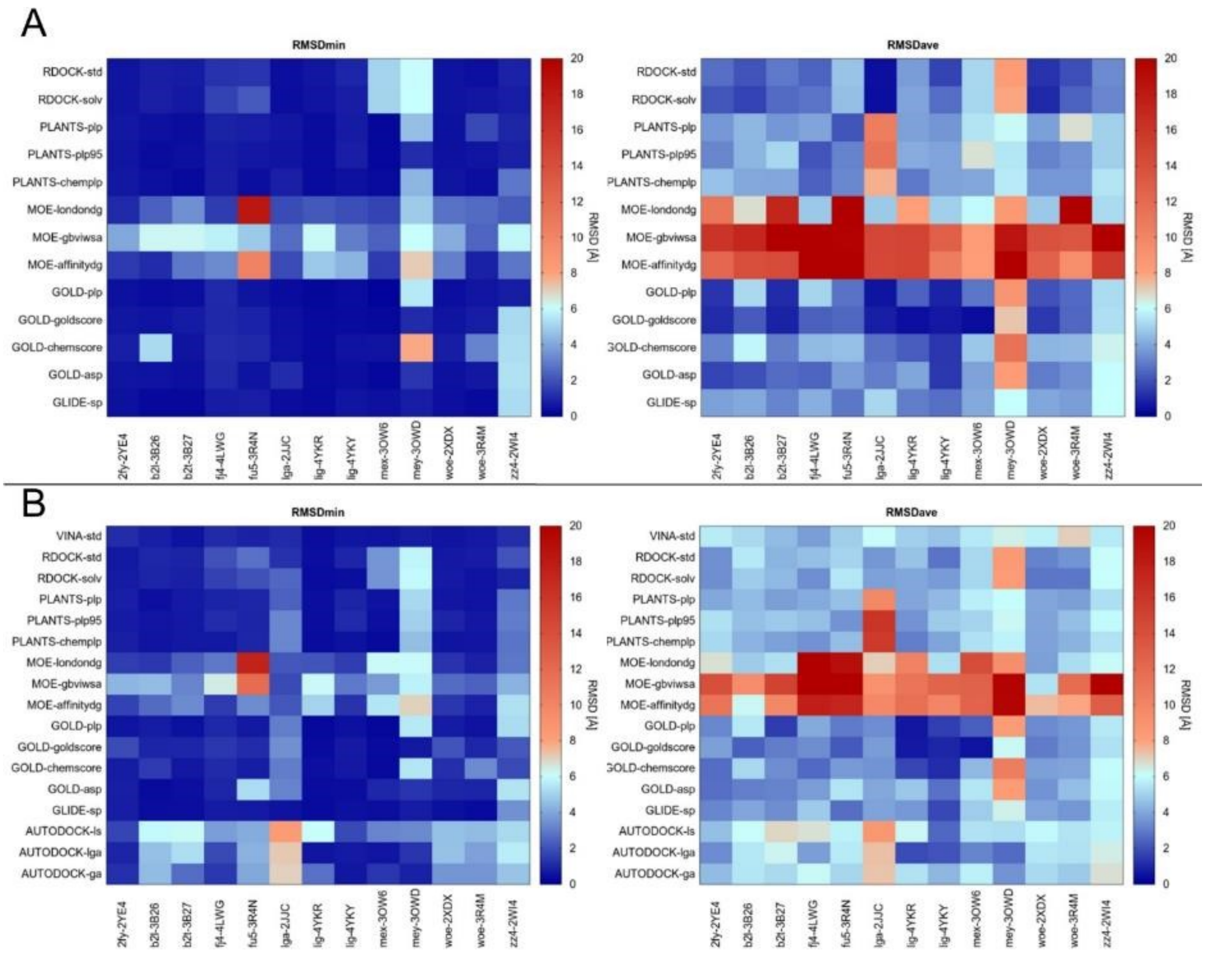

Fig. 2 Self-docking benchmark results obtained with DockBench. Two different benchmark are shown: in a a benchmark carried out including the most relevant water molecules, while in panel B the benchmark was performed on the same pool of complexes but removing all the crystallographic water molecules. For each panel two heat map are reported: the minimum RMSD values (RMSD$_{min}$) returned by the tested docking protocol (y-values) for the considered X-ray structures (x-values) and the Average RMSD values (RMSD$_{ave}$) for the 20 poses generated for each protocol considered. Values are *color coded*, *blue spots* identify the best obtained results

Docking simulations and pose selection For each ligand of the *test set* we have chosen the crystallographic structures of Hsp90 whose co-crystallized ligand had higher Tanimoto similarity (calculated as FP2 fingerprints comparison) to it. In the case of compound 44 (a benzimidazol-2-one), we have decided to dock it to two structures: 3OWD, selected on the basis of highest similarity, and 4YKR, the benzimidazol-2-one derivative bound structure proposed by the challenge organizers. In the case of compound 73, Tanimoto index was not sufficient to discriminate structures, thus, besides evaluating chemical and structural similarity of the co-crystallized ligands, we have chosen three protein structures showing different conformations of loop 104–114 near the binding site.

Finally, we have selected the docking protocols with best RMSD$_{min}$ performance for those crystallographic structures. The final report of the selected crystal structures and the relative docking protocols for each ligand of the test set is summarized in Table 1.

Table 1 List of test set ligands with relative docking protocols and protein crystallographic structures selected for docking in the pose prediction task

Ligand	Protein	Docking Algorithm	Scoring Function	Pose	Slope (DSF)
Hsp90_40	**4YKR**	**Gold**	**Goldscore**	**1**	**-30.14**
Hsp90_44	3OWD	Glide	SP	1	-12.94
	3OWD	Gold	Goldscore	2	-19.74; -19.81
	4YKR	**Gold**	**Goldscore**	**3**	**-19.81; -22.57**
				4	-17.48
Hsp90_73	3B27	Gold	PLP	1	-42.52
	3B26	Gold	Goldscore	2	-46.41; -29.07
	2WI4	**rDock**	**Solv**	**3**	**-36.71; -36.02**
	2WI4	rDock	STD	4	-8.37
Hsp90_164	4YKY	Gold	ASP	1	-29.85
				2	-37.86; -35.23
	4YKY	**Gold**	**Goldscore**	**3**	**-48.70; -47.92**
				4	-27.94
Hsp90_175	4YKY	Gold	ASP	1	-32.53; -30.17
				2	-30.25
	4YKY	**Gold**	**Goldscore**	**3**	**-56.56;-54.96**
				4	-20.75
Hsp90_179	**3B27**	**Gold**	**PLP**	**1**	**-19.85**
				2	-14.63

For each ligand the number of poses picked after docking and submitted to MD is reported, together with the slope of the DSF computed along the MD trajectory and used as final score (when two slope values are reported, the refer to the first and the second turn of the knockout tournament, respectively). In bold are indicated the poses selected on the basis of DSF slope and finally submitted to the challenge

After the preliminary validation step using the *ligand training set*, the Virtual Screening Tool of DockBench was used to perform the *ligand test set* docking simulations using the same set of parameters adopted in the validation step. A summary of information used in the docking simulations of the ligand *test set* is collected in Table 1.

After docking, we selected one or more poses resulting from each docking simulation, according to electrostatic and van der Waals interaction energy evaluation and visual inspection. Finally, we used Molecular Dynamics (MD) simulation as post-docking tool to select a unique pose for the challenge submission [29]. For each pose a 10 ns simulation was performed and the dynamic scoring function (DSF) was evaluated. This scoring is computed along the trajectory with the aim to obtain the slope coefficient as an estimation of the binding strength and of the stability of the complex.

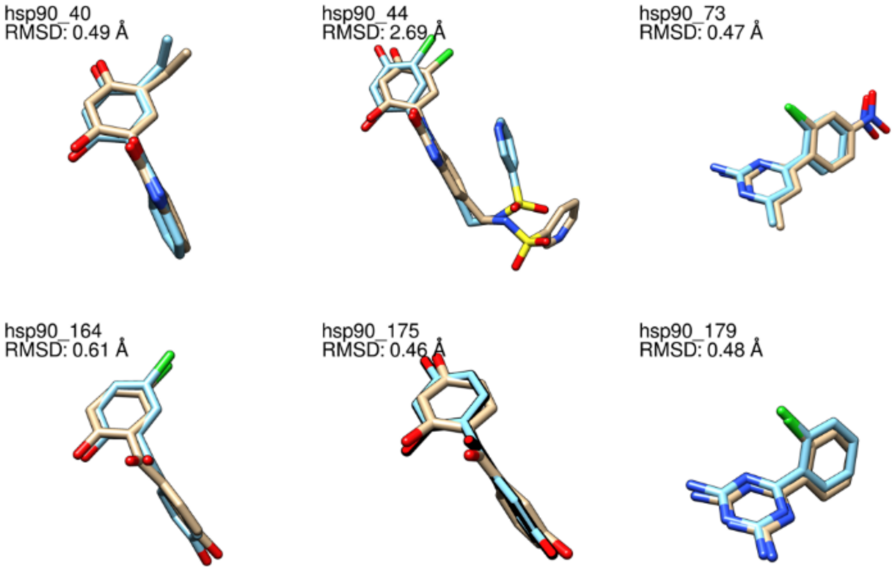

Fig. 3 Superposition of the predicted poses (*light blue*) on the experimental ones (*tan*). RMSD values were calculated on the heavy atoms

Results As anticipated, the proposed workflow was designed to produce a unique pose for each *ligand of the test set*. The superposition of the six predicted complexes on the corresponding crystallographic poses is reported on Fig. 3. The DockBench performance generally showed robust results (Table 2) with a mean RMSD of 0.86 Å considering only the heavy atoms of each docked ligand. Most notably, five complexes shown RMSD values under the 0.61 Å absolutely representative of crystallographic poses. Curiously, ligand Hsp90_44 showed a higher RMSD value, 2.69 Å, mainly ascribable to the 3-pyridinesulfon-amide moiety. This substituent in the crystal structure points out to the bulk water and is characterized by high B-factor values while in our prediction it is differently oriented establishing a pi stacking interaction with the benzimidazol-2-one scaffold (as shown in Fig. 4). Despite the shift of the 3-pyridinesulfonamide moiety, the key interactions of this scaffold are conserved as well as the orientation of the N-substituted benzimidazol-2-one portion as confirmed by the good RMSD (0.62 Å) calculated considering only this portion of the molecule.

Table 2 Summary of the results of all scoring and docking prediction

			Scoring Prediction				
Receipt-ID	Pred. name	Target/ Stage	Num. ligands	τ err (Kendall)	τ (Kendall)	ρ err (Spearman)	ρ (Spearman)
564e3304a7724	S1-A	Hsp90 Stage1	180	0.052	0.11	0.08	0.16
564e330569871	S1-B	Hsp90 Stage1	180	0.054	0.16	0.08	0.23
56afca8517dc5	S2-A	Hsp90 Stage2	180	0.05	0.21	0.07	0.3
56afca9a3644d	S2-B	Hsp90 Stage2	180	0.05	0.24	0.07	0.35
56afca7f6927b	S2-C	Hsp90 Stage2	180	0.056	0.12	0.08	0.18
5671ef9fdd7a3		MAP4K4 Stage1	18	0.15	0.32	0.2	0.46
56afc9e2ae8c8		MAP4K4 Stage2	18	0.203	-0.02	0.26	0.01

		Pose prediction			
		Num. Poses	RMSD (mean pose 1)	RMSD (mean all poses)	RMSD (mean best pose)
564e43759677e	Hsp90 Stage1	5^a	0.5	0.5	0.5
5671f1dac24a1	MAP4K4 Stage1	30	3.34	3.34	3.34

The values reported correspond to those provided by the organizers. The Values of RMSD are indicated in angstrom (Å)

[a] The final evaluation of Grand Challenge 2015 considers only 5 ligands; in the discussion the we included also the ligand Hsp90_44, resulting in a mean RMSD for 6 ligand of 0.86 Å

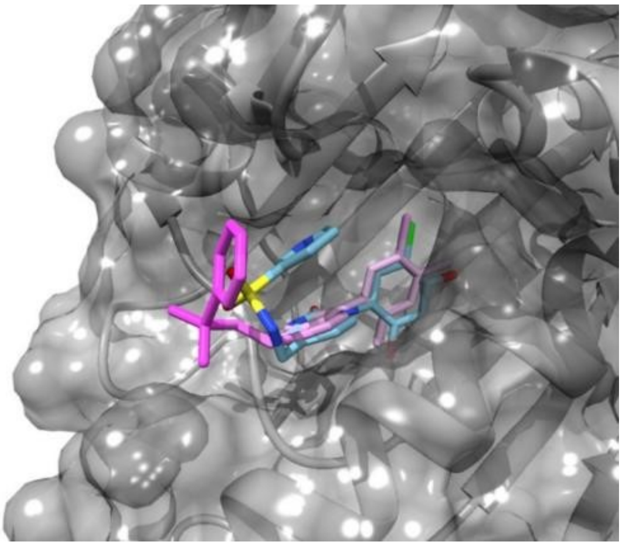

Fig. 4 Comparison of the predicted pose (*light blue*) and the experimentally derived complexes. The crystallographic ligand is colored according the B-factor in a light-to-dark pink palette corresponding to low-to-high values. While the benzimidazol-2-one scaffold is in nicely reproduced 0.62 Å the 3-pyridinesulfonamide moiety is placed out from the binding pocket is not well predicted resulting in a RMSD of 2.69 Å for the whole molecule. The binding mode of the portion establishing the key interaction is not affected by the different orientation. This observation is in agreement with the higher B-factor values of the 3-pyridinesulfonamide moiety (*dark pink*)

3.1.2 Stage 1: ranking prediction step

The aim of Hsp90 Stage 1-‘‘Ranking prediction’’ phase was to rank the affinities of 180 compounds, referred to as ‘‘*ligand test set*’’ in this paper. The workflow used for the ranking prediction is reported in Fig. 1 (on the right).

Scoring workflow As already anticipated in the Introduction, docking programs are usually successful in generating multiple poses that include binding modes similar to the crystallographically determined bound structure whereas scoring functions are much less successful at correctly ranking the ‘‘bioactive’’ binding mode. Aware of the current limitations of the scoring functions, however, we wanted to compare two ranking methodologies that represent on the one hand the most accurate ranking strategy available in our lab (S1-A) and the other the less expensive in terms of computational time (S1-B) (Fig. 1). This comparison was intriguing for us to establish the possible benefit-cost ratio of these two alternative strategies.

In the first pipeline (S1-A), we clustered the library of 180 compounds according to Tanimoto’s similarity exploiting the Fingerprint Database Clustering tool of MOE: briefly, Tanimoto’s similarity was computed for all the 180 compounds against all of them, and each cluster was composed by molecules which were similar to the same set of molecules. Each cluster was screened by structural similarity (evaluated on the basis of common scaffold search, guided by user’s chemical sensibility and experience) against the 13 ligands of the training set used in the previous benchmark. We selected the protein corresponding to the co-crystallized ligand with highest similarity to each cluster. The PDB ID of the 13 protein–ligand complexes subjected to DockBench were: 3R4M, 2YE4, 3B27, 2JJC, 3R4 N, 3B26, 3OW6, 4LWG, 2WI4, 2XDX, 3OWD, 4YKR, AND 4YKY. After merging some of the clusters according to structural similarity of compounds scaffolds (evaluated by user's chemical sensitivity and experience), we identified 4 clusters (Table SI2) corresponding to 4 different protein–ligand complexes: 3OWD (2,3-dihydro-1H-benzimidazol-5-yl-methylsulfonamide scaffold), 4YKY (benzophenone scaffold), 4YKR (1,3-dihydro-2H-benzimidazol-2-one scaffold), and 3B27 (2-amino-1,3,5-triazine scaffold) as detailed in SI. Differently to the pose prediction challenge, here we selected the docking protocol for the four complexes using, in addition to DockBench results ($RMSD_{min}$ and $RMSD_{ave}$), also the Spearman's and Kendall's correlations to evaluate the ability of the protocol to rank the near native pose at the top positions of the ranking list. Briefly, each protocol showing $RMSD_{min}$ and $RMSD_{ave}$ below 1 Å and 4 Å (Fig. 2), respectively were then compared according Spearman's and Kendall's coefficients (score vs RMSD). The final selection is reported in Table 3. We performed the docking calculation using the Virtual Screening Platform implemented in DockBenck using the same parameters adopted in the previous benchmark and the first pose (best score) for each ligand was selected. Finally, to have a homogeneous scoring method, different scoring functions were evaluated for the rescoring procedure. Briefly, we picked a subset of compounds from ChEMBL with known activity (true positive and true negative) for each cluster by a substructure search. Only for cluster2 and cluster3 we identified a sufficient number of ligands, 14 and 17 respectively (Table SI3), to have a raw indication of the classification ability of the tested scoring functions. For those clusters the Spearman and Kendall coefficient were calculated to identify the most performant scoring function (GBVI/WSA dG). The 180 compounds were finally ranked on the basis of the GBVI/WSA dG value of the selected pose.

Table 3 Combination of docking protocol, the PDB ID of protein conformation used for each cluster identify in the rank prediction stage 1 (Hsp90

Cluster	Population	Protein	Protocol	$\rho; \tau$
1	44	4YKR	Glide-sp	0.83; 0.63
2	17	3OWD	Glide-sp	0.68; 0.47
3	62	3B27	rDock-std	0.73; 0.51
4	57	4YKY	Gold-chemscore	0.75; 0,56

The size of the cluster is indicated for each protocol (population). The Spearman's and Kendall's coefficients are reported for the selected protocols (RMSD vs score)

In the ‘‘less than one hour approach'' (S1-B), we selected Glide-sp, according to the metrics resulted by the benchmark without water molecules on the protein PDB ID 3OWD ($RMSD_{min}$: 0.67 Å), chosen on the basis of its wider binding pocket, suitable, at least in principle, to accommodate different classes of compounds. The screening was performed using Glide-sp from the Dock-Benck Virtual Screening platform and for each ligand the best pose (lowest pseudo-energy) was selected. Glide score was used to rank the 180 compounds.

Scoring results As expected, both scoring strategies S1-A and S1-B showed their ineffectiveness in the ability to correctly rank ligands in terms of their binding affinities and, also, in discriminating between true positive and true negative active compounds. In fact, as reported in Table 2 their ranking performances measured by the Kendall correlation are 0.11 and 0.16 considering S1-A and S1-B ranking, respectively. These performances suggest that the apparently more accurate S1-A ranking strategy is not superior in terms of ranking accuracy respect the fast S1-B method.

3.1.3 Stage 2: ranking prediction step

The stage 2 of the D3R Grand Challenge 2015 was characterized by the release, from the organizers, of the Hsp90 crystallographic structures used as test set in the pose prediction phase of stage 1. As in the stage 1, also here it was compared the two previously ranking methodologies (S1-A and S1-B) with the aim to rank the same 180 ligands analyzed in the stage 1 but taking into account the additional available crystallographic information.

Scoring workflow The applied workflow in stage 2 retraced the pipeline described for stage 1, and reported in Fig. 1, with few exceptions. In fact, the stage 2 of the D3R Grand Challenge 2015 was characterized by the release, from the organizers, of the Hsp90 crystallographic structures used as test set in the stage 1. Consequently, we reperformed the docking benchmark study of stage 1 using Hsp90 crystallographic structures (PDB ID: 2XDX, 4YKW, 4YKY, 4YKQ, 2YE4, 4YKT, 3R4 N, 2JJC, 2WI4, 3B26, 4YKZ, 3OW6, 3B27, 3OWD, 4YKR, 4YKU, 4YKX, 4LWG, 3R4M). As previously described, also in this case all docking simulations have been carried out including the more crucial water molecules (Table SI1). The new benchmark was also interesting to retrospectively analyze the ability of the docking/scoring combinations in reproducing the new crystallographic poses and, therefore, to evaluate the goodness of our protocol selection in the stage 1. The results of the new benchmark are reported in Figure SI1 (panel A). Interestingly, the protocols selected in the stage 1 showed low RMSD_{min} also in the self-docking exercise confirming, again, the goodness in the identification of the docking protocol.

Moreover, the ranking prediction (S2-A) also retraced the S1-A pipeline. Again, we clustered the 180 ligands according Tanimoto’s similarity to the ligands co-crystallized as included in the benchmark (in presence of the most relevant water). In this way we obtained 7 clusters as listed in SI (Table SI4). For each of them, we carried out the docking calculation selecting the protocol according the RMSD_{min} and RMSD_{ave} performances but also considering the ability in discriminating the near native conformation within the family of conformations generated in the benchmark. To highlight this, we used the Spearman index correlating the RMSD versus the score. The resulting combination of cluster, protein and protocol is detailed in Table 4.

Table 4 Combination of docking protocol and PDB ID of protein conformation used for each cluster identify in the rank prediction stage 2 (Hsp90)

Cluster	Population	Protein	S2-A Protocol	S2-B Protocol
1	31	4YKU	rDock-std	Gold-goldscore
2	11	4LWG	Gold-chemscore	Plants-chemplp
3	7	3B26	Gold-asp	rDock-std
4	21	4YKZ	rDock-std	Gold-goldscore
5	63	4YKR	Gold-asp	Gold-goldscore
6	13	3R4N	Gold-plp	Gold-goldscore
7	34	4YKW	rDock-std	Gold-plp

The size of the cluster is indicated for each protocol (population). The S2-A and S2-B differ only for the protocol selected

Then, we extracted the best scoring pose for each ligand according to the scoring method proper of the protocol. Finally, to be able to rank ligands conformations originated from different docking protocols, we sorted all the best conformations by using a rescoring procedure with MOE-pKi function.

As previously mentioned, the second ranking submission (S2-B) is strictly link to the first. It was designed to highlight the effect in considering the Spearman's correlation in the protocol selection.

In more detail, all steps of this pipeline were exactly the same of the prediction S2-A except in the selection of the protocol that in this case was merely based on the RMSD_{min} and RMSD_{ave} performances obtained in the benchmark. In Table 4 is reported which protocol was assigned for each clusters.

The third and last submission in the stage 2 (S2-C) was based on the submission S1-B in stage 1 and follow the same philosophy: simplest and fastest. The workflow adopted was exactly the same of stage 1. Briefly, we performed a new benchmark on the 19 complexes (13 complexes already known at stage 1 plus the new 6 unveil complexes) removing all the water molecules. Also in this case the benchmark outputs indicated Glide-sp, as the protocol more suitable in generate the near native conformations (Figure SI1, panel B). We decided to use the same protein conformation used in S1-B (PDB ID: 30WD), which is characterized by a wider binding pocket able in principle to host different classes of compounds. The screening was carried out using the Virtual Screening tool of DockBenck selection for each ligand its more stable pose.

Scoring results Unexpectedly, the scoring performances of the stage 2 have been significantly different from those observed in phase 1. The three approaches appreciably differ in terms of ranking and classification capability (Table 2). The more articulated methods (S2-A and S2-B) outperformed the basic approach (S2-C); in the Kendall rank correlation the three predictions S2-A, S2-B, and, S2-C scored 0.24, 0.21, and, 0.12 respectively. Whereas the score of S2-C was expected due to the fact that is has been performed with the same methodology of in stage 1, the score of S2-A is doubled. The introduction of a more suitable protein conformation has improved the performance; however, the value is still far from a desirable value. Also considering the Spearmen's rank correlation, the S2-A and S2-B outperformed S2-C with a coefficient of 0.30, 0.35, and 0.18 respectively. From the performance comparison of S2-A and S2-B is interesting to note that the use of the Spearman's correlation in the protocol selection has slightly improved the quality in the rank classification as partially expected.

3.2 MAP4K4

3.2.1 Stage 1: pose prediction step

The challenge on MAP4K4 Stage 1-''Pose prediction'' step was to predict the coordinates of 30 protein–ligand complexes and to rank the affinity of 18 of these 30 compounds referred, also in these case, as ''*ligand test set*''. The workflow used for the pose prediction is reported in Fig. 5 (on the left), and it is divided again into four tasks: MAP4K4 complexes selection, selection of docking protocol, docking calculations and, finally, best pose selection.

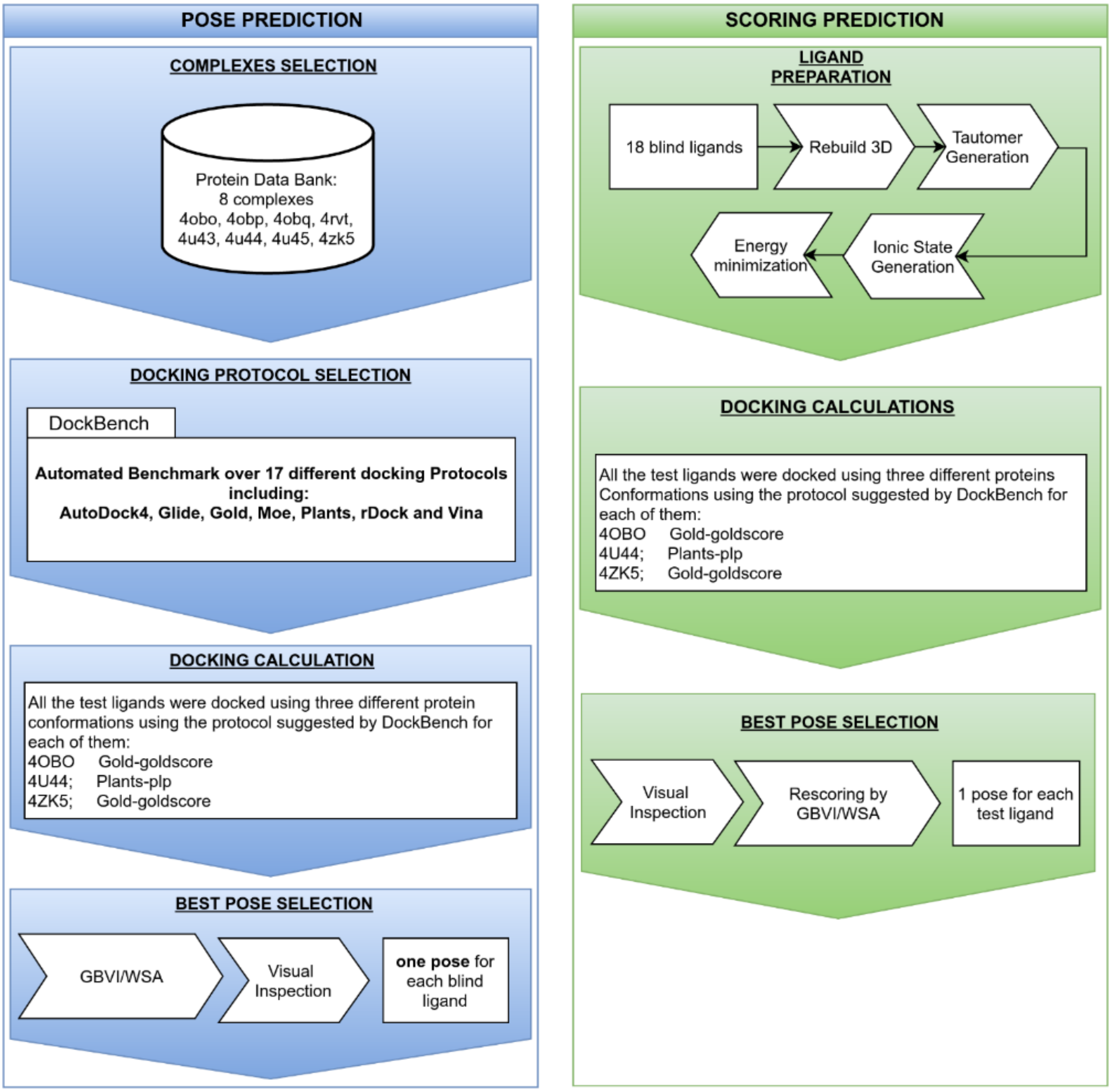

Fig. 5 Workflow for posing and scoring predictions designed for the challenge on MAP4K4. In blue panel is reported the procedure used in the docking stage divided in four main tasks as reported in the discussion section: Database selection, Docking Protocol Selection, Docking Calculation, and Pose Selection. The Scoring Prediction pipeline is schematized on the green panel. The Scoring Procedure consists in three tasks strictly correlated to the posing challenge: a first ligand preparation step, docking calculation and finally the rescoring and pose selection

MAP4K4 complexes selection Similar to what was done in stage 1 for Hsp90, we retrieved all eight ligand-MAP4K4 complexes present in the PDB (PDB ID: 4OBO [44], 4OBP [44], 4OBQ [44], 4RVT [45], 4U43 [46], 4U44 [46], 4U45 [46], and 4ZK5 [47]) in which the co-crystallized ligand will be referred again as ''*ligand training set*''. Crystallographic structures and ligand training set were prepared for molecular docking study according to the pipeline reported in the Experimental section.

Selection of docking protocol All the 8 known complexes were submitted to a self docking benchmark within DockBench using all the 17 different docking protocols available in the tool. Unlike what has been observed for Hsp90, in this case have not been highlighted water molecules that may play a crucial role in the recognition crystallized ligands. As reported in Fig. 6a, several protocols showed good results with RMSD$_{min}$ values below 2 Å. In particular, Gold and Plants software were able to reproduce the crystal pose in the majority of cases except when Gold was coupled with chemscore function. Following these preliminary information, we selected ‘‘Gold-goldscore’’ and ‘‘Plants-plp’’ as best docking/scoring combinations.

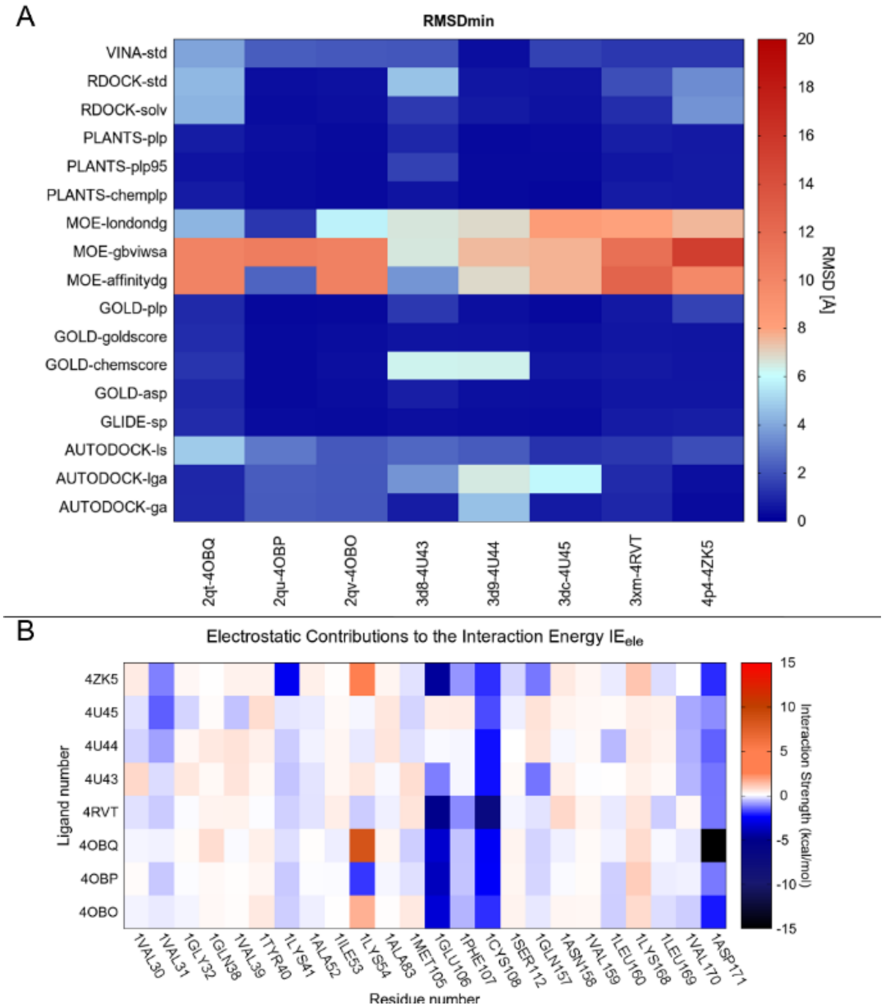

Fig. 6 a Self-docking Benchmark results obtained with DockBench on 8 complexes containing MAP4K4. The minimum RMSD values (RMSD$_{min}$) returned by the tested docking protocol (y-values) for the considered X-ray structures (x-values) for the 20 poses generated for each protocol considered. Values are *color coded*, *blue spots* identify the best obtained results. **b** Electrostatic Energy Fingerprints representing per-residue electrostatic contribution to interaction energy. This term was calculated for the eight training set complexes subjected to the benchmark. The interaction strength is coded in the heatmap using a red to blue palette going from a highly positive to a deeply negative potential. The calculation was performed for the most relevant residues for the binding. The *blue bars* corresponding to E106 and C108 highlight the relevance of this residues

Unfortunately, in this case the chemical variability of the 30 ligands of the test set didn't give us the opportunity to cluster them according to chemical similarity to the ligands of the training set, as in the case of Hsp90. Therefore, we adopted a different strategy to select MAP4K4 structures for docking: in particular, we took into consideration the interaction network of co-crystallized ligands in the PDB complexes, and selected those structures that conserved the same pattern for the docked poses of the test ligands. We used EEF to estimate the residues mainly involved in electrostatic interactions with the ligands.

Docking calculation and best pose selection The EEF of the MAP4K4 complexes suggested E106 and C108 as key residues in ligand binding; in fact, those residues are involved in strong electrostatic interactions in almost all ligand of the training set (Fig. 6b).

From this, we decided to pick the structure with lowest crystallographic resolution (PDB ID 4OBO) presenting the P-loop in a ''closed'' conformation. Among all docking/scoring combinations, Gold-goldscore was selected as docking protocol due to its good performance in reproducing the 4OBO ligand pose, as indicated by the corresponding RMSD_{min} value in Fig. 6. The Virtual Screening Tool of DockBench was used to dock the 30 ligands of the test set. Using this strategy, it was possible to select a pose showing interactions with E106 or C108 for the following ligands: MAP01, MAP02, MAP03, MAP04, MAP08, MAP09, MAP14, MAP15, MAP16, MAP18, MAP19, MAP20, MAP21, MAP23, MAP26, MAP27, MAP28, MAP32 (Figure SI2).

For the remaining ligands of the test set, alternative selection strategies have been used in the selection of both MAP4K4 crystallographic structures and docking/scoring protocols. The first important alternative was to change the protein structure in which the P-loop was in an ''open'' conformation and the crystallographic structure coded as 4U44 was selected as the best compromise between its crystallographic resolution and its DockBench performance.

Moreover, Plants-plp combination was selected as docking/scoring protocol adopted for the 12 remaining ligands (see Fig. 6) and acceptable poses interacting with either E106 or C108 were selected for MAP05, MAP06, MAP07, MAP11, MAP22, MAP25, MAP29, MAP30, MAP31as shown in Figure SI3. At the end, were only three exceptions: MAP12, MAP13 and MAP17. Since those ligands are voluminous, for these three ligands we chose the MAP4K4 crystallographic structure coded as 4ZK5, which performed well in the benchmark and whose co-crystallized ligand is the bulkiest among the training set (Figure SI4). In this specific case, we carried out the docking simulation using Gold-goldscore combination. Unfortunately, even with these changes, we were not able to find ligand poses directly interacting with E106 and C108 and, consequently, we decided to select the best poses by visual inspection.

Results The superposition of the 30 predicted complexes on the corresponding X-ray crystal structures is reported in Fig. 7. In general, the proposed workflow has shown encouraging results: the pose of several ligands were appropriately predicted but, understandably, there are a certain number of exceptions. In particular, 14 ligands were predicted with a RMSD below 2 Å and notably 11 of them below 1.5 Å. These values fall below the resolution of the crystal structures, which range from 1.59 to 3.04 Å. 4 ligands were in the range between 2 and 3 Å, whereas 12 showed a RMSD bigger than 3 Å. However, four ligands were poorly predicted (with an RMSD values >8Å). In particular, the poses of the three ligands containing the dehydro-oxepin ring were completely wrong. The poor predictions are mainly due to the erroneous pose selection performed by visual inspection. In fact, a retrospective analysis of the docking result revealed the presence of a native like poses in the ensemble of the generated conformations. Not surprisingly, a subset of small ligands with molecular weight lower than 300 Da (MAP04, MAP20, MAP22, MAP26, MAP29, MAP30, MAP31) resulted in inaccurate poses confirming the difficulties of docking protocols with fragments in particular when docked in wide binding side and in absence of a clear shape complementarity between the ligand and the docking site. In addition, the experimental structure of four of them revealed the presence of molecules of water stabilizing their conformation (MAP04, MAP20, MAP22, MAP29).

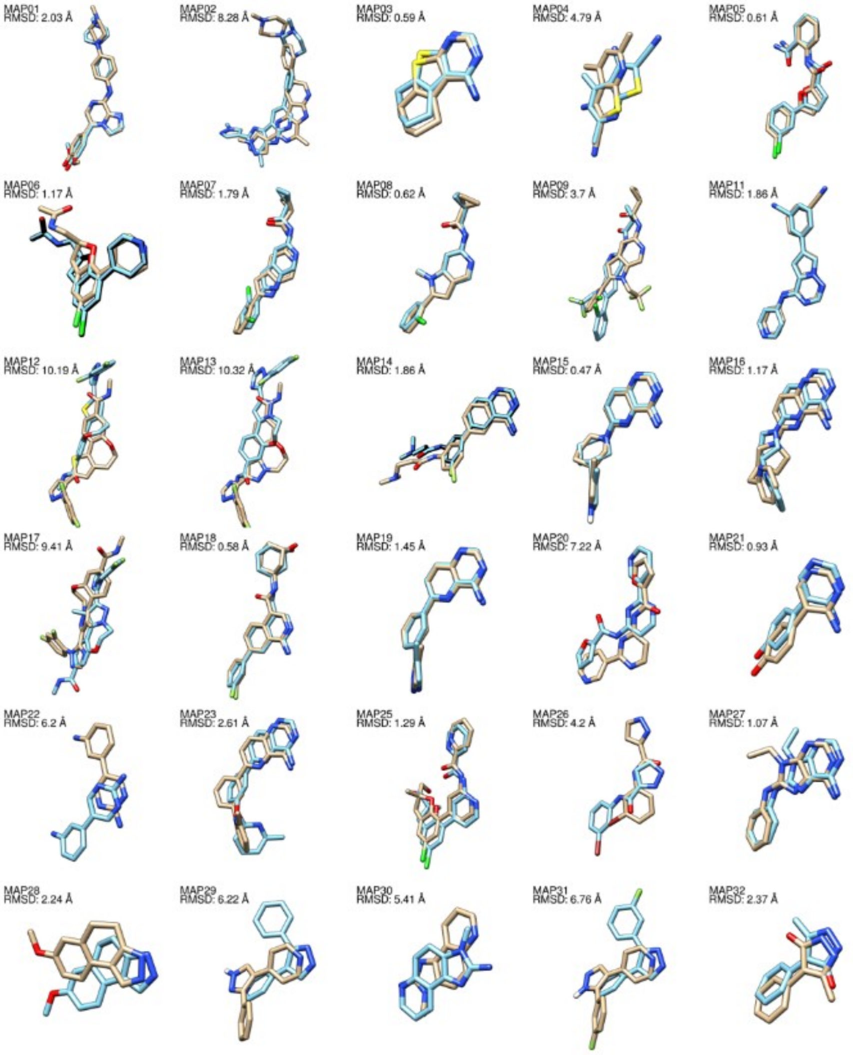

Fig. 7 Superposition of the predicted poses (*light blue*) on the experimental ones (*tan*). RMSD values were calculated on the heavy atoms

3.2.2 Stage 1 ranking prediction step

The aim of MAP4K4 Stage 1-''Ranking prediction'' phase was to rank the affinities of 18 of the 30 compounds docked in the previous phase. The workflow used for the ranking prediction is reported in Fig. 5 (on the right).

Scoring workflow The selected poses for MAP01, MAP02, MAP03, MAP04, MAP05, MAP06, MAP07, MAP08, MAP09, MAP11, MAP12, MAP13, MAP14, MAP15, MAP16, MAP17, MAP18, and MAP19 were rescored with MOE using GBVI/WSA method, in order to have a homogeneous scoring method.

Scoring results Also in this case and as expected, the scoring strategy showed its ineffectiveness in the ability to correctly rank ligands in terms of their binding affinities (Table 2). Pearson and Kendall coefficients values (0.46 and 0.32, respectively) show a modest positive correlation between affinities and GBVI/WSA scores.

3.2.3 Stage 2 ranking prediction step

Also in this case, the stage 2 of the D3R Grand Challenge 2015 was characterized by the release, from the organizers, of the MAP4K4 crystallographic structures used as test set in the pose prediction phase of stage 1. As in the ranking prediction phase of stage 1, the aim of this stage was the ranking of the same 18 ligands but taking into account the additional available crystallographic information.

Scoring workflow With the release of the new 30 MAP4K4 crystallographic structures, we re-performed to DockBench analysis (see Figure SI5). Also in this case, for each of the 18 compounds which were to be analyzed we selected the pose corresponding to the best value of $RMSD_{min}$ obtained in the benchmark (see Table 5). Finally, the complexes were rescored, and sorted, using MOE dock_pKi scoring function.

Table 5 Combination of docking protocol, the PDB ID of protein conformation used for each cluster identify in the rank prediction stage 2 (Hsp90)

Complex	Protocol	RMSDmin
lig-MAP01	Plants-chemplp	0.49
lig-MAP02	Gold-asp	0.31
lig-MAP03	Gold-goldscore	0.22
lig-MAP04	Gold-chemscore	0.28
lig-MAP05	Plants-plp95	0.26
lig-MAP06	Gold-plp	0.19
lig-MAP07	Gold-plp	0.27
lig-MAP08	Gold-chemscore	0.44
lig-MAP09	Gold-asp	0.19

Scoring stage results Also in this case, as expected, the ranking performance in the second stage was even less accurate than that obtained in the first stage. As reported in Table 2, Spearman's rank coefficient (0.01) showed absence of correlation between affinities and dock_pKi scores, and, even worse, the Kendall coefficient (-0.02) showed a tendency to negative correlation.

4. Conclusions and consideration

Our sincere feeling is that D3R Grand Challenge represented an important moment of scientific and methodological reflection regarding the real robustness of docking/scoring methodologies currently available to our scientific community. Molecular docking is certainly one of the most popular and used tools in computational medicinal chemistry and beyond. For this reason, we believe that our community must pay particular attention to point out what are the intrinsic limitations of this tool and to appropriately describe the best practice for its correct use.

In this contest, we could evaluate the predictive ability of a docking selection tool recently developed in our laboratory and called DockBench. Considering the peculiarity of the DockBench tool in facilitating the prediction of the ligand poses, we decided to concentrate our efforts in determining the best docking method able to reproduce the most accurate pose geometries.

The take home message learned from the GC2015 is that an accurate selection of both the docking protocol and protein conformation may lead in remarkable improvement of the prediction. In addition, the differences emerged in the accuracy between the two targets reveal two interesting points. First, when more data is already available as in the case of Hsp90 of which a notable number of complexes are available in the PDB, lead to better results if the similarity of between the ligand is taken into account. In particular, is not always straightforward the definition of similarity in this context and the selection of which kind of similarity can be the more appropriated (e.g. fingerprint similarity, shape similarity, substructure matching, etc.). The second point is that the role of the water molecule that improved the quality of the ligand-Hsp90 prediction. The significance of this two points are convincing us to introduce these aspects in our software also considering that the automation of these tasks into the docking pipeline would reduce the time needed to the user.

Even if the overall performance of DockBench is encouraging, from this assessment have emerged still delicate issues which limit the performance of docking/scoring algorithms and, consequently, their positive impact in the design of new drugs. Some of these are briefly summarized below:

(a) with the increasing number of docking programs (docking/scoring combinations), it becomes progressively more complex and risky to determine a priori which of these will be more accurate in reproducing a realistic poses of a ligand in its binding cavity;

(b) With the increasing number of crystal structures available in the PDB for a single protein, it becomes increasingly hazardous to determine a priori which crystallographic structure will be more appropriate to use to obtain a realistic pose of a ligand in its binding cavity;

(c) Nowadays, it is clear the crucial role of the water molecules, eventually present in the binding cavity, in determining the performance of the docking algorithms;

(d) Scoring functions are very often useless in realistically ranking a set of ligands.

As this D3R Grand Challenge has demonstrated, each docking run can be considered a singularity in a mathematical sense, or rather, a point in which a function is undefined. In fact, considering the degree of theoretical simplification of the problem we are dealing with docking and the large number of variables that define the problem itself, it is extremely difficult to determine a priori the degree of accuracy of the solution of our problem (realistic pose).

To paraphrase Albert Einstein, our take-home message may be summarized as follows: ‘‘Docking should be made as simple as possible, but not simpler.’’

References

1. Directory of in silico Drug Design tools - Docking. http://www.click2drug.org/directory_Docking.html.

2. Docking (molecular) - Wikipedia. https://en.wikipedia.org/wiki/Docking_(molecular).

3. Cuzzolin A, Sturlese M, Malvacio I, Ciancetta A, Moro S (2015) DockBench: An Integrated Informatic Platform Bridging the Gap between the Robust Validation of Docking Protocols and Virtual Screening Simulations. Molecules 20:9977–9993

4. Solit DB, Rosen N (2006) Hsp90: a novel target for cancer therapy. Curr Top Med Chem 6:1205–1214

5. Virbasius JV, Czech MP (2016) Map4k4 Signaling Nodes in Metabolic and Cardiovascular Diseases. Trends Endocrinol Metab. doi: 10.1016/j.tem.2016.04.006

6. Harvey MJ, Giupponi G, Fabritiis GD (2009) ACEMD: Accelerating Biomolecular Dynamics in the Microsecond Time Scale. J Chem Theory Comput 5:1632–1639

7. Morris GM, Huey R, Lindstrom W, Sanner MF, Belew RK, Goodsell DS, Olson AJ (2009) AutoDock4 and AutoDockTools4: Automated docking with selective receptor flexibility. J Comput Chem 30:2785–2791

8. Trott O, Olson AJ (2010) AutoDock Vina: improving the speed and accuracy of docking with a new scoring function, efficient optimization, and multithreading. J Comput Chem 31:455–461

9. Friesner RA, Banks JL, Murphy RB, et al (2004) Glide: a new approach for rapid, accurate docking and scoring. 1. Method and assessment of docking accuracy. J Med Chem 47:1739–1749

10. Halgren TA, Murphy RB, Friesner RA, Beard HS, Frye LL, Pollard WT, Banks JL (2004) Glide: a new approach for rapid, accurate docking and scoring. 2. Enrichment factors in database screening. J Med Chem 47:1750–1759

11. Verdonk ML, Cole JC, Hartshorn MJ, Murray CW, Taylor RD (2003) Improved protein-ligand docking using GOLD. Proteins 52:609–623

12. C C G (I Molecular Operating Environment (MOE).

13. Korb O, Stützle T, Exner TE (2009) Empirical scoring functions for advanced protein-ligand docking with PLANTS. J Chem Inf Model 49:84–96

14. Ruiz-Carmona S, Alvarez-Garcia D, Foloppe N, Garmendia-Doval AB, Juhos S, Schmidtke P, Barril X, Hubbard RE, Morley SD (2014) rDock: a fast, versatile and open source program for docking ligands to proteins and nucleic acids. PLoS Comput Biol 10:e1003571

15. Corbeil CR, Williams CI, Labute P (2012) Variability in docking success rates due to dataset preparation. J Comput Aided Mol Des 26:775–786

16. O'Boyle NM, Banck M, James CA, Morley C, Vandermeersch T, Hutchison GR (2011) Open Babel: An open chemical toolbox. J Cheminform 3:33

17. OpenEye Scientific Software Inc. (2016) OEChem. Santa Fe, NM, USA

18. Pettersen EF, Goddard TD, Huang CC, Couch GS, Greenblatt DM, Meng EC, Ferrin TE (2004) UCSF Chimera--a visualization system for exploratory research and analysis. J Comput Chem 25:1605–1612

19. Davies M, Nowotka M, Papadatos G, Dedman N, Gaulton A, Atkinson F, Bellis L, Overington JP (2015) ChEMBL web services: streamlining access to drug discovery data and utilities. Nucleic Acids Res 43:W612–20

20. Masciocchi J, Frau G, Fanton M, Sturlese M, Floris M, Pireddu L, Palla P, Cedrati F, Rodriguez-Tomé P, Moro S (2009) MMsINC: a large-scale chemoinformatics database. Nucleic Acids Res 37:D284–90

21. Molecular Networks GmbH CORINA. Germany

22. Labute P (2009) Protonate3D: assignment of ionization states and hydrogen coordinates to macromolecular structures. Proteins 75:187–205

23. Halgren TA (1996) Merck molecular force field. I. Basis, form, scope, parameterization, and performance of MMFF94. J Comput Chem 17:490–519

24. Berman HM, Westbrook J, Feng Z, Gilliland G, Bhat TN, Weissig H, Shindyalov IN, Bourne PE (2000) The protein data bank. Nucleic Acids Res 28:235–242

25. Wang J, Wang W, Kollman PA, Case DA (2006) Automatic atom type and bond type perception in molecular mechanical calculations. J Mol Graph Model 25:247–260

26. Case D, Babin V, Berryman J, et al (2014) Amber14, version AMBER14; http://ambermd.org/. University of California, San Francisco

27. Hornak V, Abel R, Okur A, Strockbine B, Roitberg A, Simmerling C (2006) Comparison of multiple Amber force fields and development of improved protein backbone parameters. Proteins 65:712–725

28. Wang J, Wolf RM, Caldwell JW, Kollman PA, Case DA (2004) Development and testing of a general amber force field. J Comput Chem 25:1157–1174

29. Bayly CI, Cieplak P, Cornell W, Kollman PA (1993) A well-behaved electrostatic potential based method using charge restraints for deriving atomic charges: the RESP model. J Phys Chem 97:10269–10280

30. Frisch MJ, Trucks GW, Schlegel HB, et al (2009) Gaussian 09, Revision B.01; http://gaussian.com/ Gaussian, Inc.: Wallingford, CT

31. Essmann U, Perera L, Berkowitz ML, Darden T, Lee H, Pedersen LG (1995) A smooth particle mesh Ewald method. J Chem Phys 103:8577

32. Sabbadin D, Ciancetta A, Moro S (2014) Bridging molecular docking to membrane molecular dynamics to investigate GPCR-ligand recognition: the human A_2A adenosine receptor as a key study. J Chem Inf Model 54:169–183

33. Williams T, Kelley C Gnuplot 4.5: an interactive plotting program, version 4.5; http://gnuplot.info.

34. Zehnder L, Bennett M, Meng J, et al (2011) Optimization of potent, selective, and orally bioavailable pyrrolodinopyrimidine-containing inhibitors of heat shock protein 90. Identification of development candidate 2-amino-4-{4-chloro-2-[2-(4-fluoro-1H-pyrazol-1-yl)ethoxy]-6-methylphenyl}-N-(2,2-difluoropropyl)-5,7-dihydro-6H-pyrrolo[3,4-d]pyrimidine-6-carboxamide. J Med Chem 54:3368–3385

35. Roughley SD, Hubbard RE (2011) How well can fragments explore accessed chemical space? A case study from heat shock protein 90. J Med Chem 54:3989–4005

36. Miura T, Fukami TA, Hasegawa K, et al (2011) Lead generation of heat shock protein 90 inhibitors by a combination of fragment-based approach, virtual screening, and structure-based drug design. Bioorg Med Chem Lett 21:5778–5783

37. Congreve M, Chessari G, Tisi D, Woodhead AJ (2008) Recent developments in fragment-based drug discovery. J Med Chem 51:3661–3680

38. Bruncko M, Tahir SK, Song X, et al (2010) N-aryl-benzimidazolones as novel small molecule HSP90 inhibitors. Bioorg Med Chem Lett 20:7503–7506

39. Li J, Shi F, Xiong B, He J Crystal Structure of the human Hsp90-alpha N-domain bound to the hsp90 inhibitor FJ4. To be published

40. Brough PA, Barril X, Borgognoni J, et al (2009) Combining hit identification strategies: fragment-based and in silico approaches to orally active 2-aminothieno[2,3-d]pyrimidine inhibitors of the Hsp90 molecular chaperone. J Med Chem 52:4794–4809

41. Murray CW, Carr MG, Callaghan O, et al (2010) Fragment-based drug discovery applied to Hsp90. Discovery of two lead series with high ligand efficiency. J Med Chem 53:5942–5955

42. Kang Y, Stuckey JA Structure of Heat Shock Protein 90 Bound to CS302. To Be Published

43. Kang Y, Stuckey JA Structure of Heat Shock Protein 90 Bound to CS319. To Be Published

44. Crawford TD, Ndubaku CO, Chen H, et al (2014) Discovery of selective 4-Amino-pyridopyrimidine inhibitors of MAP4K4 using fragment-based lead identification and optimization. J Med Chem 57:3484–3493

45. Schröder P, Förster T, Kleine S, Becker C, Richters A, Ziegler S, Rauh D, Kumar K, Waldmann H (2015) Neuritogenic militarinone-inspired 4-hydroxypyridones target the stress pathway kinase MAP4K4. Angew Chem Int Ed Engl 54:12398–12403

46. Wang L, Stanley M, Boggs JW, et al (2014) Fragment-based identification and optimization of a class of potent pyrrolo[2,1-f][1,2,4]triazine MAP4K4 inhibitors. Bioorg Med Chem Lett 24:4546–4552

47. Ndubaku CO, Crawford TD, Chen H, et al (2015) Structure-Based Design of GNE-495, a Potent and Selective MAP4K4 Inhibitor with Efficacy in Retinal Angiogenesis. ACS Med Chem Lett 6:913–918

Combining self- and cross-docking as benchmark tools: the performance of DockBench in the D3R Grand Challenge 2

Veronica Salmaso, Mattia Sturlese, Alberto Cuzzolin, Stefano Moro

(2017) Combining self- and cross-docking as benchmark tools: the performance of DockBench in the D3R Grand Challenge 2. J Comput Aided Mol Des. doi: 10.1007/s10822-017-0051-4

Abstract

Molecular docking is a powerful tool in the field of computer-aided molecular design. In particular, it is the technique of choice for the prediction of a ligand pose within its target binding site. A multitude of docking methods is available nowadays, whose performance may vary depending on the data set. Therefore, some non-trivial choices should be made before starting a docking simulation. In the same framework, the selection of the target structure to use could be challenging, since the number of available experimental structures is increasing. Both issues have been explored within this work. The pose prediction of a pool of 36 compounds provided by D3R Grand Challenge 2 organizers was preceded by a pipeline to choose the best protein/docking-method couple for each blind ligand. An integrated benchmark approach including ligand shape comparison and cross-docking evaluations was implemented inside our DockBench software. The results are encouraging and show that bringing attention to the choice of the docking simulation fundamental components improves the results of the binding mode predictions.

1. Introduction

Computer-Aided Drug Design (CADD) has been extensively applied in the drug discovery process, with concrete successful examples in the market [1]. The prediction of a ligand binding mode within the targeted protein is of fundamental importance in hit identification and hit-to-lead optimization. Molecular docking is the technique of choice for the prediction of a ligand position and conformation (ligand pose) within the protein binding site and has been used since its first application in the 1980s [2].

The primary requirement to perform a docking study is the availability of the target structure, so the protein data bank [3], with its pool of more than 130,000 structures, is certainly a golden goose for structure-based drug design (SBDD). The choice of the best protein structure may condition the success of the docking simulation, with holo binding sites giving the best performances [4]. The number of protein experimental structures is rapidly increasing, and more and more often a variety of three-dimensional structures are available for the same target. This puts the modeler in front of the dilemma of the protein choice in docking simulations.

Published: *J Comput Aided Mol Des. 2017 Aug 24; doi: 10.1007/s10822-017-0051-4*

In addition, various docking methods are available nowadays, with a list of more than 50 software in the Click2Drug directory [5]. The accuracy of docking algorithms and especially of scoring functions is sensitive to the dataset of proteins and compounds.

Thus, a plethora of variables should be considered before performing a docking simulation and, citing Isaac Asimov, “If knowledge can create problems, it is not through ignorance that we can solve them”, it is valuable to consider the whole pool of variables to assess the performance of the docking procedure that better suits the dataset of interest.

In this framework, docking challenges are precious because offer the possibility to realize limits and strong points of this computational technique, and to analyze the performance of computer-aided pipelines. D3R Grand Challenge 2 consisted of a two-stage process, comprising the pose and ranking prediction of a pool of 36 and 102 compounds, respectively, on the Farnesoid X receptor (FXR) target. FXR is a nuclear receptor implicated in bile acids, lipids, and glucose homeostasis; this makes it a drug target against cholestasis and lipids and glucose dysregulation [6].

Taking advantage of our experience with the previous Grand Challenge 2015 [7, 8], we have strengthened our previous pipeline improving the strategy to identify the best performing combination of docking protocol and protein structure for each ligand to be predicted. The selection of the docking protocol was assessed through a docking benchmark, which enabled to compare the performances of 16 docking-algorithm/scoring function couples. Moreover, a major effort was put on the choice of the protein structure, and a combined approach made up of ligands shape similarity evaluation to individuate congeneric series and cross-docking assessment was employed. The DockBench [9] platform was exploited and the whole procedure was set up to be completely automatic, with the aim to integrate the new-developed tools into the DockBench software.

The results of this pipeline are encouraging if compared to a simpler procedure consisting in the use of a single apoprotein and a single docking protocol for the whole pool of compounds. The detailed description of the adopted procedure will be described through this work.

2. Experimental section

2.1 Overview of the work

The main focus of this work was the pose prediction challenge, and in this framework a combined strategy was employed, comprising a choice of the protein and docking protocol on the basis of ligand similarity and on the results of a benchmark exercise.

Throughout this work, a pool of crystallographic structures (proteins and ligands) were used for the benchmark and are referred to as “training-set”, while the ligands object of the challenge are named “blind-challenge ligands”.

Two predictions were made, and the pipeline can be summarized as follows.

Prediction 1

Pose prediction phase

1. A training set of structures of the target was retrieved from the protein data bank (PDB) [3].
2. The training set complexes were clustered according to the co-crystallized ligands shape similarity.
3. A three-phase benchmark strategy was conducted to evaluate the “protein structure - docking protocol” performances:
    - CLUSTER CROSS-DOCKING: a cross-docking benchmark was executed among the complexes of each cluster, to individuate the “protein structure -docking protocol” couple able to better reproduce the crystallographic conformations of the ligands (similarly shaped) belonging to the cluster.
    - TOTAL CROSS-DOCKING: a cross-docking exercise was executed among the whole pool of PDB structures, to individuate the protein and docking-protocol able to averagely better reproduce the crystallographic conformation of all the training-set ligands (disregarding shape similarity).
    - SELF-DOCKING: as regards the clusters populated with just one PDB structure, a self-docking benchmark was performed to evaluate which docking protocol succeeded in better replicating the crystallographic binding mode.
4. The blind-challenge ligands were compared in terms of shape similarity to the representative of each cluster, previously selected in the benchmark phase. In this way, the blind challenge ligands were distributed over the pre-defined clusters, each one associated with the protein structure-docking protocol couple selected in the benchmark phase.
5. Blind-challenge ligands with no significant similarity to any of the training-set ligand were identified as outliers. They were associated with the protein structure-docking protocol couple selected for its highest performance in the total cross-docking exercise.
6. Each ligand was docked to the respectively selected protein with the selected docking protocol.

7. The top 5 scoring poses were selected and submitted.

Scoring phase

1. The highest scoring pose for each ligand was retained and submitted to a common rescoring phase.
2. The complexes obtained by docking simulation were prepared and submitted to molecular dynamics (MD) simulations.
3. MM-GBSA [10] profiles were computed along the trajectories. The MM-GBSA average value was used as common re-scoring and ranking method for all the ligands.

Prediction 2

Pose prediction phase

1. A docking simulation was performed for the blind-challenge ligands using the apoprotein crystallographic structure provided by the organizers, and employing the docking protocol that showed better performance in the total cross-docking job.
2. The top 5 scoring poses were selected and submitted.

Scoring phase

1. Docking score was used as a ranking method.

2.2 Hardware

Docking studies were carried out on a 200 cores CPU cluster based on Ubuntu operating system (distribution 14.04, 64 bit) under the Network File System (NFS) service. MD simulations were performed using Acemd [11] on a 20 NVIDIA GTX graphics cards GPU cluster.

2.3 Preparation of training set ligand–protein complexes

The protein preparation tool of MOE [12] was used to fix crystal structures problems, such as prediction of coordinates of missing atoms of partially solved residues. Co-crystallized solvent molecules and impurities (such as co-solvents) were removed, and only protein and ligand coordinates belonging to chain A of the crystal structures were retained. The Protonate-3D tool of MOE [13] was used to assign protonation states (assuming pH 7.4) of protein and the respective co-crystallized ligand.

2.4 Ligands preparation

Blind-challenge ligands were prepared using the LigPrep Tool of Schrödinger [14], retaining specified chiralities and without generating tautomers. Strong acids were deprotonated and strong basis protonated using the Wash Tool of MOE. MMFF94 Force Field has employed for ligands minimization.

2.5 Ligand similarity

RDKit [15] Shape Tanimoto Distance was employed to evaluate shape similarity among the training set ligands, as reported below.

OMEGA [16] of the OpenEye suite was used to generate 5 conformations for each blind-challenge ligand, which were submitted to the ROCS tool [17] for shape comparison to the representative of each training-set cluster.

2.6 Molecular docking

DockBench 1.0.5 [9] was used for the self-docking simulation and analysis, while the cross-docking computation and evaluation were carried out with an in-house tool that will be implemented in DockBench.

The following software packages were used to perform molecular docking calculations: AutoDock 4.2.5.1 [18], Glide 6.5 [19, 20], GOLD 5.2 [21], MOE 2015.1001 [12], PLANTS 1.2 [22, 23], rDock [24]. Either for the training set self-docking and cross-docking or for the blind-challenge ligands docking, the DockBench default parameters were used for docking simulations.

2.7 Molecular dynamics simulations

The ligand–protein complexes were prepared for MD simulations with AmberTools14 [25], assigning Gasteiger charges [26] and General Amber Force Field (GAFF) [27] parameters to the ligands and Amber14 partial charges and parameters to the proteins. Each system was solvated with explicit waters (TIP3P model) resulting in a tetragonal box with boundaries at least 11 Å far from any atom of the complex. Each system was neutralized adding Na^+/Cl^- ions to a final concentration of 0.1 M. Each system was subjected to 300 steps of conjugate-gradient minimization and to 100 ps NVE and 500 ps NPT equilibration, applying harmonic positional constraints (1 kcal mol−1 Å−2) on protein and ligands atoms. The pressure was maintained to 1 atm by Berendsen barostat and the temperature to 310 K by a Langevin thermostat.

Subsequently, three 2 ns unconstrained MD simulations in the NVT ensemble were conducted for each complex.

All MD simulations were carried out with the ACEMD engine, with a time-step of 4fs, by handling the nonbonded long-range Coulomb interactions with the particle mesh Ewald summation method (PME) [28, 29] with a cutoff distance of 9 Å and a switching distance of 7.5 Å.

2.8 MMGBSA calculations

AmberTools14 was used to perform MM-GBSA calculations, using a GB model developed by Onufriev-Bashford-Case [30] (igb = 5), a salt concentration of 0.1 M and calculating the surface area with the LCPO model [31]. 50 snapshots (every 40 ps) were collected for each trajectory, and MM-GBSA was computed along each simulation. Finally, the average value among the three replicas of the same complex was computed and used as ranking score.

3. Results and discussion

D3R Grand Challenge 2016 consisted of a two-stage process: stage 1 was devoted to the prediction of the binding mode of 36 blind compounds (FXR1-FXR36) and to the ranking of a pool of 102 blind compounds (FXR1-FXR102), containing the 36 ligands previously mentioned. Stage 2 asked for a new ranking prediction of the same pool of 102 compounds, once the FXR1-FXR36 crystallographic structures had been unveiled by the D3R Grand Challenge organizers.

The major effort of our work was devoted to the pose prediction task, using the docking protocol-protein structure couple able to better reproduce the crystallographic binding mode of ligands similarly shaped to those to be predicted. Moreover, the strong point of this work is that it is completely automated: from the choice of the docking protocol and protein structure to use to the selection of the final docking poses, the pipeline is completely performed without user's intervention.

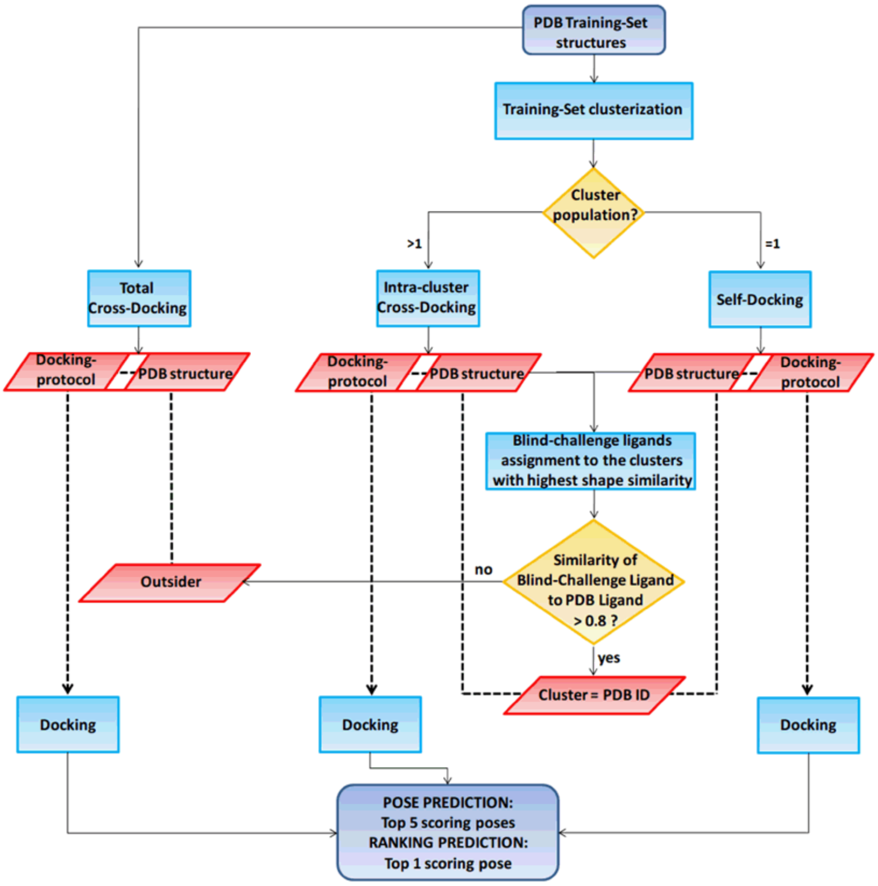
PDB Training-Set structures
Training-Set clusterization
Cluster population?
>1
=1
Total Cross-Docking
Intra-cluster Cross-Docking
Self-Docking
Docking-protocol
PDB structure
PDB structure
Docking-protocol
PDB structure
Docking-protocol
Blind-challenge ligands assignment to the clusters with highest shape similarity
Similarity of Blind-Challenge Ligand to PDB Ligand > 0.8 ?
no
yes
Outsider
Cluster = PDB ID
Docking
Docking
Docking
POSE PREDICTION: Top 5 scoring poses
RANKING PREDICTION: Top 1 scoring pose

Fig. 1 Workflow of the pipeline employed for pose prediction phase of Prediction 1

The results section is organized into two paragraphs, devoted to two separate predictions and corresponding submissions to the GrandChallenge. Prediction 1 involved the multi-step benchmark procedure described in the workflow (Fig. 1), and the results of each phase are described hereinafter, while prediction 2 employed a simpler strategy.

3.1 Prediction 1

3.1.1 Pose prediction

Training-set construction

The starting point of this work was the provision of crystal-structures of FXR to use in the docking benchmark studies. 26 complexes of human FXR with small organic ligands were retrieved from the PDB site: 1OSH [32], 3BEJ [33], 3DCT [34], 3DCU [34], 3FLI [35], 3FXV [36], 3GD2 [37], 3HC5 [38], 3HC6 [38], 3L1B [39], 3OKI [40], 3OKH [40], 3OLF [41], 3OMK [41], 3OMM [41], 3OOF [41], 3OOK [41], 3P88 [42], 3P89 [42], 3RUT [43], 3RUU [43], 3RVF [43], 4OIV [44], 4QE6 [45], 4QE8 [45], 4WVD [46].

PDB structures were filtered on the basis of the degree of completeness of the protein structure. Proteins lacking the coordinates of more than 15 residues were removed, causing the exclusion of 1OSH, 3L1B, and 4OIV structures.

In addition, structure 3OKH was removed by the collection because has two co-crystallized ligands, making it difficult to use for the docking benchmark. Also structures 4WVD was not considered because the co-crystallized high-molecular weight compound was difficult to use for docking.

Training-set ligands clusterization

Training-set proteins were clustered on the basis of the shape similarity among their co-crystallized ligands. The aim of the ligand-shape-based clustering is to divide proteins according to the footprint left by ligands on the binding site. This information will be later employed to associate each blind-challenge ligand to its best-hosting protein.

All FXR-ligand complexes were superposed by protein alignment, and the co-superposed ligands were used for shape comparison. RDKit Shape Tanimoto Distance was computed between each couple of compounds, resulting in a distance matrix. The matrix was subjected to scikit-learn [47] DBSCAN Clustering algorithm [48], using a cutoff of 0.45: structures with a distance value lower than the cutoff fell in the same cluster. The ligands, and consequently the relative protein structures, were clustered in 6 groups, as reported in Table 1.

Table 1 List of PDB training-set structures subdivided into clusters according to 3D shape similarity

Cluster	Training-set structures - PDB ID
1	3DCT, 3DCU, 3FXV, 3GD2, 3HC5, 3HC6, 3P88, 3P89, 3RUT, 3RUU, 3RVF
2	4QE8
3	3FLI
4	4QE6
5	3BEJ
6	3OKI, 3OLF, 3OMK, 3OMM, 3OOF, 3OOK

Cluster 2–5 are single-populated, while cluster 1 and 6 are characterized by more ligands having a similar chemical structure, as can be appreciated by Fig. 2: ligands of cluster 1 share an isoxazole-4-yl-methoxy-multiaryl-carboxylic acid scaffold and cluster 6 is characterized by a (2-phenyl-benzimidazol-1-yl)-2-cyclohexyl-ethanamide moiety.

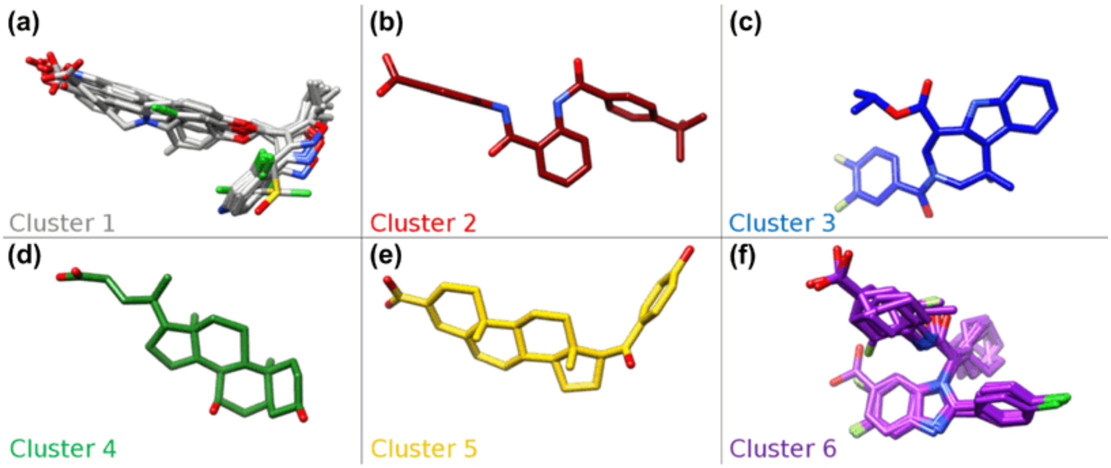

Fig. 2 Training-set clusters. The structure of the PDB training-set ligands is shown after superposition of the protein structures. The compounds of cluster 1–6 are represented in gray, red, blue, green, yellow and purple sticks, respectively

Docking-benchmark

The docking-benchmark was set up with a triple strategy, described below. In particular, the training-set clusters populated by more than one structure (clusters 1 and 6) were subjected to an intra-cluster cross-docking exercise. The structure corresponding to mono-populate clusters (structures 4QE8, 3FLI, 4QE6 and 3BEJ respectively of clusters 2–5) were used for a self-docking benchmark. Finally, the whole pool of training-set structures was used for a total cross-docking exercise.

Cross-docking

Given a pool of crystallographic structures of the same protein in complex with different ligands, cross-docking consists in docking each co-crystallized ligand to all the protein structures. The aim of this operation is to evaluate the performance of different proteins to hosts various ligands. The evaluation is made by computing the geometrical deviation of the predicted binding mode as compared to the binding mode on the crystallographic complex. The protein able to better host the higher number of ligands with a conformation similar to the crystallographic one could be a good candidate to use in a virtual screening simulation.

A cross-docking platform has been developed to automatically perform the cross-docking simulation and analysis among a group of PDB structures. Along with guiding the choice of the best protein structure, the tool aims to individuate the best docking/scoring combination for the subsequent virtual screening simulation. For this reason, the tool enables to automatically repeat the cross-docking simulation with different docking/scoring protocols.

After superposing the crystallographic complexes, the ligands were extracted, merged in a unique database and docked to each protein structure with 16 docking/scoring combination protocols, employing DockBench 1.0.5 default parameters: AutoDock-Genetic Algorithm (GA), AutoDock-Lamarckian Genetic Algorithm (LGA), AutoDock-Local Search (LS), Glide-Standard Precision (SP), GOLD-ASP, GOLD-Chemscore, GOLD-Goldscore, GOLD-PLP, MOE-Affinity dG, MOE-GBVI/WSA, MOE-London dG, Plants-ChemPLP, Plants-PLP, Plants-PLP95, rDock with (SOLV) or without (STD) the desolvation potential.

For each of the 16 docking protocols and N PDB structures, a database of N-1 ligands was docked to each of the N protein structures (the self-ligand was excluded for the cross-docking computation to follow a strict cross-docking procedure). 20 poses (or up to 20 poses in the case of Glide) were generated for each of the N(N-1) ligand–protein couples and the RMSD values between the five top-scoring poses and the crystallographic conformation of the ligand were computed. The evaluation of each protein-docking protocol couple was performed considering the mean RMSD of the five top-scoring poses of each of the N-1 ligands docked on the same protein with the same protocol (i.e. average among 5(N-1) RMSD values); this value was called Top5RMSDave. The Top5RMSDave was computed for each protein-docking protocol couple resulting in a 16N-items matrix. The matrix was rendered in the form of a heat map where each row represents a docking/scoring couple and each column represents a different PDB structure. The Top5RMSDave is rendered by a colorimetric scale going from blue to red for values from 0 to 20 Å. The protein-docking protocol couple was chosen as the one which minimized the Top5RMSDave value.

Cluster cross-docking

Clusters 1 and 6 were populated by more than one structure, so they were subjected to an intra-cluster cross-docking evaluation. This means that the results of the cross-docking simulation were organized considering the structures belonging to clusters 1 and 6 as two separate pools, and the Top5RMSDave values were computed just for the structures belonging to the same cluster. The aim of this was to choose the protein able to better host the ligands sharing a similar shape to the co-crystallized one.

The results of the Cluster cross-docking phase are reported in Fig. 3.

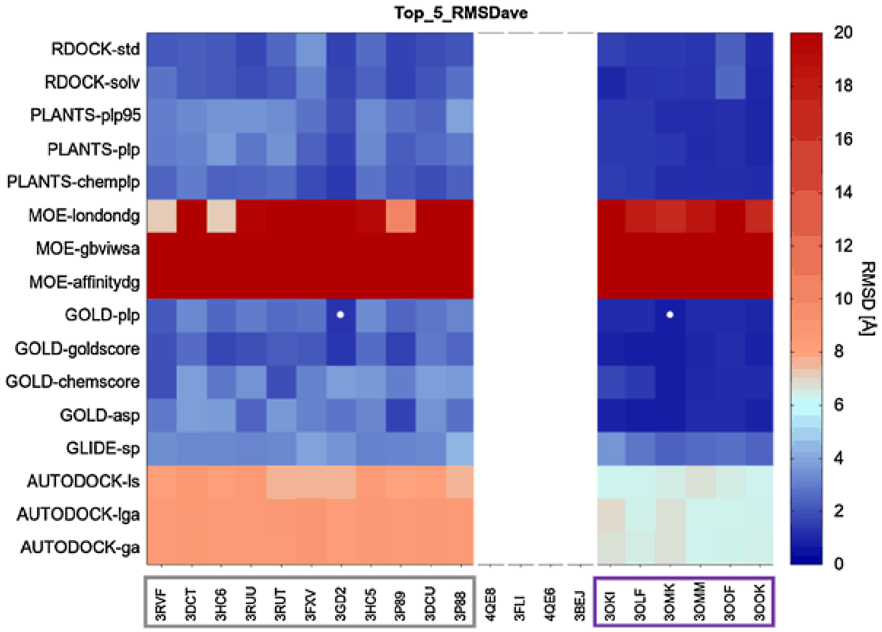

Fig. 3 Cluster cross-docking benchmark results. Structures belonging to cluster 1 (grouped together by a *gray square*) and cluster 6 (grouped together by a *purple square*) were subjected to two independent intra-cluster cross-docking runs. The mean RMSD for the five top-scoring poses of all the ligands docked to the same protein (Top5RMSDave) are reported in the heat-map. The Top5RMSDave for each protein (x-values) and docking protocol (y-values) is represented by a colorimetric scale, going from *blue* to *red* from 0 to higher RMSD values. A *white circle* highlights the selected protein-docking protocol couple for each cluster

3GD2 protein structure with GOLD-PLP docking protocol was chosen for cluster 1 and 3OMK with GOLD-PLP for cluster 6 because they respectively obtained the lowest Top5RMSDave value within their cluster.

Self-docking

Clusters 2–5 are populated by a single PDB structure, so the Cluster Cross-Docking strategy could not be adopted for them. Instead, a self-docking benchmark was performed with these structures, employing DockBench 1.0.5 and the same docking protocols mentioned above for the cross-docking phase. 20 poses (or up to 20 poses in the case of Glide) were generated for each ligand and the lowest RMSD among the poses (RMSDmin) was used to evaluate the docking performance. The RMSDmin plot obtained by DockBench is reported in Fig. 4, where the RMSDmin is reported for each protein (columns)—docking protocol (rows) couple and rendered by a colorimetric scale going from blue to red for values from 0 to 20 Å.

The following docking protocols were selected: Plants-PLP95 for protein 4QE8, rDock-SOLV for 3FLI, GOLD-Goldscore for 4QE6 and GOLD-ASP for 3BEJ.

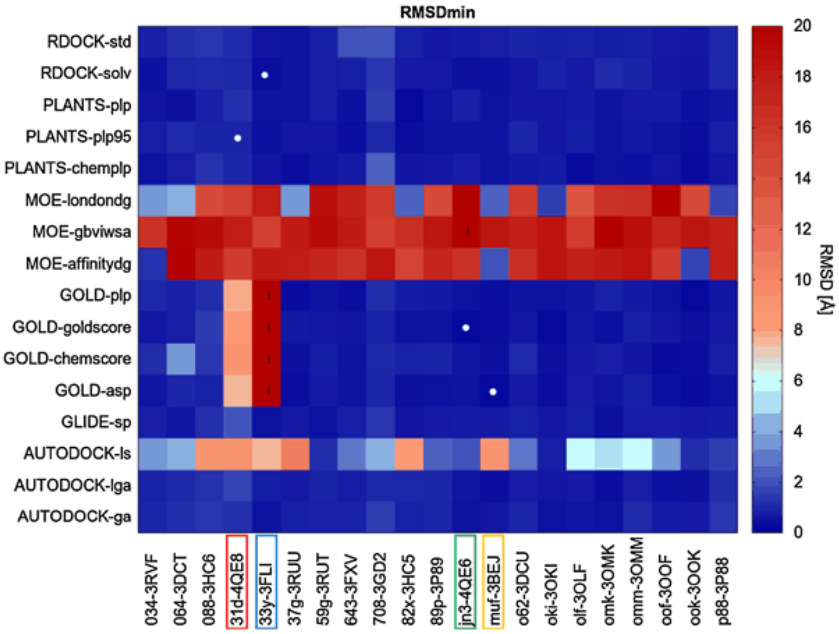

Fig. 4 Self-docking benchmark results. The minimum RMSD values (RMSDmin) returned by each docking protocol (y-values) for each training-set PDB structure (x-values) are represented by a colorimetric scale, going from *blue* to *red* from 0 to higher RMSD value. A *white circle* highlights the selected docking protocol for structure 4QE8 (cluster 2, *red squares*), 3FLI (cluster 3, *blue squared*), 4QE6 (cluster 4, *green squared*), 3BEJ (cluster 5, *yellow squared*)

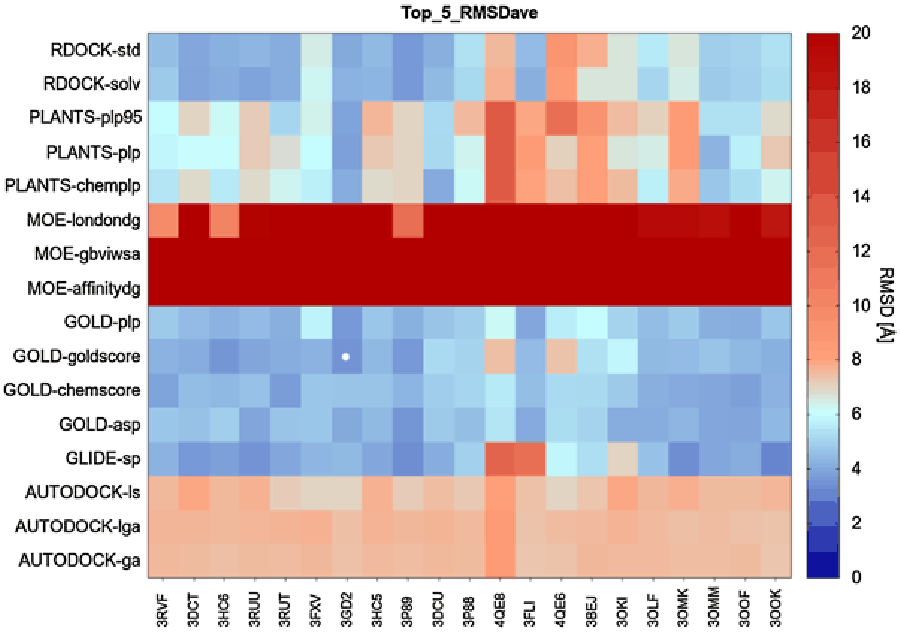

Fig. 5 Total cross-docking benchmark results. The mean RMSD for the five top-scoring poses of all the ligands docked to the same protein (Top5RMSDave) are reported in the heat-map. The Top5RMSDave for each protein (x-values) and docking protocol (y-values) is represented by a colorimetric scale, going from *blue* to *red* from 0 to higher RMSD values. A *white circle* highlights the selected protein-docking protocol couple

Total cross-docking

In addition, a cross-docking simulation was performed considering the total pool of available PDB structures (21 complexes), in order to evaluate the protein that could better host differently shaped compounds.

This simulation resulted in the choice of 3GD2 protein along with GOLD-Goldscore protocol, as can be seen in the Top5RMSDave heat map reported in Fig. 5.

Blind-challenge ligands clusterization

After the selection of one PDB structure per cluster, blind-challenge ligands were screened against the representatives of each cluster using the ROCS tool. In particular, TanimotoComboShapeSimilarity was computed between 5 conformations of each blind-challenge ligand and the representatives of each cluster. A 0.8 TanimotoComboShapeSimilarity cutoff was used to distribute blind-challenge ligands to the clusters identified by the training-set ligands.

Ligands with similarity lower than the cutoff to any of the training-set clusters representatives were collected in the so-called "outliers" cluster, composed of 29 compounds.

The so-defined blind-challenge ligands clusters were associated with the protein-docking protocol couple selected in the docking benchmark phase for each cluster. The outliers cluster was associated with the protein-docking protocol couple identified as a winner in the total cross-docking exercise, because of the higher efficacy of this couple in docking ligands with a different shape to a conformation close to the experimental one.

Table 2 summarizes the results of blind-challenge ligands clusterization, reporting the protein and the docking protocol associated with each ligand.

Cluster 6 is populated by 57 ligands, with 47 of them sharing the 1,2-disubstituted benzimidazole scaffold with the 3OMK ligand. Cluster 1 hosts two ligands presenting the isoxazole-4-yl-methoxy-multiaryl-carboxylic acid typical of the training-set cluster. As regards the other clusters, the compounds do not have a common scaffold with the cluster representative, even if they were associated to it by 3D shape similarity.

20 poses of each blind-challenge ligand were obtained by docking to the associated protein with the selected docking protocol and the 5 top scoring poses of compounds FXR1-36 were automatically selected and submitted to the D3R Grand Challenge 2.

Table 2 Organization of blind-challenge compounds into clusters

Cluster ID	Selected protein PDB ID	Selected docking/scoring protocol	Benchmark Strategy	Blind-challenge compounds
1	3GD2	GOLD-PLP	Cluster cross-docking	**FXR33***, FXR65
2	4QE8	Plants-PLP95	self-docking	**FXR23**, FXR101
3	3FLI	rDock-SOLV	self-docking	**FXR3**, **FXR5**
4	4QE6	GOLD-Goldscore	self-docking	**FXR34**
5	3BEJ	GOLD-ASP	self-docking	**FXR16**, FXR79, FXR92, FXR94, FXR97
6	3OMK	GOLD-PLP	Cluster cross-docking	**FXR2**, **FXR4**, **FXR6**, **FXR7**, **FXR8**, **FXR9**, **FXR13**, **FXR14**, **FXR17**, **FXR18**, **FXR19**, **FXR20**, **FXR21**, **FXR22**, **FXR24**, **FXR25**, **FXR26**, **FXR27**, **FXR28**, **FXR29**, **FXR30**, **FXR31**, **FXR32**, **FXR35**, **FXR36**, FXR37, FXR39, FXR40, FXR42, FXR46, FXR47, FXR48, FXR49, FXR50, FXR51, FXR52, FXR53, FXR54, FXR55, FXR56, FXR57, FXR58, FXR59, FXR60, FXR61, FXR62, FXR63, FXR64, FXR66, FXR67, FXR68, FXR69, FXR70, FXR71, FXR72, FXR91, FXR93, FXR95, FXR96, FXR98, FXR100
outliers	3GD2	GOLD-Goldscore	Total cross-docking	**FXR1**, **FXR10**, **FXR11**, **FXR12**, **FXR15**, FXR38, FXR41, FXR43, FXR44, FXR45, FXR73, FXR74, FXR75, FXR76, FXR77, FXR78, FXR80, FXR81, FXR82, FXR83, FXR84, FXR85, FXR86, FXR87, FXR88, FXR89, FXR90, FXR99, FXR102

The protein structure and docking/scoring protocol used to dock the members of each cluster are indicated. The "Benchmark Strategy" column shows the benchmark method employed for the choice of protein structure and docking/scoring method. Compound FXR1-FXR36 are indicated in bold to highlight that pose prediction was required for them

*Compound FXR33 was removed from pose prediction evaluation

Poses evaluation

Poses evaluation was performed in terms of mean RMSD values between the predicted poses and the crystal structures unveiled by the Grand Challenge organizers. In particular, three RMSD values were employed: the mean RMSD of the first top scoring poses of each ligand (RMSDpose1), the mean RMSD of the whole pool of submitted poses (5 for each compound) (RMSDave) and the mean RMSD of the lowest RMSD poses of each ligand (RMSDbest). The mean values over the pool of 35 ligands (FXR1 to FXR36, excluding compound FXR33 because of crystal artifacts) results in 3.92, 3.81 and 3.25 Å (Table 3), respectively.

The superposition of each ligand pose to the relative crystal structure unveiled by the Grand Challenge organizers is shown in Fig. 6 (pose 1) and in Figs. SI1, SI2, SI3, SI4 (poses 2–5).

Table 3 Evaluation of the pose prediction results in terms of mean RMSD of the first top scoring poses of each ligand (RMSDpose1), mean RMSD of the whole pool of submitted poses (5 for each compound) (RMSDave) and mean RMSD of the lowest RMSD poses of each ligand (RMSDbest), for prediction 1 and 2

Prediction	Submission ID	RMSDpose1 (Å)	RMSDave (Å)	RMSDbest (Å)
1	gfifa	3.92 Å	3.81 Å	3.25 Å
2	knz3v	7.67 Å	6.09 Å	4.84 Å

Results are taken from D3R Challenge web site: https://drugdesigndata.org/about/grand-challenge-2

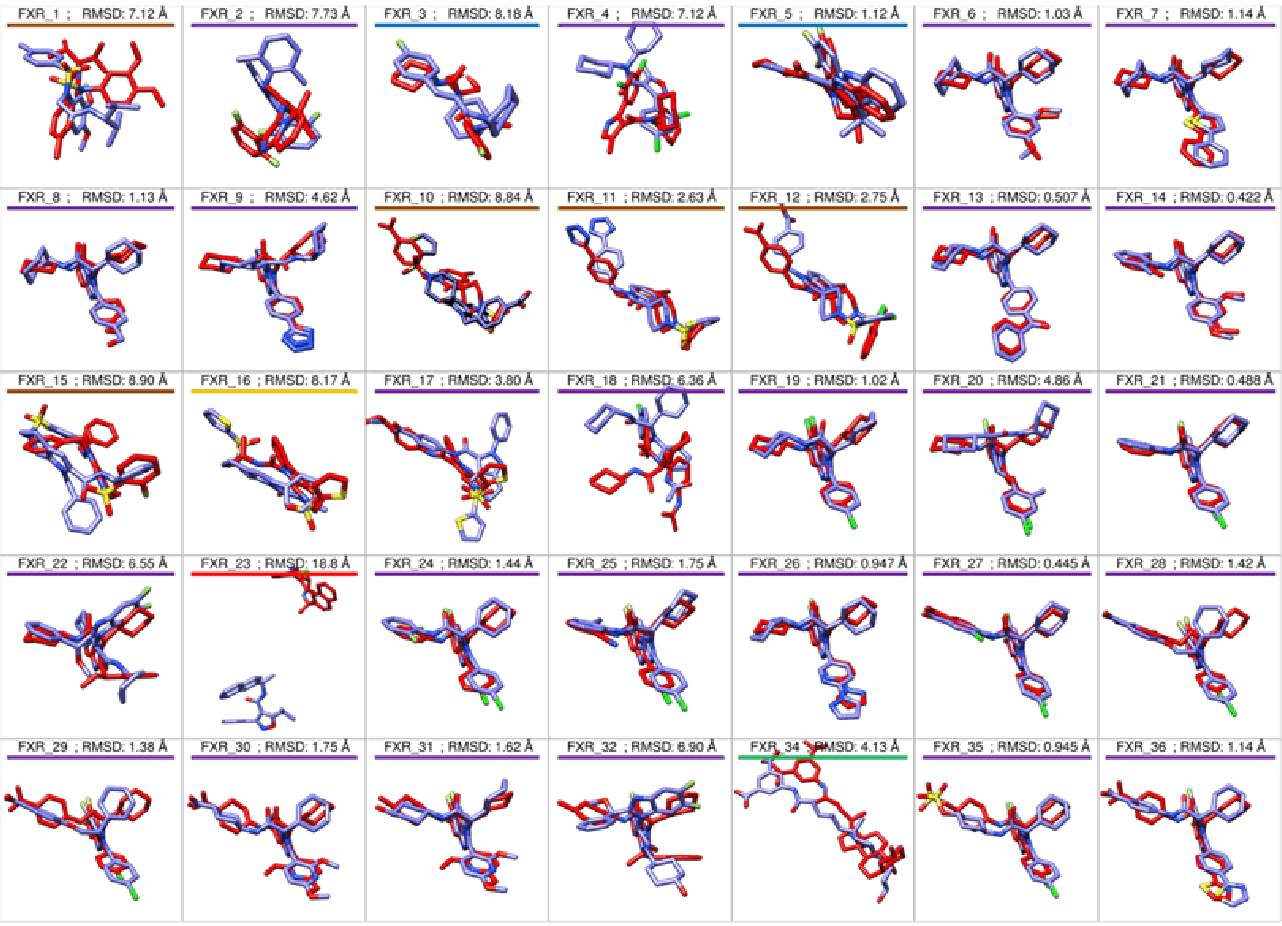

Fig. 6 Superposition of the first top scoring predicted poses (pose1) of compounds FXR1-FXR36, prediction 1 (*light blue sticks*), on the experimental ones (*red sticks*). Compound FXR33 was excluded from the comparison because of crystal artifacts. Compounds FXR1, FXR2, FXR3, FXR4, FXR10, FXR11, FXR13, FXR15, FXR16, FXR18, FXR21, FXR22, FXR23, FXR25, FXR26, FXR28, FXR29, FXR32, FXR34, and FXR35 were superposed to chain A, compound FXR7 to chain AA, compounds FXR12 and FXR14 to chain AB, compounds FXR5, FXR8, FXR17, FXR19, FXR20, FXR24, FXR27, FXR30, FXR31 and FXR36 to chain C, compound FXR6 to chain CA, compound FXR9 to chain E, as in the results provided by the GrandChallenge organizers. RMSD values are reported for each pose. Each compound name is underscored by a *red, blue, green, yellow, purple, brown line*, meaning it belongs to cluster 2–6, "outliers", respectively

Cluster 6 played a major role in lowering the whole RMSD values. In fact, as can be appreciated by Fig. 7a, the mean RMSD values relative to cluster 6 are lower than the values of the other clusters: the mean RMSDpose1, RMSDave, and RMSDbest of the 25 ligands of cluster 6 are respectively 2.66, 2.48 and 1.95 Å, while the mean values of the remaining 10 compounds (organized in clusters 2, 3, 4, 5 and outliers) are 7.06, 7.14 and 6.50 Å, respectively. Focusing on cluster 6, 20 ligands (i.e. FXR6, FXR7, FXR8, FXR9, FXR13, FXR14, FXR19, FXR21, FXR22, FXR24, FXR25, FXR26, FXR27, FXR28, FXR29, FXR30, FXR31, FXR32, FXR35, FXR36) present at least one pose with RMSD lower or near 2 Å, as summarized in Fig. 7a. It is valuable to notice that these ligands constitute the set of compounds with common 1,2-disubstituted benzimidazole scaffold, typical of the respective training set cluster. Compound FXR20 is an exception, since, even sharing the before mentioned structure, was not accurately predicted. Among these 20 compounds, the best pose coincides with the top scoring one just for compounds FXR13, FXR19, FXR21. However, in most of the cases, there are no big RMSD differences between the top scoring pose and the lowest RMSD one, except for compounds FXR9, FXR22, and FXR32. So, given our completely automatic procedure, the selection of just one pose for each ligand would have resulted in a worse scenario. In some cases, the automatic procedure gave discouraging results. Here compound FXR23 is reported as an example, with all poses showing RMSD values higher than 18.0 Å. All the 5 selected poses fall out of the binding site of the receptor. However, considering the whole pool of 20 poses predicted by PLANTS-plp95, the 11th -scoring pose is located within the protein binding site (Fig. SI5). Thus, it is clear that selecting poses just on the basis of the score may be not a good strategy. Honestly, pose shown in Fig. SI5 is still far from the experimental one, with an RMSD of 6.5 Å. Problems related to protein conformations could be excluded since the conformation of the binding site of the unveiled crystallographic structure and the one used for docking (4QE8) do not differ a lot (Cα-RMSD 1.7 Å), so the bad prediction is due to docking bad sampling.

3.1.2 Ligand scoring

Scoring protocol

As regards Stage 1 scoring phase, the first top scoring pose of each blind-challenge (FXR1-FXR102) ligand was submitted to MD simulation. Each MD system was prepared as reported in the Molecular Dynamics Simulations paragraph of the experimental section and three replicas of 2 ns MD simulations were performed. The average MM-GBSA value over the three simulations was used as rescoring method.

As regards Stage 2, the same rescoring method was adopted, but docking poses of compounds FXR1-FXR36 were substituted by the unveiled crystal structures. The crystallographic complexes were prepared and submitted to the same protocol of MD simulation and MM-GBSA evaluation described before.

Ranking evaluation

Kendall's and Spearman's coefficients were used for ranking evaluation. Both values were near 0 and slightly negative (Table 4) as regards Stage 1, meaning a disagreement between our prediction and the experimental binding data. Stage 2 turned out to be slightly improved in the ranking prediction, with a feeble positive value both for Kendall's and Spearman's coefficients, which are still far from the unity value meaning good correlation.

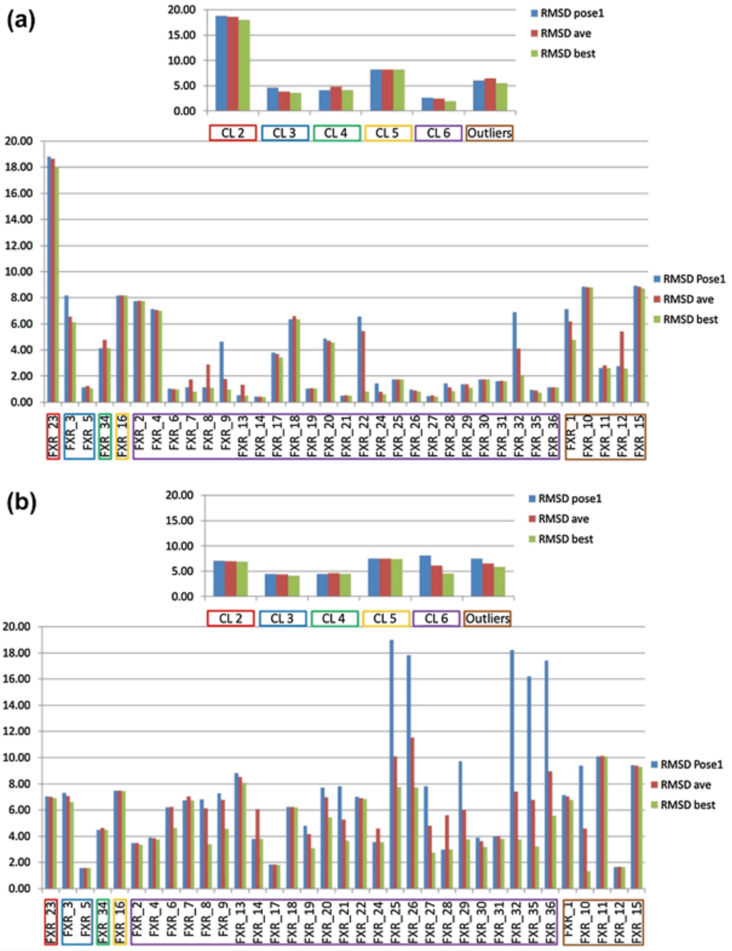

Fig. 7 Representation of the RMSDs of the top score pose (RMSDpose1, *blue* histograms), the average RMSDs over the 5 poses (RMSDave, *red* histograms) and the minimum RMSDs (RMSDbest, *green* histograms), decomposed for each ligand. Values relative to prediction 1 and 2 are shown in **a** and **b**, respectively. The graph on the *top* of both panels represents the mean RMSDpose1, RMSDave and RMSDbest values over the compounds belonging to cluster 2 (*red squares*), 3 (*blue squared*), 4 (*green squared*), 5 (*yellow square*), 6 (*purple squared*) and "outliers" (*brown squared*)

Table 4 Evaluation of the ranking results in terms of Kendall's and Spearman's coefficients, as provided by Grand Challenge 2 organizers

Stage	Submission ID	Kendall's Tau	Kendall's Tau Error	Spearman's Rho	Spearman's Rho Error
1-prediction 1	cs2lm	-0.0896	0.0595	-0.146	0.0894
2-prediction 1	vxvhq	0.185	0.0651	0.274	0.0936
1-prediction 2	jr0oc	-0.394	0.0574	-0.549	0.0762

Kendall's and Spearman's coefficient and errors are indicated for the ranking prediction 1 (stage 1 and 2) and ranking prediction 2 (stage 1). Results are taken from D3R Challenge web site: https://drugdesigndata.org/about/grand-challenge-2

Moreover, Kendall's and Spearman's coefficients were computed for the subset of 35 compounds (FXR1-FXR36, excluding compound FXR33) whose docking pose was substituted by the crystallographic one during Stage 2. They were respectively −0.0655 and −0.0944 as regards Stage 1, while 0.173 and 0.269 for Stage 2. Thus, a shift from negative to positive coefficients can be noted when considering crystallographic poses instead of docking poses. This observation suggests that poorly predicted poses were part of the problem in Stage 1 ranking prediction. Nevertheless, the correlation coefficients values are still low after Stage 2, meaning that the employed MM-GBSA score is not correlated to the experimental binding affinity of the ligands. However, the prediction of compounds affinity still remains a very delicate issue, as demonstrated by Kendall's coefficient of 0.46 as best GrandChallenge value (Submission ID: f2wjs).

3.2 Prediction 2

3.2.1 Pose prediction

Pose prediction protocol

Along with the above-described procedure, a simpler pipeline was adopted to predict the binding mode of the blind challenge ligands, with the aim to compare these results with that of the previous procedure. The crystallographic structure of the apo form of the Farnesoid receptor was used for docking simulation. The results of the total cross-docking exercise were exploited and the GOLD-Goldscore protocol was chosen since it gave the best performance in terms of lowest Top5RMSDave value.

20 poses of each blind-challenge ligand were obtained by docking and the 5 top scoring poses of compounds FXR1-36 were submitted to the D3R Grand Challenge 2.

Poses evaluation

In the case of prediction 2, the mean RMSD of the first top scoring poses of each ligand (RMSDpose1), the mean RMSD of the whole pool of submitted poses (5 for each compound) (RMSDave) and the mean RMSD of the lowest RMSD poses of each ligand (RMSDbest) are 7.67, 6.09 and 4.84 Å (Table 3), respectively. These values are higher than those of prediction 1, in particular, RMSDpose1 is nearly twofold the previous value.

Figure 7b shows that the high deviation from X-ray structures is spread over the whole pool of predicted poses, with compounds FXR5, FXR12, and FXR17 constituting few singular exceptions.

The results decomposition into the previously defined clusters (Fig. 7b) shows that the mean RMSD values of each cluster are very similar. The 8.11 Å RMSDpose1, 6.11 Å RMSDave and 4.53 Å RMSDbest values for cluster 6 are in line with the values of the other clusters and are more than double the mean values of cluster 6 of prediction 1.

The superposition of each ligand pose to the relative crystal structure unveiled by the Grand Challenge organizers is shown in Figs. SI6, SI7, SI8, SI9, SI10 (poses 1–5).

3.2.2 Ligand scoring

Scoring protocol

The first top-scoring poses were considered for ranking evaluation, and Goldscore Fitness score was used as a scoring method.

Ranking evaluation

Kendall’s and Spearman’s coefficients are both negative (Table 4), meaning a wrong correlation among the experimental binding data and the ranking based on the docking scoring function.

4. Conclusions

D3R Grand Challenge gave us the possibility to test an in-house totally automatic procedure to predict ligands binding modes to their protein target. An overall high mean RMSD value of the predicted poses from the X-ray structures is compensated by the comparison of the results between the two protocols we have employed. In fact, the application of a combined procedure which took into account ligand shape similarity and results of a cross-docking-benchmark improved the results, giving a reduction of the average RMSD (RMSDpose1) of the first top-scoring poses of nearly a half. Evaluating the ability of a crystallographic protein structure to host compounds that share a similar chemical shape constituted a strategy that ameliorated the prediction of the binding mode for a subset of 20 compounds on a pool of 35. This strategy seems to help more when ligands share a common scaffold with the compound co-crystallized with the protein used for docking. In fact, this is the case of the 20 before-mentioned compounds, which have a 1,2-disubstituted benzimidazole scaffold in common with the 3OMK compound. For this reason, the entire pipeline presented in this work will be implemented in a new version of DockBench, adding different chemical similarity methods in addition to shape-similarity in the clustering phase.

Moreover, the cross-docking work is highly demanding, but the integration of the described process into automatic pipeline lays the foundations for the application of the same protocol to virtual screening campaigns.

Given the high total mean RMSD values, there are great margins of improvement. Poor results may be obtained relying just on the docking score for pose selection; computing the interaction network of the predicted bound state and comparing this interaction fingerprint with that of a true positive ligand could be more valuable. In addition, the role of key water molecules should be taken into account in the different passages of the proposed pipeline.

References

1. Talele TT, Khedkar SA, Rigby AC (2010) Successful applications of computer aided drug discovery: moving drugs from concept to the clinic. Curr Top Med Chem 10:127–141

2. Kuntz ID, Blaney JM, Oatley SJ, Langridge R, Ferrin TE (1982) A geometric approach to macromolecule-ligand interactions. J Mol Biol 161:269–288

3. Berman HM, Westbrook J, Feng Z, Gilliland G, Bhat TN, Weissig H, Shindyalov IN, Bourne PE (2000) The protein data bank. Nucleic Acids Res 28:235–242

4. McGovern SL, Shoichet BK (2003) Information decay in molecular docking screens against holo, apo, and modeled conformations of enzymes. J Med Chem 46:2895–2907

5. Directory of in silico Drug Design tools. http://www.click2drug.org/

6. Claudel T, Staels B, Kuipers F (2005) The Farnesoid X receptor: a molecular link between bile acid and lipid and glucose metabolism. Arterioscler Thromb Vasc Biol 25:2020–2030

7. Salmaso V, Sturlese M, Cuzzolin A, Moro S (2016) DockBench as docking selector tool: the lesson learned from D3R Grand Challenge 2015. J Comput Aided Mol Des 30:773–789

8. Gathiaka S, Liu S, Chiu M, et al (2016) D3R grand challenge 2015: Evaluation of protein-ligand pose and affinity predictions. J Comput Aided Mol Des 30:651–668

9. Cuzzolin A, Sturlese M, Malvacio I, Ciancetta A, Moro S (2015) DockBench: An Integrated Informatic Platform Bridging the Gap between the Robust Validation of Docking Protocols and Virtual Screening Simulations. Molecules 20:9977–9993

10. Kollman PA, Massova I, Reyes C, et al (2000) Calculating structures and free energies of complex molecules: combining molecular mechanics and continuum models. Acc Chem Res 33:889–897

11. Harvey MJ, Giupponi G, Fabritiis GD (2009) ACEMD: Accelerating Biomolecular Dynamics in the Microsecond Time Scale. J Chem Theory Comput 5:1632–1639

12. Chemical Computing Group (CCG) Inc. (2016) Molecular Operating Environment (MOE). http://www.chemcomp.com

13. Labute P (2009) Protonate3D: assignment of ionization states and hydrogen coordinates to macromolecular structures. Proteins 75:187–205

14. Schrödinger (2017) Schrödinger Release 2017-1: LigPrep. New York, NY

15. RDKit: Open-source cheminformatics. http://www.rdkit.org.

16. Hawkins PCD, Skillman AG, Warren GL, Ellingson BA, Stahl MT (2010) Conformer generation with OMEGA: algorithm and validation using high quality structures from the Protein Databank and Cambridge Structural Database. J Chem Inf Model 50:572–584

17. Hawkins PCD, Skillman AG, Nicholls A (2007) Comparison of shape-matching and docking as virtual screening tools. J Med Chem 50:74–82

18. Morris GM, Huey R, Lindstrom W, Sanner MF, Belew RK, Goodsell DS, Olson AJ (2009) AutoDock4 and AutoDockTools4: Automated docking with selective receptor flexibility. J Comput Chem 30:2785–2791

19. Friesner RA, Banks JL, Murphy RB, et al (2004) Glide: a new approach for rapid, accurate docking and scoring. 1. Method and assessment of docking accuracy. J Med Chem 47:1739–1749

20. Halgren TA, Murphy RB, Friesner RA, Beard HS, Frye LL, Pollard WT, Banks JL (2004) Glide: a new approach for rapid, accurate docking and scoring. 2. Enrichment factors in database screening. J Med Chem 47:1750–1759

21. Verdonk ML, Cole JC, Hartshorn MJ, Murray CW, Taylor RD (2003) Improved protein-ligand docking using GOLD. Proteins 52:609–623

22. Korb O, Stützle T, Exner TE (2007) An ant colony optimization approach to flexible protein–ligand docking. Swarm Intelligence 1:115–134

23. Korb O, Stützle T, Exner TE (2009) Empirical scoring functions for advanced protein-ligand docking with PLANTS. J Chem Inf Model 49:84–96

24. Ruiz-Carmona S, Alvarez-Garcia D, Foloppe N, Garmendia-Doval AB, Juhos S, Schmidtke P, Barril X, Hubbard RE, Morley SD (2014) rDock: a fast, versatile and open source program for docking ligands to proteins and nucleic acids. PLoS Comput Biol 10:e1003571

25. D.A. Case, V. Babin, J.T. Berryman, R.M. Betz, Q. Cai, D.S. Cerutti, T.E. Cheatham, III, T.A. Darden, R.E.Duke, H. Gohlke, A.W. Goetz, S. Gusarov, N. Homeyer, P. Janowski, J. Kaus, I. Kolossváry, A. Kovalenko,T.S. Lee, S. LeGrand, T. Luchko, R. Luo, B. Madej, K.M. Merz, F. Paesani, D.R. Roe, A. Roitberg, C. Sagui,R. Salomon-Ferrer, G. Seabra, C.L. Simmerling, W. Smith, J. Swails, R.C. Walker, J. Wang, R.M. Wolf, X.Wu and P.A. Kollman (2014) AMBER 14.

26. Gasteiger J, Marsili M (1980) Iterative partial equalization of orbital electronegativity—a rapid access to atomic charges. Tetrahedron 36:3219–3228

27. Wang J, Wolf RM, Caldwell JW, Kollman PA, Case DA (2004) Development and testing of a general amber force field. J Comput Chem 25:1157–1174

28. Darden T, York D, Pedersen L (1993) Particle mesh Ewald: An N·log(N) method for Ewald sums in large systems. J Chem Phys 98:10089

29. Essmann U, Perera L, Berkowitz ML, Darden T, Lee H, Pedersen LG (1995) A smooth particle mesh Ewald method. J Chem Phys 103:8577

30. Onufriev A, Bashford D, Case DA (2004) Exploring protein native states and large-scale conformational changes with a modified generalized born model. Proteins 55:383–394

31. Weiser J, Shenkin PS, Still CW (1999) Approximate atomic surfaces from linear combinations of pairwise overlaps (LCPO). J Comput Chem

32. Downes M, Verdecia MA, Roecker AJ, et al (2003) A chemical, genetic, and structural analysis of the nuclear bile acid receptor FXR. Mol Cell 11:1079–1092

33. Soisson SM, Parthasarathy G, Adams AD, Sahoo S, Sitlani A, Sparrow C, Cui J, Becker JW (2008) Identification of a potent synthetic FXR agonist with an unexpected mode of binding and activation. Proc Natl Acad Sci U S A 105:5337–5342

34. Akwabi-Ameyaw A, Bass JY, Caldwell RD, et al (2008) Conformationally constrained farnesoid X receptor (FXR) agonists: Naphthoic acid-based analogs of GW 4064. Bioorg Med Chem Lett 18:4339–4343

35. Flatt B, Martin R, Wang T-L, et al (2009) Discovery of XL335 (WAY-362450), a highly potent, selective, and orally active agonist of the farnesoid X receptor (FXR). J Med Chem 52:904–907

36. Feng S, Yang M, Zhang Z, et al (2009) Identification of an N-oxide pyridine GW4064 analog as a potent FXR agonist. Bioorg Med Chem Lett 19:2595–2598

37. Bass JY, Caldwell RD, Caravella JA, et al (2009) Substituted isoxazole analogs of farnesoid X receptor (FXR) agonist GW4064. Bioorg Med Chem Lett 19:2969–2973

38. Akwabi-Ameyaw A, Bass JY, Caldwell RD, et al (2009) FXR agonist activity of conformationally constrained analogs of GW 4064. Bioorg Med Chem Lett 19:4733–4739

39. Lundquist JT, Harnish DC, Kim CY, et al (2010) Improvement of physiochemical properties of the tetrahydroazepinoindole series of farnesoid X receptor (FXR) agonists: beneficial modulation of lipids in primates. J Med Chem 53:1774–1787

40. Richter HGF, Benson GM, Blum D, et al (2011) Discovery of novel and orally active FXR agonists for the potential treatment of dyslipidemia & diabetes. Bioorg Med Chem Lett 21:191–194

41. Richter HGF, Benson GM, Bleicher KH, et al (2011) Optimization of a novel class of benzimidazole-based farnesoid X receptor (FXR) agonists to improve physicochemical and ADME properties. Bioorg Med Chem Lett 21:1134–1140

42. Bass JY, Caravella JA, Chen L, et al (2011) Conformationally constrained farnesoid X receptor (FXR) agonists: heteroaryl replacements of the naphthalene. Bioorg Med Chem Lett 21:1206–1213

43. Akwabi-Ameyaw A, Caravella JA, Chen L, et al (2011) Conformationally constrained farnesoid X receptor (FXR) agonists: alternative replacements of the stilbene. Bioorg Med Chem Lett 21:6154–6160

44. Xu X, Xu X, Liu P, Zhu Z, Chen J, Fu H, Chen L, Hu L, Shen X (2015) Structural Basis for Small Molecule NDB (N-Benzyl-N-(3-(tert-butyl)-4-hydroxyphenyl)-2,6-dichloro-4-(dimethylamino) Benzamide) as a Selective Antagonist of Farnesoid X Receptor α (FXRα) in Stabilizing the Homodimerization of the Receptor. J Biol Chem 290:19888–19899

45. Kudlinzki, D., Merk, D., Linhard, V.L., Saxena, K., Sreeramulu, S., Nilsson, E., Dekker, N., Wissler, L., Bamberg, K., Schubert-Zsilavecz, M., Schwalbe, H. FXR with CDCA and NCoA-2 peptide.

46. Jin L, Feng X, Rong H, et al (2013) The antiparasitic drug ivermectin is a novel FXR ligand that regulates metabolism. Nat Commun 4:1937

47. Pedregosa F, Varoquaux G, Gramfort A, et al (2011) Scikit-learn: Machine Learning in Python. Journal of Machine Learning Research

48. Ester M, Kriegel H-P, Sander J, Xu X A density-based algorithm for discovering clusters in large spatial databases with noise.

Sulfonamido-derivatives of unsubstituted carbazole as BACE1 Inhibitors

Simone Bertini, Elisa Ghilardi, Valentina Asso, Filippo Minutolo, Simona Rapposelli, Maria Digiacomo, Giuseppe Saccomanni, Veronica Salmaso, Mattia Sturlese, Stefano Moro, Marco Macchia, Clementina Manera

(2017) Sulfonamido-derivatives of unsubstituted carbazoles as BACE1 inhibitors. Bioorg Med Chem Lett 27:4812–4816

Abstract

A novel series of variously substituted N-[3-(9H-carbazol-9-yl)-2-hydroxypropyl]-arylsulfonamides has been synthesized and assayed for β-Secretase (BACE1) inhibitory activity. BACE1 is a widely recognized drug target for the prevention and treatment of Alzheimer's Disease (AD). The introduction of benzyl substituents on the nitrogen atom of the arylsulfonamide moiety has so far led to the best results, with three derivatives showing IC50 values ranging from 1.6 to 1.9 µM. Therefore, a significant improvement over the previously reported series of N-carboxamides (displaying IC50's ≥ 2.5 µM) has been achieved, thus suggesting an active role of the sulfonamido-portion in the inhibition process. Preliminary molecular modeling studies have been carried out to rationalize the observed structure-activity relationships.

Alzheimer's disease (AD) is the most common form of dementia, which occurs predominantly in older people (over 65 years of age). It is a progressive and irreversible neurodegenerative disorder, which compromises cognitive functions (memory, thinking, reasoning) and behavioral skills in such a way as to interfere with daily life and with the fulfillment of the simplest tasks. The main neuropathological features of AD are extracellular senile plaques, essentially made of amyloid β peptide (Aβ) [1], and intracellular neurofibrillary tangles, caused by the aggregation of phosphorylated tau proteins [2].

The Aβ peptide is generated through proteolytic processing of the amyloid precursor protein (APP) first by β-secretase (BACE1) followed by γ-secretase. In particular, the cleavage operated by BACE1 produces the secreted amino-terminal part of APP (sAPPβ) and the membrane-bound carboxy-terminal fragment, which is 99 amino acids in length (C99). γ-Secretase subsequently cleaves the C99 fragment, releasing the Aβ peptide, which aggregates to form toxic amyloid plaques in the brain [3]. It has been demonstrated that BACE1 knockout (BACE1 −/−) mice are unable to generate C99 and Aβ, are viable [4], and drastically ameliorate the pathology when crossed with APP transgenic mice (a mouse model of AD) [5]. Therefore, BACE1 is an attractive drug target for lowering brain levels of amyloid beta and, consequently, for the treatment or prevention of AD.

Many BACE1-inhibitors studied to date are peptidomimetics and incorporate the hydroxyethylamine (HEA) moiety [6], which is known to well mimic the transition state of aspartyl proteases (like BACE1) substrates

[7]. These compounds have in general high molecular weights and suffer from poor blood brain barrier permeability [8]. So, in recent years, more efforts have been dedicated to the development of non-peptidomimetic BACE1-inhibitors, with the aim of obtaining smaller active molecules and, therefore, more drug-like agents for the treatment of AD [9-11]. Among those, only a few compounds have entered in advanced clinical phases [11,12].

We previously reported a series of α-naphthylaminoalcohol derivatives of unsubstituted carbazole showing a BACE1 inhibitory activity in the low µM range [13]. Furthermore, we recently reported that *N*-carboxamido-derivatives are still active against this enzyme (Fig. 1) [14].

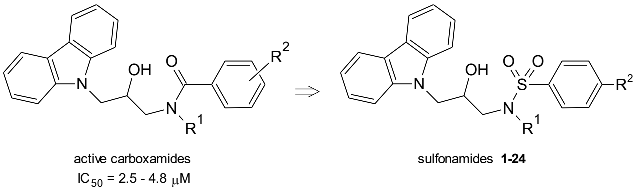

Fig. 1 General structure of already reported *N*-[3-(9*H*-carbazol-9-yl)-2-hydroxypropyl]-arylcarboxamides and novel variously substituted *N*-[3-(9*H*-carbazol-9-yl)-2-hydroxypropyl]-arylsulfonamides (**1**–**24**, see also Table 1).

In this work, we describe the synthesis and the evaluation of BACE1 inhibitory activity of a further series of derivatives, in which the unsubstituted carbazole-methyl carbinol portion was kept constant and the *N*-atom was sulfonylated with different groups (**1**–**24**, Fig. 1). A focused screening in the literature of this type of compounds was primarily carried out, and six derivatives were found commercially available (**1**–**3**, **5**, **11** and **22**, see Table 1).

These sulfonamido-derivatives were synthesized as shown in Scheme 1. Commercially available carbazole **25** was alkylated with epichlorohydrin (2.5 eq., added dropwise at 0 °C) in the presence of KOH (1.2 eq.) in DMF, affording epoxide **26**. Reaction of this intermediate with the appropriate amine (2.0 eq.) in EtOH afforded aminoalcohols **27**–**38**. These derivatives were then treated with variously substituted aryl-sulfonyl-chlorides (1.1 eq.) in the presence of PS-DIEA (1.2 eq.) and DMAP (catalytic amount) in CH_2Cl_2, obtaining final compounds **1**–**24**.

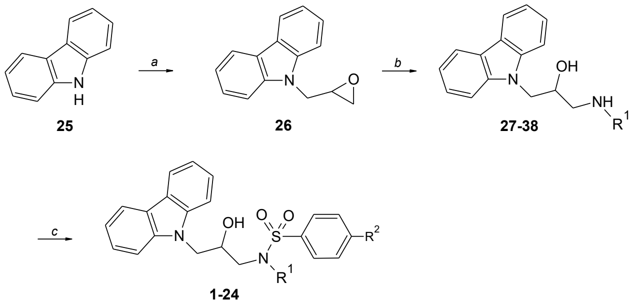

Scheme 1 Reagents and conditions: a) epichlorohydrin, KOH, DMF, 0 °C, 5 h, 50%; b) R^1-NH_2, EtOH, 65 °C, overnight, 40–79%; c) $ArSO_2Cl$, PS-DIEA, DMAP, CH_2Cl_2, r. t., overnight, 13–86%.

Table 1 Structures and BACE1 inhibitory activities of novel variously substituted arylsulfonamides **1**–**24**.

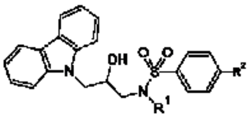

Compd	R^1	R^2	$IC_{50}{}^a$ (μM)	$logBB_{pred}{}^b$
1	Ph	H	3.0	-0.58
2	Ph	CH_3	2.6	-0.57
3	Ph	Cl	2.9	-0.61
4	Ph	OCH_3	2.4	-0.64
5	4-CH_3-Ph	H	7.1	-0.57
6	4-Cl-Ph	H	> 10	-0.61
7	4-CF_3-Ph	H	3.6	-0.60
8	4-NO_2-Ph	H	3.8	-0.79
9	4-F-Ph	H	> 10	-0.63
10	Bn	H	1.9	-0.61
11	Bn	CH_3	2.7	-0.61
12	Bn	Cl	1.7	-0.65
13	Bn	OCH_3	1.6	-0.67
14	4-CH_3-Bn	H	> 10	-0.61
15	4-Cl-Bn	H	2.7	-0.65
16	4-OCH_3-Bn	H	5.7	-0.68
17	Phenethyl	H	2.8	-0.60
18	Phenethyl	CH_3	2.5	-0.59
19	Phenethyl	Cl	3.8	-0.63
20	Phenethyl	OCH_3	3.0	-0.66
21	Cyclohexyl	H	4.1	-0.61
22	Cyclohexyl	CH_3	3.9	-0.60
23	Cyclohexyl	Cl	6.5	-0.65
24	Cyclohexyl	OCH_3	3.2	-0.67

[a] IC_{50} measurements were performed as reported in Ref. 15. Data represent mean values for at least three separate experiments. Standard errors are not shown for the sake of clarity and were never higher than 15% of the means.
[b] Predicted blood-brain barrier permeation ($logBB_{pred}$ = log[Brain]/[Blood]) [28].

The inhibitory activity of the newly synthesized compounds towards BACE1 was determined by a previously reported fluorescence-based assay [15] and the results are shown in Table 1.

The introduction of a simple phenyl substituent on the sulfonamide nitrogen (R^1), together with the presence of an unsubstituted or substituted aryl sulfonamide (compounds **1**–**4**, IC_{50} ranging from 2.4 to 3.0 μM), leads to a BACE1-inhibitory activity comparable to that of some of the most active compounds included in the previous series of *N*-carboxamides (IC_{50} = 2.5 μM) [14]. When the sulfonamide aromatic ring is unsubstituted (R^2 = H) and the phenyl on the sulfonamide nitrogen is substituted in position 4, the activity worsens slightly (compounds **7** and **8**), significantly (compound **5**) or is completely lost (compounds **6** and **9**). The presence of a benzyl substituent on the sulfonamide nitrogen causes an appreciable increase in the inhibitory activity, except in one case (compound **11**); compounds **10**, **12** and **13** proved to be the most potent inhibitors of this series, with IC_{50} values ranging from 1.6 to 1.9 µM. The *para*-substitution of the benzyl group (leaving the aryl sulfonamide unsubstituted) generally causes a decrement in the activity (compounds **14**–**16**). If a phenethyl group is introduced on the sulfonamide nitrogen, regardless the presence of substituents in position 4 of the aryl sulfonamide moiety (compounds **17**–**20**), the activity is preserved or slightly decreased respect to the most active compounds of the previous series of *N*-carboxamides (IC_{50} = 2.5 µM) [14]. The activity generally decreases when R^1 is a completely aliphatic group, such as a cyclohexyl (compounds **21**–**24**). Regarding to the substituent on the sulfonamide aromatic ring, when R^2 = H and R^1 = phenyl, 4-substituted phenyl, 4-substitutedbenzyl, phenethyl or cyclohexyl, the BACE1 inhibitory activity worsens slightly (compounds **1**, **7**–**8**, **15**–**17** and **21**) or is lost (compounds **6**, **9** and **14**). When R^2 = Me, the activity is preserved (compounds **2**, **11** and **18**) or slightly worsened (compounds **22**). When the phenyl ring of the sulfonamide is substituted with an alogen atom (Cl in this case) or a methoxy group, the activity is almost preserved (compounds **3** and **4**), improved (compounds **12** and **13**) or worsened (compounds **19**, **23**, **20** and **24**). In general, the BACE1 inhibitory activity of this kind of molecules is mostly influenced by the substituent on the sulfonamide nitrogen (R^1) and the *N*-benzyl-substituted compounds are the most active (except **11**) regardless the substitution on the 4-position of the sulfonamide phenyl ring (R^2).

A molecular docking study of the sulfonamide derivatives in BACE1 active site was conducted to give an interpretation of the structure-activity relationship at a molecular level. First, BACE1 holo crystal structures were retrieved from the Protein Data Bank, resulting in 302 ligand-BACE1 complexes. The preliminary operations of our work were devoted to the identification of the best protein structure and docking protocol to use in the subsequent docking calculations.

According to a previously validated protocol [16], crystal structures were filtered according to chemical similarity of their co-crystallized ligand to compound **13**, chosen as representative of the series of inhibitors herein described because of its highest potency (IC_{50} = 1.6 µM). MACCS Tanimoto similarity was computed exploiting RDKit [17] functionalities, and the 6 structures characterized by highest similarity values were selected (PDB ID: 2WF2 [18], 2WF3 [18], 2WF4 [19], 2VNN [20], 2VKM [21], 4FCO, with the addition of structure 1W51 [22] used in a previous study [14]). The selected structures were subjected to a docking benchmark study to evaluate the performance of different docking protocols and scoring functions in the self-docking exercise. The co-crystallized ligands were prepared by adding hydrogens using the Protonate3D tool of MOE [23], while the proteins were prepared by exploiting the Protein-preparation tool and the Protonate3D of the same software suite.

DockBench tool [24] was employed to automatically perform the docking benchmark, and, after the analysis of the benchmark results, the protein 2WF4 with the Gold-goldscore [25] protocol were chosen because of the high performance in DockBench Protocol Score.

The structures of the sulfonamide derivatives (stereoisomer *R* and *S* of each compound) were constructed by using the MOE builder function, the starting conformation was initially generated exploiting Corina [26] and then minimized using PM3 theory. The docking calculations were performed for each compound, limiting the conformational search within a 20 Å radius sphere centered on the center of mass of the co-crystallized ligand in the corresponding complex.

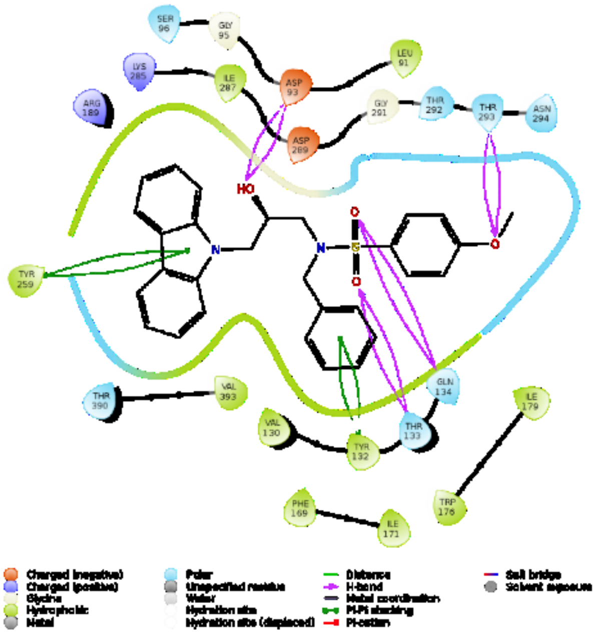

Fig. 2 Schematic representation of the principal interactions resulting from the docking study of compound **13**.

Both *R* and *S* stereoisomers find a good accommodation within the active site of BACE1, with the (2-hydroxypropyl)sulfonamide portion protected behind the flap region and the benzylic and carbazolic moieties pointing toward two hydrophobic clefts positioned on left and right. The interaction established by compound **13** are depicted in Fig. 2 using the ligand interaction diagram as implemented in the Schrodinger suite [27]. In detail, the predicted binding mode of compound **13** is reported in Fig. 3, panel A. The benzylic moiety attached to the sulfonamide nitrogen is inserted into a hydrophobic pocket defined by Leu91, Ile179, Trp176, Ile171, and Phe169. Also, the carbazole portion leans on a hydrophobic portion of the protein, characterized by Tyr259, Ile287, and Val393. The sulfonamide function acts as a hydrogen bond acceptor with Gln134 positioned in the flap region. The hydroxyl groups of both *R* and *S*stereoisomers are involved in a hydrogen bond with one of the two catalytic aspartates: in particular, the *R*-enantiomer interacts with

Asp93, while the *S*enantiomer with Asp289. Moreover, both enantiomers are stabilized by a further hydrogen bond between the methoxy group in R^2 and Thr293. The pose of compound **13** (Fig. 3, panel B) is similar to that displayed by the crystallographic binding mode of the co-crystallized ligand (PDB ID: 2WF4; ligand ID: ZY4) within the protein conformation used in our docking calculations. The (2-hydroxypropyl)sulfonamide of compound **13** resembles the *gem*-diol group of the (2,2-dihydroxypropyl)amide moiety of the crystallographic compound: here the amide carbonyl group makes a hydrogen bond with Gln134 and the two hydroxyls are engaged as donors in two hydrogen bonds with Asp93.

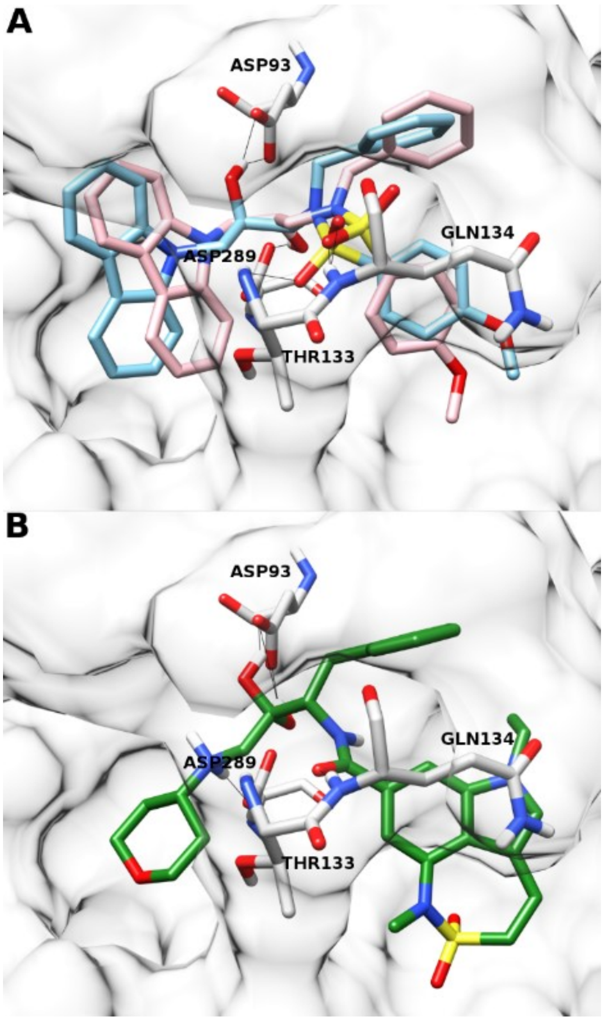

Fig. 3 (A) Docking results of compound **13** in BACE1. Both (*R*) and (*S*)-stereoisomer are respectively shown in cyan and pink. (B) The obtained docking result is compared to the crystallographic binding mode of ligand ZY4 within the BACE1 conformation selected for docking studies (PDB ID: 2WF4).

This makes plausible the binding of both the stereoisomers of compound **13** to the BACE1 binding site. A binding mode similar to that of compound **13** was obtained by docking simulations for almost all the other sulfonamide derivatives, as reported in Video-S1 (Supplementary Material).

All the BACE1 inhibitors are meant to have central nervous system (CNS) activity, so they are expected to cross the blood-brain barrier (BBB). Thus, the logBB was computed with the Stardrop software [28] for all compounds, to estimate their capability to distribute from blood to the CNS. The logBB predicted values, being higher than −0.8 in all cases, fall under the -1 limit for passing the blood-brain barrier, so they seem to satisfy the CNS permeability expectation. Compound **8**, which is characterized by the presence of a nitrophenyl substituent, shows the highest value of this series (logBB = −0.79), due to the relatively high polarity of the NO_2 group, thus making its putative BBB permeation less promising than those of the other analogues.

In conclusion, we have synthesized a series of BACE1 inhibitors possessing a *N*-[3-(9*H*-carbazol-9-yl)-2-hydroxypropyl]-arylsulfonamido structure. Among the 24 derivatives, 21 active analogues were found, with three highly active compounds (IC_{50} values ranging from 1.6 to 1.9 μM). The docking study showed that both enantiomers of the most active compound of this series (**13**) find a good accommodation within the active site of BACE1; a similar binding mode was obtained by docking simulations of almost all the other sulfonamide derivatives, as reported in Video-S1 (Supplementary Material). Moreover, the predicted logBB values of all compounds (ranging from −0.57 to −0.79) indicate satisfactory BBB permeabilities.

References

1. Hardy J, Selkoe DJ (2002) The amyloid hypothesis of Alzheimer's disease: progress and problems on the road to therapeutics. Science 297:353–356

2. Gendron TF, Petrucelli L (2009) The role of tau in neurodegeneration. Mol Neurodegener 4:13

3. Kandalepas PC, Vassar R (2012) Identification and biology of β-secretase. J Neurochem 120 Suppl 1:55–61

4. (a) Luo Y, Bolon B, Kahn S, et al (2001) Mice deficient in BACE1, the Alzheimer's beta-secretase, have normal phenotype and abolished beta-amyloid generation. Nat Neurosci 4:231–232

   (b) Roberds SL, Anderson J, Basi G, et al (2001) BACE knockout mice are healthy despite lacking the primary beta-secretase activity in brain: implications for Alzheimer's disease therapeutics. Hum Mol Genet 10:1317–1324

5. McConlogue L, Buttini M, Anderson JP, et al (2007) Partial reduction of BACE1 has dramatic effects on Alzheimer plaque and synaptic pathology in APP Transgenic Mice. J Biol Chem 282:26326–26334

6. (a) Kumar AB, Anderson JM, Melendez AL, Manetsch R (2012) Synthesis and structure-activity relationship studies of 1,3-disubstituted 2-propanols as BACE-1 inhibitors. Bioorg Med Chem Lett 22:4740–4744

   (b) De Strooper B, Vassar R, Golde T (2010) The secretases: enzymes with therapeutic potential in Alzheimer disease. Nat Rev Neurol 6:99–107

   (c) Ghosh AK, Gemma S, Tang J (2008) beta-Secretase as a therapeutic target for Alzheimer's disease. Neurotherapeutics 5:399–408

   (d) Hills ID, Vacca JP (2007) Progress toward a practical BACE-1 inhibitor. Curr Opin Drug Discov Devel 10:383–391

7. (a) Dohnálek J, Hasek J, Dusková J, Petroková H, Hradilek M, Soucek M, Konvalinka J, Brynda J, Sedlácek J, Fábry M (2002) Hydroxyethylamine isostere of an HIV-1 protease inhibitor prefers its amine to the hydroxy group in binding to catalytic aspartates. A synchrotron study of HIV-1 protease in complex with a peptidomimetic inhibitor. J Med Chem 45:1432–1438

   (b) Ghosh AK, Fidanze S (1998) Transition-State Mimetics for HIV Protease Inhibitors: Stereocontrolled Synthesis of Hydroxyethylene and Hydroxyethylamine Isosteres by Ester-Derived Titanium Enolate Syn and Anti-Aldol Reactions. J Org Chem 63:6146–6152

   (c) Tucker TJ, Lumma WC, Payne LS, Wai JM, de Solms SJ, Giuliani EA, Darke PL, Heimbach JC, Zugay JA, Schleif WA (1992) A series of potent HIV-1 protease inhibitors containing a hydroxyethyl secondary amine transition state isostere: synthesis, enzyme inhibition, and antiviral activity. J Med Chem 35:2525–2533

8. Yuan J, Venkatraman S, Zheng Y, McKeever BM, Dillard LW, Singh SB (2013) Structure-based design of β-site APP cleaving enzyme 1 (BACE1) inhibitors for the treatment of Alzheimer's disease. J Med Chem 56:4156–4180

9. Chiriano G, De Simone A, Mancini F, et al (2012) A small chemical library of 2-aminoimidazole derivatives as BACE-1 inhibitors: Structure-based design, synthesis, and biological evaluation. Eur J Med Chem 48:206–213

10. Butler CR, Ogilvie K, Martinez-Alsina L, et al (2017) Aminomethyl-Derived Beta Secretase (BACE1) Inhibitors: Engaging Gly230 without an Anilide Functionality. J Med Chem 60:386–402

11. Scott JD, Li SW, Brunskill APJ, et al (2016) Discovery of the 3-Imino-1,2,4-thiadiazinane 1,1-Dioxide Derivative Verubecestat (MK-8931)-A β-Site Amyloid Precursor Protein Cleaving Enzyme 1 Inhibitor for the Treatment of Alzheimer's Disease. J Med Chem 59:10435–10450

12. Ghosh AK, Brindisi M, Tang J (2012) Developing β-secretase inhibitors for treatment of Alzheimer's disease. J Neurochem 120 Suppl 1:71–83

13. Asso V, Ghilardi E, Bertini S, Digiacomo M, Granchi C, Minutolo F, Rapposelli S, Bortolato A, Moro S, Macchia M (2008) alpha-Naphthylaminopropan-2-ol Derivatives as BACE1 Inhibitors. ChemMedChem 3:1530–1534

14. Bertini S, Asso V, Ghilardi E, et al (2011) Carbazole-containing arylcarboxamides as BACE1 inhibitors. Bioorg Med Chem Lett 21:6657–6661

15. Porcari V, Magnoni L, Terstappen GC, Fecke W (2005) A continuous time-resolved fluorescence assay for identification of BACE1 inhibitors. Assay Drug Dev Technol 3:287–297

16. Salmaso V, Sturlese M, Cuzzolin A, Moro S (2016) DockBench as docking selector tool: the lesson learned from D3R Grand Challenge 2015. J Comput Aided Mol Des 30:773–789

17. RDKit: Open-source cheminformatics. http://www.rdkit.org.

18. Charrier N, Clarke B, Demont E, et al (2009) Second generation of BACE-1 inhibitors part 2: Optimisation of the non-prime side substituent. Bioorg Med Chem Lett 19:3669–3673

19. Charrier N, Clarke B, Cutler L, et al (2009) Second generation of BACE-1 inhibitors part 3: Towards non hydroxyethylamine transition state mimetics. Bioorg Med Chem Lett 19:3674–3678

20. Charrier N, Clarke B, Cutler L, et al (2008) Second generation of hydroxyethylamine BACE-1 inhibitors: optimizing potency and oral bioavailability. J Med Chem 51:3313–3317

21. Ghosh AK, Kumaragurubaran N, Hong L, et al (2008) Potent memapsin 2 (beta-secretase) inhibitors: design, synthesis, protein-ligand X-ray structure, and in vivo evaluation. Bioorg Med Chem Lett 18:1031–1036

22. Patel S, Vuillard L, Cleasby A, Murray CW, Yon J (2004) Apo and inhibitor complex structures of BACE (beta-secretase). J Mol Biol 343:407–416

23. Chemical Computing Group (CCG) Inc. (2016) Molecular Operating Environment (MOE). http://www.chemcomp.com

24. Cuzzolin A, Sturlese M, Malvacio I, Ciancetta A, Moro S (2015) DockBench: An Integrated Informatic Platform Bridging the Gap between the Robust Validation of Docking Protocols and Virtual Screening Simulations. Molecules 20:9977–9993

25. Verdonk ML, Cole JC, Hartshorn MJ, Murray CW, Taylor RD (2003) Improved protein-ligand docking using GOLD. Proteins 52:609–623

26. Molecular Networks GmbH CORINA; Germany

27. Schrödinger (2017) Schrödinger Release 2017–1: Maestro; New York, NY

28. StarDrop. Optibrium Ltd, 7221 Cambridge Research Park, Beach Drive, Cambridge, CB25 9TL, UK. http://www.optibrium.com/

Synthesis, structure-activity relationships and biological evaluation of 7-phenyl-pyrroloquinolinone 3-amide derivatives as potent antimitotic agents

Davide Carta, Roberta Bortolozzi, Mattia Sturlese, Veronica Salmaso, Ernest Hamel, Giuseppe Basso, Laura Calderan, Luigi Quintieri, Stefano Moro, Giampietro Viola, Maria Grazia Ferlin

(2017) Synthesis, structure-activity relationships and biological evaluation of 7-phenyl-pyrroloquinolinone 3-amide derivatives as potent antimitotic agents. Eur J Med Chem 127:643–660

Abstract

A small library of 7-pyrrolo[3,2-*f*]quinolinones was obtained by introducing benzoyl, sulfonyl and carbamoyl side chains at the 3-*N* position, and their cytotoxicity against a panel of leukemic and solid tumor cell lines was evaluated. Most of them showed high antiproliferative activity with GI_{50}s ranging from micro-to sub-nanomolar values, and these values correlated well with the inhibitory activities of the compounds against tubulin polymerization. Based on a recently proposed colchicine bind site inhibitors (CBSIs) pharmacophore, the interactions of the novel 7-PPyQs at the colchicine domain were rationalized. The most active compounds (**4a** and **4b**) did not induce significant cell death in normal human lymphocytes, suggesting that the compounds may be selective against cancer cells. In particular, **4a** was a potent inducer of apoptosis in both the HeLa and Jurkat cell lines. On the other hand, the sulfonyl derivative **4b** exhibited a lower potency in comparison with **4a**. With both compounds, induction of apoptosis was associated with dissipation of the mitochondrial transmembrane potential and production of reactive oxygen species, suggesting that cells treated with the compounds followed the intrinsic pathway of apoptosis.

1. Introduction

Drugs interfering with microtubules (MTs) represent a class of compounds of great interest in the area of anticancer therapy. MTs are an essential component of the cellular cytoskeleton, as they regulate and participate in a variety of cellular functions that include motility, morphology, intracellular transport, signal transduction, and cell division [1]. MTs are composed of α/β tubulin heterodimers that have polymerized into cylindrical structures, and, therefore, both natural and synthetic agents able to interfere with tubulin polymerization or depolymerization, thereby altering MT dynamics, continue to attract considerable attention in the field of chemotherapeutic research [2]. Not only are there clinically used natural and semisynthetic antimitotics (such as, paclitaxel, other taxanes, eribulin, ixabepilone and vinca akaloids), but there is also a large number of structurally dissimilar small molecules with high affinity for the colchicine site on tubulin. These compounds are able to inhibit the proliferation of a wide variety of human cancer cells [3].

Moreover, these agents can also affect the tumor endothelial vasculature required for the growth of tumor mass. These types of tubulin inhibitors might provide new therapeutic approaches to treat cancers and overcome limitations of existing tubulin interactive drugs [4]. In the last decade, we have been developing phenylpyrroloquinolinone (PPyQ) derivatives that show interesting *in vitro* and in *vivo* antitumor activity. Both 2-PPyQs and 7-PPyQs act as tubulin polymerization inhibitors by binding at the colchicine site in β-tubulin [5, 6]. . Although less cytotoxic, the 2-PPyQ compounds were also found to exhibit interesting *in vitro* and *in vivo* antiangiogenic properties [7]. The more cytotoxic 7-PPyQ derivatives showed very remarkable *in vitro* biological properties and good antitumor activity *in vivo.* In particular, some 7-PPyQs, characterized by alkyl substitutions at the pyrrole nitrogen, showed increased cytotoxicity with nanomolar GI_{50}values, and these compounds overcame the resistance observed with the clinically used agents vincristine and taxol [8, 9]. In the latter series, the 3*N*-cyclopropyl methyl 7-PPyQ derivative MG 2477 (Fig. 1, **10**), was taken as lead compound due to its very strong cytotoxicity (nanomolar range GI_{50}s) and its potent interaction with tubulin. Its activities as an inhibitor of tubulin polymerization and of colchicine binding to tubulin were similar to those of the reference compound combretastatin A-4: 0.90 µM assembly $IC_{50}$and 83% inhibition of colchicine binding for compound **10** versus values of 1.1 and 99%, respectively, for CA-4 [10, 11]. Compound **10** was also demonstrated to induce autophagy in the A549 cell line [12]. Very recently, in an effort to produce additional highly active compounds, numerous related analogues were designed, synthesized and studied, resulting in the discovery of a potent 3*N*-acyl derivative MG 2603 (Fig. 1, **11**) showing low nanomolar GI_{50} values. Compound **11**, too, showed an anti-tubulin mechanism profile similar to that of **10**, but it was also able to inhibit a number of kinases involved in tumor progression. Moreover, **11** showed reduced toxicity in non tumor cell lines and synergized with conventional chemotherapeutic agents in inhibiting leukemia cell proliferation [13].

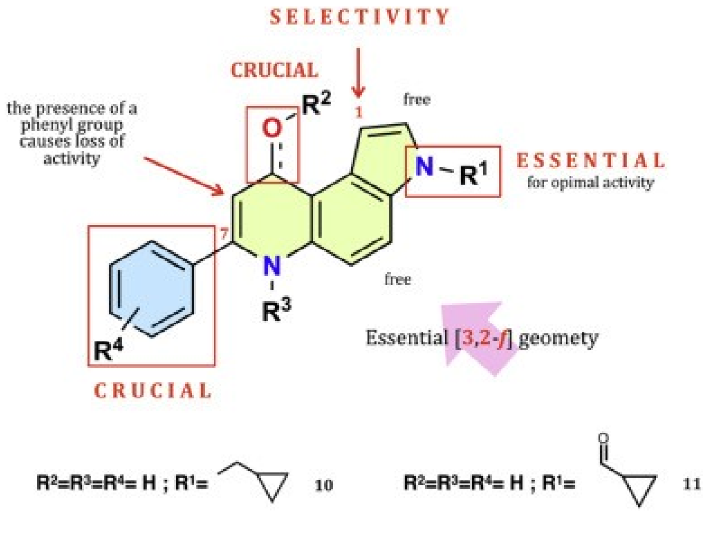

Fig. 1 Structure-activity relationships of 7-phenyl-pyrrolo[3,2-*f*]quinolinones.

Driven by the SARs we have collected during the development of the PPyQs [14] (Fig. 1) and remembering the recent results with the 3*N*-acyl 7-PPyQ derivative, the aim of the present work was the design, synthesis and evaluation of novel analogues substituted at the pyrrole N with acyl, sulfonyl and carbamoyl side chains. In designing the novel derivatives, we preserved the structural elements crucial for the best antiproliferative activity, such as the [3,2-*f*] geometry of the pyrroloquinoline core, the un-substituted phenyl ring at the 7 and the carbonyl group at the 9 position, without any other substitutions except for the 3 position (Fig. 1). Biological investigations included cellular cytotoxicity, tubulin inhibition assays and an apoptosis assay, together with docking simulations in the colchicine site of β-tubulin. This allowed us to obtain more knowledge on the key substitutions at the pyrrole N for effective interactions at the colchicine site.

2. Results and discussion

2.1 Chemistry

Scheme 1 shows the route to 7-PPyQs bearing a side chain bound to the pyrrole N via a carbonyl group according to the previously reported general synthesis to 7-PPyQs [7]. The starting commercial 5-nitroindole was reacted with various acyl and sulfonyl chlorides in order to obtain directly the 3*N*-substituted indole derivatives **1a-d.** Compound **1e** was prepared by means of a one-pot procedure consisting first of activation of 5-nitroindole with *p*-nitrophenylchloroformate to give the reactive 3-*p*-nitrophenylcarbamate intermediate and then reaction with cyclopropylamine (19% yield). The next reduction step of 5-nitro- to 5-aminoindole intermediates was accomplished by a chemical procedure with $SnCl_2{\cdot}2H_2O$, 37% HCl in methanol at reflux to give indole derivatives **2a-d**. In the case of **1e**, the reduction did not produce any corresponding amino compound. While, by a catalytic procedure with H_2 and C/Pd 10% in EtOAc/EtOH at atmospheric pressure, indoline compounds **5a, b, d** and **e** were obtained. Note that by the above chemical method aminoindole derivative **2a** was obtained in poor yields due to the formation of a mixture of various chloro-derivatives (not shown). Therefore the synthesis to **4a** did not proceed beyond the c step. Aminoindole derivatives **2b-d** were then condensed with ethyl benzoyl acetate to provide the eneamine intermediates **3b-d**to be then thermally cyclized into the final 7-PPyQs **4b-d**. In the same way, indolines **5a, b, d** and **e** gave eneamine derivatives **6a, b, d** and **e** with benzoyl acetate. However, when these were submitted to thermal cyclization in diphenyl ether, **6a, b** and **d** gave a mixture of isomeric compounds angular **7a, b, d** and linear **8a, b**, **d**, whereas derivative **6e** did not react. It is worth emphasizing that, by the catalytic procedure at the reaction conditions used here, we never observed the formation either of aminoindolines or the subsequent cyclization to linear tricyclic compounds.

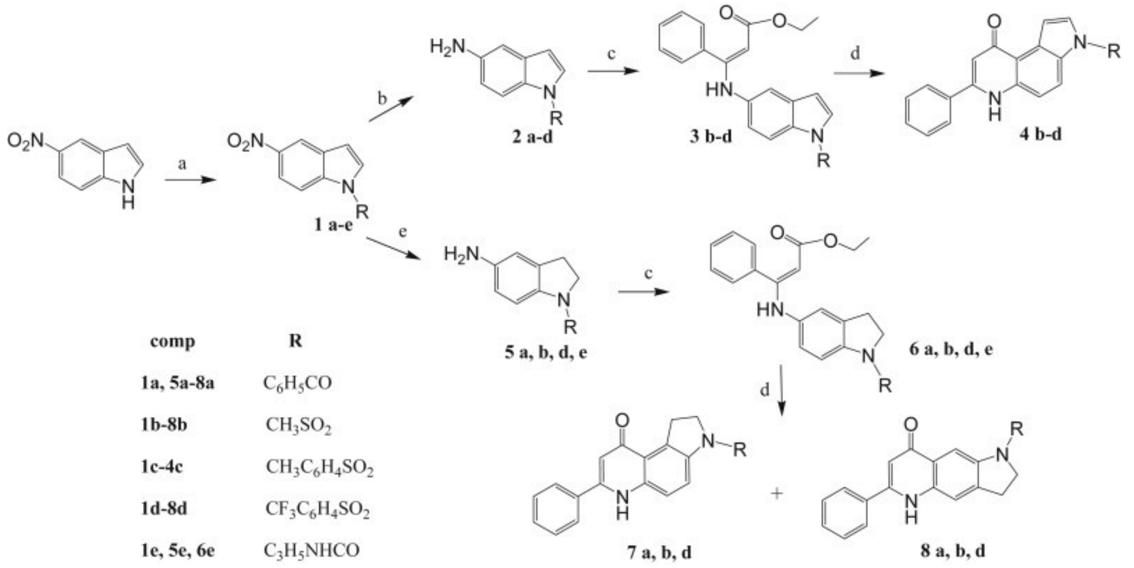

comp	R
1a, 5a-8a	C_6H_5CO
1b-8b	CH_3SO_2
1c-4c	$CH_3C_6H_4SO_2$
1d-8d	$CF_3C_6H_4SO_2$
1e, 5e, 6e	C_3H_5NHCO

Scheme 1 a) Benzoyl chloride, methansulfonyl chloride, *p*-methylbenzensulfonyl chloride, *p*-trifluoromethylbenzensulfonylchloride, NaH (60%), anhydrous DMF, rt, 2 h, 92%; *p*-nitrophenylchloroformate and cyclopropylamine, THF, 3 h, 87%; b) $SnCl_2 \cdot 2H_2O$, HCl 37%, methanol, reflux, 36 h, 53%; c) ethylbenzoyl acetate, absolute ethanol, cat CH_3COOH, drierite, reflux, 36 h, 60%; d) diphenyl ether, reflux, 15 min, 79%; e) H_2, Pd/C 10%, EtOAc, atmospheric pressure, 50 °C, 24 h, 95%.

Scheme 2 shows an alternative method to obtain the final compounds **4a** and **4e**, which could not be prepared by the route shown in Scheme 1. The previously described 7-PPyQ **9** [8], available in our laboratory, was submitted to an acylation reaction with benzoyl chloride. After a laborious purification procedure, 7-PPyQ **4a** was obtained in a 37% yield. Compound **4e** was obtained by the same one pot procedure described above, consisting of the reaction of 7-PPyQ **9** to give the intermediate 3-*p*-nitrophenylcarbamate, which was not isolated, followed by reaction with cyclopropylamine (30% yield).

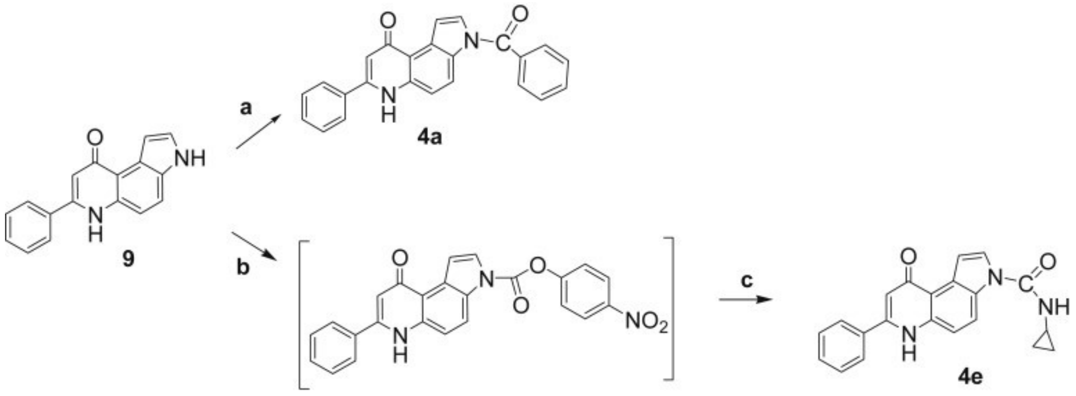

Scheme 2 a) Benzoyl chloride, NaH (60%), anhydrous DMF, rt, 3 h, 37%; c) *p*-nitrophenylchloro formate; NaH (60%), cyclopropyl amine, THF, rt, 3 h, 30%.

2.2. Biological evaluation

2.2.1. In vitro antiproliferative activities and SAR analysis

On the basis of previous biological activity data on 7-PPyQs and docking simulations of **11** into the colchicine site of tubulin [13], the new compounds were designed to obtain additional SAR information by modifying the nature and size of substituents at the 3 position of the 7-PPyQ tricycle. Evaluation of antiproliferative activities of **4a-e, 7a,b, 7d,**and **8a,b** was performed with the 3-(4,5-dimethylthiazol-2-yl)-2,5-diphenyltetrazolium bromide (MTT) assay against a panel of 11 human tumor cell lines (CCRF-CEM, HL-60, RS4; 11, Jurkat, SEM, MV4; 11, THP-1, HeLa, A549, HT-29, MCF-7). GI_{50} values, the concentrations that inhibit cell growth by 50%, are presented in Table 1. Most of the novel 7-PPyQs possessed antiproliferative activity, inhibiting cell growth with nanomolar to micromolar GI_{50} values, except for the linear 1,2-dihydro **8b** (GI_{50} > 10000 nM) having a methanesulfonyl group at the 3 position. In contrast, its angular isomer **7b** showed GI_{50}values in a high nanomolar range, demonstrating that for partially hydrogenated pyrroloquinolinones the [3,2-*f*] geometry is also preferred for cytotoxic activity as it was for fully aromatic compounds. Comparable behavior was also observed for the benzamidic derivatives **7a** and **8a**, although not as dramatic: the linear **8a** showed GI_{50} values in the micromolar, while the angular compound **7b** had IC_{50} values in the sub-micromolar range. Moreover, from the data presented in Table 1, it is evident that the angular, fully aromatic 7-PPyQs **4a,b,d** were more cytotoxic than the corresponding hydrogenated analogues **7a,b,d**. This was most remarkable for the pair **4a** and **7a**, with the former having GI_{50} values in the 0.1–10 nM range and the latter GI_{50} values in the 250–2650 nM range. Of particular note were the low nanomolar and sub-nanomolar GI_{50}values obtained with the series **4a-4e**, in both the leukemic and solid tumor cell lines. Overall, the most active of the new compounds was the benzamidic derivative **4a**, with subnanomolar concentrations in five of the eleven cell lines, with slightly lower GI_{50}values in the solid tumor lines (GI_{50}s 0.2, 0.1 and 0.2 nM in the HeLa, HT-29 and MCF-7 cells, respectively). Previously, we had observed that 7-PPyQs were more cytotoxic against leukemic cells. Thus, the preferential activity of **4a** against solid tumor cell lines is worth emphasizing. The same relative activity against the solid tumor cell lines was also observed for sulfamidic derivatives **4b-d,** but not for the ureidic derivative **4e.** We also note that there did not appear to be a significant steric hindrance factor among the compounds evaluated here, with similar antiproliferative activities observed among the series **4a-4e** and the previously evaluated compound **11**.

We conclude that the 7-PPyQ derivatives **4a-e**, chemically modified at 3 position with substitutions such as carbonyl, sulfonyl and carbamoyl groups, maintained strong cytotoxicity against tumor cell lines. These substitutions were made to further explore the SARs, and they have confirmed what was observed previously with carbonyl compound **11**. Substitutions with oxygenated groups, although of diverse nature and volume, onfer very high antiproliferative activity on 7-PPyQs. Due to their broad spectrum of potent activity, **4a** and **4b** were selected for further biological investigations on mechanism of action.

Table 1 In vitro cell growth inhibitory effects of compounds **4a-e**, **7a**,**b**,**d**, **8a-b**, and **11**

cmp	GI50 (nM)a										
	CCRF-CEM	HL-60	RS 4; 11	Jurkat	SEM	MV 4; 11	THP-1	HeLa	A549	HT-29	MCF-7
4a	12	2	0.3	16	0.9	2	5	0.2	10	0.1	0.2
	± 0.2	± 0.8	± 0.1	± 6	± 0.1	± 0.9	± 1	± 0.04	± 6	± 0.08	± 0.1
4b	42	215	18	34	23	49	92	36	3	7	152
	± 7	± 81	± 9	± 4	± 6	± 16	± 31	± 9	± 0.7	± 2	± 95
4c	32	335	48	55	33	65	222	26	52	5	195
	± 1	± 74	± 16	± 13	± 15	± 18	± 71	± 2	± 5	± 1	± 51
4d	32	39	147	81	33	86	42	22	63	23	5
	± 1	± 16	± 43	± 3	± 2	± 22	± 9	± 2	± 8	± 3	± 2
4e	92	155	27	145	11	85	66	212	171	255	96
	± 14	± 63	± 3	± 61	± 4	± 12	± 19	± 61	± 32	± 75	± 31
7a	1045	2640	256	1345	918	1543	2166	331	918	1586	1112
	± 212	± 309	± 133	± 302	± 211	± 223	± 614	± 55	± 268	± 145	± 178
7b	235	291	35	372	271	352	71	563	451	623	521
	± 56	± 13	± 4	± 26	± 1	± 36	± 2	± 65	± 54	± 59	± 96
7d	435	1625	211	256	336	356	846	373	541	255	475
	± 085	± 35	± 32	± 21	± 25	± 63	± 152	± 25	± 29	± 62	± 47
8a	818	3740	132	2316	1656	1978	2323	1447	3562	5436	6323
	± 154	± 233	± 51	± 407	± 185	± 326	± 945	± 416	± 624	± 852	± 845
8b	>10000	>10000	>10000	>10000	>10000	>10000	>10000	7638 ±1126	>10000	>10000	>10000
11b	17 ± 4	2	0.1	0.3	0.4	19	74	1.6	9	1	5
		± 0.6	± 0.05	± 0.03	± 0.01	± 8	± 25	± 0.6	± 0.4	± 0.5	± 1

[a] IC_{50} = compound concentration required to inhibit tumor cell proliferation by 50%. Data are expressed as the mean ± SE from the dose-response curves of at least three independent experiments.
[b] Data taken from ref. [13].

2.2.2. Evaluation of cytotoxicity in human non-cancer cells

To obtain a preliminary indication of the cytotoxic potential of these derivatives in normal human cells, the two most active compounds (**4a** and **4b**) were evaluated *in vitro* against peripheral blood lymphocytes (PBL) from healthy donors (Table 2). Compound **4a** showed a GI_{50} of 28 µM in quiescent lymphocytes, while in the presence of the mitogenic stimulus phytohematoaglutinin (PHA), the GI_{50} decreased to about 15 µM. Notably, this value was almost 1000–2000 times higher than that observed against the lymphoblastic cell lines CCRF-CEM and Jurkat. These results indicate that **4a** has a significant effect in rapidly proliferating cells but not in quiescent cells, as previously observed for other antimitotic derivatives developed by our group [13]. Compound **4b** was completely inactive in both quiescent and proliferating lymphocytes.

Table 2 Cytotoxicity of **4a-b** for human peripheral blood lymphocytes (PBL).

	IC50 (µM)[a]	
	4a	4b
$PBL_{resting}$[b]	28.0 ± 2.3	> 100
PBL_{PHA}[c]	15.2 ± 6.9	> 100

Values are the mean ± SEM from three separate experiments.

[a] Compound concentration required to reduce cell growth inhibition by 50%.

[b] PBL not stimulated with PHA.

[c] PBL stimulated with PHA.

2.2.3. Inhibition of tubulin polymerization and colchicine binding

To evaluate the tubulin interaction properties of compounds **4a-e**, we investigated their effects on inhibition of tubulin polymerization and the binding of [^{3}H]colchicine to tubulin (Table 3) [15, 16]. For comparison, CA-4 and **3c** were examined in contemporaneous experiments as references compounds. Among the test compounds, **4a** strongly inhibited tubulin assembly assay with an IC_{50} of 0.89 µM, a value that was lower than that obtained for the reference compound CA-4 (IC_{50} = 1.2 µM). Compounds **4b** and **4c** showed an IC_{50} similar to that of CA-4 while **4d** and **4e** were less effective than the reference compound (IC_{50} = 2.2–2.4 µM). These results correlate well with the growth inhibitory effects exhibited by the test compounds, indicating that their antiproliferative activity derives from an interaction with tubulin.

Table 3 Inhibition of tubulin polymerization and colchicine binding by compounds **4a-e** and CA-4.

Compound	Tubulin assembly[a] IC_{50}±S.D. (µM)	Colchicine binding[b] % inhibition ±S.D.
4a	0.89 ± 0.04	70 ± 2
4b	1.2 ± 0.01	42 ± 4
4c	1.1 ± 0.04	37 ± 5
4d	2.4 ± 0.2	29 ± 3
4e	2.2 ± 0.3	18 ± 4
CA-4	1.2 ± 0.1	98 ± 0.7

[a] Inhibition of tubulin polymerization. Tubulin was at 10 µM.

[b] Inhibition of [^{3}H]colchicine binding. Tubulin and colchicine were at 1 and 5 µM concentrations, respectively.

In the colchicine studies, compound **4a** was the most active inhibitor of the binding of [^{3}H]colchicine to its domain on tubulin, with 70% inhibition occurring with this derivative at 5 µM. Nevertheless, **4a** was less potent than CA-4 in this assay. In these experiments CA-4 inhibited colchicine binding by 98% at 5 µM. The other investigated compounds (**4b-e**) showed weaker inhibitory activity, with less than 50% inhibition of colchicine binding to tubulin.

2.2.4. Computational studies

Docking studies were carried out to investigate the binding mode of the novel inhibitors with the aim of interpreting experimental affinity data. A relevant number of experimentally derived complex structures of colchicine binding site inhibitors (CBSI) were recently deposited in the Protein Data Bank (PDB) [17]. Interestingly, the superposition of the different crystal structures reveals a significant variability in the sidechains of the residues belonging to the colchicine site depending on the chemical nature of the ligand, as shown in SI_Fig. 1 (see Supplementary Material). Moreover, the resolution of the crystal structures spanned a broad range (2.19–3.75 Å). As a consequence of this heterogeneity, we carried out a benchmark study, using the DockBench tool [18], to identify the most accurate docking model among 14 different ones and to determine which protein conformation was most appropriate to model our analogues. The benchmark study on the self-docking procedure was performed on 14 tubulin–CBSI complexes from the PDB as listed in table SI_Table 1. The benchmark results, summarized in SI_Fig. 2, revealed that several protocols showed a good ability to reproduce the experimental complex geometries for most of the experimental structures. Among them, GOLD software coupled to the PLP/goldscore/chemscore scoring function, gave the best results. In particular, GOLD protocols returned accurate predictions for the complete dataset. As a consequence of the overall good performance of the benchmark, we focused our attention on the identification of the most suitable crystallographic protein structure for the docking simulation of the PPyQ class of compounds. This step was crucial because of the variety of different sidechain orientations for certain residues in the colchicine site such as βGlu200, βCys239, βLeu248, and βLeu255, as shown in SI_Fig. 1. We have addressed this critical issue by comparing the shape similarity and the pharmacophoric determinants conservation between the ligands present in the complexes (summarized in SI_Table 1) and our representative compound, **4a**. Plinabulin (PDB ID: 5C8Y) showed the highest shape similarity according Tversky coefficient (>0.7) and, more notably, the plinabulin key moieties for the tubulin interaction are nicely conserved as shown in Fig. 2, Panel A. Not surprisingly, all analogues showed a common binding mode similar to that of plinabulin, as shown by SI_Video 1. As depicted in Fig. 2 (Panel B), the diketopiperazinic core of plinabulin is mimicked by the pyrroloquinolinone core, maintaining the key hydrogen bond interaction with the backbone of βVal236 as anticipated by the shape-based superposition (plinabulin and **4a**, Fig. 2, Panel A). In addition to the conserved hydrogen bond, the pyrroloquinolinone scaffold guarantees strong hydrophobic interactions with βLeu253, βAla314 and βIle368. The phenyl ring in position 7 reproduced the same scheme of interaction to the benzylidene moiety of plinabulin through hydrophobic interactions with residues βPhe167, βTyr200, and βLeu250. The substituents at the *N*-pyrrole were placed in the pocket formed by residues: βLys350, βThr351, βAla314, βAla352 and, for the more bulky substituents, also αThr179. Notably, this binding mode is compatible with a competitive mechanism of action at the colchicine site. The 1,2-dihydro derivatives showed minor differences in their orientation. The main difference is the reduction in the interaction strength with βVal236, in particular for the linear isomers (**8a** and **8b**) (SI_Video 1).

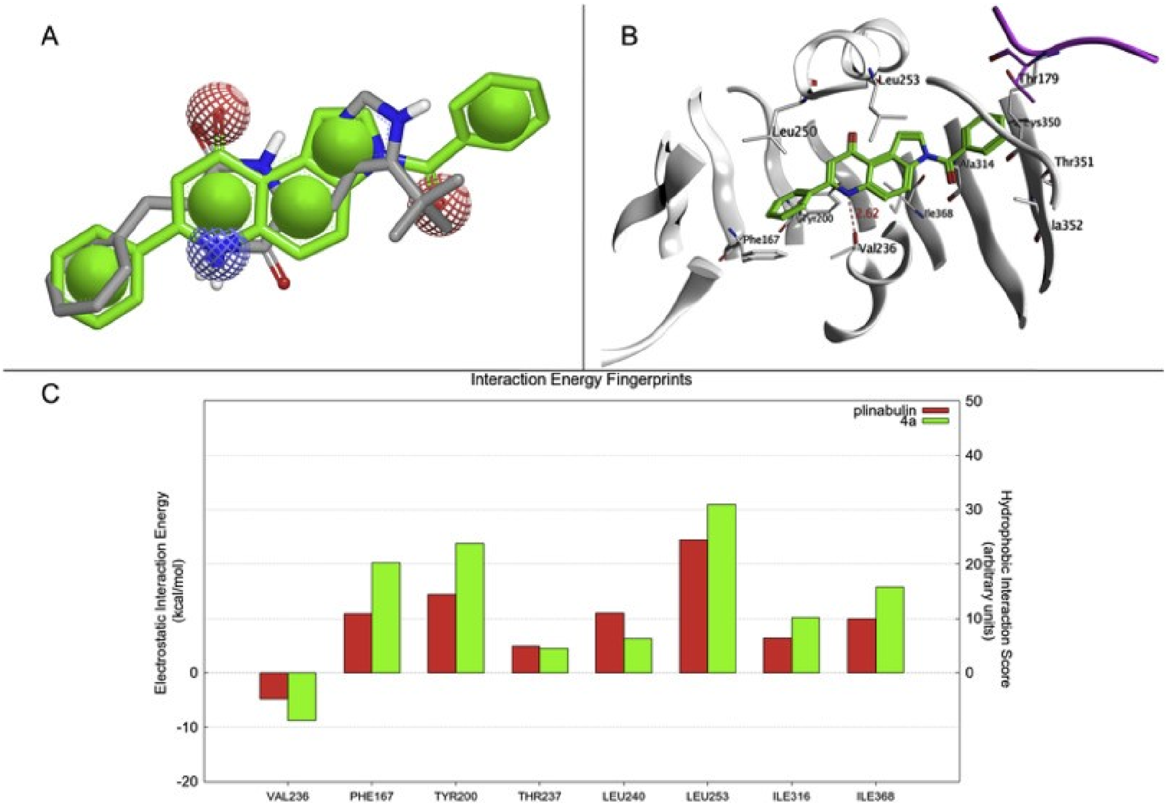

Fig. 2 Panel A. Superposition of **4a** (green sticks, grey surface) and plinabulin (grey sticks) derived from the shape similarity calculations. Panel B. The energetically most favorable pose of **4a** (in green) obtained by molecular docking simulation using the protein conformation of the plinabulin complex (PDB ID: 5C8Y). The ribbon as well as the residue atoms of the colchicine binding site are colored according the subunit to which they belong: white for β-tubulin and magenta for α-tubulin. Hydrogen atoms are not shown. Panel C. Per-residue analysis of the protein-ligand interaction for compound 4a (green) and plinabulin (red). (For interpretation of the references to colour in this figure legend, the reader is referred to the web version of this article.)

To evaluate if molecular docking was also able to explain the differences in the inhibition of colchicine binding by compounds **4a**-**e,** we performed a per-residue analysis along the series, in which the contribution for each residue belonging to the binding site is computed for each synthesized compound (Fig. 2, Panel C). In particular, we measured the electrostatic interaction energy and score, taking into account hydrophobic interactions. In SI_Video 1 is reported the per-residue analysis for all the analogues in Table 1, including the reference compound **11**. The resulting heatmap suggests a very similar pattern of interaction for all the compounds. In this context, the narrow differences in colchicine binding and tubulin assembly inhibition are difficult to rationalize. The higher inhibition in the colchicine binding of **4a** among the **4a-4e** derivatives could be ascribed to the orientation of the benzamidic moiety that is directed between the βLys350 and αThr179 residues, while in the **4b-4e** analogues the N substituent assumes a slightly different orientation. The differences in the cell growth inhibition data are difficult to rationalize only with tubulin docking, possibly because of the involvement of other targets [13]. A clearer interpretation can be made for compound **8b**, since its inhibition of tumor cell growth was negligible, and this analogue showed poor scores in molecular docking primarily because of a poor interaction with βVal236, as shown in the per residue analysis (SI_Video 1).

*2.2.5. Compounds **4a** and **4b** induce mitotic arrest of the cell cycle*

To investigate whether compounds **4a** and **4b** affected cell cycle progression, we evaluated by flow cytometry the effect of different concentrations of compounds after a 24 h of treatment of HeLa and Jurkat cells. As shown in Fig. 3, compound **4a** caused a significant G2/M arrest in a concentration-dependent manner in both cell lines, with a rise in G2/M cells occurring at a concentration of 50 nM, while at the highest concentration (100 nM) more than 50% of the cells were arrested in G2/M. In the HeLa cells, the G2/M block was accompanied by a significant reduction of both G1 and S phase cells, suggesting that cell proliferation is impaired. For compound **4b**, we observed a similar behavior but less marked as compared with **4a**, in good agreement with the respective IC$_{50}$ values found in the tubulin polymerization assay.

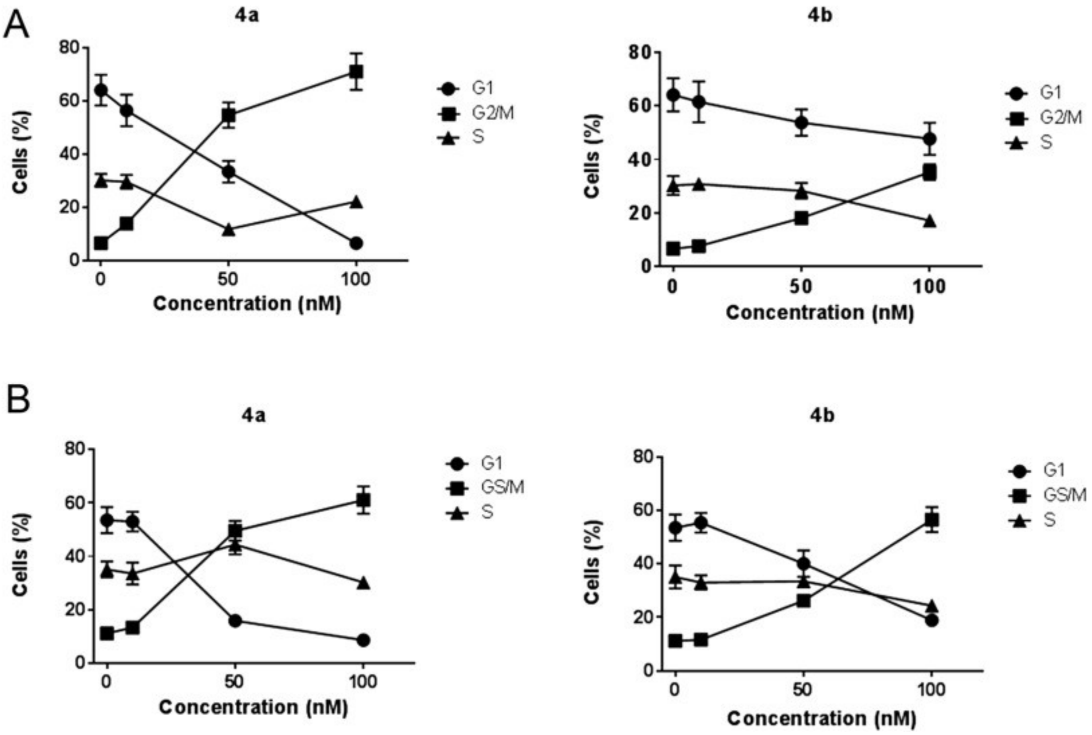

Fig. 3 Percentage of cells in each phase of the cell cycle in HeLa (Panel A) and Jurkat cells (Panel B) treated with compounds **4a** or **4b** at the indicated concentrations for 24 h. Cells were fixed and labeled with PI and analyzed by flow cytometry as described in the Experimental Section. Data are presented as mean of two independent experiments with similar results.

2.2.6. Compounds **4a** and **4b** induce apoptosis through the mitochondrial death pathway

To evaluate the mode of cell death induced by **4a** and **4b**, we performed the annexin-V/propidium iodide (PI) assay by flow cytometry. Staining with annexin-V and with PI allows discrimination between live cells (annexin-V-/PI-), early apoptotic cells (annexin-V+/PI-), late apoptotic cells (annexin-V+/PI+) and necrotic cells (annexin-V-/PI+). The experiments were carried out both in Hela and Jurkat cells. As shown in Fig. 4 ; Fig. 5, compounds **4a** and **4b** induce a significant time- and concentration-dependent increase of apoptotic cells in both cell lines. In particular, after 24 h we found a significant accumulation of early apoptotic (annexin-V+/PI-) cells starting from the lower concentrations and an increase of late apoptotic cells (annexin-V+/PI+) after 48 h treatments, indicating that the compounds trigger cells to a massive apoptotic cell death. In good agreement with the respective GI_{50} values (Table 1), compound **4a** is the more potent inducer of apoptosis both in Hela and Jurkat cells at the 50 nM concentration.

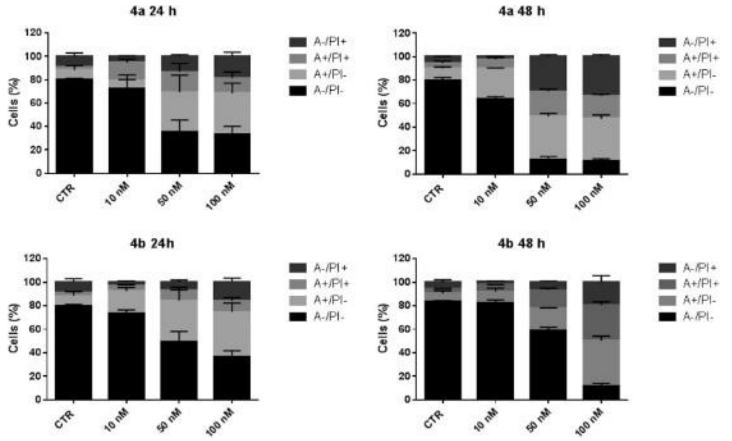

Fig. 4 Flow cytometric analysis of apoptotic cells after treatment of HeLa cells with **4a** or **4b** at the indicated concentrations after incubation for 24 or 48 h. The cells were harvested and labeled with annexin-V-FITC and PI and analyzed by flow cytometry. Data are presented as mean ± SEM of three independent experiments.

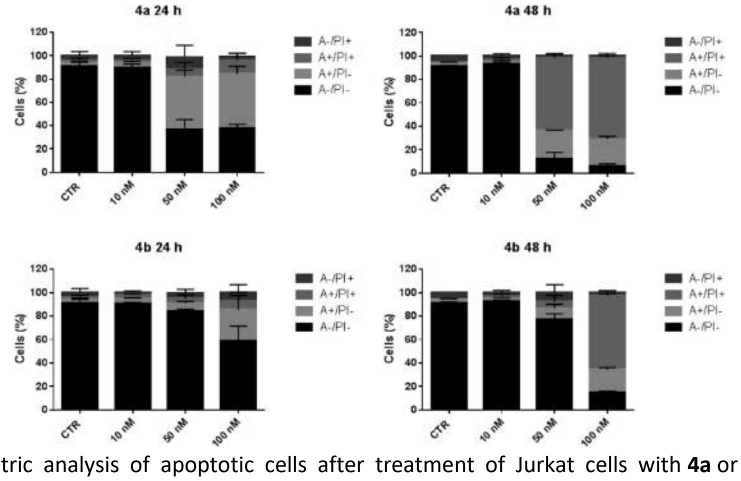

Fig. 5 Flow cytometric analysis of apoptotic cells after treatment of Jurkat cells with **4a** or **4b** at the indicated concentrations after incubation for 24 or 48 h. The cells were harvested and labeled with annexin-V-FITC and PI and analyzed by flow cytometry. Data are presented as mean ± SEM of three independent experiments.

Loss of mitochondrial transmembrane potential ($\Delta\psi_{mt}$) and release of apoptogenic factor has been described as an early event in the apoptotic process [19, 20]. $\Delta\psi_{mt}$ was evaluated by flow cytometry using the fluorescence of the dye JC-1. In normal conditions (high $\Delta\psi_{mt}$), JC-1 displays a red fluorescence (590 nm), while mitochondrial depolarization is indicated by a shift to green fluorescence (525 nm).

In both Hela and Jurkat cells, treatment with **4a** and **4b** induced a marked increase in the percentage of cells with low $\Delta\psi_{mt}$ (Fig. 6), and this occurred in a time- and concentration-dependent fashion. Depolarization of mitochondrial potential leads to the induction of the intrinsic pathway of apoptosis and is associated with the appearance of annexin-V positivity in the treated cells, as shown above and indicating the cells are in an early apoptotic stage. In fact, the disruption of $\Delta\psi_{mt}$ and the intrinsic activation of apoptosis are characteristic of antimitotic drugs and have been observed with both microtubule stabilizing and destabilizing agents in different cell types. It is also well known that mitochondrial potential impairment and the resulting damage to mitochondrial function induce generation of reactive oxygen species (ROS) [21, 22]. Superoxide anion is produced by mitochondria due to a shift from the normal 4-electron reduction of O_2 to a 1-electron reduction when cytochrome *c* is released from mitochondria upon apoptosis [23, 24].

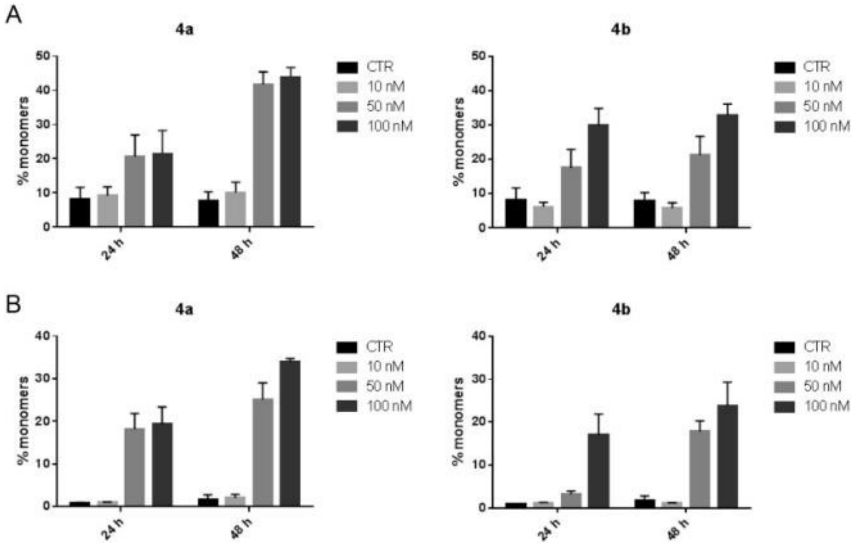

Fig. 6 Assessment of mitochondrial membrane potential ($\Delta\psi_{mt}$) after treatment of HeLa (Panel A) or Jurkat (Panels B) cells with the indicated compounds. Cells were treated with the indicated concentration of compound for 24 or 48 h and then stained with the fluorescent probe JC-1 for analysis of mitochondrial potential. Cells were then analyzed by flow cytometry as described in the Experimental Section. Data are presented as mean ± SEM of three independent experiments.

Using dichlorodihydrofluorescein diacetate (H_2-DCFDA), which is oxidized to the fluorescent compound dichlorofluorescein (DCF) upon ROS induction [23], we measured ROS production after treatment with compounds **4a** and **4b**. As shown in Fig. 7 (Panels B and D), the two compounds induced the production of large amounts of ROS in comparison with control cells. This was observed in both the Jurkat and HeLa cells, in good agreement with the dissipation of $\Delta\psi_{mt}$ described above.

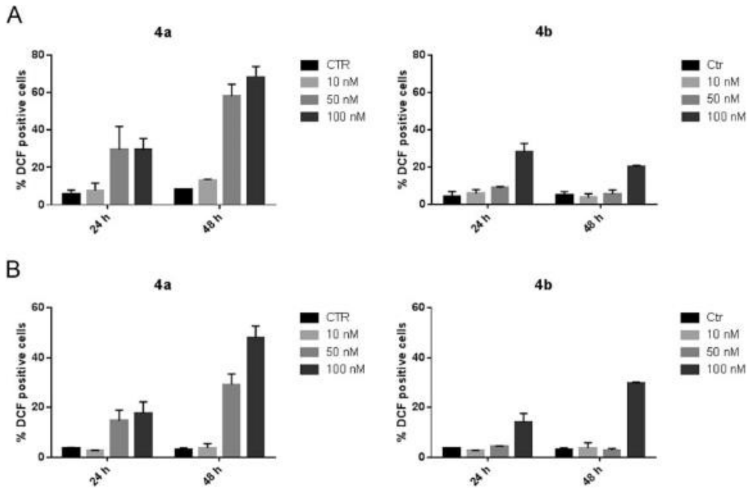

Fig. 7 Assessment of ROS production after treatment of HeLa (Panel A) or Jurkat (Panel B) cells with the indicated compounds. Cells were treated with the indicated concentration of compound for 24 or 48 h and then stained with H_2-DCFDA for the evaluation of ROS levels. Cells were then analyzed by flow cytometry as described in the Experimental Section. Data are presented as mean ± SEM of three independent experiments.

*2.2.7. Metabolic stability of **4a** in human liver microsomes*

Liver microsomal oxidation and hydrolysis represent major routes of drug metabolism in mammals, including humans [25]. *In vitro* studies were therefore carried out to get preliminary information on the stability of compound **4a** to oxidative and hydrolytic metabolism by human liver microsomes. As shown in Fig. 8 (panel A), compound **4a** (10 µM) was relatively stable in human liver microsomes (1 mg/mL) with more than 60% compound remaining after 60 min incubation at 37 °C. Interestingly, compound **4a** disappearance was not influenced by the presence of NADPH (Fig. 8, panel A), a cofactor for both cytochrome P450- and flavin monooxygenase-mediated oxidations [25], and was accompanied by formation of a fluorescent metabolite whose retention time corresponded exactly to that of authentic compound **9** (panel B). Collectively, these findings indicate that compound **4a** is partially susceptible to microsomal enzyme hydrolysis and that this catabolism produce compound **9** which retain a significant antiproliferative activity as previously demonstrated [8].

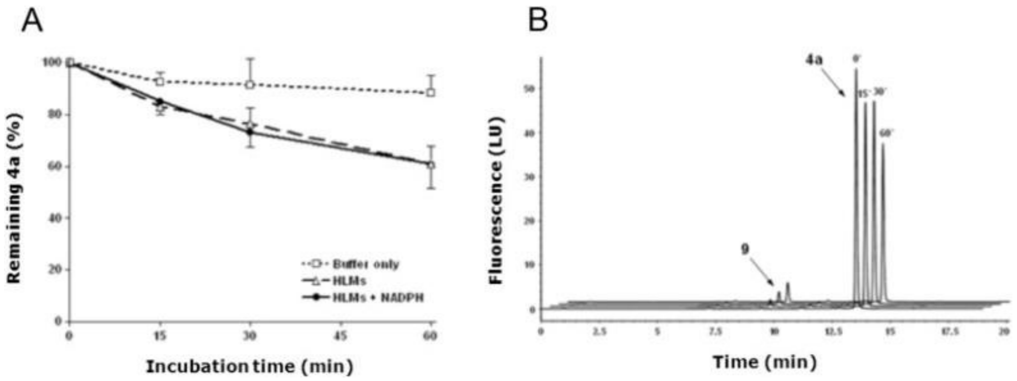

Fig. 8 Assessment of metabolic stability of 4a in human liver microsomes. (**A**) **4a** (10 µM) was incubated in the presence of human liver microsomes (1.0 mg/mL; HLMs; —△—), HLMs plus NADPH (1 mM; —●—), or buffer only (0.1 M KH_2PO_4, pH 7.4; --□--), for 0, 15, 30 or 60 min at 37 °C. The data are expressed as percent of parent compound (**4a**) remaining at each time compared with time 0 min, and represent the mean ± SD of n = 3 or 4 independent determinations. (**B**) Representative stacked HPLC-fluorescence traces of supernatants from mixtures containing **4a** (10 µM) and HLMs (1.0 mg/mL), incubated for 0, 15, 30 or 60 min at 37 °C. M, **4a** metabolite.

3. Conclusion

With the aim to further explore the SARs of the 7-PPyQ class of compounds, we examined the effects of various oxygenated functionalities at the 3 N position. A small series of novel derivatives was synthesized, and their antiproliferative activities and with their mechanism of action were investigated. The chemical series included both angular and linear compounds and fully aromatic and partially hydrogenated derivatives. Most compounds had significant antiproliferative activity, inhibiting cell growth with nanomolar to micromolar GI_{50} values, thus confirming that, in general, oxygenated substitutions at the 3 position improve cytotoxicity. In the series, the [3,2-*f*] angular geometry once again was required for obtaining potent cytotoxic compounds, and this [3,2-*f*] configuration was present both in the fully aromatic benzoyl **4a** and the methanesulfonyl **4b**. Compound **4a** was the most active of the new agents, even having sub-nanomolar GI_{50}s in some of the cell lines studied. Thus, compound **4a** was even more cytotoxic than the previously described compound **11.** Moreover, **4a** had a significant effect only in rapidly proliferating cells but not in quiescent and proliferating lymphocytes. Investigations on the mechanism of action of **4a** confirmed that it was a strong inhibitor of tubulin polymerization, as were previously described 7-PPyQ derivatives. Both in the Hela and Jurkat cell lines, **4a** was more effective than **4b** in blocking the cell cycle at the G_2M phase, inducing apoptosis through the mitochondrial death pathway with production of ROS. In agreement with the experimental results obtained in this work, docking simulations suggested that the synthesized inhibitors had high affinity for the colchicine site of tubulin, with interactions with the binding site most similar to those observed with the known inhibitor plinabulin. The 1,2-dihydro derivative **8b** was slightly penalized by affecting the geometry of the hydrogen bond with βVal236.

Published: *Eur J Med Chem. 2017 Feb 15;127:643–660*

Additionally, *in vitro* metabolic stability studies indicated that a human liver microsomes esterases can catalyze the cleavage of the amide bond of **4a,** leading to formation of an active metabolite, namely compound **9**. These findings may be valuable for future *in vivo* studies.

4. Experimental section

4.1. Chemistry

Melting points were determined on a Buchi M − 560 capillary melting point apparatus and are uncorrected. Infrared spectra were recorded on a PerkinElmer 1760 FTIR spectrometer with KBr pressed disks and on a Varian ATR FTIR; all values are expressed in cm^{-1}. UV−vis spectra were recorded on a Thermo Helyos α spectrometer. ^1H NMR spectra were determined on Bruker 300 and 400 MHz spectrometers, with the solvents indicated; chemical shifts are reported in *δ* (ppm) downfield from tetramethylsilane as internal reference. Coupling constants are given in Hertz. In the case of multiplets, chemical shifts were measured starting from the approximate center. Integrals were satisfactorily in line with those expected on the basis of compound structure. Elemental analyses were performed in the Microanalytical Laboratory, Department of Pharmaceutical Sciences, University of Padova, on a PerkinElmer C, H, N elemental analyzer model 240B, and analyses indicated by the symbols of the elements were within ±0.4% of the theoretical values. Analytical data are presented in detail for each final compound in the Supporting Information. Mass spectra were obtained on a Mat 112 Varian Mat Bremen (70 eV) mass spectrometer and on an Applied Biosystems Mariner System 5220 LC/MS (nozzle potential 140 eV). Column flash chromatography was performed on Merck silica gel (250–400 mesh ASTM); chemical reactions were monitored by analytical thin-layer chromatography (TLC) on Merck silica gel 60 F- 254 glass plates. Solutions were concentrated on a rotary evaporator under reduced pressure. Starting materials were purchased from Sigma-Aldrich and Alfa Aesar, and solvents were from Carlo Erba, Fluka and Lab-Scan. DMSO was obtained anhydrous by distillation under vacuum and stored on molecular sieves.

The purity of new tested compounds was checked by HPLC using the instrument HPLC VARIAN ProStar model 210, with detector DAD VARIAN ProStar 335. The analysis was performed with a flow of 1 mL/min, a C-18 column of dimensions 250 mm × 4.6 mm, a particle size of 5 µm, and a loop of 10 µL. The detector was set at 300 nm. The mobile phase consisted of phase A (Milli-Q H_2O, 18.0 MΩ, TFA 0.05%) and phase B (95% MeCN, 5% phase A). Gradient elution was performed as reported: 0 min, % B = 10; 0–20 min, % B = 90; 25 min, % B = 90; 26 min, % B = 10; 31 min, % B = 10.

*4.1.1. General procedure for the synthesis of 1N-substituted nitroindoles (**1a**−**e**)*

As a typical procedure, the synthesis of 1-benzoyl-5-nitro-1*H*-indole **1a** is described in detail. Into a two-necked 50 mL round-bottomed flask, 0.666 g (27.7 mmol, 3 eq.) of NaH, 60% dispersion in mineral oil, was placed and washed with toluene (3 × 10 mL). With stirring, a solution of commercial 5-nitroindole, 1.50 g (9.25 mmol, 1 eq.) in 5 mL of anhydrous DMF, was dropped into the flask, and the initial yellow color changed to red with the formation of H_2 gas. After 30 min at room temperature, a solution of benzoyl chloride, 3.21 mL (27.7 mmol, d = 1.21 g/mL, 3 eq.) in 3 mL dry DMF, was added, and the reaction mixture was stirred for 2 h. The reaction was monitored by TLC analysis (eluent toluene/*n*-Hex/EtOAc, 1:1:1). At the end of the reaction, 25 mL of water was added, and the solvent was evaporated under reduced pressure, leaving a residue, which was extracted with EtOAc (3 × 50 mL). The organic phase, washed with water and dried over anhydrous Na_2SO_4, was concentrated under vacuum giving a crude yellow solid (2.446 g). This crude product was purified with a silica gel chromatographic column 3 × 35 cm, 230–400 mesh, eluent toluene/*n*-Hex/EtOAc, 1:1:1, yielding 2.345 g of a pure yellow solid.

4.1.1.1. 1-Benzoyl-5-nitro-1H-indole (**1a**)

Yield: 94.9%. R*f* = 0.83 (eluent toluene/*n*-Hex/EtOAc, 1:1:1); ^{1}H NMR (400 MHz, DMSO-d_6) δ = 8.67 (d, *J* = 2.25 Hz, 1H, H-4), 8.43 (d, *J* = 9.12 Hz, 1H, H-7), 7.74 (m, 1H, H-4′), 8.28 (dd, *J* = 9.12 Hz and 2.37 Hz, 1H, H-6), 7.82 (m, 2H, H-2′ and -H-6′), 7.64 (m, 2H, H-3′ and H-5′), 7.62 (d, *J* = 3.64 Hz, 1H, H-2), 7.00 ppm (dd, *J* = 3.78 Hz and *J* = 0.60 Hz, 1H, H-3); ^{13}C NMR (75 MHz, DMSO-d_6) δ = 109.74 (C-3),113.19 (C-6), 117.05 (C-7), 120.55 (C-4), 129.69 (C-2′ and C-6′), 130.27 (C-3′ and C-5′), 131.56 (C-4′), 132.39 (C-2), 133.55 (C-3a), 133.94 (C-7a), 139.43 (C-1′), 144.66 (C-5), 169.24 ppm (C═O); HRMS (ESI-MS, 140 eV): *m/z* [M + H$^+$] calculated for $C_{15}H_{11}N_2O_3^+$, 267.0779; found, 267.0787.

4.1.1.2. 1-Methanesulfonyl-5-nitro-1H-indole (**1b**)

Compound **1b** was prepared as for compound **1a** by reacting 0.888 g of NaH 60% (37.03 mmol, 3 eq.) and 2 g (12.34 m mol) of 5-nitroindole dissolved in 5 mL of DMF and 2.86 mL of methanesulfonyl chloride (37.03 mmol, d = 1.48 g/mL, 3 eq.). Reaction time: 2 h (TLC, eluent EtOAc/*n*-Hex, 2:1). 2.564 g of a solid bright yellow solid was obtained, and this was used in the next synthetic step without further purification. Yield: 91.9%. R*f* = 0.54 (eluent EtOAc/n-Hex, 2:1); ^{1}H NMR (400 MHz, DMSO-d_6) δ = 8.67 (d, *J* = 2.20 Hz, 1H, H-4), 8.25 (dd, *J* = 9.14 Hz and *J* = 2.30 Hz, 1H, H-6), 8.05 (d, *J* = 9.16 Hz, 1H, H-7), 7.85 (d, *J* = 3.68 Hz, 1H, H-2), 7.08 (dd, *J* = 7.08 Hz and *J* = 0.72 Hz, 1H, H-3), 3.60 ppm (s, 3H, SO_2CH_3); ^{13}C NMR (101 MHz, DMSO-d_6) δ = 42.07 (SO_2CH_3), 109.22 (C-3), 114.08 (C-7), 119.81 (C-6), 130.33 (C-2), 130.58 (C-3a), 137.71 (C-7a), 143.96 ppm (C-5); HRMS (ESI-MS, 140 eV): *m/z* [M + H$^+$] calculated for $C_9H_9N_2O_4S^+$, 241.0283; found, 241.0236.

4.1.1.3. 1-(4-Methylbenzenesulfonyl)-5-nitro-1H-indole (**1c**)

Compound **1c** was prepared as for compound **1a** by reacting 0.444 g of NaH 60% (18.51 mmol, 3 eq.) and 1 g (6.17 mmol) of 5-nitroindole dissolved in 5 mL of DMF and 5.53 g of *p*-toluenesulfonyl chloride (18.51 mmol, 3 eq.). Reaction time: 2 h (TLC, eluent *n*-Hex/EtOAc, 9:1). 1.786 g of a solid bright orange solid was obtained which was used in the next synthetic step without any additional further purification. Yield: 91.6%. R*f* = 0.76 (eluent EtOAc/n-Hex, 9:1); ^{1}H NMR (400 MHz, DMSO-*d*$_6$) *δ* = 8.59 (d, *J* = 1.88 Hz, 1H, H-4), 8.21 (dd, *J* = 9.18 Hz and *J* = 2.26 Hz, 1H, H-6), 8.15 (dt, *J* = 9.18 Hz and *J* = 0.98 Hz, 1H, H-7), 8.07 (d, *J* = 3.72 Hz, 1H, H-2), 7.94 (m, AA'BB', *J* = 8.44 Hz, *J* = 2.11 Hz and *J* = 1.83 Hz, 2H, H-2' and H-6'), 7.43 (m, AA'BB', *J* = 8.58 Hz and *J* = 0.62 Hz, 2H, H-3' and H-5'), 7.07 (dd, *J* = 3.70 Hz and *J* = 0.66 Hz), 1H, H-3, 2.23 ppm (s, 3H, -CH$_3$); ^{13}C NMR (75 MHz, DMSO-*d*$_6$) *δ* = 21.91 (-CH$_3$), 110.93 (C-3), 114.54 (C-7), 118.85 (C-4), 120.55 (C-6), 127.77 (C-2' and C-6'), 130.90 (C-2), 131.34 (C-3a), 131.37 (C-3' and C-5'), 134.59 (C-4'), 137.81 (C-7a), 144.61 (C-5), 147.09 ppm (C-1'); HRMS (ESI-MS, 140 eV): *m/z* [M + H$^+$] calculated for $C_{15}H_{13}N_2O_4S^+$, 317.0596; found, 317.0585.

4.1.1.4. 5-Nitro-1-[4-(trifluoromethyl)benzenesulfonyl]-1H-indole (**1d**)

Compound **1d** was prepared as described for compound **1a** by reacting 0.670 g of NaH 60% (27.75 mmol, 3 eq.) and 1.5 g (9.25 mmol) of 5-nitroindole dissolved in 5 mL of DMF and 3.39 g of 4-(trifluoromethyl)benzenesulfonyl chloride (13.87 mmol, 1.5 eq.). Reaction time: 1 h (TLC, eluent *n*-Hex/EtOAc, 9:1). 2.845 g of a solid bright yellowish powdery solid was obtained, and this was used in the next synthetic step without further purification. Yield: 82.7%. R*f* = 0.79 (eluent EtOAc/n-Hex/toluene, 1:1:1); ^{1}H NMR (400 MHz, DMSO-*d*$_6$) *δ* = 8.60 (d, *J* = 2.12 Hz, 1H, H-4), 8.29 (m, AA'BB', *J* = 8.28 Hz, 2H, H-2' and H-6'), 8.22 (dd, *J* = 9.20 Hz and *J* = 2.16 Hz, 1H, H-6), 8.18 (d, *J* = 9.16 Hz, 1H, H-7), 8.13 (d, *J* = 3.72 Hz, 1H, H-2), 8.01 (m, AA'BB', *J* = 8.44 Hz, 2H, H-3' and H-5'), 7.13 ppm (d, *J* = 3.72 Hz, 1H, H-1); ^{13}C NMR (75 MHz, DMSO-*d*$_6$) *δ* = 111.29 (C-3), 114.17 (C-7), 118.59 (C-4), 120.49 (C-6), 123.41 (q, *J* = 273.30 Hz, -CF$_3$), 127.8250 (q, *J* = 3.65 Hz, C-3' and C-5'), 128.46 (C-2' and C-6'), 130.44 (C-2), 131.12 (C-3a), 134.84 (q, *J* = 32.69 Hz, C-4'), 137.42 (C-7a), 140.53 (C-1'), 144.46 ppm (C-5); HRMS (ESI-MS, 140 eV): *m/z* [M + H$^+$] calculated for $C_{15}H_{10}F_3N_2O_4S^+$, 371.0313; found, 371.0309.

4.1.1.5. *N*-cyclopropyl-5-nitro-1H-indole-1-carboxamide (**1e**)

To a stirred slurry of NaH (0.630 g of a 60% mineral oil dispersion, 26.27 mmol, 3 eq.) in THF (25 mL) at 0 °C, under N$_2$, was cautiously added 5-nitroindole (1.42 g, 8.75 mmol, 1eq.) previously dissolved in THF (5 mL). The reaction mixture was stirred at 0 °C for 60 min, then transferred, via cannula, to a solution of 4-nitrophenyl chloroformate (2.11 g, 10.5 mmol, 1.2 eq.) in THF (8.5 mL). The resultant reaction mixture was stirred at ambient temperature for 15 h (TLC, eluent *n*-Hex/EtOAc, 2:1), prior to removal of the solvent by concentration in vacuo. The residue obtained was suspended in EtOAc (100 mL), then filtered and washed with EtOAc and Et$_2$O to give 2.515 g (87.6%) of a pale yellow solid. The resulting activated carbamate 5-nitro-1-(4-nitrophenoxycarbonyl)indole was immediately used as follows: a 2.0 M solution of cyclopropylamine (0.382 mL, 5.48 mmol, d = 0.824 g/mL, 8 eq.) in THF (2.75 mL) was added to a solution of 5-nitro-1-(4-nitrophenoxycarbonyl)indole (0.245 g, 0.686 mmol, 1eq.) in THF (5 mL). The resultant reaction mixture was stirred at ambient temperature for 4 h and monitored by TLC (eluent *n*-Hex/EtOAc, 2:1), prior to removal of the solvent by concentration to dryness in vacuo. The residue obtained was partitioned between EtOAc (100 mL) and H_2O (100 mL). The layers were separated, and the aqueous phase was extracted with EtOAc (2 × 30 mL). The combined organic extracts were washed with sat'd $NaHCO_3$ (100 mL), brine and finally dried over $NaSO_4$ and concentrated in vacuo to give a yellow solid which was suspended in Et_2O (35 mL), filtered and washed with Et_2O (2 × 20 mL) to give 0.066 g of a pale yellow solid. Yield: 39.1%. R*f* = 0.26 (eluent *n*-Hex/EtOAc, 2:1); ^{1}H NMR (400 MHz, DMSO-*d*$_6$) *δ* = 8.59 (d, *J* = 2.25 Hz, 1H, H-4), 8.50 (d, *J* = 2.31 Hz, 1H, NH), 8.39 (d, *J* = 9.18 Hz, 1H, H-7), 8.15 (dd, *J* = 9.21 Hz and *J* = 2.40 Hz, 1H, H-6), 8.02 (d, *J* = 3.89 Hz, 1H, H-2), 6.92 (dd, *J* = 3.69 Hz and J = 0.55, 1H, H-3), 2.80 (sex *J* = 3.12 Hz, 1H, NH-C*H*), 0.8–0.6 ppm (m, 4H, -CH_2CH_2-); ^{13}C NMR (75 MHz, DMSO-*d*$_6$) *δ* = 6.75 (-CH_2CH_2-), 22.75 (N*C*H-CH_2CH_2-), 104.32 (C-3), 112.16 (C-7), 116.74 (C-6), 117.62 (C-4), 127.30 (C-2), 129.55 (C-3a),135.38 (C-7a), 140.95 (C-5), 160.11 ppm (C═O); HRMS (ESI-MS, 140 eV): *m/z* [M + H$^+$] calculated for $C_{12}H_{12}N_3O_3^+$, 246.0879; found, 246.0871.

*4.1.2. General procedure for the synthesis of 1N-substituted aminoindoles **2a–d***

As a typical procedure, the synthesis of 1-benzoyl-5-amino-1*H*-indole **2a** is described in detail. Into a two-necked 50 mL round-bottomed flask, 3.241 g of 1-benzoyl-5-nitro-1*H*-indole (**1a**) (12.17 mmol, 1 eq.), 10.986 g of $SnCl_2 \cdot 2H_2O$ (48.68 mmol, 4 eq.), 2 mL of HCl 37% and 30 mL of methanol were added. The reaction mixture was refluxed for 3 h, and the reaction progress was monitored by TLC (*n*-Hex/EtOAc, 1:1). At the end, the solvent was evaporated, the residue was taken up with aqueous NaOH 20% (20 mL), and the resulting suspension was extracted with diethyl ether (4 × 50 mL). The combined extracts, washed with brine and treated with anhydrous Na_2SO_4, were evaporated to dryness on a rotary evaporator to yield 1.536 g of a semisolid yellow product, made up of three different reaction products. In order to obtain the desired pure 1-benzoyl-5-amino-1*H*-indole, the raw powder was purified in a silica gel chromatographic column 3 × 28 cm, 230–400 mesh, eluent *n*-Hex/EtOAc, 1:1, yielding 0.267 g of a pure yellow solid.

4.1.2.1. 1-Benzoyl-5-amino-1H-indole (**2a**)

Yield: 19.5%. R*f* = 0.33 (eluent *n*-Hex/EtOAc, 1:1); ^{1}H NMR (400 MHz, DMSO-*d*$_6$) *δ* = 7.98 (d, *J* = 8.73 Hz, 1H, H-7), 7.70 (m, 2H, H-2′ and H-6′), 7.66 (m, 1H, H-4′), 7.59 (m, 2H, H-3′ and H-5′), 7.16 (d, *J* = 3.72 Hz, 1H, H-3), 6.75 (d, *J* = 2.07 Hz, 1H, H-4), 6.65 (dd, *J* = 8.74 Hz and *J* = 2.20 Hz, 1H, H-6), 6.51 (d, *J* = 3.42 Hz, 1H, H-2), 5.05 ppm (s, 2H, NH_2); ^{13}C NMR (75 MHz, DMSO-*d*$_6$) *δ* = 101.99 (C-3), 113.14 (C-7), 115.82 (C-6), 118.34 (C-4), 128.44 (C-2′ and C-6′), 129.04 (C-3′ and C-5′), 129.47 (C-4′), 131.83 (C-1′), 133.84 (C-2), 134.72 (C-3a), 137.46 (C-7a), 144.04 (C-5), 172.01 ppm (C═O); HRMS (ESI-MS, 140 eV): *m/z* [M + H$^+$] calculated for $C_{15}H_{13}N_2O^+$, 237.1028; found, 237.1031.

4.1.2.2. 1-Methanesulfonyl-5-amino-1H-indole (**2b**)

Compound **2b** was prepared as described for compound **2a** by reacting 1 g (4.16 mmol, 1 eq.) of the appropriate 5-nitroindole derivative **1b** and 4.69 g of $SnCl_2·2H_2O$ (20.80 mmol, 5 eq.), obtaining 0.963 g of a slightly brown solid. Yield: 80.6%; R*f* = 0.37 (eluent *n*-Hex/EtOAc, 1:1); ^{1}H NMR (400 MHz, DMSO-*d*$_6$) *δ* = 7.48 (dt, *J* = 8.76 Hz and *J* = 0.66 Hz, 1H, H-7), 7.34 (d, *J* = 3.96 Hz, 1H, H-2), 6.75 (dd, *J* = 2.20 Hz and *J* = 0.50 Hz, 1H, H-4), 6.67 (dd, *J* = 8.76 Hz and *J* = 2.24 Hz, 1H, H-6), 6.59 (dd, *J* = 3.64 Hz and *J* = 0.75 Hz, 1H, H-3), 4.95 (bs, 2H, NH_2), 3.24 ppm (s, 3H, SO_2CH_3); ^{13}C NMR (101 MHz, DMSO-*d*$_6$) *δ* = 41.06 (SO_2CH_3), 105.02 (C-4), 108.96 (C-3), 113.92 (C-7), 114.21 (C-6), 127.28 (C-3a), 127.82 (C-2), 132.35 (C-7a), 145.95 ppm (C-5); HRMS (ESI-MS, 140 eV): *m*/*z* [M + H$^+$] calculated for $C_9H_{11}N_2O_2S^+$, 211.0541; found, 211.0542.

4.1.2.3. 1-[4-(Trifluoromethyl)benzenesulfonyl]-5-amino-1H-indole (**2d**)

Compound **2d** was prepared as described for compound **2a** by reacting 1.25 g (3.37 mmol, 1 eq.) of the appropriate 5-nitroindole derivative **1d** and 3.80 g of $SnCl_2·2H_2O$ (16.87 mmol, 5 eq.), obtaining 1.160 g of a slightly brown solid. Yield: 99.9%; R*f* = 0.30 (eluent *n*-Hex/EtOAc/toluene, 1:1:1); ^{1}H NMR (400 MHz, DMSO-*d*$_6$) = *δ*: 7.77 (m, *J* = 8.40 Hz, J = 1.98 and *J* = 1.76 Hz, 2H, H-3′ and H-5′), 7.67 (d, *J* = 8.76 Hz, 1H, H-7), 7.58 (d, *J* = 3.60 Hz, 1H, H-2), 7.30 (m, *J* = 8.12 Hz, 2H, H-2′ and H-6′), 6.77 (d, *J* = 2.04 Hz, 1H, H-4), 6.73 (dd, *J* = 8.72 Hz and *J* = 2.09 Hz, 1H, H-6), 6.61 (dd, *J* = 3.64 Hz and *J* = 0.60 Hz, 1H, H-3), 4.98 ppm (bs, 2H, -NH_2); ^{13}C NMR (101 MHz, DMSO-*d*$_6$) *δ*: 105.92 (C-4), 110.02 (C-3), 114.18 (C-7), 114.51 (C-6), 124.55 (q, *J* = 245.01 Hz, CF_3), 127.00 (C-3′ and C-5′), 127.50 (C-2), 127.81 (C-3a), 130.45 (C-2′ and C-6′), 133.83 (q, *J* = 33.01 Hz, C-4′), 134.69 (C-7a), 143.98 (C-5), 145.87 ppm (C-1′); HRMS (ESI-MS, 140 eV): *m*/*z* [M + H$^+$] calculated for $C_{15}H_{12}F_3N_2O_2S^+$, 341.0572; found, 341.0569.

*4.1.3. General procedure for the synthesis of 1N-substituted aminoindoles **2c, 5a, 5b, 5d, 5e***

As a typical procedure, the synthesis of 1-(4-methylbenzenesulfonyl)-5-amino-1*H*-indole **2c** is described in detail. Into a three-necked flask of 500 mL, previously dried in an oven, about 0.300 g of C/Pd 10% and approximately 60 mL of EtOAc were placed. After connecting the flask to an elastomer balloon containing H_2 gas, the mixture was stirred at room temperature for 1 h in order to saturate the suspension of C/Pd with H_2. Then, 1.9 g (6.00 mmol) of the appropriate 5-nitroindole derivative **1c** in 15 mL of EtOAc was added dropwise to the suspension, and the mixture was stirred under H_2 at atmospheric pressure and heated by means of an oil bath at 50–60 °C for 15 h, monitoring the progress of the reaction by TLC analysis (EtOAc/*n*-Hex, 9:1). At the end of the reaction, the mixture was filtered, and the solution was concentrated to dryness on a rotary evaporator to give 1.680 g of semisolid dark purple sticky product.

4.1.3.1. 1-(4-Methylbenzenesulfonyl)-5-amino-1H-indole (**2c**)

Yield: 97.8%. R*f* = 0.76 (eluent *n*-Hex/EtOAc, 9:1); ^{1}H NMR (400 MHz, DMSO-d_6) δ = 7.77 (m, AA'BB', *J* = 8.40 Hz, *J* = 1.98 Hz and *J* = 1.76 Hz, 2H, H-2' and H-6'), 7.67 (d, *J* = 8.76 Hz, 1H, H-7), 7.58 (d, *J* = 3.60 Hz, 1H, H-2), 7.30 (m, AA'BB', *J* = 8.12 Hz, 2H, H-3' and H-5'), 6.77 (d, *J* = 2.04 Hz, 1H, H-4), 6.73 (dd, *J* = 8.72 Hz and *J* = 2.09 Hz, 1H, H-6), 6.61 (dd, *J* = 3.64 Hz and *J* = 0.60 Hz, 1H, H-3), 4.95 (bs, 2H, -NH$_2$), 2.26 ppm (s, 3H, -CH$_3$); ^{13}C NMR (101 MHz, DMSO-d_6) δ = 21.40 (-CH$_3$), 105.92 (C-4), 110.02 (C-3), 114.18 (C-7), 114.51 (C-6), 127.00 (C-2' and C-6'), 127.50 (C-2), 127.81 (C-3a), 130.45 (C-3' and C-5'), 132.27 (C-4'), 134.69 (C-7a), 143.98 (C-5), 145.87 ppm (C-1'); HRMS (ESI-MS, 140 eV): *m/z* [M + H$^+$] calculated for $C_{15}H_{15}N_2O_2S^+$, 287.0854; found, 287.0851.

4.1.3.2. 1-Benzoyl-2,3-dihydro-5-amino-1H-indole (**5a**)

Yield: 98.8%. R*f* = 0.54 (eluent *n*-Hex/EtOAc, 5:4); ^{1}H NMR (400 MHz, DMSO-d_6) δ = 7.94 (d, J = 8.40, 1H, H-6), 7.49 (m, 6H, H-7, H-2', H-3', H-4', H-5' and H-6'), 6.48 (d, J = 1.89, 1H, H-4), 4.98 (bs, 2H, -NH$_2$), 3.87 (t, *J* = 8.15 Hz, 2H, H$_2$-2), 2.93 ppm (t, J = 8.14, 2H, H$_2$-3); ^{13}C NMR (101 MHz, DMSO-d_6) δ = 29.27 (*N*-CH$_2$*C*H$_2$), 51.24 (*N*-*C*H$_2$CH$_2$), 110.98 (C-4), 113.94 (C-6), 115.98 (C-7), 128.24 (C-2' and C-6'), 128.99 (C-3' and C-5'), 129.32 (C-4'), 132.37 (C-3a), 134.23 (C-7a), 135.54 (C-1'), 143.82 (C-5), 166.83 ppm (C═O); HRMS (ESI-MS, 140 eV): *m/z* [M + H$^+$] calculated for $C_{15}H_{15}N_2O^+$, 239.1184; found, 239.1179.

4.1.3.3. 1-Methanesulfonyl-2,3-dihydro-5-amino-1H-indole (**5b**)

Yield: 94.8%. R*f* = 0.15 (eluent *n*-Hex/EtOAc, 2:1); ^{1}H NMR (400 MHz, DMSO-d_6) δ = 6.95 (d, *J* = 8.48 Hz, 1H, H-7), 6.50 (m, *J* = 2.37 Hz, 1H, H-4), 6.39 (dd, *J* = 8.50 Hz and *J* = 2.34 Hz, 1H, H-6), 4.91 (bs, 2H, -NH$_2$), 3.82 (t, *J* = 8.24 Hz, 2H, *N*-C*H2*CH$_2$), 2.96 (t, *J* = 8.20 Hz, 2H, *N*-CH$_2$C*H2*), 2.81 ppm (s, 3H, SO$_2$CH$_3$); ^{13}C NMR (101 MHz, DMSO-d_6) δ = 28.30 (*N*-CH$_2$*C*H$_2$), 33.48 (SO$_2$CH$_3$), 50.39 (*N*-*C*H$_2$CH$_2$), 111.26 (C-4), 112.92 (C-6), 115.57 (C-7), 131.88 (C-3a), 133.66 (C-7a), 146.17 ppm (C-5); HRMS (ESI-MS, 140 eV): *m/z* [M + H$^+$] calculated for $C_9H_{13}N_2O_2S^+$, 213.0698; found, 213.0663.

4.1.3.4. 1-[4-(Trifluoromethyl)benzenesulfonyl]-2,3-dihydro-5-amino-1H-indole (**5d**)

Yield: 98.2%. R*f* = 0.51 (eluent *n*-Hex/EtOAc/toluene, 1:1:1); ^{1}H -NMR (400 MHz, DMSO-d_6) δ = 7.90 (m, *J* = 8.98 Hz, 2H, H-3' and H-5'), 7.40 (m, *J* = 8.98 Hz, 2H, H-2' and H-6'), 7.19 (d, *J* = 8.52 Hz, 1H, H-7), 6.41 (dd, *J* = 8.50 Hz and *J* = 2.26 Hz, 1H, H-6), 6.33 (d, *J* = 2.16 Hz, 1H, H-4), 4.99 (s, 2H, -NH$_2$), 3.85 (t, *J* = 8.11 Hz, 2H, H$_2$-3), 2.56 ppm (t, *J* = 8.10 Hz, 2H, H$_2$-2); ^{13}C NMR (101 MHz, DMSO-d_6) δ = 28.17 (C-2), 50.69 (C-3), 111.00 (C-4), 113.13 (C-6), 116.93 (C-7), 126.27 (q, *J* = 3.80 Hz, C-3' and C-5'), 127.35 (q, *J* = 269.56 Hz, CF$_3$), 128.57 (C-2' and C-6'), 132.44 (C-3a), 133.35 (q, *J* = 32.32 Hz, C-4'), 134.44 (C-7a), 140.59 (C-1'), 146.93 ppm (C-5).; HRMS (ESI-MS, 140 eV): *m/z*[M + H$^+$] calculated for $C_{15}H_{14}F_3N_2O_2S^+$, 341.0572; found, 341.0569.

4.1.3.5. *N*-cyclopropyl-2,3-dihydro-5-amino-1H-indole-1-carboxamide (**5e**)

Yield: 91.2%. R*f* = 0.23 (eluent *n*-Hex/EtOAc, 2:1); ^{1}H NMR (400 MHz, DMSO-*d*$_6$) *δ* = 7.56 (d, *J* = 8.43 Hz, 1H, H-7), 6.46 (m, 2H, H-4 and NH), 6.35 (dd, *J* = 8.44 Hz and *J* = 2.32 Hz, 1H, H-6), 4.63 (s, 2H, -NH$_2$), 3.77 (t, *J* = 8.58 Hz, 2H, H$_2$-2), 2.99 (t, *J* = 8.53 Hz, 2H, H$_2$-3), 2.60 (sex, *J* = 3.46 Hz, 1H, NH-C*H*-CH$_2$CH$_2$-), 0.6–0.4 ppm (m, 4H, -CH$_2$CH$_2$-); ^{13}C NMR (101 MHz, DMSO-*d*$_6$) *δ* = 6.42 (-CH$_2$CH$_2$-), 23.47 (C-3), 27.89 (C-2), 46.89 (NH-*C*H-CH$_2$CH$_2$-), 111.27 (C-4), 112.39 (C-6), 115.04 ppm (C-7), 130.32 (C-3a), 133.83 (C-7a), 143.82 (C-5), 162.35 ppm (C═O); HRMS (ESI-MS, 140 eV): *m/z*[M + H$^+$] calculated for $C_{12}H_{16}N_3O^+$, 218.1293; found, 218.1245.

*4.1.4. General procedure for the synthesis of acrylate derivatives **3b–d** and **6a, 6b, 6d**and **6e***

As a typical procedure, the synthesis of (*E*,*Z*)-Ethyl 3-(1-(methanesulfonyl)-1*H*-indol-5-ylamino)-3-phenylacrylate **3b** is described in detail. In a 100 mL round-bottomed flask, 1.4 g (6.66 mmol, 1 eq.) of 1-methanesulfonyl-5-amino-1*H*-indole **2a** in 25 mL of absolute ethanol was condensed with 1.73 mL (9.99 mmol; d = 1.11 g/mL, 1.5 eq.) of commercial ethyl benzoylacetate and 0.5 mL of glacial acetic acid in the presence of 100 mg of Drierite (anhydrous CaSO$_4$). The mixture was refluxed for about 24 h, the reaction being monitored by TLC analysis (eluent *n*-Hex/EtOAc, 2:1). Even though the reaction was not complete after 24 h, the mixture was cooled and filtered to remove the Drierite; the resulting solution was evaporated to dryness under vacuum and the residue (2.420 g) purified by silica gel chromatography (3 × 35 cm, 230–400 mesh, eluent *n*-Hex/EtOAc, 2:1) to yield 1.54 g of a deep yellow powdery solid.

4.1.4.1. (*E*,*Z*)-Ethyl 3-(1-(methanesulfonyl)-1H-indol-5-ylamino)-3-phenylacrylate (**3b**)

Yield: 60.2%. R*f* = 0.65 (eluent *n*-Hex/EtOAc, 2:1); ^{1}H NMR (400 MHz, DMSO-*d*$_6$) *δ* = 10.25 (s, 1H, NH), 7.58 (d, *J* = 8.80 Hz, 1H, H-7), 7.49 (d, *J* = 3.68 Hz, 1H, H-2), 7.36 (m, 5H, 2'-,3'-,4'-,5'-,6'-H), 7.02 (d, *J* = 2.16 Hz, 1H, H-4), 6.84 (dd, *J* = 8.82 Hz and 2.18 Hz, 1H, H-6), 6.62 (dd, *J* = 3.68 Hz and *J* = 0.72 Hz, 1H, H-3), 4.94 (s, 1H, C═C-H), 4.15 (q, *J* = 7.09 Hz, 2H, OCH$_2$CH$_3$), 3.38 (s, 3H, SO$_2$CH$_3$), 1.24 ppm (t, *J* = 7.10 Hz, 3H, OCH$_2$CH$_3$); ^{13}C NMR (101 MHz, DMSO-*d*$_6$) *δ* = 14.76 (OCH$_2$*C*H$_3$), 41.35 (SO$_2$CH$_3$), 59.21 (O*C*H$_2$CH$_3$), 90.70 (C═*C*-H), 109.09 (C-3), 113.26 (C-7), 115.26 (C-4), 120.62 (C-6), 127.80 (C-2), 128.45 (C-2' and C-6'), 128.94 (C-3' and C-5'), 130.00 (C-4'), 130.77 (C-3a), 131.07 (C-1'), 135.80 (C-7a), 136.22 (C-5), 159.49 (*C*═C-H), 169.45 ppm (*C*OO-CH$_2$CH$_3$); HRMS (ESI-MS, 140 eV): *m/z* [M + H$^+$] calculated for $C_{20}H_{21}N_2O_4S^+$, 385.1222; found, 385.1213.

4.1.4.2. (*E*,*Z*)-Ethyl 3-(1-(*p*-toluenesulfonyl)-1H-indol-5-ylamino)-3-phenylacrylate (**3c**)

Compound **3c** was prepared as described for compound **3b** by reacting 3.177 g (11.10 mmol) of the appropriate 5-aminoindole derivative **2c**, obtaining after column chromatography 2.336 g of a brownish sticky semisolid product. Yield: 45.7%. R*f* = 0.62 (eluent *n*-Hex/EtOAc, 2:1); ^{1}H NMR (400 MHz, DMSO-*d*$_6$) *δ* = 10.18 (s, 1H, NH), 7.79 (m, AA'BB', *J* = 8.32 Hz, 2H, H-2' and H-6'), 7.69 (d, *J* = 3.64 Hz, 1H, H-2), 7.65

(d, *J* = 8.84 Hz, 1H, H-7), 7.35 (m, AA’BB’, *J* = 8.61 Hz, 2H, H-3’ and H-5’), 7.31 (m, 5H, H-2”, H-3”,H -4”, H-5” and H-6”), 6.92 (d, *J* = 1.88 Hz, 1H, H-4), 6.78 (dd, *J* = 8.61 Hz and *J* = 1.82 Hz, 1H, H-6), 6.61 (d, *J* = 3.68 Hz, 1H, H-3), 4.92 (s, 1H, C=C-H), 4.12 (q, *J* = 7.14 Hz, 2H, -OCH$_2$CH$_3$), 2.31 (s, 3H, -CH$_3$), 1.22 ppm (t, *J* = 7.17 Hz, 3H, -OCH$_2$CH$_3$); ^{13}C NMR (101 MHz, DMSO-*d*$_6$) *δ* = 14.85 (-OCH$_2$*C*H$_3$), 21.46 (-CH$_3$), 59.34 (-OCH$_2$CH$_3$), 90.99 (C=*C*-H), 109.72 (C-3), 113.65 (C-7), 115.30 (C-4), 120.87 (C-6), 127.13 (C-2’ and C-6’), 128.24 (C-2), 128.53 (C-2” and C-6”), 129.03 (C-3” and C-5”), 130.11 (C-4”), 130.65 (C-3’ and C-5’), 130.91 (C-3a), 131.26 (C-1”), 134.53 (C-4’), 135.85 (C-7a), 136.69 (C-5), 145.95 (C-1’), 159.39 (*C*=C-H), 169.48 ppm (COOCH$_2$CH$_3$); HRMS (ESI-MS, 140 eV): *m/z* [M + H$^+$] calculated for C$_{26}$H$_{25}$N$_2$O$_4$S$^+$, 461.1535; found, 461.1539.

4.1.4.3. (*E*,*Z*)-Ethyl-3-(1-(4-(trifluoromethyl)benzenesulfonyl)-1H-indol-5-ylamino)-3-phenylacrylate (**3d**)

Compound **3c** was prepared as described for compound **3b** by reacting 1.160 g (3.41 mmol) of the appropriate 5-aminoindole derivative **2d**, obtaining after column chromatography 1.020 g of a yellow powdery solid. Yield: 58.1%. R*f* = 0.78 (eluent *n*-Hex/EtOAc, 8:2); ^{1}H NMR (400 MHz,DMSO-*d*$_6$) = *δ*: 10.18 (s, 1H, NH), 7.79 (m, AA’BB’, *J* = 8.32 Hz, 2H, H-2’ and H-6’), 7.69 (d, *J* = 3.64 Hz, 1H, H-2), 7.65 (d, *J* = 8.84 Hz, 1H, H-7), 7.35 (m, AA’BB’, *J* = 8.61 Hz, 2H, H-3’ and H-5’), 7.31 (m, 5H, H-2”, H-3”,H -4”, H-5” and H-6”), 6.92 (d, *J* = 1.88 Hz, 1H, H-4), 6.78 (dd, *J* = 8.61 Hz and *J* = 1.82 Hz, 1H, H-6), 6.61 (d, *J* = 3.68 Hz, 1H, H-3), 4.92 (s, 1H, C=C-H), 4.12 (q, *J* = 7.14 Hz, 2H, -OCH$_2$CH$_3$), 1.22 ppm (t, *J* = 7.17 Hz, 3H, -OCH$_2$CH$_3$); ^{13}C NMR (101 MHz, DMSO-*d*$_6$) *δ* = 14.84 (-OCH$_2$CH$_3$), 59.37 (-OCH$_2$CH$_3$), 90.90 (C=C-H), 109.71 (C-3), 113.64 (C-7), 115.36 (C-4), 120.89 (C-6), 127.11 (C-2’ and C-6’), 128.28 (C-2), 128.52 (C-2” and C-6”), 128.99 (q, *J* = 269.28 Hz, CF$_3$), 129.01 (q, *J* = 3.85 Hz, C-3” and C-5”), 130.65 (C-3’ and C-5’), 130.91 (C-3a), 131.26 (C-1”), 133.28 (q, *J* = 32.35 Hz, C-4”) 134.53 (C-4’), 135.85 (C-7a), 136.69 (C-5), 145.95 (C-1’), 159.39 (C=C-H), 170.01 ppm (COOCH$_2$CH$_3$); HRMS (ESI-MS, 140 eV): *m/z* [M + H$^+$] calculated for C$_{26}$H$_{22}$F$_3$N$_2$O$_4$S$^+$, 515.1252; found, 515.12.49.

4.1.4.4. (*E*,*Z*)-Ethyl 3-(1-(benzoyl)-2,3-dihydro-1H-indol-5-ylamino)-3-phenylacrylate (**6a**)

Compound **5a** was prepared as described for compound **3b** by reacting 1.96 g (8.22 mmol) of the appropriate 5-aminoindole derivative **5a**, obtaining after column chromatography 0.940 g of a brown viscous oil. Yield: 27.7%. R*f* = 0.70 (eluent *n*-Hex/EtOAc/toluene, 1:1:1); ^{1}H NMR (400 MHz, DMSO-*d*$_6$) *δ* = 10.14 (s, 1H, NH), 7.95 (m, 2H, H-2’ and H-6’), 7.68 (m, 1H, H-4’), 7.60 (m, 1H, H-4”), 7.60–7.32 (m, 8H, H-2”, -3”, -5”, -6” and H-3’, -5’, and H-6, H-7), 6.72 (d, *J* = 1.32 Hz, 1H, H-4), 4.90 (s, 1H, C=CH-), 4.14 (q, *J* = 7.08 Hz, 2H, -OCH$_2$CH$_3$) 3.92 (t, *J* = 8.23 Hz, 2H, H-3), 2.90 (t, *J* = 8.32 Hz, 2H, H-2), 1.20 ppm (t, *J* = 7.09 Hz, 3H, -CH$_2$CH$_3$); ^{13}C NMR (101 MHz, DMSO-*d*$_6$) *δ* = 15.24 (-OCH$_2$CH$_3$), 29.23 (C-3), 52.26 (C-2), 58.92 (-OCH$_2$CH$_3$), 91.07 (C=C-H), 114.23 (C-7), 116.32 (C-4), 119.28 (C-6), 127.11 (C-2’ and C-6’), 128.52 (C-2” and C-6”), 129.91 (C-3” and C-5”), 130.23 (C-3’ and C-5’), 130.91 (C-3a), 131.18 (C-1”), 133.84 (C-4”) 134.82 (C-4’), 135.75 (C-7a), 136.82 (C-5), 146.23 (C-1’), 158.83 (C=C-H), 165.24 (NC=O), 171.91 ppm (COOCH$_2$CH$_3$); HRMS (ESI-MS, 140 eV): *m/z* [M + H$^+$] calculated for C$_{26}$H$_{25}$N$_2$O$_3$$^+$, 413.1865; found, 413.1859.

4.1.4.5. (*E*,*Z*)-Ethyl 3-(1-(methanesulfonyl)-2,3-dihydro-1H-indol-5-ylamino)-3-phenylacrylate (**6b**)

Compound **6b** was prepared as described for compound **3b** by reacting 0.460 g (2.16 mmol) of the appropriate 5-aminoindole derivative **5b**, obtaining after column chromatography 0.540 g of a brown sticky oil. Yield: 64.8%. R*f* = 0.37 (eluent *n*-Hex/EtOAc, 2:1); ^{1}H NMR (400 MHz, DMSO-d_6) δ = 10.11 (s, 1H, NH), 7.38 (m, 1H, H-4′), 7.34 (m, 4H, H-2′, -3′, -5′ and 6′), 6.96 (d, *J* = 8.56 Hz, 1H, H-7), 6.72 (d, *J* = 2.20 Hz, 1H, H-4), 6.52 (dd, *J* = 8.72 Hz and *J* = 2.22 Hz, 1H, H-6), 4.90 (s, 1H, C=C-H), 4.31 (q, *J* = 7.09 Hz, 2H, OCH_2CH_3), 3.86 (t, *J* = 8.46 Hz, 2H, H-2), 2.93 (t, *J* = 8.44 Hz, 2H, H-3), 2.90 (s, 3H, SO_2CH_3), 1.23 ppm (t, *J* = 7.08 Hz, 3H, OCH_2CH_3); ^{13}C NMR (101 MHz, DMSO-d_6) δ = 14.74 (OCH_2CH_3), 27.68 (C-3), 34.38 (SO_2CH_3), 50.31 (C-2), 59.21 (OCH_2CH_3), 90.63 (C=*C*-H), 113.64 (C-7), 120.18 (C-4), 122.20 (C-6), 128.38 (C-2′ and C-6′), 129.92 (C-3′ and C-5′), 130.03 (C-4′), 133.07 (C-3a), 135.75 (C-7a), 136.46 (C-1′), 138.14 (C-5), 159.19 (*C*=C-H), 169.39 ppm ($COOCH_2CH_3$); HRMS (ESI-MS, 140 eV): *m/z* [M + H$^+$] calculated for $C_{20}H_{23}N_2O_4S^+$, 387.1379; found, 387.1381.

4.1.4.6. (*E*,*Z*)-Ethyl 3-(1-(4-(trifluoromethyl)benzenesulfonyl)-2,3-dihydro-1H-indol-5-ylamino)-3-phenylacrylate (**6d**)

Compound **6d** was prepared as described for compound **3b** by reacting 1.560 g (4.55 mmol) of the appropriate 5-aminoindole derivative **5d**, obtaining after column chromatography 1.29 g of a bright yellow powdery solid. Yield: 54.8%. R*f* = 0.75 (eluent *n*-Hex/EtOAc, 8:2); ^{1}H -NMR (400 MHz, DMSO-d_6) δ = 10.15 (s, 1H, NH), 7.92 (m, *J* = 8.98 Hz, 2H, H-3″ and H-5″), 7.45 (m, *J* = 8.98 Hz, 2H, H-2″ and H-6″), 7.38 (m, 1H, H-4′), 7.34 (m, 4H, H-2′, -3′, -5′ and -6′), 6.96 (d, *J* = 8.56 Hz, 1H, H-7), 6.72 (d, *J* = 2.20 Hz, 1H, H-4), 6.52 (dd, *J* = 8.72 Hz and *J* = 2.22 Hz, 1H, H-6), 4.96 (s, 1H, C=C-H), 4.24 (q, *J* = 7.09 Hz, 2H, OCH_2CH_3), 3.96 (t, *J* = 8.46 Hz, 2H, H-2), 2.86 (t, *J* = 8.44 Hz, 2H, H-3), 1.15 ppm (t, *J* = 7.08 Hz, 3H, OCH_2CH_3); ^{13}C-NMR (101 MHz, DMSO-d_6) δ = 14.74 (OCH_2CH_3), 27.68 (C-3), 50.31 (C-2), 59.21 (OCH_2CH_3), 90.63 (C=C-H), 113.64 (C-7), 120.18 (C-4), 122.20 (C-6), 126.47 (q, *J* = 3.75 Hz, C-3″ and C-5″), 127, 98 (q, *J* = 265.67 Hz, CF_3), 128.38 (2′- and 6′-C), 128.81 (C-2′′ and C-6″), 129.92 (3′- and 5′-C), 130.03 (C-4′), 133.07 (C-3a), 134.72 (q, *J* = 32.81 Hz, C-4″), 135.75 (C-7a), 136.46 (C-1′), 138.14 (C-5), 159.19 (C=C-H), 169.39 ppm ($COOCH_2CH_3$); HRMS (ESI-MS, 140 eV): *m/z* [M + H$^+$] calculated for $C_{26}H_{24}F_3N_2O_4S^+$, 517.1409; found, 517.1401.

4.1.4.7. (*E*,*Z*)-Ethyl 3-(1-(*N*-cyclopropyl-1-carboxamide)-2,3-dihydro-1H-indol-5-ylamino)-3-phenylacrylate (**6e**)

Compound **6e** was prepared as described for compound **3b** by reacting 0.128 g (0.589 mmol) of the appropriate 5-aminoindole derivative **5e**, obtaining after column chromatography 0.139 g of a dark brown tarry oil. Yield: 60.4%. R*f* = 0.56 (eluent $CHCl_3$/MeOH, 95:5); ^{1}H NMR (400 MHz, DMSO-d_6) δ = 10.08 (s, 1H, NH), 7.52 (d, *J* = 8.55 Hz, 1H, H-7), 7.33 (m, 5H, H-2′, -3′, -4′, -5′ and -6′), 6.62 (m, 2H, H-4 and NH), 6.41 (dd, *J* = 8.55 Hz and *J* = 2.16 Hz, 1H, H-6), 4.83 (s, 1H, C=CH), 4.12 (q, *J* = 7.08 Hz, 2H, -OCH_2CH_3), 3.74

(t, J = 8.71 Hz, 2H, H_2-2), 2.90 (t, J = 8.70 Hz, 2H, H_2-3), 2.51 (m, 1H, -*N*-CH-CH_2CH_2-), 1.23 (t, J = 7.08 Hz, 3H, -CH_3), 0.6–0.4 ppm (m, 4H, -CH_2CH_2-); ^{13}C NMR (101 MHz, DMSO-d_6) δ = 6.35 (-CH_2CH_2-), 14.96 (-CH_3), 21.24 (C-3), 45.95 (NH-CH), 47.15 (-OCH_2CH_3), 59.06 (C-2), 90.24 (C═*C*H), 115.21 (C-7), 116.15 (C-6), 118.43 (C-4), 127.13 (C-3a), 127.45 (C-2′ and C-6′), 128.74 (C-3′ and C-5′), 130.14 (C-4′), 132.16 (C-7a), 132.74 (C-1′), 146.09 (C-5), 159.16 (*C*═CH), 161.45 (NC═ONH), 170.23 ppm ($COOCH_2CH_3$); HRMS (ESI-MS, 140 eV): *m/z* [M + H$^+$] calculated for $C_{23}H_{26}N_3O_3$, 329.1974; found, 392.1971.

4.1.5. General procedure for the synthesis of phenylpyrroloquinolinones ***4b–d, 7a, 7b, 7d*** *and* ***8a, 8b, 8d***

As a typical procedure, the synthesis of 3-methanesulfonyl-7-phenyl-6*H*-pyrrolo[3,2-*f*]quinolin-9-one **4b** is described in detail. In a two-necked round-bottomed flask, 20 mL of diphenyl ether was heated to boiling. To this 0.383 g (4.2 mmol) of the appropriate phenylacrylate derivative **3b** was added portionwise, and the resulting mixture was refluxed for 15 min. After cooling to room temperature, 25 mL of diethyl ether was added, and the mixture was left for 12 h. The precipitate was collected by filtration and washed many times with diethyl ether. The product (0.437 g) was additionally purified by silica gel column chromatography (2.5 × 30 cm, 230–400 mesh, eluent $CHCl_3$/MeOH, 95:5), obtaining 0.303 g of a slightly brown solid.

4.1.5.1. 3-Methanesulfonyl-7-phenyl-6H-pyrrolo*[3,2-f]*quinolin-9-one (**4b**)

Yield: 89.9%; R*f* = 0.16 (blue fluorescent spot, eluent $CHCl_3$/MeOH, 95:5); mp: 321.5 °C (decomposition); UV-Vis (H_2O/MeOH, 99:1): λ_{max} (A) = 274 (A = 0.874), 347 nm (A = 0.432); fluorescence (H_2O): λ_{exc} = 350.1 nm, λ_{ems} = 488.8 nm; IR (KBr): v = 3403.20 (NH), 3088 (C-H aromatic), 2958 (C-H aliphatic), 1610.20 (C═O), 1449.01 (C═C) 1170.20 cm^{-1} (SO_2N); ^{1}H NMR (400 MHz, DMSO-d_6) δ = 11.87 (s, 1H, NH), 8.19 (d, J = 9.12 Hz, 1H, H-4), 7.92 (d, J = 3.52 Hz, 1H, H-1), 7.87 (m, J = 6.60 Hz and J = 4.20 Hz, 2H, H-2′ and H-6′), 7.82 (d, J = 9.08 Hz, 1H, H-5), 7.72 (d, J = 3.48 Hz, 1H, H-2), 7.62 (m, 1H, 4′-H), 7.60 (m, 2H, H-3′ and H-5′), 6.45 (d, J = 1.80 Hz, 1H, H-8), 3.50 ppm (s, 3H, SO_2CH_3); ^{13}C NMR (101 MHz, DMSO-d_6) δ = 41.90 (SO_2CH_3), 109.08 (C-8), 109.78 (C-1), 116.19 (C-5), 117.30 (C-9a), 117.85 (C-4), 125.95 (C-9b), 127.56 (C-2), 127.80 (C-2ʻ and C-6′), 129.36 (C-3ʻ and C-5′), 129.56 (C-1′), 130.70 (C-4′), 133.82 (C-3a), 137.79 (C-5a), 148.37 (C-7), 177.48 ppm (C-9); HRMS (ESI-MS, 140 eV): *m/z*[M + H$^+$] calculated for $C_{18}H_{15}N_2O_3S^+$, 339.0803; found, 339.0798; RP-C18 HPLC: t_R = 11.7 min, 97.5%.

4.1.5.2. 3-(*p*-Toluenesulfonyl)-7-phenyl-6H-pyrrolo*[3,2-f]*quinolin-9-one (**4c**)

Compound **4c** was prepared as described for compound **4b** by reacting 2.336 g (5.07 mmol) of the appropriate phenylacrylate derivative **3c** to yield 1.197 g of a slightly brown solid product. Yield: 56.9%; R*f* = 0.64 (blue fluorescent spot, eluent $CHCl_3$/MeOH, 9:1); mp: 277.6 °C (decomposition); UV-Vis (H_2O/MeOH, 99:1): λ_{max} (A) = 275 (A = 0.985), 347 nm (A = 0.569); fluorescence (H_2O): λ_{exc} = 350.1 nm, λ_{ems} = 489.1 nm; IR (KBr): v = 3410.50 (NH), 3080 (C-H aromatic), 2965 (C-H aliphatic), 1611.40 (C═O), 1460.01 (C═C) 1170.17 cm^{-1} (SO_2N); ^{1}H NMR (400 MHz, DMSO-*d*$_6$) *δ* = 11.85 (s, 1H, NH), 8.29 (d, *J* = 9.18 Hz, 1H, H-4), 7.90 (m, 1H, H-2), 7.89 (m, AA'BB', *J* = 8.54 Hz, 2H, H-2' and H-6'), 7.88 (m, 1H, H-1), 7.83 (m, 2H, H-2" and H-6"), 7.79 (d, *J* = 9.18 Hz, 1H, H-5), 7.58 (m, 3H, H-3", H-5" and H-4"), 7.38 (m, 2H, H-3" and H-5"), 6.40 (s, 1H, H-8), 2.30 ppm (s, 3H, -CH_3); ^{13}C NMR (75 MHz, DMSO-*d*$_6$) *δ* = 21.91 (-CH_3), 109.62 (C-8), 111.66 (C-1), 117.04 (C-5), 118.36 (C-9a), 118.51 (C-4), 127.54 (C-2' and C-6'), 127.61 (C-9b), 128.29 (C-2" and C-6"), 128.49 (C-2), 129.84 (C-3" and C-5"), 130.59 (C-4"), 131.14 (C-3' and C-5'), 131.20 (C-1"), 134.94 (C-4'), 135.08 (C-3a), 139.07 (C-5a), 146.49 (C-1'), 149.65 (C-7), 178.48 ppm (C-9); HRMS (ESI-MS, 140 eV): *m/z* [M + H$^+$] calculated for $C_{24}H_{19}N_2O_3S^+$, 415.1226; found, 415.1299; RP-C18 HPLC: t_R = 14.7 min, 99.7%.

4.1.5.3. 3-((4-(Trifluoromethyl)benzene)sulfonyl)-7-phenyl-6H-pyrrolo*[3,2-f]*quinolin-9-one (**4d**)

Compound **4d** was prepared as described for compound **4b** by reacting 1.555 g (3.02 mmol) of the appropriate phenylacrylate derivative **3d** to yield 0.414 g of a brownish solid product. Yield: 29.3%; R*f* = 0.65 (blue fluorescent spot, eluent $CHCl_3$/MeOH, 9:1); mp: 341 °C (decomposition); UV-Vis (H_2O/MeOH, 99:1): λ_{max} (A) = 270 (A = 0.279), 345 nm (A = 0.169); fluorescence (H_2O): λ_{exc} = 345.7 nm, λ_{ems} = 491.1 nm; IR (KBr): *v* = 3402.50 (NH), 3078 (C-H aromatic), 2969 (C-H aliphatic), 1608.30 (C═O), 1458.01 (C═C) 1169.37 (SO_2N), 1325.12 cm^{-1} (C-F); ^{1}H NMR (DMSO-*d*$_6$): *δ* = 11.90 (s, 1H, NH), 8.32 (dd, *J* = 9.16 Hz and 0.68 Hz, 1H, H-4), 8.23 (m, *J* = 8.28 Hz, 2H, H-2' and H-6'), 7.99 (m, 1H, H-2), 7.99 (m, 2H, H-3" and H-5"), 7.93 (d, *J* = 3.32 Hz, 1H, H-1) 7.84 (m, 2H, H-2" and H6") 7.82 (d, *J* = 9.08 Hz, 1H, H-5), 7.59 (m, 1H, 4'), 7.59 (m, 2H, H-3' and H-5'), 6.46 ppm (bs, 1H, H-8); ^{13}C NMR (DMSO-*d*$_6$): *δ* = 109.30 (C-8), 112.06 (C-1), 117.23 (C-5), 117.62 (C-9a), 118.03 (C-4), 126.41 (C-9b), 126.62 (q, J = 247.23, CF_3), 127.29 (C-2), 127.65 (q, *J* = 32.40 Hz, C-3" and C-5"), 127.94 (C-2" and C-6"), 128.10 (C-2' and C-6'), 129.48 (C-3' and C-5'), 130.85 (C-4'), 131.24 (C-3a), 134.52 (q, J = 32.40, C-4"), 135.70 (C-1'), 139.53 (C-5a), 141.19 (C-1"), 155.26 (C-7), 180.72 ppm (C-9); HRMS (ESI-MS, 140 eV): *m/z* [M + H$^+$] calculated for $C_{24}H_{16}F_3N_2O_3S^+$, 469.1027; found, 469.1040; RP-C18 HPLC: t_R = 16.45 min, 98.5%.

4.1.5.4. 3-Benzoyl-1,2-dihydro-7-phenyl-6H-pyrrolo[3,2-f]quinolin-9-one (**7a**) and 1n-benzoyl-2,3-dihydro-6-phenyl-5H-pyrrolo[2,3-g]quinolin-8-one (**8a**)

Compounds **7a** and **8a** were prepared as described for compound **4b** by reacting 1.100 g (2.66 mmol) of the appropriate phenylacrylate derivative **6a** to yield 0.443 g of a raw powdery solid consisting of the two isomers **7a** and **8a**. The two desired compounds were purified by liquid column chromatography (eluent $CHCl_3$/MeOH, 95:5).

3-benzoyl-1,2-dihydro-7-phenyl-6*H*-pyrrolo[3,2-*f*]quinolin-9-one (**7a**). 0.128 g were obtained. Yield: 15.3%; R*f* = 0.49 (blue fluorescent spot, eluent $CHCl_3$/MeOH, 9:1); mp: 322 °C (decomposition); UV−Vis (H_2O/MeOH, 99:1): λ_{max} (A) = 221 (0.717), 293 (0.670), 343 nm (0.320); λ_{min} (A) = 258 (0.226), 318 nm (0.172); fluorescence

(H_2O): λ_{exc} = 300 nm, λ_{ems} = 451 nm; IR (KBr): $\tilde{\nu}$ = 3180, 2950, 2880, 1615, 1490 cm^{-1}; ^1H NMR (400 MHz, DMSO)-d_6) δ = 11.69 (s, 1H, NH), 7.82 (m, 2H, H-2″ and H-6″), 7.61 (m, 7H, H-3″, -4″, -5″, H-2′ and H-6′, H-4 and H-5), 7.52 (m, 3H, H-3′, -5′ and 4′), 6.24 (d, *J* = 1.82 Hz, 1H, H-8), 4.09 (t, *J* = 8.65 Hz, 2H, H-2), 3.68 ppm (t, *J* = 8.65 Hz, 2H, H-1); ^{13}C NMR (DMSO-d_6): δ = 25.34 (C-3), 50.17 (C-2), 115.24 (C-4), 109.45 (C-8), 117.83 (C-9a), 121.73 (C-5), 122.24 (C-9b), 127.12 (C-2′ and C-6′), 127.64 (C-2″ and C-6″), 128.41 (C-3″ and C-5″), 128.58 (C-3′ and C-5′), 129.45 (C-4′), 130.14 (C-4″), 132.13 (C-1′), 134.32 (C-3a), 135.23 (C-1″), 139.45 (C-5a), 154.13 (C-7), 165.34 (C$=$O), 178.34 ppm (C-9); HRMS (ESI-MS, 140 eV): *m/z* [M + H^+] calculated for $C_{24}H_{19}N_2O_2^+$, 367.1447; found, 367.1439; RP-C18 HPLC: t_R = 12.38 min, 97.4%.

1*N*-benzoyl-2,3-dihydro-6-phenyl-5*H*-pyrrolo[2,3-*g*]quinolin-8-one (**8a**). 0.141 g were obtained. Yield: 16.8%; R*f* = 0.37 (greenish fluorescent spot, eluent $CHCl_3$/MeOH, 9:1); mp: 319 °C (decomposition); UV−Vis (H_2O/MeOH, 99:1): λ_{max} (A) = 222 (0.514), 284 (0.498), 350 nm (0.320); λ_{min} (A) = 258 (0.226), 318 nm (0.172); fluorescence (H_2O), λ_{exc} = 350 nm, λ_{ems} = 468 nm; IR (KBr): $\tilde{\nu}$ = 3380, 3190, 2960, 1610, 1480 cm^{-1}; ^1H NMR (400 MHz, DMSO)-d_6) δ = 11.72 (s, 1H, NH), 7.84 (m, 2H, H-2″ and H-6″), 7.72 (m, 7H, H-3″, -4″, -5″, H-2′ and H-6′, H-4 and H-9), 7.55 (m, 3H, H-3′, -5′ and 4′), 6.35 (s, 1H, H-7), 4.01 (t, *J* = 8.72 Hz, 2H, H-2), 3.28 ppm (t, *J* = 8.71 Hz, 2H, H-1); ^{13}C NMR (DMSO-d_6): δ = 26.28 (C-3), 49.24 (C-2), 116.16 (C-4), 108.24 (C-7), 118.13 (C-8a), 120.34 (C-9), 121.04 (C-3a), 126.92 (C-2′ and C-6′), 127.04 (C-2″ and C-6″), 127.97 (C-3″ and C-5″), 128.18 (C-3′ and C-5′), 129.05 (C-4′), 130.14 (C-4″), 131.14 (C-1′), 133.16 (C-9a), 136.14 (C-1″), 140.36 (C-4a), 153.16 (C-6), 166.18 (C$=$O), 177.90 ppm (C-8); HRMS (ESI-MS, 140 eV): *m/z* [M + H^+] calculated for $C_{24}H_{19}N_2O_2^+$, 367.1447; found, 367.1448; RP-C18 HPLC: t_R = 12.02 min, 97.5%.

4.1.5.5. 3-Methanesulfonyl-1,2-dihydro-7-phenyl-6H-pyrrolo[3,2-f]quinolin-9-one (**7b**) and 1N-methanesulfonyl-2,3-dihydro-6-phenyl-5H-pyrrolo[2,3-g]quinolin-8-one (**8b**). Compounds **7b** and **8b** were prepared as described for compound **4b** by reacting 0.488 g (1.27 mmol) of the appropriate phenylacrylate derivative **6b** to yield 0.210 g of a raw powdery solid consisting of the two isomers **7b** and **8b**. The two desired compounds were purified by liquid column chromatography (eluent $CHCl_3$/MeOH, 95:5)

4.1.5.5.1. 3-Methanesulfonyl-1,2-dihydro-7-phenyl-6H-pyrrolo[3,2-f]quinolin-9-one (**7b**)

0.084 g of a pale yellow solid were obtained. Yield: 19.4%; R*f* = 0.21 (blue fluorescent spot, eluent $CHCl_3$/MeOH, 95:5); mp: 311.4 °C (decomposition); UV−Vis (H_2O/MeOH, 99:1): λ_{max} (A) = 206 (1.435), 270 (1.341), 345 nm (0.642); λ_{min} (A) = 195 (0.453), 247 (0.600), 314 nm (0.344); fluorescence (H_2O): λ_{exc} = 350 nm, λ_{ems} = 458 nm; IR (ATR ZnSe): *v* = 3370, 3010, 2978, 1640, 1478, 1057 cm^{-1}; ^1H NMR (400 MHz, DMSO-d_6) δ = 11.64 (s, 1H, NH), 7.82 (m, 2H, H-2′ and H-6′), 7.68 (d, *J* = 9.23 Hz, 1H, H-4), 7.63 (d, *J* = 8.87 Hz, 1H, H-5), 7.58 (m, 3H, H-3′, H-5′ and H-4′), 6.25 (s_b, 1H, H-8), 4.02 (t, *J* = 8.60 Hz, 2H, H-2), 3.70 (t, *J* = 8.56 Hz, 2H, H-3), 2.97 ppm (s, 3H, SO_2CH_3); ^{13}C NMR (101 MHz, DMSO-d_6) δ = 30.15 (C-1), 35.05 (SO_2CH_3), 51.63 (C-2), 108.77 (C-8), 119.32 (C-5), 119.58 (C-4), 119.79 (C-9a), 128.14 (C-2′ and C-6′), 129.84 (C-3′ and C-5′), 129.95

(C-4′), 131.00 (C-1′), 131.28 (C-9b), 134.88 (C-3a), 138.74 (C-5a), 150.45 (C-7), 178.97 ppm (C-9); HRMS (ESI-MS, 140 eV): *m/z* [M + H$^+$] calculated for $C_{18}H_{17}N_2O_3S^+$, 341.1211; found, 341.1250; RP-C18 HPLC: t_R = 10.99 min, 96.8%.

4.1.5.5.2. 1N-methanesulfonyl-2,3-dihydro-6-phenyl-5H-pyrrolo[2,3-g]quinolin-8-one (**8b**)

0.068 g of a yellowish solid were obtained. Yield: 15.7; R*f* = 0.10 (blue fluorescent spot, eluent $CHCl_3$/MeOH, 95:5); mp: 317.7 °C (decomposition); UV–Vis (H_2O/MeOH, 99:1): λ_{max} (A) = 210 (1.137), 275 (0.875), 352 nm (0.447); λ_{min} (A) = 190 (0.104), 247 (0.650), 314 nm (0.346); fluorescence (H_2O): λ_{exc} = 350 nm, λ_{ems} = 475 nm; IR (ATR ZnSe): *ν* = 3250, 2986, 1615, 1476, 1055 cm^{-1}; ^{1}H NMR (400 MHz, DMSO-*d*$_6$) *δ* = 11.70 (s, 1H, NH), 7.91 (s, 1H, H-9), 7.81 (m, 2H, H-2′ and H-6′), 7.64 (s, 1H, H-4), 7.59 (m, 3H, H-3′, H-5′ and H-4′), 6.30 (bs, 1H, H-6), 4.01 (t, *J* = 8.26 Hz, 2H, H-2), 3.28 (t, *J* = 8.16 Hz, 2H, H-1), 3.03 ppm (s, 3H, SO_2CH_3); ^{13}C NMR (101 MHz, DMSO-*d*$_6$) *δ* = 27.91 (C-1), 34.40 (SO_2CH_3), 50.49 (C-2), 107.24 (C-7), 107.35 (C-9), 115.80 (C-4), 125.03 (C-9a), 127.80 (C-2′ and C-6′), 129.48 (C-3′ and C-5′), 130.84 (C-4′), 134.60 (C-1′), 137.83 (C-8a), 138.51 (C-3a), 139.011 (C-4a), 149.48 (C-7), 176.66 ppm (C-8); HRMS (ESI-MS, 140 eV): *m/z* [M + H$^+$] calculated for $C_{18}H_{17}N_2O_3S^+$, 341.1211; found, 341.1226; RP-C18 HPLC: t_R = 10.52 min, 98.5%.

4.1.5.6. 3-((4-(Trifluoromethyl)benzene)sulfonyl)-1,2-dihydro-7-phenyl-6H-pyrrolo[3,2-f]quinolin-9-one (**7d**) and 1N-((4-(trifluoromethyl)benzene)sulfonyl)-2,3-dihydro-6-phenyl-5H-pyrrolo[2,3-g]quinolin-8-one (**8d**)

Compounds **7d** and **8d** were prepared as described for compound **4b** by reacting 1.100 g (2.12 mmol) of the appropriate phenylacrylate derivative **6d** to yield 0.920 g of a raw sticky viscous tar. The tar was triturated with Et_2O and purified by liquid column chromatography (eluent $CHCl_3$/MeOH, 9:1) yielding 0.587 g of a powdery white solid consisting of an irresolvable mixture of the two isomers **7d** and **8d**. Yield: 58.6%; R*f* = 0.61 (eluent $CHCl_3$/MeOH, 9:1); mp: 301 °C (decomposition); UV-Vis (H_2O/MeOH, 99:1): 275 nm (A = 0.337), 351 nm (A = 0.258); IR (KBr): *ν* = 3432.80 (NH), 3078 (C-H aromatic), 2980 (C-H aliphatic), 1600 (C═O), 1498 (C═C) 1171.51 (SO_2N), 1323.63 cm^{-1} (C-F); ^{1}H NMR (400 MHz, DMSO-*d*$_6$): *δ* = 11.69 (s, 1H, NH), 11.67 (s, 1H, NH), 8.21 (m, *J* = 8.94 Hz, 2H), 8.14 (s, 1H), 8.02 (d, *J* = 9.17 Hz, 1H), 7.98 (m, 4H), 7.92 (d, *J* = 9.46 Hz, 1H), 7.80 (m, *J* = 8.22 Hz, 2H), 7.72 (d, *J* = 3.03 Hz, 1H), 7.69 (m, *J* = 8.23 Hz, 2H), 7.66 (d, *J* = 8.66 Hz, 2H), 7.61 (m, 2H), 7.41 (t, *J* = 2.05 Hz, 1H), 7.36 (s, 1H), 6.58 (s, 1H), 6.32 (s, 1H), 4.07 (t, *J* = 7.81 Hz, 4H), 3.54 (t, *J* = 7.83 Hz, 2H), 3.15 ppm (t, *J* = 8.23 Hz, 2H); ^{13}C NMR (101 MHz, DMSO-*d*$_6$): *δ* = 27.33, 29.03, 50.21, 50.87, 104.52, 105.27, 106.95, 112.24, 113.50, 118.56, 119.39, 119.65, 121.42, 121.55, 124.83 (q, *J* = 4.01 Hz), 126.29, 126.67 (q, *J* = 249.26 Hz), 126.88 (q, *J* = 247.28 Hz), 127.38, 127.59, 127.92, 128.09, 128.48, 128.99, 129.06, 129.37, 129.99, 130.43, 130.74, 131.60, 133.72 (q, *J* = 33.01 Hz), 134.02 (q, *J* = 32.72 Hz), 136.93, 137.25, 139.86, 150.67, 152.13, 179.12, 180.02 ppm; HRMS (ESI-MS, 140 eV): *m/z* [M + H$^+$] calculated for $C_{24}H_{18}F_3N_2O_3S^+$, 471.1234; found, 471.1221; RP-C18 HPLC:

t_R = 15.50 min, 82.0% and t_R = 16.47 min, 17.4%. (NB: 32 H in NMR. If this represents both isomers, shouldn't there be 34 H, unless some are silent?)

4.1.5.7. 3-Benzoyl-7-phenyl-6H-pyrrolo[3,2-f]quinolin-9-one (**4a**)

Into a two-necked 50 mL round-bottomed flask, 0.041 g (1.7 mmol, 3 eq.) of NaH, 60% dispersion in mineral oil, was placed and washed with toluene (3 × 10 mL). With stirring, a solution of 7-phenyl-3*H*,6*H*-pyrrolo[3,2-*f*]quinolin-9-one (**9**, prepared as previously reported [8]), 0.150 g (0.57 mmol, 1 eq.) in 7 mL of anhydrous DMF, was dropped into the flask. After 30 min at room temperature, a solution of benzoyl chloride, 0.2 mL (1.7 mmol, d = 1.21 g/mL, 3 eq.) in 2 mL dry DMF, was added, and the reaction mixture was stirred for 2 h. The reaction was monitored by TLC analysis (eluent $CHCl_3$/MeOH, 9:1). At the end of the reaction, 25 mL of water was added, and the solvent was evaporated under reduced pressure, leaving a residue, which was extracted with EtOAc (3 × 50 mL). The organic phase, washed with water, a 10% Na_2CO_3 solution, and brine was dried over anhydrous Na_2SO_4 and concentrated under vacuum to yield a crude yellow solid (0.171 g). This crude product was purified with a silica gel chromatographic column (3 × 35 cm, 230–400 mesh, $CHCl_3$/MeOH, 9:1), yielding 0.057 g of a pure yellowish solid. Yield: 27.2%; R*f* = 0.48 (blue fluorescent spot, eluent $CHCl_3$/MeOH, 9:1); mp: 316.8 °C (decomposition); UV–Vis (H_2O/MeOH, 99:1): λ_{max} (A) = 204 (0.992), 279 (1.557), 352 nm (0.281); λ_{min} (A) = 195 (0.322), 237 (0.443), 336 nm (0.225); fluorescence (H_2O), λ_{exc} = 277 nm, λ_{ems} = 460 nm; IR (KBr): v = 3327 (NH), 1790 (C═O amidic), 1678 (C═O), 1660 cm^{-1} (C═C); ^1H NMR (400 MHz, DMSO-d_6): δ = 11.87 (s, 1H, NH), 8.60 (d, J = 9.16 Hz, 1H, H-4), 7.88 (m, 2H, H-2′ and H-6′), 7.87 (d, J = 2.96 Hz, 1H, H-1), 7.82 (m, 2H, H-2″ and H-6″), 7.80 (d, J = 8.42 Hz, 1H, H-5), 7.73 (m, J = 7.51 Hz, J = 2.12 Hz and J = 1.22 Hz, 1H, H-4″), 7.65 (m, 2H, H-3″ and H-5″), 7.61 (m, 3H, H-3′, H-5′ and H-4′), 7.51 (d, J = 3.56 Hz, 1H, H-2), 6.44 ppm (d, J = 1.16 Hz, 1H, H-8); ^{13}C NMR (101 MHz, DMSO-d_6): δ = 109.13 (C-8), 110.23 (C-1), 116.18 (C-5), 117.21 (C-9a), 120.64 (C-4), 127.33 (C-9b), 127.93 (C-2′ and C-6′), 129.23 (C-3′ and C-5′), 129.37 (C-2), 129.46 (C-3′ and C-5′), 129.75 (C-2″ and C-6″), 130.79 (C-4′), 131.51 (C-1′), 132.79 (C-4″), 134.20 (C-1″), 137.00 (C-3a), 138.96 (C-5a), 149.20 (C-7), 168.99 (NC═O), 178.45 ppm (C-9); HRMS (ESI-MS, 140 eV): m/z [M + H^+] calculated for $C_{24}H_{17}N_2O_2^+$, 365.1385; found, 365.1382; RP-C18 HPLC: t_R = 13.95 min, 96.5%.

4.1.5.8. *N*-cyclopropyl-7-phenyl-6H-pyrrolo[3,2-f]quinolin-9-one-3-carboxamide (**4e**)

To a stirred slurry of NaH (0.041 g of a 60% mineral oil dispersion, 1.73 mmol, 3 eq.) in THF (2 mL) at 0 °C, under N_2, was cautiously added 7-phenyl-3*H*,6*H*-pyrrolo[3,2-*f*]quinolin-9-one (**9**, 0.15 g, 0.57 mmol, 1eq., prepared as reported [8]) previously dissolved in THF (7 mL). The reaction mixture was stirred at 0 °C for 60 min, then transferred, via cannula, to a solution of 4-nitrophenyl chloroformate (0.140 g, 0.69 mmol, 1.2 eq.) in THF (2 mL). The resultant reaction mixture was stirred at ambient temperature for 15 h (TLC, eluent *n*-Hex/EtOAc, 2:1), prior to removal of the solvent by concentration in vacuo. The residue obtained was suspended in EtOAc (100 mL), then filtered and washed with EtOAc and Et_2O to yield 0.255 g (99.0%) of a pale yellow solid. The resulting activated *N*-(4-nitro)phenyl-7-phenyl-6*H*-pyrrolo[3,2-*f*]quinolin-9-one-3-carboxamide was immediately used as follows: a 2.0 M solution of cyclopropylamine (0.382 mL, 5.48 mmol, d = 0.824 g/mL, 8 eq.) in THF (2.75 mL) was added to a solution of the activated carbamate (0.255 g, 0.60 mmol, 1eq.) in THF (5 mL). The resultant reaction mixture was stirred at ambient temperature for 4 h and monitored by TLC (eluent $CHCl_3$/MeOH, 85:15) prior to removal of the solvent by concentration to dryness, in vacuo. The residue obtained was partitioned between EtOAc (100 mL) and H_2O (100 mL). The layers ware separated, and the aqueous phase was extracted with EtOAc (2 × 30 mL). The combined organic extract was washed with saturated $NaHCO_3$(100 mL) and brine, dried over $NaSO_4$ and concentrated in vacuo to give a yellow solid that was suspended in Et_2O (35 mL), filtered and washed with Et_2O (2 × 20 mL) to give 0.062 g of a yellowish solid. Yield: 30.1%. R*f* = 0.29 (eluent $CHCl_3$/MeOH, 85:15); mp: 314 *C (decomposition); UV−Vis (H_2O/MeOH, 99:1): λ_{max} (A) = 338 (0.081), 270 (0.162), 204 nm (0.169); λ_{min} (A) = 312 nm (0.046), 246 nm (0.079); fluorescence (H_2O): λ_{exc} = 215.00 nm, λ_{em} = 430.00 nm; IR (KBr): *v* = 3311.56 (NH), 1618 (C=C) cm^{-1}; ^1H NMR (400 MHz, DMSO-d_6): δ = 11.80 (s, 1H, NH), 8.56 (d, *J* = 9.12 Hz, 1H, H-4), 8.40 (d, *J* = 2.91 Hz, 1H, C=ONH), 7.91 (d, *J* = 3.54 Hz, 1H, H-2), 7.85 (m, 2H, H-2′ and H-6′), 7.75 (d, *J* = 2.67 Hz, 1H, H-1), 7.68 (d, *J* = 9.15 Hz, 1H, H-5), 7.58 (m, 3H, H-3′, H-5′ and H-4′), 6.41 (bs, 1H, H-8), 2.81 (m, *J* = 3.24 Hz, 1H, NH-CH), 0.80–0.60 ppm(m, 4H, $-CH_2CH_2-$); ^{13}C NMR (101 MHz, DMSO-d_6): δ = 6.31 ($-CH_2CH_2-$), 23.82 (NH-CH), 108.05 (C-1), 108.93 (C-8), 115.15 (C-5), 117.86 (C-9a), 120.14 (C-4), 124.15 (C-9b), 125.81 (C-2), 127.86 (C-2′ and C-6′), 129.43 (C-3′ and C-5′), 130.59 (C-4′), 130.85 (C-1′), 131.39 (C-3a), 134.85 (C-5a), 153.12 (C-7), 165.21 (NC=ONH), 178.43 ppm (C-9); HRMS (ESI-MS, 140 eV): *m/z* [M + H^+] calculated for $C_{21}H_{18}N_3O_2^+$, 344.1999; found, 344.1994; RP-C18 HPLC: t_R = 10.93 min, 98.5%.

4.2. Biological assays

4.2.1. Cell growth conditions and antiproliferative assay

Human T-leukemia (CCRF-CEM and Jurkat), human B-leukemia (RS4; 11, SEM) cells and human myeloid leukemia (HL-60, THP-1, MV4; 11) cells, were grown in RPMI-1640 medium (Gibco, Milano, Italy). Breast adenocarcinoma (MCF-7), human cervix carcinoma (HeLa), non small cell lung adenocarcinoma (A549) and human colon adenocarcinoma (HT-29) cells were grown in DMEM medium (Gibco, Milano, Italy), all supplemented with 115 units/mL penicillin G (Gibco, Milano, Italy), 115 μg/mL streptomycin (Invitrogen, Milano, Italy), and 10% fetal bovine serum (Invitrogen, Milano, Italy). Stock solutions (10 mM) of the different compounds were obtained by dissolving them in DMSO. Individual wells of a 96-well tissue culture microtiter plate were inoculated with 100 µL of complete medium containing 8 × 10^3 cells. The plates were incubated at 37 °C in a humidified 5% CO_2 incubator for 18 h prior to the experiments. After medium removal, 100 µL of fresh medium containing the test compound at different concentrations was added to each well in triplicate and incubated at 37 °C for 72 h. Cell viability was assayed by MTT test as previously described [26]. The GI_{50} was defined as the compound concentration required to inhibit cell proliferation by 50%. Peripheral blood lymphocytes (PBL) from healthy donors were obtained by separation on Lymphoprep (Fresenius KABI Norge AS) gradient. After extensive washing, cells were resuspended (1.0×10^6 cells/mL) in RPMI-1640 with 10% fetal bovine serum and incubated overnight. For cytotoxicity evaluations in proliferating PBL cultures, non-adherent cells were resuspended at 5×10^5 cells/mL in growth medium, containing 2.5 µg/mL PHA (Irvine Scientific). Different concentrations of the test compounds were added, and viability was determined 72 h later by the MTT test. For cytotoxicity evaluations in resting PBL cultures, non-adherent cells were resuspended (5×10^5 cells/mL) and treated for 72 h with the test compounds, as described above.

4.2.2. Effects on tubulin polymerization and on colchicine binding to tubulin

To evaluate the effect of the compounds on tubulin assembly *in vitro* [15], varying concentrations of compounds were preincubated with 10 µM bovine brain tubulin in glutamate buffer at 30 °C and then cooled to 0 °C. After addition of 0.4 mM GTP (final concentration), the mixtures were transferred to 0 °C cuvettes in a recording spectrophotometer and warmed to 30 °C. Tubulin assembly was followed turbidimetrically at 350 nm. The IC_{50} was defined as the compound concentration that inhibited the extent of assembly by 50% after a 20 min incubation. The ability of the test compounds to inhibit colchicine binding to tubulin was measured as described [16], except that the reaction mixtures contained 1 µM tubulin, 5 µM [^{3}H]colchicine and 5 µM test compound.

4.2.3. Molecular modeling

Compounds in Table 1 were built and their partial charges calculated after semi-empirical (PM6) energy minimization using the MOE2015 [27] program. Fourteen crystallographic structures were selected to perform docking studies (see SI_Table 1). Only the ligands occupying the colchicine binding site and the protein chain in the proximity of 4.5 Å were considered and subjected to the structure preparation tool of MOE 2015. Finally, Protonate 3D tool was used to assign the ionic state of each complex [28]. To identify the more appropriate docking protocol for the eleven complexes, we performed a self-docking benchmark using DockBench 1.01, a tool that compared the performance of 14 different posing/scoring protocols [29]. The active site was defined using a radius of 12 Å from the center of mass of the co-crystallized ligand. Each ligand was docked 20 times. All synthesized compounds were docked using GOLD using PLP [30], using the virtual screening tool of DockBench adopting the parameters already used in the benchmark study. Finally, the obtained conformations were rescored with the dock_pKi MOE function. The similarity studies were carried out with vROCS considering the Tversky coefficient [31].

To facilitate the visualization and analysis of data obtained from the docking simulations, we implemented an in-house tool, named MMsDocking video maker, for the automated production of a video that shows the most relevant docking data, such as docking poses, per residue IEhyd and IEele data, experimental binding data and scoring values. Videos were mounted using MEncoder [32], starting from images obtained with the following procedure: the heat maps in the background were drawn with GNUPLOT 4.6 [33] starting from per residue IEhyd and IEele data computed with MOE. Two dimensional depictions of compounds were generated using the open-source cheminformatics toolkit RDKit [34]. Representations of docking poses within the binding site were constructed using CHIMERA [35].

4.2.4. Flow cytometric analysis of cell cycle distribution

5 × 10^5 HeLa or Jurkat cells were treated with different concentrations of the test compounds for 24 h. After the incubation period, the cells were collected, centrifuged, and fixed with ice-cold ethanol (70%). The cells were then treated with lysis buffer containing RNase A and 0.1% Triton X-100 and stained with PI. Samples were analyzed on a Cytomic FC500 flow cytometer (Beckman Coulter). DNA histograms were analyzed using MultiCycle for Windows (Phoenix Flow Systems).

4.2.5. Apoptosis assay

Cell death was determined by flow cytometry of cells double stained with annexin V/FITC and PI. The Coulter Cytomics FC500 (Beckman Coulter) was used to measure the surface exposure of PS on apoptotic cells according to the manufacturer's instructions (Annexin-V Fluos, Roche Diagnostics).

4.2.6. Analysis of mitochondrial potential and reactive oxygen species (ROS)

The mitochondrial membrane potential was measured with the lipophilic cation JC-1 (Molecular Probes, Eugene, OR, USA), while the production of ROS was followed by flow cytometry using the fluorescent dye H_2DCFDA (Molecular Probes), as previously described [11].

*4.2.7. Evaluation of the metabolic stability of compound **4a** in human liver microsomes*

4.2.7.1. Incubation procedure

Compound **4a** (final concentration, 10 µM) was incubated in a medium (final volume, 0.2 mL) containing 0.1 M KH_2PO_4 (pH 7.4) and 1.0 mg/mL of pooled mixed-gender human liver microsomes (Xenotech LLC, Lenexa, USA; HLMs), in the absence or presence of 1 mM NADPH (Sigma-Aldrich). Control incubations were performed in the absence of both HLMs and NADPH (buffer only-incubations). The reactions were started by adding the microsomes following a 3-min thermal equilibration at 37 °C, conducted at 37 °C for different time periods (i.e. 0, 15, 30 and 60 min), and terminated by adding 0.1 mL of ice-cold acetonitrile. Samples were then centrifuged (4 °C) at 20,000*g* for 10 min, and aliquots of the supernatants were analyzed by HPLC with fluorescence detection, as described below

4.2.7.2. HPLC analysis

The chromatographic system consisted of a Hewlett-Packard 1100 HPLC system (Agilent Technologies Inc., formerly Hewlett-Packard, Palo Alto, USA) equipped with a degasser, a quaternary pump, an autosampler, a column oven, and a fluorescence detector; chromatographic data were collected and integrated using the Agilent ChemStation software. Chromatographic conditions were as follows: column, Agilent Zorbax SB C18 (4.6 × 75 mm, 3.5 µm); mobile phase, 0.1% HCOOH in H_2O (solvent A) and 0.1% HCOOH in acetonitrile (solvent B); elution program, isocratic elution with 95% solvent A for 2 min, linear gradient from 5 to 40% solvent B in 8 min, followed by a further linear gradient from 40 to 60% solvent B in 2 min, and an isocratic elution with 60% solvent B for 7 min; post-run time, 5 min; flow rate, 1.0 mL/min; injection volume, 50 µL; column temperature, 30 °C; detection, fluorescence (excitation wavelength, 344 nm; emission wavelength, 493 nm). Under the above conditions, the retention time of **4a** was 13.4 min. Metabolic stability of **4a**, expressed as percent of compound remaining, was calculated by comparing the corresponding chromatographic peak area at each time point relative to that at time 0 min.

References

1. Islam MN, Iskander MN (2004) Microtubulin binding sites as target for developing anticancer agents. Mini Rev Med Chem 4:1077–1104

2. Desai A, Mitchison TJ (1997) Microtubule polymerization dynamics. Annu Rev Cell Dev Biol 13:83–117

3. Jordan MA (2002) Mechanism of action of antitumor drugs that interact with microtubules and tubulin. Curr Med Chem Anticancer Agents 2:1–17

4. Dumontet C, Jordan MA (2010) Microtubule-binding agents: a dynamic field of cancer therapeutics. Nat Rev Drug Discov 9:790–803

5. Van Vuuren RJ, Visagie MH, Theron AE, Joubert AM (2015) Antimitotic drugs in the treatment of cancer. Cancer Chemother Pharmacol 76:1101–1112

6. Nitika V, Kapil K (2013) Microtubule Targeting Agents: A Benchmark in Cancer Therapy. Current Drug Therapy 189-196.

7. Ferlin MG, Chiarelotto G, Gasparotto V, Dalla Via L, Pezzi V, Barzon L, et al. Synthesis and in vitro and in vivo antitumor activity of 2-phenylpyrroloquinolin-4-ones. J Med Chem. 2005 May 5;48(9):3417–3427.

7. Ferlin MG, Chiarelotto G, Gasparotto V, Dalla Via L, Pezzi V, Barzon L, Palù G, Castagliuolo I (2005) Synthesis and in vitro and in vivo antitumor activity of 2-phenylpyrroloquinolin-4-ones. J Med Chem 48:3417–3427

8. Gasparotto V, Castagliuolo I, Chiarelotto G, Pezzi V, Montanaro D, Brun P, Palù G, Viola G, Ferlin MG (2006) Synthesis and biological activity of 7-phenyl-6,9-dihydro-3H-pyrrolo[3,2-f]quinolin-9-ones: a new class of antimitotic agents devoid of aromatase activity. J Med Chem 49:1910–1915

9. Ferlin MG, Conconi MT, Urbani L, Oselladore B, Guidolin D, Di Liddo R, Parnigotto PP (2011) Synthesis, in vitro and in vivo preliminary evaluation of anti-angiogenic properties of some pyrroloazaflavones. Bioorg Med Chem 19:448–457

10. Gasparotto V, Castagliuolo I, Ferlin MG (2007) 3-substituted 7-phenyl-pyrroloquinolinones show potent cytotoxic activity in human cancer cell lines. J Med Chem 50:5509–5513

11. Ferlin MG, Bortolozzi R, Brun P, Castagliuolo I, Hamel E, Basso G, Viola G (2010) Synthesis and in vitro evaluation of 3h-pyrrolo[3,2-f]-quinolin-9-one derivatives that show potent and selective anti-leukemic activity. ChemMedChem 5:1373–1385

12. Viola G, Bortolozzi R, Hamel E, Moro S, Brun P, Castagliuolo I, Ferlin MG, Basso G (2012) MG-2477, a new tubulin inhibitor, induces autophagy through inhibition of the Akt/mTOR pathway and delayed apoptosis in A549 cells. Biochem Pharmacol 83:16–26

13. Carta D, Ferlin MG (2014) An overview on 2-arylquinolin-4(1H)-ones and related structures as tubulin polymerisation inhibitors. Curr Top Med Chem 14:2322–2345

14. Carta D, Bortolozzi R, Hamel E, Basso G, Moro S, Viola G, Ferlin MG (2015) Novel 3-Substituted 7-Phenylpyrrolo[3,2-f]quinolin-9(6H)-ones as Single Entities with Multitarget Antiproliferative Activity. J Med Chem 58:7991–8010

15. Hamel E (2003) Evaluation of antimitotic agents by quantitative comparisons of their effects on the polymerization of purified tubulin. Cell Biochem Biophys 38:1–22

16. Verdier-Pinard P, Lai JY, Yoo HD, et al (1998) Structure-activity analysis of the interaction of curacin A, the potent colchicine site antimitotic agent, with tubulin and effects of analogs on the growth of MCF-7 breast cancer cells. Mol Pharmacol 53:62–76

17. Wang Y, Zhang H, Gigant B, Yu Y, Wu Y, Chen X, Lai Q, Yang Z, Chen Q, Yang J (2016) Structures of a diverse set of colchicine binding site inhibitors in complex with tubulin provide a rationale for drug discovery. FEBS J 283:102–111

18. Chemical Computing Group (CCG) Inc. (2016) Molecular Operating Environment (MOE). http://www.chemcomp.com.

19. Xiong S, Mu T, Wang G, Jiang X (2014) Mitochondria-mediated apoptosis in mammals. Protein Cell 5:737–749

20. Rovini A, Savry A, Braguer D, Carré M (2011) Microtubule-targeted agents: when mitochondria become essential to chemotherapy. Biochim Biophys Acta 1807:679–688

21. Zamzami N, Marchetti P, Castedo M, Decaudin D, Macho A, Hirsch T, Susin SA, Petit PX, Mignotte B, Kroemer G (1995) Sequential reduction of mitochondrial transmembrane potential and generation of reactive oxygen species in early programmed cell death. J Exp Med 182:367–377

22. Rothe G, Valet G (1990) Flow cytometric analysis of respiratory burst activity in phagocytes with hydroethidine and 2’,7'-dichlorofluorescin. J Leukoc Biol 47:440–448

23. Cai J, Jones DP (1998) Superoxide in apoptosis. Mitochondrial generation triggered by cytochrome c loss. J Biol Chem 273:11401–11404

24. Nohl H, Gille L, Staniek K (2005) Intracellular generation of reactive oxygen species by mitochondria. Biochem Pharmacol 69:719–723

25. Parkinson A, Ogilvie BW (2008) Biotransformation of xenobiotics. Casarett & Doull’s toxicology: The Basic Science of Poisons, 7th ed. pp 161–304

26. Romagnoli R, Baraldi PG, Lopez-Cara C, et al (2013) Concise synthesis and biological evaluation of 2-Aroyl-5-amino benzo[b]thiophene derivatives as a novel class of potent antimitotic agents. J Med Chem 56:9296–9309

27. Stewart JJP (2007) Optimization of parameters for semiempirical methods V: modification of NDDO approximations and application to 70 elements. J Mol Model 13:1173–1213

28. Labute P (2009) Protonate3D: assignment of ionization states and hydrogen coordinates to macromolecular structures. Proteins 75:187–205

29. Cuzzolin A, Sturlese M, Malvacio I, Ciancetta A, Moro S (2015) DockBench: An Integrated Informatic Platform Bridging the Gap between the Robust Validation of Docking Protocols and Virtual Screening Simulations. Molecules 20:9977–9993

30. GOLD suite, version 5.2. Cambridge Crystallographic Data Centre: 12 Union Road, Cambridge CB2 1EZ, UK. http://www.ccdc.cam.ac.uk

31. Santa Fe, NM, USA OpenEye Scientific Software Inc. OEChem (2016). http://www.eyesopen.com

32. MEncoder. http://www.mplayerhq.hu/design7/projects.html

33. Gnuplot. http://www.gnuplot.info/index.html

34. RDKit: Open-source cheminformatics. http://www.rdkit.org

35. Pettersen EF, Goddard TD, Huang CC, Couch GS, Greenblatt DM, Meng EC, Ferrin TE (2004) UCSF Chimera--a visualization system for exploratory research and analysis. J Comput Chem 25:1605–1612

Published: *Eur J Med Chem. 2017 Feb 15;127:643–660*

The role of 5-arylalkylamino- and 5-piperazino- moieties on the 7-aminopyrazolo[4,3-d]pyrimidine core in affecting adenosine A_1 and A_{2A} receptor affinity and selectivity profiles

Lucia Squarcialupi, Marco Betti, Daniela Catarzi, Flavia Varano, Matteo Falsini, Annalisa Ravani, Silvia Pasquini, Fabrizio Vincenzi, Veronica Salmaso, Mattia Sturlese, Katia Varani, Stefano Moro & Vittoria Colotta*

(2017) The role of 5-arylalkylamino- and 5-piperazino- moieties on the 7-aminopyrazolo[4,3-d]pyrimidine core in affecting adenosine A1 and A2A receptor affinity and selectivity profiles. J Enzyme Inhib Med Chem 32:248–263

Abstract

New 7-amino-2-phenylpyrazolo[4,3-d]pyrimidine derivatives, substituted at the 5-position with aryl(alkyl)amino- and 4-substituted-piperazin-1-yl- moieties, were synthesized with the aim of targeting human (h) adenosine A_1 and/or A_{2A} receptor subtypes. On the whole, the novel derivatives 1–24 shared scarce or no affinities for the off-target hA_{2B} and hA_3 ARs. The 5-(4-hydroxyphenethylamino)- derivative 12 showed both good affinity (Ki = 150 nM) and the best selectivity for the hA_{2A} AR while the 5-benzylamino-substituted 5 displayed the best combined hA_{2A} (Ki = 123 nM) and A_1 AR affinity (Ki = 25 nM). The 5-phenethylamino moiety (compound 6) achieved nanomolar affinity (Ki = 11 nM) and good selectivity for the hA_1 AR. The 5-(N4-substituted-piperazin-1-yl) derivatives 15–24 bind the hA_1 AR subtype with affinities falling in the high nanomolar range. A structure-based molecular modeling study was conducted to rationalize the experimental binding data from a molecular point of view using both molecular docking studies and Interaction Energy Fingerprints (IEFs) analysis.

1. Introduction

Adenosine receptors (ARs) are classified as A_1, A_{2A}, A_{2B} and A_3 subtypes [1, 2] and typically inhibit (A_1 and A_3) or activate (A_{2A} and A_{2B}) adenylyl cyclase. A1 receptor is highly expressed in brain areas, such as the hippocampus and prefrontal cortex [3, 4], implicated in the control of emotions and cognition functions. Therefore, A_1 AR antagonists are investigated as therapeutic agents for mental dysfunctions, such as dementia and anxiety [3–5]. The A_{2A} AR subtype is present in the brain with the highest concentration in the striatum, nucleus accumbens, hippocampus and cortex, and its blockade has proven to be effective in neurodegenerative pathologies such as Parkinson’s disease (PD) [6–8]. The A_{2A} AR antagonist istradefylline has been recently approved for marketing in Japan for the treatment of PD patients [9]. In preclinical studies, dual A_1/A_{2A} antagonists have also turned out to be useful for PD therapy because they reduce both motor (A_{2A}) and cognitive (A_1) impairment associated with this pathology [5, 10-12].

Recent studies have highlighted new therapeutic applications of A_{2A} AR antagonists [12]. If topically administered, they diminish scar size and promote restoration of skin integrity [13]. A_{2A} AR antagonists have also demonstrated efficacy in enhancing immunologic response, especially by markedly improving anti-tumor immunity in mouse models, thus promoting tumor regression. A_{2A} AR antagonists have been shown to improve the effect of tumor vaccines during T-cell activation, and may work in concert with other immune checkpoint inhibitors in cancer immunotherapy [12, 14].

In our laboratory, much research has been addressed to the study of AR antagonists belonging to different classes [15–26], including the 2-arylpyrazolo[4,3-d]pyrimidine derivatives [20,22,24,26] which display a broad range of affinity for the various AR subtypes, depending on the nature of the substituents at the 5- and 7-positions of the bicyclic scaffold. One recent study aimed at targeting the A_1 and A_{2A} ARs highlighted that the presence of a free 7- amino group, combined with a benzyl or, even better, a 3-phenylpropyl chain at the 5-position (Figure 1, compounds **A** and **C**) shifted affinity toward these two AR subtypes [24].

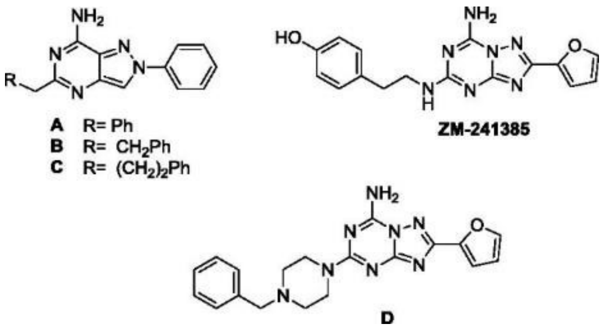

Fig. 1 Previously reported pyrazolo[4,3-*d*]pyrimidines **A–C** and triazolotriazines ZM-241385 and **D**.

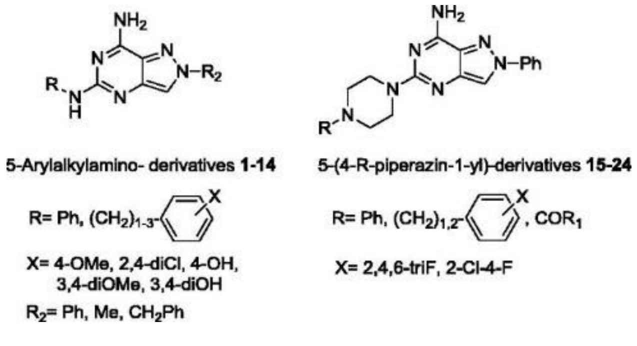
NH2
N–R2
R
NH2
N–Ph
R
5-Arylalkylamino- derivatives 1-14
5-(4-R-piperazin-1-yl)-derivatives 15-24
R= Ph, (CH2)1-3-
X
X= 4-OMe, 2,4-diCl, 4-OH, 3,4-diOMe, 3,4-diOH
R2= Ph, Me, CH2Ph
R= Ph, (CH2)1,2-
X
, COR1
X= 2,4,6-triF, 2-Cl-4-F

Fig. 2 Herein reported pyrazolo[4,3-*d*]pyrimidine derivatives **1–24**.

Hence, to further explore the structural requirements for addressing affinity toward the A_1 and/or A_{2A} ARs, various aryl(alkyl)amino- and 4-substituted-piperazin-1-yl- moieties were appended at the 5-position of the scaffold (compounds **1–24**, Figure 2). These substituents were selected since they are a common feature of potent A_1 and/or A_{2A} AR antagonists structurally correlated to our pyrazolopyrimidine derivatives [12,27,28] (such as the triazolotriazines ZM-241385 and **D**, Figure 1). The pyrazolopyrimidines **1–24** were tested in binding assays to evaluate their affinity at cloned hA_1, hA_{2A} and hA_3 ARs, stably expressed in CHO cells. Compounds were also tested at the hA_{2B} receptor by measuring their inhibitory effects on NECA-stimulated cAMP levels in CHO cells.

A structure-based molecular modeling study was performed on the new derivatives to rationalize the experimental binding data from a molecular point of view, using molecular docking studies in tandem with Interaction Energy Fingerprints (IEFs) analysis.

2. Chemistry

The 7-amino-pyrazolo[4,3-d]pyrimidine derivatives **1–14**, bearing an arylalkylamino moiety at the 5-position, were obtained as displayed in Scheme 1.

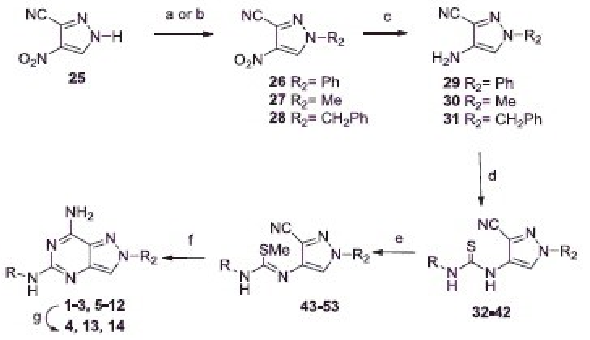

	R	R_2		R	R_2
32, 43, 1	Ph	Ph	**38, 49, 8**	Ph	Me
33, 44, 2	4-OMe-C_6H_4	Ph	**39, 50, 9**	Ph-CH_2	Me
34, 45, 3	2,4-diClC_6H_3	Ph	**40, 51, 10**	Ph-CH_2	CH_2Ph
4	4-OH-C_6H_4	Ph	**41, 52, 11**	4-OMe-C_6H_4-$(CH_2)_2$	Ph
35, 46, 5	Ph-CH_2	Ph	**42, 53, 12**	3,4-diOMe-C_6H_3-$(CH_2)_2$	Ph
36, 47, 6	Ph-$(CH_2)_2$	Ph	**13**	4-OH-C_6H_4-$(CH_2)_2$	Ph
37, 48, 7	Ph-$(CH_2)_3$	Ph	**14**	3,4-diOH-C_6H_3-$(CH_2)_2$	Ph

Scheme 1 Reagents and conditions: (a) Ph-B$(OH)_2$, Cu$(OAc)_2$, pyridine, CH_2Cl_2, 4 Å molecular sieves, room temperature; (b) MeI or $PhCH_2Br$, NaH, anhydrous THF, room temperature; (c) cyclohexene, Pd/C, 150 °C, mw; (d) R–N=C=S, DMF, room temperature; (e) 0.1 M aqueous NaOH, CH_3I, room temperature; (f) NH_4Cl, formamide, 110–150 °C mw; (g) compounds **2**, **11**, **12**, BBr_3, anhydrous CH_2Cl_2, room temperature or reflux.

Both the 1-phenyl (**26**) and 1-alkyl substituted pyrazoles (**27**, **28**) were synthesized from a common starting compound: the readily available 4-nitro-1H-pyrazole-3-carbonitrile **25** [26] which was a good substrate for both regioselective N-alkylation and Narylation. The latter was achieved by a cross-coupling reaction with phenylboronic acid in the presence of cupric acetate and activated molecular sieves. The 1-phenyl-pyrazole derivative **26** was thus prepared with higher yield than those previously obtained in our laboratory through another synthetic pathway [22]. The 1-methyl- and 1-benzyl-pyrazoles **27** and **28** were prepared from compound **25** as already described [26]. The 4-nitropyrazolo-3-carbonitriles **26–28** were transformed into the corresponding 4- amino derivatives **29–31** [26] by reduction with cyclohexene and Pd/C, under microwave-assisted conditions. Reaction of compounds **29–31** with isothiocyanates in anhydrous DMF yielded the corresponding N-(1-substituted-3-cyano-pyrazol-4-yl)thiourea derivatives **32–42**. Phenyl-, 4-methoxyphenyl-, 2,4-dichlorophenyl and benzyl-isothiocyanates were commercially available, the others were synthesized as previously reported, i.e. allowing the corresponding arylalkylamines to react with CS2, in 30% hydrogen peroxide aqueous solution (phenylethyl-, phenylpropyl- and 3,4-dimethoxyphenyl-isothiocyanates) [29,30] or with thiophosgene and potassium carbonate, in CH2Cl2 under nitrogen atmosphere (4-methoxyphenylisothiocyanate) [31].

Compounds **32–42** were reacted with iodomethane in anhydrous DMF to give the corresponding S-methylisothiourea derivatives **43–53** which were cyclized to the desired 7-amino-5- arylalkylamino-pyrazolo[4,3-d]pyrimidines **1–3**, **5–12** by reaction with ammonium chloride in formamide, under microwave irradiation. The methoxy-substituted derivatives **2**, **11** and **12** were transformed into the corresponding hydroxy derivatives **4**, **13** and **14** by treatment with BBr3 in anhydrous CH2Cl2.

The 7-amino-pyrazolo[4,3-d]pyrimidine derivatives **15–22**, bearing N-substituted-piperazine moieties at the 5-position, were obtained utilizing the synthetic route as described in Scheme 2.

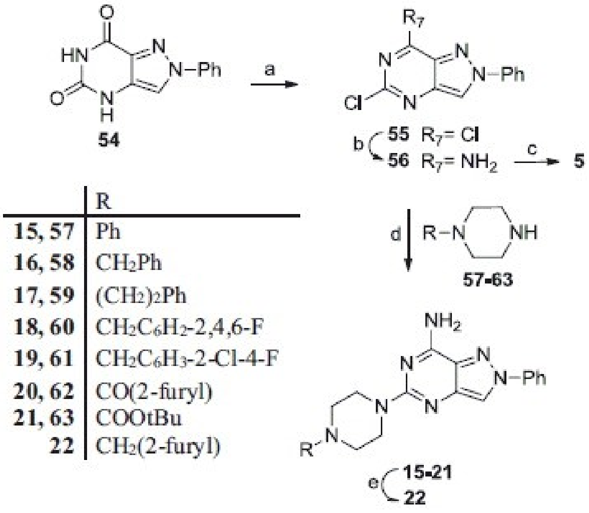

	R
15, 57	Ph
16, 58	CH_2Ph
17, 59	$(CH_2)_2Ph$
18, 60	$CH_2C_6H_2$-2,4,6-F
19, 61	$CH_2C_6H_3$-2-Cl-4-F
20, 62	CO(2-furyl)
21, 63	COOtBu
22	CH_2(2-furyl)

Scheme 2 Reagents and conditions: (a) N,N-dimethylaniline, $POCl_3$, 150 °C, mw; (b) 33% aqueous NH_3, 100 °C, mw; (c) benzylamine, ethyldiisopropylamine, tert-butanol, 200 °C, mw; (d) ethyldiisopropylamine, N-methylpyrrolidone, 130–150 °C, mw; (e) compound **20**, $LiAlH_4$, anhydrous THF, room temperature.

Allowing the 1-phenylpyrazolo[4,3-d]pyrimidine-5,7-dione **54** [20] to react with phosphorus oxychloride and N,N-dimethylaniline under microwave irradiation, the 5,7-dichloro-derivative **55** was prepared, which was reacted with 33% aqueous ammonia solution under microwave irradiation at 100°C to give the 7-amino- 5-

chloro-pyrazolopyrimidine **56** as the only regioisomer. The 7-amino structure of **56** was expected on the basis of the well-known different mobility of the two chlorine atoms in the pyrimidine ring, also condensed with diverse heterocyclic systems [32–34]. To confirm the structure, derivative **56** was treated with benzylamine in tert-butanol, in the presence of diisopropylethylamine, and the 7-amino-5-benzylaminopyrazole derivative **5**, already synthesized through the unambiguous synthesis as depicted in Scheme 1, was obtained. This reaction was carried out under prolonged microwave irradiation (about 1 h at 200°C) but conversion of derivative **56** into **5** occurred with unsatisfactory yields. The ^{1}H NMR spectrum of the crude reaction (data not shown) displayed the presence of both the 5-benzylamino derivative **5** and the starting material **56** (ratio about 3.5:1), besides degradation compounds, thus indicating the poor reactivity of the C5 atom toward the primary benzyl ammine group. Instead, microwave-assisted reaction of the 5-chloro derivative **56** with the N-substituted piperazines **57–63**, in N-methylpyrrolidone and in the presence of diisopropylethylamine, proceeded to completion, thus giving the desired pyrazolopyrimidine derivatives **15–20** with good yields (48–85%). The piperazine derivatives **57, 58, 62** and **63** were commercially available, while derivatives **59** and **61** were prepared as previously described [35, 36]. The piperazine derivative **60** was synthesized starting from the reductive alkylation of N-Boc-piperazine **63** with 2,4,6- trifluorobenzaldeyde and triacetoxy sodium borohydride. The obtained tert-butyl 4-(2,4,6-trifluorobenzyl)piperazine-1-carboxylate was hydrolyzed with trifluoroacetic acid to give the 1-(2,4,6-trifluorobenzyl)piperazine **60**, isolated as trifluoroacetate salt.

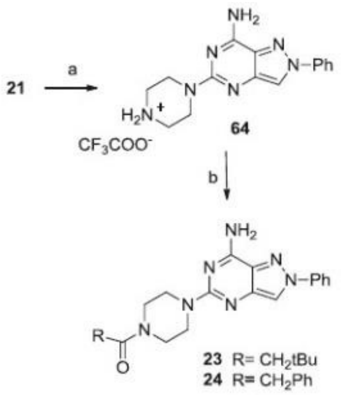

Scheme 3 Reagents and conditions: (a) CF_3COOH, CH_2Cl_2, reflux; (b) RCOCl, NEt_3, anhydrous THF, room temperature.

Reduction of the 2-furoyl carbonyl group of compound **20** with LiAlH4 in anhydrous THF provided derivative **22**. Finally, the pyrazolopyrimidines **23–24**, bearing an acyl moiety on the piperazine nitrogen, were synthesized as depicted in Scheme 3. Treatment of the N-Boc derivative **21** with trifluoroacetic acid furnished compound **64** which was reacted with suitable acyl chlorides, in the presence of triethylamine in anhydrous tetrahydrofuran, to provide the desired **23–24**.

3. Results and discussion

3.1 Structure–affinity relationship studies

The results of binding experiments and cAMP assays carried out on the new 5-substituted-pyrazolopyrimidines 1–14 and 15–24 are displayed, respectively, in Tables 1 and 2. Table 1 also includes the affinity data of the pyrazolopyrimidines A–C and of ZM- 241385 reported as references.

Table 1 Binding affinity at hA$_1$, hA$_{2A}$ and hA$_3$ ARs and potencies at hA$_{2B}$ ARs.

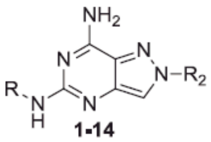

1-14

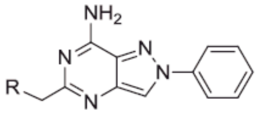

A-C

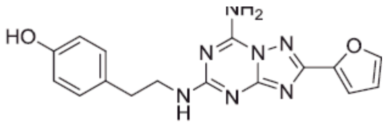

ZM-241385

			Binding experiments[a]			cAMP assays
				Ki (nM) or I%		IC50 (nM) or I%
	R	R$_2$	hA$_1$[b]	hA$_{2A}$[c]	hA$_3$[d]	hA$_{2B}$[e]
1	Ph	Ph	67±5	412±37	13±2	2%
2	4-OMe-C6H4	Ph	33%	8%	27±3	1%
3	2,4-diClC6H3	Ph	1%	1%	61±8	2%
4	4-OH-C6H4	Ph	481±42	40%	8%	10%
5	Ph-CH2	Ph	25±3	123±11	28±3	2%
6	Ph-CH2CH2	Ph	11.5±1.2	40%	38%	1%
7	Ph-CH2CH2CH2	Ph	785±72	29%	24%	1%
8	Ph	Me	1%	4%	1%	1%
9	Ph-CH2	Me	9%	1%	20%	1%
10	Ph-CH2	CH2Ph	19%	1%	1%	1%
11	4-OMe-C6H4-CH2CH2	Ph	153±11	26%	19%	1%
12	4-OH-C6H4-CH2CH2	Ph	27%	150±14	1%	1%
13	3,4-diOMe-C6H3-(CH2)2	Ph	415±39	189±18	22%	17%
14	3,4-diOH-C6H3-(CH2)2	Ph	71±6	238±24	3%	1%%
A[f]	Ph	-	150±12	110±10	39%	420±38
B[f]	Ph-CH2	-	15%	35%	17%	2%
C[f]	Ph-CH2CH2	-	5.31±0.42	55±5	12%	42%
ZM-241385[g]		-	714	1.6	743	75[h]

[a] K$_i$ values are means ± SEM of four separate assays each performed in duplicate. Percentage of inhibition (I%) are determined at 1 µM concentration of the tested compounds.

[b] Displacement of specific [^{3}H]DPCPX competition binding assays to hA$_1$CHO cells.

[c] Displacement of specific [^{3}H]ZM241385 competition binding to hA$_{2A}$CHO cells.

[d] Displacement of specific [^{125}I]AB-MECA competition binding to hA$_3$CHO cells.

[e] cAMP experiments in hA$_{2B}$CHO cells, stimulated by 200 nM NECA. Percentage of inhibition (I%) are determined at 1 µM concentration of the tested compounds.

[f] Ref. 24.

[g] Ref. 5.

[h] K$_i$ value obtained from binding experiments at recombinant hA$_{2B}$.

Table 2 Binding affinity at hA_1, hA_{2A} and hA_3 ARs and potencies at hA_{2B} ARs.

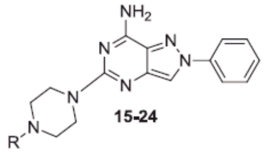

	R	Binding experiments[a] Ki (nM) or I%			cAMP assays I%
		hA_1[b]	hA_{2A}[c]	hA_3[d]	hA_{2B}[e]
15	Ph	647±53	20%	20%	1%
16	CH_2Ph	162±14	1%	1%	1%
17	$(CH_2)_2Ph$	518±42	40%	40%	1%
18	$CH_2C_6H_2$-2,4,6-F	204±18	34%	39%	1%
19	$CH_2C_6H_3$-2-Cl-4-F	193±17	29%	1%	2%
20	CO-2-furyl	580±47	16%	13%	2%
21	COOtBu	615±49	33%	21%	1%
22	CH_2-2-furyl	92±8	38%	5%	16%
23	$COCH_2tBu$	29%	2%	1%	2%
24	$COCH_2Ph$	429±36	3%	1%	3%

[a] K_i values are means ± SEM of four separate assays each performed in duplicate. Percentage of inhibition (I%) are determined at 1 µM concentration of the tested compounds.
[b] Displacement of specific [^{3}H]DPCPX competition binding assays to hA_1CHO cells.
[c] Displacement of specific [^{3}H]ZM241385 competition binding to hA_{2A}CHO cells.
[d] Displacement of specific [^{125}I]AB-MECA competition binding to hA_3CHO cells.
[e] cAMP experiments in hA_{2B}CHO cells, stimulated by 200 nM NECA. Percentage of inhibition (I%) are determined at 1 µM concentration of the tested compounds.

As expected, the new derivatives **1–24** shared scarce or no affinities for the off-target hA_{2B} and hA_3 ARs, except the 5-anilino and 5-benzylamino derivatives **1–3** and **5**, respectively which displayed nanomolar affinity for the hA_3 subtype (Ki = 13–61 nM). In particular, compounds **2** and **3** are worth noting, being also highly hA_3 selective.

Since the purpose of the work was to target hA_1 and hA_{2A} ARs, SAR discussion was focused on hA_1 and hA_{2A} binding data. In this respect, results of some interest have been obtained from the 5- arylalkylamino-pyrazolopyrimidines **1–14**. In fact, compound **12** showed both good affinity and the best selectivity for the hA_{2A} AR, while compounds **1**, **5**, **13** and **14** were able to bind both the hA_1 and hA_{2A} ARs. Moreover, a derivative having nanomolar affinity and high selectivity for the hA_1 AR subtype was identified (compound **6**).

The new 5-phenyl(alkyl)amino derivatives **1**, **5** and **6** were designed as analogs of our previously reported antagonists 5-phenyl(alkyl) derivatives **A**, **B** and **C** [24] whose methylene linker at the 5-position of the bicyclic core was replaced with an NH. This modification, suggested by the structure of potent A_{2A} antagonists bearing arylalkylamino moieties as key substituents [12], was thought to change the flexibility of the 5-lateral chain and, hopefully, to increase the affinity for the targeted ARs. Actually, the NH linker enhanced the hA_1 AR affinity (compare **1** and **5** to **A** and **B**, respectively) or maintained it in the nanomolar range (compare **6** to **C**). Instead, the hA_{2A} AR binding was ameliorated in one case, i.e. the 5-benzylamino derivative **5** which was more active than the corresponding phenylalkyl-derivative **B**.

Analyzing the hA_1 and hA_{2A} AR binding data of **1–6** in detail, it can be observed that 5-phenylamino derivative **1** binds to the hA_{2A} and hA_1 AR subtypes with scarce (Ki = 412 nM) and good affinity (Ki = 67 nM), respectively. Introduction of either a 4- methoxy group or 2,4-dichloro substituents on the 5-aniline moiety of **1** (compounds **2** and **3**) dropped affinity for hA_1 and hA_{2A} ARs. Instead, the presence of a 4-hydroxy residue (compound **4**) reduced the hA_{2A} affinity while conserving some ability to bind the hA_1 receptor (Ki = 481 nM). Homologation of the 5-phenylamino moiety (derivative **1**) to the 5-benzylamino group (derivative **5**) produced some improvement in the binding activity at both hA_1 (Ki = 25 nM) and hA_{2A} ARs (Ki = 123 nM). Quite unexpectedly, homologation of the alkyl chain of compound **5**, to obtain the 5-phenethylamino- and the 5-phenylpropylamino derivatives **6** and **7**, caused a drastic reduction of the hA_{2A} AR affinity and, in the former, it increased the hA_1 one, thus affording a selective hA_1 receptor ligand (Ki = 11.5 nM).

Replacement of the 2-phenyl group of derivatives **1** and **5** with a methyl residue, to give compounds **8** and **9**, was performed to verify whether a reduction in the volume of the molecule might permit a better accommodation inside the recognition site of the targeted hARs. This modification, instead, annulled the capability to bind the target hARs. The same detrimental effect was obtained when the 2-phenyl ring of **5** was replaced with the more flexible benzyl moiety (derivative **10**).

Insertion of the para hydroxy substituent on the 5-phenethylamino moiety of derivative **6**, to give compound **12**, was based on the structure of the well-known potent and selective hA_{2A} AR antagonist ZM-241385 [5,12] (Figure 1). Accordingly, we also thought it would be interesting to evaluate the 3,4-dihydroxy substitution (compound **14**), as well as the 4-methoxy- and the 3,4-dimethoxysubstituents (derivatives **11** and **13**). As expected, the presence of the 4-hydroxy group was able to shift the affinity toward the hA_{2A} AR. In fact, the 4-hydroxy-substituted derivative **12** showed good hA_{2A} affinity (Ki = 150 nM) and the best selectivity among all the ligands reported here. In contrast, reversed selectivity was demonstrated by the 4-methoxy derivative **11**, which displayed good affinity for the hA_1 AR but not for the hA_{2A} subtype. Instead, the 3,4-dimethoxy substituted derivative **13** bound both hA_1 and hA_{2A} receptors and also the 3,4-dihydroxy derivative **14** showed quite good affinity for both the receptors, but especially for the hA_1 one.

Finally, to further explore the SARs in this class of AR ligands, various N-substituted piperazine moieties were appended at the 5-position (derivatives **15–24**, Table 2), in accordance with the structure of known potent and selective hA_{2A} AR antagonists [27, 28]. In contrast to our expectations, none of the 5-(N4-R-piperazin-1-yl) derivatives **15–24** were able to bind effectively the A_{2A} AR while they possessed affinity for the hA_1 AR subtype, falling in the high nanomolar range. The most active compounds proved to be **22** (Ki = 92 nM) and **16** (Ki =162 nM) which bear, respectively, the (2-furyl)-methyl and 2-benzyl pendant on the N4-piperazine moiety. Introduction of halogen atoms on the benzyl moiety of **16** left almost unchanged the hA_1 AR affinity (compounds **18** and **19**) while elongation of the benzyl chain decreased it (compound **17**). Also the other substituents evaluated on the piperazine ring, i.e. acyl moieties (derivatives **20**, **23**, **24**) and the tert-butoxycarbonyl group (derivative **21**) did not ameliorate the hA_1 AR affinities.

3.2 Molecular modeling studies

A structure-based molecular modeling study was conducted to rationalize the experimental binding data from a molecular point of view. Minor attention was devoted to the hA_{2B} AR subtype, since no significant binding affinity has been estimated for any of the compounds under investigation. Docking was performed on hA_1, hA_{2A} and hA_3 AR subtypes, and the resulting poses were evaluated according to the van der Waals and electrostatic interactions, as previously reported [37,38] and described in detail in the “Experimental” section. Positive electrostatic and van der Waals values were used as filters to reject unfavorable docking poses. One pose for each ligand was selected on the basis of the Interaction Energy Fingerprints (IEFs) and by visual inspection.

An overview of the most favorable poses of all compounds on hA_1, hA_{2A} and hA_3 ARs is reported in video SM1-SM2-SM3, included in Supplementary Material. The heat map depicted in the background reports the electrostatic and hydrophobic contributions of the residues mainly involved in binding (“ele” and “hyd” labels identify the major contribution type of the residue) by a colorimetric scale going from blue to green for negative to positive values. These crucial residues are mainly positioned on the superior half of TM6 and TM7 and EL2, and the overall binding modes of the compounds under examination are very consistent among them. Here, we describe in detail the poses of compound **1** as an example, because of its high binding affinity for all three AR subtypes taken into consideration (Ki = 67 nM for hA_1, Ki = 412 nM for hA_{2A} and Ki = 13 nM for hA_3).

With regard to the hA_1 AR, Glu172 (EL2) and Asn254 (6.55), represented by blue bars on electrostatic IEFs (Figure 3, panel A on the left), emerge as important residues for electrostatic contribution, together with a slight contribution of Trp247 (6.48) and His251 (6.52). Asn254 (6.55) and Glu172 (EL2) are engaged in a three hydrogen bond pattern with N1 of pyrazole and with the exocyclic amine group at position 7 of compound **1**, as shown in Figure 4, panel A. The aromatic pyrazolopyrimidine scaffold is involved in a π–π stacking interaction with Phe171 (EL2), which is one of the residues appearing to have the strongest hydrophobic interaction on the hydrophobic IEFs (green bars in Figure 3, panel A on the right). Val87 (3.32), Leu88 (3.33), Trp247 (6.48), Leu250 (6.51), Tyr271 (7.36) and Ile274 (7.39) are also involved in significant hydrophobic contacts, with Val87 (3.32), Leu88 (3.33), Trp247 (6.48) defining the bottom of the binding pocket.

The residues involved in binding at hA_{2A} AR are positioned equivalently to those just described for the hA_1 subtype. Glu169 (EL2) and Asn253 (6.55) are involved in hydrogen bonds and Phe168 (EL2) makes a π–π stacking interaction, as can be seen in Figure 4, panel B. Trp246 (6.48) and His250 (6.52), together with Glu169 and Asn253, give stabilizing electrostatic contributions to the binding of **1**, while Leu85 (3.33), Leu167 (EL2), Phe168 (EL2), Trp246 (6.48), Leu249 (6.51), Tyr271 (7.36) are interested by hydrophobic contacts (Figure 3, panel B).

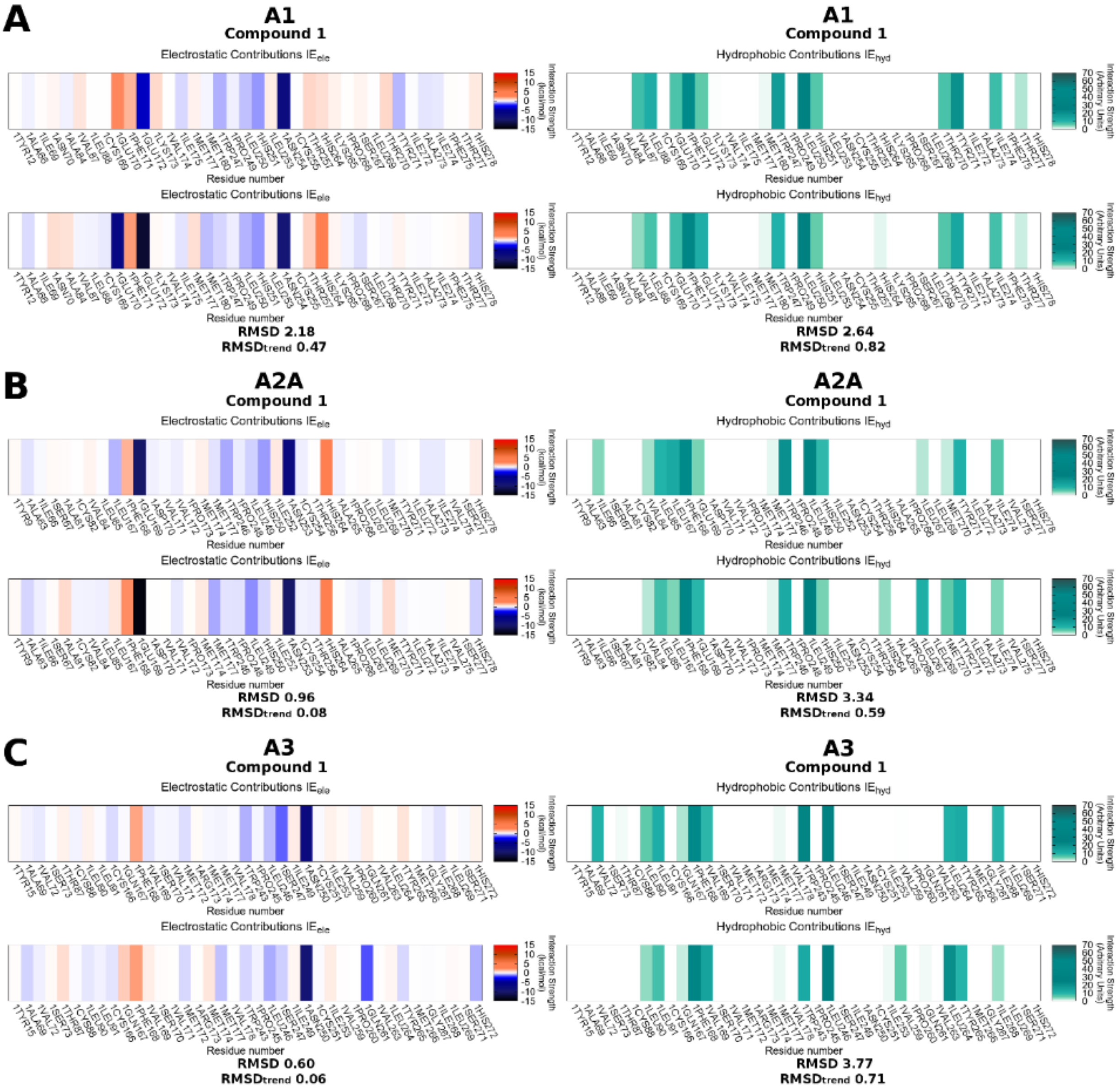

Fig. 3 Interaction Energy Fingerprints (IEFs) comparison between compound **1** and compound ZM-241385 used as reference. Panels A, B and C report the comparison analysis for hA_1, hA_{2A} and hA_3 receptor subtypes, respectively. On the left side is shown the electrostatic contribution comparison, while on the right the hydrophobic one. In each subsection, the IEFs of compound **1** are shown above the IEFs of the reference ZM-241385

The binding of compound **1** to the hA_3 subtype mainly engages Trp243 (6.48), Ser247 (6.52) and Asn250 (6.55) for electrostatic interactions, and Leu91 (3.33), Phe168 (EL2), Val169 (EL2), Trp243 (6.48), Leu246 (6.51), Leu264 (7.35), Tyr265 (7.36), Ile268 (7.39) for hydrophobic interactions, as can be seen in Figure 3, panel C. In this case only Asn250 can be involved in the hydrogen bond network (Figure 4, panel C), since in the A_3 AR the position equivalent to Glu172 of the hA1 and Glu169 of the A_{2A} AR is occupied by Val169, which cannot establish a hydrogen bond with the amino group at position 5 of compound **1**.

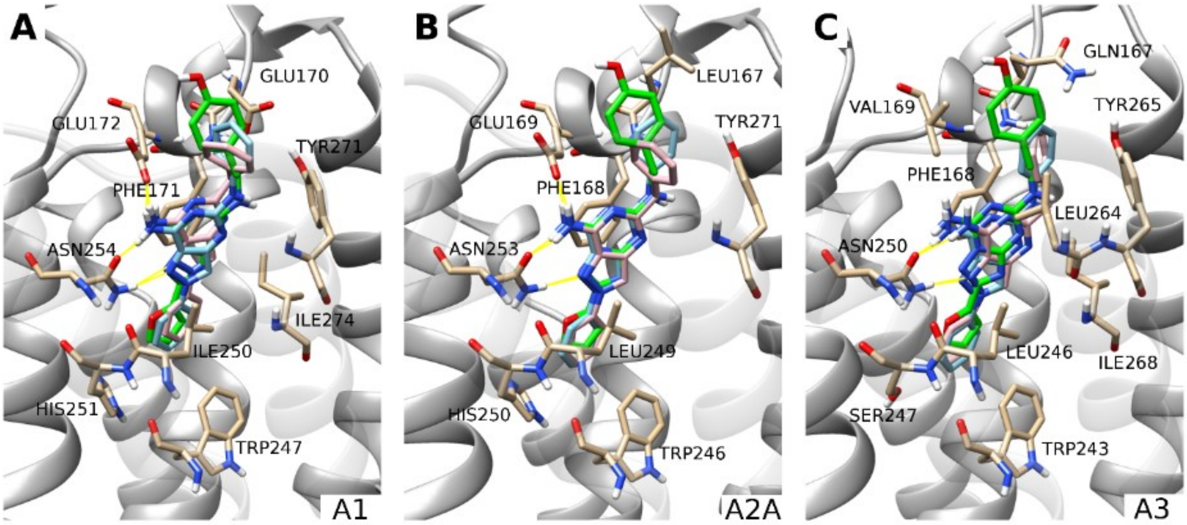

Fig. 4 Comparison of the proposed binding mode of compound **1** (sky blue), compound **A** (pink), and reference pose of ZM-241385 (green) on hA_1, hA_{2A} and hA_3 subtype receptors (panels A, B and C, respectively). Protein residues mainly involved in binding are shown as sticks (tan). The zoom makes TM1 not visible, while TM6 and TM7 are rendered in a transparent manner to give a more clear visualization of the binding site.

Most of the poses resemble the conformation that ZM-241385 assumes in the binding site of the hA_{2A} AR crystal structure and of hA_1 and hA_3 AR models. The benzene ring at position 2 occupies the position of the furan ring of ZM-241385, the 7-amino-pyrazolopyrimidine scaffold is well superimposed on the reference 7-amino-triazolotriazine and the arylalkylamino group at position 5 points in the same direction as the para-hydroxyphenyl-ethylamino fragment. The similarity of the binding modes confirms the expectation provided by the IEFs comparison between **1** and ZM-241385 (Figure 3, panels A, B and C). To quantitatively compare the calculated IEFs profiles, two novel analyses have been proposed called RMSD and $RMSD_{trend}$ analysis (see the Experimental Section for more details). In the case of derivative **1** both RMSD and $RMSD_{trend}$ between electrostatic and hydrophobic IEFs on each hAR subtype are quite low. However, the electrostatic RMSD (2.18 kcal/mol) and the electrostatic $RMSD_{trend}$ (0.47 kcal/mol) for the hA_1 subtype are higher than the values observed for hA_{2A} and hA_3 ARs. This does not seem to fit with the low Ki (67 nM) for the hA_1 receptor;

however, it appears that the major unfavorable contribution is provided by Glu170, which may probably be corrected by a slight rotation of the phenyl group of the compound.

Subsequently, we compared the binding behavior of compound **1** to that of its analog derivative **A** (Ki = 150 nM for hA_1, Ki = 110 nM for hA_{2A} and I% = 39 at 1 mM for hA_3), having a methylene instead of the NH linker at the 5-position. The IEFs comparison did not allow a complete rationalization of the different selectivity profiles of compounds **1** and **A** (Figure SM1). Electrostatic RMSD and $RMSD_{trend}$ values on the hA_3 receptor (1.10 and 0.18 kcal/mol, respectively) are higher than those of compound **1** (0.60 and 0.06 kcal/mol, respectively), in accordance with the lower potency of derivative **A** (I = 39% at 1 mM) compared with 1 (Ki = 13 nM). On the other hand, we have to honestly observe that also compound **A** presents higher RMSD and $RMSD_{trend}$ values (1.49 and 0.18 kcal/mol, respectively) on the hA_{2A} receptor as compared with compound **1** (0.96 and 0.08 kcal/mol, respectively), but in this case the affinity of the former (110 nM) is higher than that of the latter (412 nM). The result of the IEFs comparison is confirmed by the similarity of the binding modes of derivatives **1** and **A** at all receptor binding sites, as reported in Figure 4 (panels A, B and C). In this case docking is not sufficient to rationalize the difference in binding affinities. In fact, the mere examination of the final state of the binding process may not be sufficient to explain differences in the activity or selectivity profiles. The presence of water molecules and the entropic effect are only two among the pool of binding contributions that we are not taking into consideration during our docking simulations.

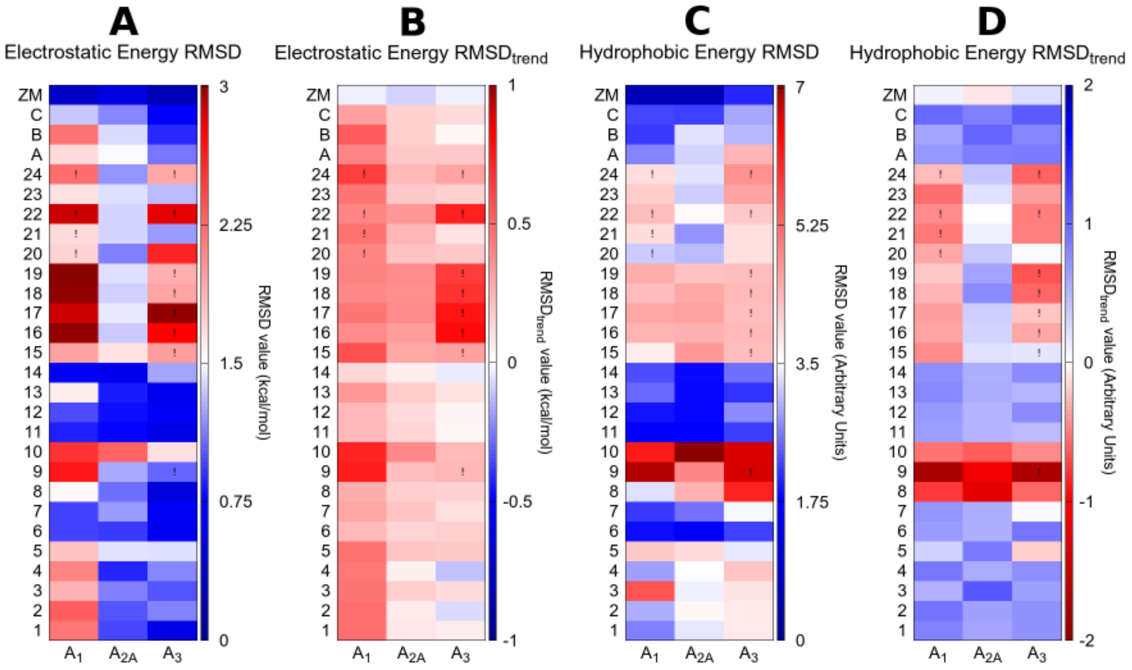

Fig. 5 Results of the IEFs comparison between all compounds and reference compound ZM-241385. RMSDs and $RMSD_{trend}$ between electrostatic (panels A and B, respectively) and hydrophobic (panels C and D, respectively) Energy Fingerprints of each compound (*y*-axis) and reference ZM-241385 are reported for hA_1, hA_{2A} and hA_3 receptors (*x*-axis). A colorimetric scale going from blue to red represents favorable to unfavorable values. An exclamation point identifies those poses that have a positive van der Waals and/or electrostatic potential (and for which was not possible to select an alternative pose with negative values).

Similar considerations can be made observing the results of IEFs comparison for all the dataset compounds on the different AR subtypes (Figure 5). We would have expected to find blue and red rectangles associated with good and bad binders, respectively, but this prevision was not satisfied: a major similarity of the IEFs between the target and the reference compounds are not always related to good binding affinity of the ligand. However, an interesting example is provided by compounds **8**, **9** and **10**, which have no affinity for any of the receptors. Red rectangles cross horizontally almost the whole hydrophobic RMSD and $\text{RMSD}_{\text{trend}}$ table, meaning that there is a considerable loss in the binding hydrophobic contribution in comparison with the reference. As a control experiment, ZM-241385 has been docked into the three AR subtypes, the IEFs have been computed for the selected poses and compared with that of the reference pose of ZM241385: as expected, the electrostatic and hydrophobic RMSD and $\text{RMSD}_{\text{trend}}$ values are close to zero (Figure 5).

The 5-(N4-R-piperazin-1-yl) compounds **15–24** are hA_1 AR selective. These derivatives find a steric hindrance in the hA_3 binding site and the van der Waals values of the selected poses are positive (as indicated by exclamation points in Figure 5). However, from the IEFs comparison analysis (Figure 5), we would have predicted a hA_{2A} versus hA_1 selectivity (blue versus red rectangles). In fact, while at the hA_{2A} binding site the predicted poses of these compounds behave like ZM-241385, at the hA_1 binding site they deviate a little from the reference position, losing some of the canonical interactions (Video SM1-SM2). Interestingly, this diversion results in a gain for compounds **16**, **17**, **18**, **19** and **22**: the protonated amine at position 4 of the piperazine moiety is involved in an ionic interaction with Glu170 (EL2), which is confirmed by a highly negative electrostatic contribution reported on the heat map in the background of Video SM1. The absence of a negatively charged residue at a position equivalent to Glu170 on hA_{2A} (Leu167) and hA_3 (Gln167) receptors may be associated with the hA_1 selectivity of these compounds.

4. Conclusion

The herein reported structural investigation was carried out to identify new antagonists targeting the hA_{2A} AR or both the hA_1/hA_{2A} ARs. Hence, various arylalkylamino- and 4-substituted-piperazin-1-yl- moieties were appended at the 5-position of the pyrazolo[4,3-d]pyrimidine scaffold. The 4-hydroxyphenylethylamino group was the most profitable, since the ZM-241385-based compound **12** showed both good hA_{2A} affinity (Ki = 150 nM) and the highest selectivity among all the ligands reported here. The 5-benzylamino moiety (compound **5**) achieved the best combined hA_{2A} (Ki = 123 nM) and hA_1 affinity (Ki = 25 nM) while the 5-phenethylamino pendant (compound **6**) afforded nanomolar affinity (Ki = 11 nM) and good selectivity for the hA_1 AR. The 5-(N4 -substituted-piperazin-1-yl) derivatives **15–24** were inactive at the hA_{2A} AR while the hA_1 affinities spanned the high nanomolar range. These outcomes provide new insights about the structural requirements of our pyrazolopyrimidine series for hA_{2A}- and hA_1-receptor ligand interaction. Nevertheless, the obtained results do not prompt us to synthesize further derivatives of this series featured by 5-arylalkyamino- and 5-piperazino- moieties.

A structure-based molecular modeling study was conducted to rationalize the experimental binding data from a molecular point of view using molecular docking studies in tandem with Interaction Energy Fingerprints (IEFs) analysis. Moreover, to quantitatively compare IEFs profiles and, consequently, to address the similarity of the binding modes of different compounds in different receptor subtypes, two novel analyses have been proposed, called RMSD and $\text{RMSD}_{\text{trend}}$ analyses. Even if, we are conscious that the simple inspection of the final state of the binding process may not be sufficient to explain differences in the activity or selectivity profiles, these novel tools can facilitate the mode of representation and interpretation of the docking data obtained by analyzing simultaneously several compounds against different receptor subtypes.

5. Experimental section

5.1 Chemistry

The microwave-assisted syntheses were performed using an Initiator EXP Microwave Biotage instrument (frequency of irradiation: 2.45 GHz). Analytical silica gel plates (Merck F254), preparative silica gel plates (Merck F254, 2 mm) and silica gel 60 (Merck, 70–230 mesh) were used for analytical and preparative TLC, and for column chromatography, respectively. All melting points were determined on a Gallenkamp melting point apparatus and are uncorrected. Elemental analyses were performed with a Flash E1112 Thermofinnigan elemental analyzer for C, H, N and the results were within ±0.4% of the theoretical values. All final compounds revealed a purity not less than 95%. The IR spectra were recorded with a Perkin-Elmer Spectrum RX I spectrometer in Nujol mulls and are expressed in cm^{-1} . The ^{1}H NMR spectra were obtained with a Bruker Avance 400 MHz instrument. The chemical shifts are reported in δ (ppm) and are relative to the central peak of the solvent which was CDCl3 or DMSO-d_6. The assignment of exchangeable protons (OH, and NH) was confirmed by addition of D2O. The following abbreviations are used: s = singlet, d = doublet, t = triplet, m = multiplet, br = broad and ar = aromatic protons.

4-Nitro-1-phenyl-1H-pyrazole-3-carbonitrile 26 [26]

The title compound was prepared with a different procedure from that previously described by us [26]. Briefly, phenylboronic acid (2.4 mmol), cupric acetate (1.8 mmol) and activated 4 Å molecular sieves (750 mg) were added to a solution of 4-nitro- 1H-pyrazole-3-carbonitrile [26] (1.2 mmol) in anhydrous dichloromethane (8 mL) and pyridine (2.4 mmol). The mixture was stirred at room temperature, under air, in a loosely capped flask for two days, then it was diluted with chloroform (20–30 mL) and filtered through celite. The solution was extracted with 0.1 M HCl (15 ml for three times), the organic phase was anhydrified (Na_2SO_4) and evaporated at reduced pressure to give a solid which was collected by suction, washed with water and then cyclohexane and recrystallized. Yield 75%; m.p. 143–145°C (cyclohexane/EtOH); ^{1}H NMR (DMSO-d_6) 7.54–7.63 (m, 3H, ar), 7.74–7.76 (m, 2H, ar), 8.71 (s, 1H, H-5).

General procedure for the synthesis of 3-substituted-1-(3-cyano-1- R2–1H-pyrazol-4-yl)thioureas 32–42

The commercially available phenyl-, 4-methoxyphenyl-, 2,4-dichlorophenyl- and benzyl-isothiocyanates or the suitably synthesized phenethyl- [29], 4-methoxyphenethyl- [31], 3,4-dimethoxyphenethyl- [30], phenylpropyl-isothiocyanates [29] (1.97 mmol) were added to a solution of the 1-substituted-4-amino-pyrazole-3-carbonitriles **29–31** [26] (1.64 mmol) in anhydrous DMF (1.5 mL). The mixture was stirred at room temperature for 3–4 h (compounds **32–34**, **38**, **39**), for 16 h (compounds **35**, **40**, **42**) and for 24 h (compounds **36**, **37**, **41**).

The obtained dark slurry was treated with water (20 mL) and, in the case of compounds **33–35** and **39**, a solid precipitated which was collected by filtration. For derivatives **32**, **36–38**, **40–42**, the aqueous mixture was extracted with EtOAc (30 mL X3). The combined organic extracts were anhydrified (Na_2SO_4) and the solvent evaporated at reduced pressure. The obtained solid was treated with Et_2O (5–10 mL) and isolated by filtration. Crude compound **42** was purified by column chromatography (eluent:cyclohexane/ EtOAc/MeOH 6:4:1). Derivatives **32**, **38–40**, as well as **42**, were unstable upon recrystallization, hence they were used as such for the next step.

1-(3-Cyano-1-phenyl-1H-pyrazol-4-yl)-3-phenylthiourea 32

Yield 89%; ^{1}H NMR (DMSO-d_6) 7.19 (t, 1H, ar, J = 7.4 Hz), 7.36 (t, 2H, ar, J = 7.6 Hz), 7.46 (t, 1H, ar, J = 7.4 Hz), 7.51 (d, 2H, ar, J = 7.6 Hz), 7.58 (t, 2H, ar, J = 7.5 Hz), 7.88 (d, 2H, ar, J = 7.7 Hz), 8.97 (s, 1H, pyrazole proton), 9.68 (br s, 1H, NH), 10.04 (br, s, 1H, NH).

1-(3-Cyano-1-phenyl-1H-pyrazol-4-yl)-3-(4-methoxyphenyl)thiourea 33

Yield 95%; m.p. 165–167°C (cyclohexane/EtOAc); ^{1}H NMR (DMSO-d_6) 3.75 (s, 3H, OCH3), 6.95 (d, 2H, ar, J = 8.9 Hz), 7.33 (d, 2H, ar, J = 8.9 Hz), 7.46 (t, 1H, ar, J = 7.6 Hz), 7.58 (t, 2H, ar, J = 7.3 Hz), 7.89 (d, 2H, ar, J = 7.6 Hz), 8.95 (s, 1H, pyrazole proton), 9.56 (br s, 1H, NH), 9.89 (br s, 1H, NH). Anal. Calc. for $C_{18}H_{15}N_5OS$.

1-(3-Cyano-1-phenyl-1H-pyrazol-4-yl)-3-(2,4-dichlorophenyl)thiourea 34

Yield 98%; m.p. 166–169°C (cyclohexane/EtOAc); ^{1}H NMR (DMSO-d_6) 7.44–7.60 (m, 5H, ar), 7.80 (s, 1H, ar), 7.96 (d, 2H, ar, J = 7.9 Hz), 9.02 (s, 1H, pyrazole proton), 9.82 (br s, 1H, NH), 9.98 (br s, 1H, NH). Anal. Calc. for $C_{17}H_{11}Cl_2N_5S$.

1-Benzyl-3-(3-cyano-1-phenyl-1H-pyrazol-4-yl)thiourea 35

Yield 74%; m.p. 180–183°C (EtOH). ^{1}H NMR (DMSO-d$_6$) 4.75 (d, 2H, CH2, J = 4.6 Hz), 7.26–7.34 (m, 5H, ar), 7.45 (t, 1H, ar, J = 7.3 Hz), 7.57 (t, 2H, ar, J = 7.4 Hz), 7.87 (d, 2H, ar, J = 8.1 Hz), 8.49 (br s, 1H, NH), 8.99 (s, 1H, H-5), 9.55 (br s, 1H, NH). Anal. Calc. for $C_{18}H_{15}N_5S$.

1-Phenylethyl-3-(3-cyano-1-phenyl-1H-pyrazol-4-yl)thiourea 36

Yield 55%; m.p. 161–164°C (cyclohexane/EtOAc). ^{1}H NMR (DMSO-d$_6$) 2.88 (t, 2H, CH2, J =7.5 Hz), 3.69–3.70 (m, 2H, CH2), 7.23–7.34 (m, 5H, ar), 7.46 (t, 1H, ar, J = 7.0 Hz), 7.58 (t, 2H, ar, J = 7.7 Hz), 7.89 (d, 2H, ar, J = 7.7 Hz), 8.09 (br s, 1H, NH), 8.91 (s, 1H, pyrazole proton), 9.50 (s, 1H, NH). Anal. Calc. for $C_{19}H_{17}N_5S$.

1-(3-Cyano-1-phenyl-1H-pyrazol-4-yl)-3-phenylpropylthiourea 37

Yield 57%; m.p. 133–136°C (cyclohexane/EtOAc). ^{1}H NMR (DMSOd^6) 1.82–1.90 (m, 2H, CH2), 2.63 (t, 2H, CH2, J = 7.3 Hz), 3.49–3.50 (m, 2H, CH2), 7.17–7.31 (m, 5H, ar), 7.45 (t, 1H, ar, J = 7.4 Hz), 7.57 (t, 2H, ar, J = 7.8 Hz), 7.88 (d, 2H, ar, J = 7.9 Hz), 8.09 (br s, 1H, NH), 8.95 (s, 1H, pyrazole proton), 9.42 (s, 1H, NH). Anal. Calc. for $C_{20}H_{19}N_5S$.

1-(3-Cyano-1-methyl-1H-pyrazol-4-yl)-3-phenylthiourea 38

Yield 45%; ^{1}H NMR (DMSO-d$_6$) 3.92 (s, 3H, CH3), 7.17 (t, 1H, ar, J = 7.3 Hz), 7.36 (t, 2H, ar, J = 7.8 Hz), 7.48 (d, 2H, ar, J = 7.7 Hz), 7.95 (s, 1H, pyrazole proton), 8.39 (br s, 1H, NH), 12.11 (br s, 1H, NH).

1-Benzyl-3-(3-cyano-1-methyl-1H-pyrazol-4-yl)thiourea 39

Yield 56%; ^{1}H NMR (DMSO-d$_6$) 3.95 (s, 3H, CH3), 5.84 (br s, 2H, CH2), 7.19–7.39 (m, 5H, ar), 7.70 (s, 1H, pyrazole proton), 8.39 (br s, 1H, NH), 9.47 (br s, 1H, NH).

1-Benzyl-3-(1-benzyl-3-cyano-1H-pyrazol-4-yl)thiourea 40

Yield 50%; ^{1}H NMR (DMSO-d$_6$) 4.71 (d, 2H, CH2, J = 4.5 Hz), 5.40 (s, 2H, CH2), 7.26–7.40 (m, 10H, ar), 8.44 (br s, 1H, NH); 8.51 (s, 1H, pyrazole proton), 9.47 (s, 1H, NH).

1-(3-Cyano-1-phenyl-1H-pyrazol-4-yl)-3-(4-methoxyphenylethyl)thiourea 41

Yield 62%; m.p. 260–262°C (cyclohexane/EtOAc). ^{1}H NMR (DMSO-d$_6$) 2.81 (t, 2H, CH2, J = 7.2 Hz), 3.65–3.67 (m, 2H, CH2), 3.72 (s, 3H, CH3), 6.88 (d, 2H, ar, J = 8.9 Hz), 7.17 (d, 2H, ar, J = 8.9 Hz), 7.46 (t, 1H, ar, J = 7.0 Hz), 7.58 (t, 2H, ar, J = 7.7 Hz), 7.87 (d, 2H, ar, J = 7.7 Hz), 8.05 (br s, 1H, NH), 8.91 (s, 1H, pyrazole proton), 9.48 (s, 1H, NH). Anal. Calc. for $C_{20}H_{19}N_5OS$.

1-(3-Cyano-1-phenyl-1H-pyrazol-4-yl)-3-[2-(3,4-dimethoxyphenyl)ethyl]thiourea 42

Yield 55%; ^{1}H NMR (DMSO-d$_6$) 2.81 (t, 2H, CH2, J = 7.2 Hz), 3.69–3.72 (m, 5H, OCH3 + CH2), 3.75 (s, 3H, OCH3), 6.76 (d, 1H, ar, J = 8.1 Hz), 6.84 (s, 1H, ar), 6.89 (d, 1H, ar, J = 8.2 Hz), 7.46 (t, 1H, ar, J = 7.2 Hz), 7.58 (t, 2H, ar, J = 7.1 Hz), 7.86 (d, 2H, ar, J = 8.0 Hz), 8.04 (br s, 1H, NH), 8.91 (s, 1H, pyrazole proton), 9.48 (br s, 1H, NH). Anal. Calc. for $C_{21}H_{21}N_5O_2S$.

General procedure for the synthesis of S-methylisothiourea derivatives 43–53

A mixture of the suitable thiourea derivatives **32–42** (0.92 mmol) and iodomethane (3.69 mmol) in 0.1 N NaOH solution (11.8 mL) was stirred at room temperature until the disappearance of the starting material (12–24 h). Then, glacial acetic acid was added until pH 6. The solid which precipitated was collected by filtration and dried, except compounds **46** and **51** which were isolated from the reaction mixture by extraction with EtOAc (30 mL X3). Evaporation of the anhydrified (Na_2SO_4) organic phase gave a solid which was collected by filtration. These S-methylisothiourea derivatives were unstable upon recrystallization, thus they were used for the next step without further purification. It was observed that derivatives **43–45** and **51** exist in two tautomeric forms in DMSO solution. In fact, in their ^{1}H NMR spectra there are two signals assignable to the SCH3 and to the pyrazole proton. Compounds **44** and **51** also display, two signals assignable to the OCH3 and SCH3 substituents, respectively (see below for details).

N-(3-Cyano-1-phenylpyrazolo-4-yl)-N' -phenyl-S-methylisothiourea 43

Yield 86%; ^{1}H NMR (DMSO-d$_6$) mixture of two tautomers (ratio about 1:2.7) 2.35 (s, SCH3), 2.38 (s, SCH3), 7.30–7.31 (m, ar), 7.42–7.60 (m, ar +2 NH), 7.98 (d, ar, J = 8.0 Hz), 8.89 (s, pyrazole proton), 8.93 (s, pyrazole proton).

N-(3-Cyano-1-phenylpyrazolo-4-yl)-N'-4-methoxyphenyl-S-methylisothiourea 44

Yield 98%; ^{1}H NMR (DMSO-d$_6$) mixture of two tautomers (ratio about 1:3.2) 2.41 (s, SCH3), 2.43 (s, SCH3), 3.86 (s, OCH3), 3.88 (s, OCH3), 7.41–7.72 (m, ar), 7.96–8.01 (m, ar), 8.93 (s, pyrazole proton), 9.01 (br s, pyrazole proton + NH).

N'-2,4-Dichlorophenyl-N-(3-cyano-1-phenylpyrazolo-4-yl)-S-methylisothiourea 45

Yield 95%; ^{1}H NMR (DMSO-d$_6$) mixture of two tautomers (ratio about 1:3.6) 2.36 (s, SCH3), 2.42 (s, SCH3), 7.09–7.70 (m, ar), 8.00–8.16 (m, ar + NH), 9.00 (s, pyrazole proton), 9.18 (s, pyrazole proton).

N′ -Benzyl-N-(3-cyano-1-phenylpyrazolo-4-yl)-S-methylisothiourea 46

Yield 98%; ^{1}H NMR (DMSO-d$_6$) 2.48 (s, 3H, SCH3), 5.47 (br s, 2H, CH2) 7.24–7.34 (m, 5H, ar), 7.44 (t, 1H, ar, J = 7.3 Hz), 7.57 (t, 2H, ar, J = 7.6 Hz), 7.97 (d, 2H, ar, J = 8.0 Hz), 8.13 (br s, 1H, NH), 8.80 (s, 1H, pyrazole proton).

N-(3-Cyano-1-phenylpyrazolo-4-yl)-N′ -phenylethyl-S-methylisothiourea 47

Yield 86%; ^{1}H NMR (DMSO-d$_6$) 2.56 (s, 3H, CH3), 3.04 (t, 2H, CH2, J = 7.1 Hz), 4.33 (t, 2H, CH2, J = 7.1 Hz), 7.25–7.41 (m, 5H, ar), 7.43 (t, 1H, ar, J = 9.2 Hz), 7.57 (t, 2H, ar, J = 9.2 Hz), 7.98 (d, 2H, ar, J = 9.2 Hz), 8.14 (s, 1H, NH), 8.86 (s, 1H, pyrazole proton).

N-(3-Cyano-1-phenylpyrazolo-4-yl)-N′ -phenylpropyl-S-methylisothiourea 48

Yield 86%; ^{1}H NMR (DMSO-d$_6$) 2.03–2.05 (m, 2H, CH2), 2.51 (s, 3H, CH3), 2.71 (t, 2H, CH2, J = 7.4 Hz), 4.16 (t, 2H, CH2, J = 7.4 Hz), 7.21 (t, 1H, ar, J = 9.0 Hz), 7.27–7.32 (m, 4H, ar), 7.42 (t, 1H, ar, J = 9.0 Hz), 7.56 (t, 2H, ar, J = 9.0 Hz), 7.96 (d, 2H, ar, J = 9.0 Hz), 8.03 (s, 1H, NH), 8.83 (s, 1H, pyrazole proton).

N-(3-Cyano-1-methylpyrazolo-4yl)-N′ -phenyl-S-methylisothiourea 49

Yield 87%; ^{1}H NMR (DMSO-d$_6$) 2.23 (s, 3H, SCH3), 3.39 (s, 3H, CH3), 7.33–7.35 (m, 2H, ar), 7.52–7.60 (m, 3H, ar), 8.07 (s, 1H, pyrazole proton).

N′ -Benzyl-N-(3-cyano-1-methylpyrazolo-4-yl)-S-methylisothiourea 50

Yield 84%; ^{1}H NMR (DMSO-d$_6$) 2.43 (s, 3H, SCH3), 3.99 (s, 3H, CH3), 5.42 (br s, 2H, CH2), 7.20–7.30 (m, 5H, ar), 7.75 (s, 1H, NH), 8.05 (s, 1H, pyrazole proton).

N′ -Benzyl-N-(3-cyano-1-benzylpyrazolo-4-yl)-S-methylisothiourea 51

Yield 81%; ^{1}H NMR (DMSO-d$_6$) mixture of two tautomers (ratio about 1:6) 2.40 (s, SCH3) 2.43 (s, SCH3), 5.41 (br s, CH2), 5.48 (s, CH2), 7.14–7.39 (m, ar), 7.81 (br s, NH), 8.25 (s, pyrazole proton), 8.17 (s, pyrazole proton).

N′ -4-Methoxyphenylethyl-N-(3-cyano-1-phenylpyrazolo-4-yl)-Smethylisothiourea 52

Yield 86%; ^{1}H NMR (DMSO-d$_6$) 2.56 (s, 3H, SCH3), 2.97 (t, 2H, CH2, J = 7.3 Hz), 3.75 (s, 3H, OCH3), 4.29 (t, 2H, CH2, J = 7.3 Hz), 6.91 (d, 2H, ar, J = 9.5 Hz), 7.24 (d, 2H, ar, J = 9.5 Hz), 7.43 (t, 1H, ar, J = 9.5 Hz), 7.57 (t, 2H, ar, J = 9.3 Hz), 7.98 (d, 2H, ar, J = 9.3 Hz), 8.11 (s, 1H, NH), 8.85 (s, 1H, pyrazole proton).

N′ -3,4-Dimethoxyphenylethyl-N-(3-cyano-1-phenylpyrazolo-4-yl)-Smethylisothiourea 53

Yield 73%; ^{1}H NMR (DMSO-d$_6$) 2.58 (s, 3H, SCH3), 2.98 (t, 2H, CH2, J = 8.5 Hz), 3.73 (s, 3H, OCH3), 3.76 (s, 3H, OCH3), 4.34 (t, 2H, CH2, J = 7.2 Hz), 6.83–6.93 (m, 4H, 3 ar + NH), 7.45 (t, 1H, ar, J = 7.3 Hz), 7.59 (t, 2H, ar, J = 7.8 Hz), 7.99 (d, 2H, ar, J = 8.3 Hz), 8.95 (s, 1H, pyrazole proton).

General procedure for the synthesis of 5-aryl(alkyl)amino-7-amino- 2H-pyrazolo[4,3-d]pyrimidine derivatives 1–3, 5–12

A mixture of the suitable S-methylisothioureas **43–53** (1 mmol) and NH_4Cl (20 mmol) in formamide (2 mL) was microwave irradiated at 110°C for 20 min (compounds **9**, **10**), at 130°C for 40 min (compound **12**) and for 2 h (compounds **2**, **3**), at 150°C for 15 min (compounds **1**, **5**, **8**) and for 20 min (compounds **6**, **7**, **11**). The suspension was then treated with $NaHCO_3$ saturated solution until pH 7 and the obtained solid was collected by filtration to give compounds **1–3**. To isolate derivatives **5–12**, the mixture was extracted with CHCl3 (15 mL X3), the organic phase was washed with water (15 mL X2) and anhydrified (Na_2SO_4). Evaporation of the solvent at reduced pressure afforded a residue which was taken up with diethyl ether (2–3 mL) and collected by filtration. The crude derivatives were purified by recrystallization, except compounds **1**, **6**, **7**, **10**, **11** which were first purified by column chromatography or preparative TLC (see below for details).

7-Amino-5-phenylamino-2-phenyl-2H-pyrazolo[4,3-d]pyrimidine 1

Purified by column chromatography (Et_2O/cyclohexane/EtOAc 3:1:1). Yield 66%; m.p. 252–254°C (EtOH). ^1H NMR (DMSO-d_6) 6.86 (t, 1H, ar, J = 7.3 Hz), 7.23 (t, 2H, ar, J = 7.6 Hz), 7.41–7.45 (m, 3H, 1 ar + NH2), 7.58 (t, 2H, ar, J = 7.6 Hz), 7.90 (d, 2H, ar, J = 8.5 Hz), 8.03 (d, 2H, ar, J = 8.5 Hz), 8.74 (s, 1H, H-3), 8.76 (br s, 1H, NH). Anal. Calc. for $C_{17}H_{14}N_6$.

7-Amino-5-(4-methoxyphenyl)amino-2-phenyl-2H-pyrazolo[4,3- d]pyrimidine 2

Yield 62%; m.p. 253–255°C (cyclohexane/EtOAc); ^1H NMR (DMSO-d_6) 3.82 (s, 3H, OCH3), 6.84 (d¸ 2H, ar, J = 8.9 Hz), 7.45–7.40 (m, 3H, 1 ar + NH2), 7.58 (t, 2H, ar, J = 7.7 Hz), 7.75 (d, 2H, J = 8.9 Hz), 8.02 (d, 2H, ar, J = 8.2 Hz), 8.57 (s, 1H, NH), 8.68 (s, 1H, H-3). Anal. Calc. for $C_{18}H_{16}N_6O$.

7-Amino-5–(2,4-dichlorophenyl)amino-2-phenyl-2H-pyrazolo[4,3- d]pyrimidine 3

Yield 58%; m.p. 251–252°C (cyclohexane/EtOAc); ^1H NMR (DMSO-d_6) 7.40–7.48 (m, 3H, 2 ar + NH), 7.54 (s, 1H, ar), 7.53–7.61 (m, 2H, ar), 7.61–7.79 (br s, 2H, NH2), 8.02 (d, 2H, J = 7.9 Hz), 8.67 (d, 1H, J = 8.9 Hz), 8.82 (s, 1H, H-3). Anal. Calc. for $C_{17}H_{12}Cl_2N_6$.

7-Amino-5-benzylamino-2-phenyl-2H-pyrazolo[4,3-d]pyrimidine 5

Purified by preparative TLC (Et_2O/cyclohexane/EtOAc 3:1:1). Yield 60%; m.p. 143–145°C (cyclohexane/EtOAc). ^1H NMR (DMSO-d_6) 4.49 (d, 2H, CH2, J = 6.3 Hz), 6.71 (t, 1H, NH, J = 6.3 Hz), 7.18 (t, 1H, ar, J = 7.1 Hz), 7.26–7.34 (m, 6H, 4 ar + NH2), 7.39 (t, 1H, ar, J = 7.4 Hz), 7.55 (t, 2H, ar, J = 7.5 Hz), 7.95 (d, 2H, ar, J = 7.6 Hz), 8.48 (s, 1H, H-3). Anal. Calc. for $C_{18}H_{16}N_6$.

7-Amino-5-(2-phenylethyl)amino-2-phenyl-2H-pyrazolo[4,3-d]pyrimidine 6

Purified by column chromatography (cyclohexane/ EtOAc/MeOH 6:4:1). Yield 65%; m.p. 168–171°C (cyclohexane/ EtOAc). ^{1}H NMR (DMSO-d_6) 2.86 (t, 2H, CH2, J = 7.1 Hz), 3.45–3.50 (m, 2H, CH2), 6.12 (br s, 1H, NH), 7.18–7.32 (m, 7H, 5 ar + NH2), 7.39 (t, 1H, ar, J = 7.5 Hz), 7.56 (t, 2H, ar, J = 7.5 Hz), 7.98 (d, 2H, ar, J = 7.7 Hz), 8.52 (s, 1H, H-3). Anal. Calc. for $C_{19}H_{18}N_6$.

7-Amino-5-(3-phenylpropyl)-2-phenyl-2H-pyrazolo[4,3-d]pyrimidines 7

Purified by column chromatography (eluent cyclohexane/ EtOAc/MeOH 6:4:1). Yield 58%; m.p. 159–162°C (EtOAc). ^{1}H NMR (DMSO-d_6) 1.83–1.86 (m, 2H, CH2), 2.64 (t, 2H, CH2, J = 7.4 Hz), 3.27 (m, 2H, CH2), 6.20 (br s, 1H, NH), 7.19–7.30 (m, 7H, 5 ar + NH2), 7.40 (t, 1H, ar, J = 9.0 Hz), 7.56 (t, 2H, ar, J = 7.6 Hz), 7.97 (d, 2H, ar, J = 7.9 Hz), 8.50 (s, 1H, H-3). Anal. Calc. for $C_{20}H_{20}N_6$.

7-Amino-2-methyl-5-phenylamino-2H-pyrazolo[4,3-d]pyrimidine 8

Yield 42%; m.p. 252–254°C (EtOH). ^{1}H NMR (DMSO-d_6) 4.05 (s, 3H, Me), 6.84 (t, 1H, ar, J = 7.2 Hz), 7.19–7.21 (m, 4H, 2 ar + NH2), 7.75 (d, 2H, ar, J = 7.2 Hz), 7.87 (s, 1H, H-3), 8.62 (br s, 1H, NH). Anal. Calc. for $C_{12}H_{12}N_6$.

7-Amino-5-benzylamino-2-methyl-2H-pyrazolo[4,3-d]pyrimidine 9

Yield 80%; m.p. 213–214°C (EtOH); ^{1}H NMR (DMSO-d_6) 3.98 (s, 3H, CH3), 4.45 (d, 2H, CH2, J = 6.4 Hz), 6.47 (br s, 1H, NH), 7.05 (br s, 2H, NH2), 7.16–7.32 (m, 5H, ar), 7.70 (s, 1H, H-3). IR: 3326, 3179, 1658. Anal. Calc. For $C_{13}H_{14}N_6$.

7-Amino-2-benzyl-5-benzylamino-2H-pyrazolo[4,3-d]pyrimidine 10

Yield 40%; m.p. 174–175°C (cyclohexane/EtOAc). ^{1}H NMR (DMSOd$_6$) 4.45 (d, 2H, CH2, J = 6.3 Hz), 5.45 (s, 2H, CH2), 6.58 (br s, 1H, NH), 7.11 (br s, 2H, NH2), 7.15–7.36 (m, 10H, ar), 7.87 (s, 1H, H-3). Anal. Calc. for $C_{19}H_{18}N_6$.

7-Amino-5-[2–(4-methoxyphenyl)ethyl]amino-2-phenyl-2H-pyrazolo[4,3-d]pyrimidine 11

Purified by column chromatography (cyclohexane/EtOAc/MeOH 6:4:1), Yield 58%; m.p. 142–145°C (cyclohexane/EtOAc). ^{1}H NMR (DMSO-d_6) 2.73 (t, 2H, CH2, J = 7.3 Hz), 3.38–3.41 (m, 2H, CH2), 3.73 (s, 3H, OCH3), 6.03 (br s, 1H, NH), 6.69 (d, 2H, ar, J = 8.9 Hz), 7.04 (d, 2H, ar, J = 8.9 Hz), 7.22 (br s, 2H, NH2), 7.41 (t, 1H, ar, J = 7.3 Hz), 7.57 (t, 2H, ar, J = 7.6 Hz), 7.98 (d, 2H, ar, J = 7.9 Hz), 8.51 (s, 1H, H-3). Anal. Calc. for $C_{20}H_{20}N_6O$.

7-Amino-5-[2-(3,4-dimethoxyphenyl)ethyl]amino-2-phenyl-2H-pyrazolo[4,3-d]pyrimidine 12

Purified by preparative TLC (cyclohexane/ EtOAc/MeOH 6:4:1). Yield 45%; m.p. 100–102°C (H2O/MeOH). ^{1}H NMR (DMSO-d_6) 2.79 (t, 2H, CH2, J = 7.2 Hz), 3.43–3.48 (m, 2H, CH2), 3.72 (s, 3H, OCH3), 3.74 (s, 3H, OCH3), 6.10 (br s, 1H, NH), 6.75 (d, 1H, ar, J = 6.5 Hz), 6.84–6.87 (m, 2H, ar), 7.27 (br s, 2H, NH2), 7.39 (t, 1H, ar, J = 7.2 Hz), 7.56 (t, 2H, ar, J = 7.7 Hz), 7.97 (d, 2H, ar, J = 7.8 Hz), 8.51 (s, 1H, H-3). Anal. Calc. for $C_{21}H_{22}N_6O_2$.

General procedure for the synthesis of the pyrazolo[4,3-d]pyrimidine-7-amine derivatives 4, 13 and 14

To a suspension of the methoxy-substituted pyrazolopyrimidine derivatives **2**, **11** and **12** (1.02 mmol) in anhydrous CH_2Cl_2 (20 mL), a 1 M BBr_3 solution (2.60 mL for **2**, **11** and 5.2 mL for **12**) in CH_2Cl_2 was added at 0°C, under nitrogen atmosphere. The mixture was stirred at room temperature for 20–24 h (compounds **4**, **13**) or 16 h (compound **14**), then was diluted with water (10 mL) and neutralized with $NaHCO_3$ saturated solution. The organic solvent was removed under reduced pressure and the obtained precipitate was collected by filtration and recrystallized. The crude derivative **4** was first purified by column chromatography (eluent $CHCl_3$/ MeOH 9:1) and then recrystallized.

7-Amino-5-(4-hydroxyphenyl)amino-2-phenyl-2H-pyrazolo[4,3- d]pyrimidine 4

Yield 67%; m.p. 223–225°C (EtOAc/cyclohexane); ^1H NMR (DMSO-d_6) 6.65 (d, 2H, ar, J = 8.8 Hz), 7.30–7.45 (m, 3H, 2 ar + NH2), 7.57 (t, 2H, ar, J = 7.6 Hz), 7.63 (d, 2H, ar, J = 8.8 Hz), 8.01 (d, 2H, ar, J = 8.3 Hz), 8.41 (s, 1H, NH), 8.65 (s, 1H, H-3), 8.85 (s, 1H, OH). Anal. Calc. for $C_{17}H_{14}N_6O$.

7-Amino-5-(4-hydroxyphenethyl)amino-2-phenyl-2H-pyrazolo[4,3- d]pyrimidine 13

Yield 89%; m.p. 241–244°C (EtOAc/EtOH). ^1H NMR (DMSO-d_6) 2.73 (t, 2H, CH2, J = 7.3 Hz), 3.38–3.40 (m, 2H, CH2), 6.03 (br s, 1H, NH), 6.68 (d, 2H, ar, J = 8.3 Hz), 7.04 (d, 2H, ar, J = 8.3 Hz), 7.22 (br s, 2H, NH2), 7.41 (t, 1H, ar, J = 7.4 Hz), 7.56 (t, 2H, ar, J = 7.7 Hz), 7.97 (d, 2H, ar, J = 7.8 Hz), 8.51 (s, 1H, H-3), 9.14 (s, 1H, OH). Anal. Calc. for $C_{19}H_{18}N_6O$.

7-Amino-5-(3,4-dihydroxyphenethyl)amino-2-phenyl-2H-pyrazolo[4,3-d]pyrimidine 14

Yield 50%; m.p. 242–243°C (EtOH). ^1H NMR (DMSO-d_6) 2.65 (t, 2H, CH2, J = 7.1 Hz), 3.37–3.41 (m, 2H, CH2), 6.03 (t, 1H, NH, J = 5.8 Hz), 6.59–6.47 (d, 1H, ar, J = 8.0 Hz), 6.63–6.66 (m, 2H, ar), 7.23 (br s, 2H, NH2), 7.40 (t, 1H, ar, J = 7.4 Hz), 7.56 (t, 2H, ar, J = 7.6 Hz), 7.97 (d, 2H, ar, J = 7.7 Hz), 8.51 (s, 1H, H-3), 8.62 (br s, 1H, OH), 8.74 (br s, 1H, OH). Anal. Calc. for $C_{19}H_{18}N_6O_2$.

Synthesis of 5,7-dichloro-2-phenyl-2H-pyrazolo[4,3-d]pyrimidine 55

A suspension of the pyrazolopyrimidine-5,7-dione derivative **54** [20] (2 mmol) and N,N-dimethylaniline (3.95 mmol) in phosphorus oxychloride (5 mL) was microwave irradiated at 150°C for 20 min. The excess of phosphorus oxychloride was distilled off under reduced pressure and the residue was treated with water (about 5-10 mL). The crude product was collected by filtration and recrystallized. Yield 96%; m.p. 252–254°C (EtOH). ^1H NMR (DMSO-d_6) 7.62 (t, 1H, ar, J = 9.1 Hz), 7.69 (t, 2H, ar, J = 9.3 Hz), 8.17 (d, 2H, ar, J = 9.1 Hz), 9.69 (s, 1H, H-3). Anal. Calc. for $C_{11}H_6N_4Cl_2$.

Synthesis of 7-amino-5-chloro-2-phenyl-2H-pyrazolo[4,3-d]pyrimidine 56

A suspension of the suitable 5,7-dichloropyrazolopyrimidine derivative **55** (1.72 mmol) in aqueous 33% ammonia solution (10 mL) was microwave irradiated at 100°C for 30 min. The suspension was cooled at room temperature and the solid was collected by filtration and recrystallized. Yield 90%; m.p. 260–261°C (2-ethoxyethanol). ^{1}H NMR (DMSO-d_6) 7.50 (t, 1H, ar, J = 8.0 Hz), 7.62 (t, 2H, ar, J = 8.0 Hz), 8.05 (d, 2H, ar, J = 8.0 Hz), 8.35 (br s, 1H, NH2), 8.38 (br s, 1H, NH2), 9.05 (s, 1H, H-3). Anal. Calc. for $C_{11}H_8ClN_5$.

General procedure for the synthesis of 5-(4-R-piperazin-1-yl)-substituted pyrazolo[4,3-d]pyrimidines 15–21

A mixture of the 5-chloro-pyrazolopyrimidine derivative **56** (0.41 mmol), the suitable N-substituted piperazine **57–63** (0.82 mmol) and ethyldiisopropylamine (0.49 mmol) in N-methylpyrrolidone (2 mL) was heated by microwave irradiation in the conditions described below for each compound. The obtained slurry was poured dropwise into water (50 mL) under vigorous stirring. The solid which precipitated was collected by filtration, purified by chromatography (column or preparative TLC, as reported below for each derivative) and then recrystallized, except derivative **16** which was directly recrystallized. The not commercially available 1-substituted piperazines were prepared as reported below (**60**) or as previously described (**59**, **61**) [35,36].

7-Amino-2-phenyl-5-(4-phenylpiperazin-1-yl)-2H-pyrazolo[4,3-d]pyrimidine 15

The reaction mixture was microwave irradiated at 150°C for 15 min. Column chromatography, eluent: acetonitrile. Yield 48%; m.p. 183–185°C (cyclohexane/EtOAc). ^{1}H NMR (DMSO-d_6) 3.18–3.20 (m, 4H, piperazine protons), 3.80–3.85 (m, 4H, piperazine protons), 6.80 (t, 1H, ar, J = 7.1 Hz), 7.00 (d, 2H, ar, J = 7.3 Hz), 7.24 (t, 2H, ar, J = 7.3 Hz), 7.40–7.46 (m, 3H, 1 ar, +NH2), 7.57 (t, 2H, ar, J = 7.5 Hz), 8.00 (d, 2H, ar, J = 8.4 Hz), 8.59 (s, 1H, H-3). Anal. Calc. for $C_{21}H_{21}N_7$.

7-Amino-5-(4-benzylpiperazin-1-yl)-2-phenyl-2H-pyrazolo[4,3-d]pyrimidine 16

The reaction mixture was microwave irradiated at 130°C for 25 min. Yield 74%; m.p. 201–202°C (diisopropyl ether/ MeOH). ^{1}H NMR (DMSO-d_6) 2.39–2.42 (m, 4H, piperazine protons), 3.50 (s, 2H, CH2), 3.67–3.71 (m, 4H, piperazine protons), 7.24–7.29 (m, 1H, ar), 7.33–7.35 (m, 4H, ar), 7.39–7.42 (m, 3H, 1 ar + NH2), 7.56 (t, 2H, ar, J = 7.6 Hz), 7.97 (d, 2H, ar, J = 7.7 Hz), 8.55 (s, 1H, H- 3). Anal. Calc. for $C_{22}H_{23}N_7$.

7-Amino-5-(4-phenylethylpiperazin-1-yl)-2-phenyl-2H-pyrazolo[4,3- d]pyrimidine 17

The reaction mixture was microwave irradiated at 150°C for 1 h. Column chromatography: eluent EtOAc/CH_2Cl_2/ MeOH, 8:3:1. Yield 65%; m.p. 198–200°C (cyclohexane/EtOAc). ^{1}H NMR (DMSO-d_6) 2.63–2.70 (m, 6H, 4 piperazine protons + CH2), 2.87–2.91 (m, 2H, CH2), 3.88–3.90 (m, 4H, piperazine protons), 5.53 (br s, 2H, NH2), 7.23–7.34 (m, 5H, ar), 7.41 (t, 1H, ar, J = 7.4 Hz), 7.53 (t, 2H, ar, J = 8.2 Hz), 7.81 (d, 2H, ar, J = 7.6 Hz), 8.08 (s, 1H, H- 3). Anal. Calc. for $C_{23}H_{25}N_7$.

7-Amino-5-(4-(2,4,6-trifluoro)benzylpiperazin-1-yl)-2-phenyl-2H-pyrazolo[4,3-d]pyrimidine 18

The reaction mixture was microwave irradiated at 150°C for 1 h and 45 min. Column chromatography: eluent cyclohexane/EtOAc 7:3. Yield 85%; m.p. 233–235°C (cyclohexane/EtOAc). ^{1}H NMR (DMSO-d_6) 2.43 (br s, 4H, piperazine protons), 3.57 (s, 2H, CH2), 3.67 (br s, 4H, piperazine protons), 7.20 (t, 1H, ar, J = 8.3 Hz), 7.41 (t, 2H, ar, J = 7.2 Hz), 7.50 (br s, 2H, NH2), 7.56 (t, 2H, ar, J = 7.7 Hz), 7.97 (d, 2H, ar, J = 8.0 Hz), 8.55 (s, 1H, H- 3). Anal. Calc. for $C_{22}H_{20}N_7F_3$.

7-Amino-5-(4-(2-chloro-4-fluoro)benzylpiperazin-1-yl)-2-phenyl-2Hpyrazolo[4,3-d]pyrimidine 19

The reaction mixture was microwave irradiated at 150°C for 1 h and 15 min. Column chromatography: eluent cyclohexane/EtOAc 7:3. Yield 53%; m.p. 203–205°C. ^{1} H NMR (DMSO-d_6) 2.47 (br s, 4H, piperazine protons), 3.57 (s, 2H, CH2), 3.70 (br s, 4H, piperazine protons), 7.24 (t, 1H, ar, J = 6.2 Hz), 7.41–7.60 (m, 7H, ar + NH2), 7.98 (d, 2H, ar, J = 7.8 Hz), 8.56 (s, 1H, H-3). Anal. Calc. for $C_{22}H_{21}N_7ClF$.

7-Amino-2-phenyl-5-[(4-(2-furoyl)piperazin-1-yl]-2H-pyrazolo[4,3- d]pyrimidine 20

The reaction mixture was microwave irradiated at 150°C for 1 h. Preparative TLC: eluent cyclohexane/EtOAc/ MeOH 3:6:1. Yield 84%; m.p. 263–264°C (EtOH). ^{1}H NMR (DMSOd$_6$) 3.74–3.79 (m, 8H, CH2), 6.65–6.66 (m, 1H, furan proton), 7.03–7.04 (m, 1H, furan proton), 7.42 (t, 1H, ar, J = 7.4 Hz), 7.51 (br s, 2H, NH2), 7.57 (t, 2H, ar, J = 7.8 Hz), 7.87 (m, 1H, furan proton), 7.99 (d, 2H, ar, J = 7.6 Hz), 8.60 (s, 1H, H-3). Anal. Calc. for $C_{20}H_{19}N_7O_2$.

Tert-butyl 4-(7-amino-2-phenyl-2H-pyrazolo[4,3-d]pyrimidin-5-yl)piperazine 1-carboxylate 21

The reaction mixture was microwave irradiated at 150°C for 1 h and 30 min. Column chromatography: eluent cyclohexane/EtOAc 6:4. Yield 76%; m.p. 169–171°C. ^{1} H NMR (DMSO-d_6) 1.43 (s, 9H, t-But), 3.34–3.38 (m, 4H, piperazine protons), 3.63–3.68 (m, 4H, piperazine protons), 7.42 (t, 1H, ar, J = 7.3 Hz), 7.50 (br s, 2H, NH2), 7.57 (t, 2H, ar, J = 7.8 Hz), 7.99 (d, 2H, ar, J = 8.2 Hz), 8.59 (s, 1H, H-3). Anal. Calc. for $C_{20}H_{25}N_7O_2$.

Synthesis of 2-phenyl-5-(4-(methyl-2-furyl)piperazin-1-yl)-2H-pyrazolo[4,3-d]pyrimidin-7-amine 22

A solution of the 5-(4-(2-furoyl)piperazin-1-yl) derivative 20 (1 mmol) in anhydrous THF (5 mL) was added to a suspension of LiAlH4 (3 mmol) in anhydrous THF (20 mL) at 0°C. The suspension was stirred for 16 h at room temperature, then treated with water (10 mL) and the solid which precipitated was filtered off. The clear solution was diluted with water (about 30 mL) and extracted with EtOAc (3 X 20 mL). The organic phase was anhydrified and the solvent removed at reduced pressure to give a solid which was purified by preparative TLC (eluent: cyclohexane/EtOAc/MeOH 5:5:0.4). Yield 65%; m.p. 199–200°C. ^{1}H NMR (DMSO-d_6) 2.40–2.43 (m, 4H, piperazine protons), 3.53 (s, 2H, CH2), 3.67–3.69 (m, 4H, piperazine protons), 6.30–6.32 (m, 1H, furan proton), 6.41–6.43 (m, 1H, furan proton), 7.38–7.43 (m, 3H, 1 ar + NH2), 7.56–7.70 (m, 3H, 2 ar +1 furan proton), 7.98 (d, 2H, ar, J = 7.4 Hz), 8.54 (s, 1H, H-3). Anal. Calc. for $C_{20}H_{21}N_7O$.

Synthesis of 1-(2,4,6-trifluorobenzyl)piperazinium trifluoroacetate 60

A solution of N-(Boc)piperazine **63** (2.06 mmol) and 2,4,6-trifluorobenzaldehyde (1.87 mmol) in anhydrous CH_2Cl_2 (20 mL) was stirred at room temperature for 1.5 h, then triacetoxy sodium borohydride (7.47 mmol) was added portion wise. The mixture was refluxed for 48 h, then treated with iced water (10 mL) and diluted with CH_2Cl_2 (15 mL). The aqueous phase was extracted with CH_2Cl_2 (10 mL X 3) and the organic phases were collected and anhydrified (Na_2SO_4). Evaporation of the solvent at reduced pressure gave the crude tert-butyl-4–(2,4,6-trifluorobenzyl)piperazine-1-carboxylate which was purified by preparative TLC (eluent: CH_2Cl_2/acetonitrile/cyclohexane, 9:1:1) and obtained as a yellow oil. Yield 91%; ^{1}H NMR ($CDCl_3$) 1.46 (s, 9H, t-But), 2.41–2.45 (m, 4H, piperazine protons), 3.42–3.46 (m, 4H, piperazine protons), 3.67 (s, 2H, CH2), 6.69 (t, 2H, ar, J = 7.8 Hz). This derivative was then transformed into the title compound as follows. A solution of concentrated trifluoroacetic acid (2.5 mL) in anhydrous CH_2Cl_2 (2.5 mL) was added dropwise to a solution of tert-butyl-4–(2,4,6-trifluorobenzyl)piperazine-1-carboxylate (1.04 mmol) in anhydrous CH_2Cl_2 (20 mL). The solution was stirred at room temperature for 3 h, then the solvent and the excess of the acid were removed at reduced pressure. The residue was treated with Et_2O (5 mL) to give a solid which was collected by filtration and dried. The crude compound was used for the next step without further purification. Yield 67%; ^{1}H NMR ($CDCl_3$) 2.29–3.31 (m, 4H, piperazine protons), 3.49–3.52 (m, 4H, piperazine protons), 4.12 (s, 2H, CH2), 6.73 (t, ar, J = 7.8 Hz).

Synthesis of 4-(7-amino-2-phenyl-2H-pyrazolo[4,3-d]pyrimidin-5- yl)piperazin-1-ium trifluoroacetate 64

The title compound was obtained by treatment of compound **21** (1.04 mmol) with trifluoroacetic acid, in the conditions described previously to prepare compound **60** from the corresponding N-Boc-derivative. The crude compound was used directly for the next step without purification. Yield 68%; ^{1}H NMR (DMSO-d_6) 3.22–3.29 (m, 4H, piperazine protons), 3.98–4.02 (m, 4H, piperazine protons), 7.51 (t, 1H, ar, J = 7.3 Hz), 7.63 (t, 2H, ar, J = 7.8 Hz), 8.03 (d, 2H, ar, J = 8.2 Hz), 8.69 (s, 1H, H-3), 9.25 (br s, 2H, NH2 $^+$).

General procedure for the synthesis of 5–(4-acylpiperazin-1-yl)substituted-2H-pyrazolo[4,3-d]pyrimidin-7-amines 23 and 24

A mixture of derivative **64** (0.98 mmol) and triethylamine (1.96 mmol) in anhydrous THF (20 ml) was stirred at room temperature for 1 h. Then, 3,3-dimethylbutiryl chloride (1.17 mmol) or phenylacetyl chloride (1.17 mmol) was added and the solution was stirred at room temperature for 5 h or 3 h, respectively. The mixture was diluted with water (15 ml) and extracted with EtOAc (20 X 3 ml). The organic phase was anhydrified (Na_2SO_4) and the solvent evaporated at reduced pressure to give a solid which was taken up with cyclohexane and EtOAc, collected by filtration and purified by column chromatography (eluent $CHCl_3$/MeOH 10:0.5 for compound **23**, MeOH for derivative **24**).

7-Amino-2-phenyl-5-(4-(3,3-dimethylbutiryl)piperazin-1-yl)-2H-pyrazolo[4,3-d]pyrimidine 23

Yield 32%; m.p. 178–180°C. ^{1}H NMR (DMSO-d_6) 1.02 (s, 9H, t-But), 2.29 (s, 2H, CH2), 3.58–3.60 (m, 4H, piperazine protons), 3.69–3.72 (m, 4H, piperazine protons), 7.42–7.46 (m, 3H, 1 ar þ NH2) 7.59 (t, 2H, ar, J = 7.4 Hz), 8.00 (d, 2H, ar, J = 7.9 Hz), 8.60 (s, 1H, H-3). Anal. Calc. for $C_{21}H_{27}N_7O$.

7-Amino-2-phenyl-5-(4-phenylacetylpiperazin-1-yl)-2H-pyrazolo[4,3- d]pyrimidine 24

Yield 69%; m.p. 207–209°C (CH3NO2). ^{1}H NMR (DMSO-d_6) 3.52–3.57 (m, 4H, piperazine protons), 3.60–3.66 (m, 4H, piperazine protons), 3.77 (s, 2H, CH2), 7.21–7.34 (m, 5H, ar), 7.42–7.50 (m, 3H, 1 ar + NH2), 7.57 (t, 2H, ar, J = 7.9 Hz), 7.98 (d, 2H, ar, J = 8.2 Hz), 8.59 (s, 1H, H-3). Anal. Calc. for $C_{23}H_{23}N_7O$.

5.2 Molecular modeling studies

5.2.1 Software overview

MOE suite (Molecular Operating Environment, version 2015.1001) [39] was used to perform most general molecular modeling operations.

Docking simulations were performed using the GOLD (Genetic Optimization for Ligand Docking, version 5.2) suite [40]. Quantum mechanical calculation of PM3 charges was carried out with the software MOPAC [41] as implemented in the MOE suite.

Analyses of docking poses in terms of energy calculation and visual inspection were executed taking advantage of the MOE suite.

Molecular modeling studies have been performed on a 8 CPU (Intel® Xeon® CPU E5-1620 3.70 GHz) linux workstation.

5.2.2 Three-dimensional structures of adenosine receptors

Among all the available crystallographic structures of hA_{2A} AR cocrystallized with a ligand in the orthosteric binding site, we opted for a complex with the antagonist ZM-241385 because of the structural similarity of its ([1,2,4]triazolo[1,5,a][1,3,5]triazin-5,7-yl)diamine scaffold with the (pyrazolo[4,3-d]pyrimidin-5,7-yl)diamine scaffold of the compounds under investigation. The crystallographic structure identified with 4EIY PDB code [42] was selected among all the structures co-crystallized with ZM-241385, because of its highest resolution (1.80 Å).

Since to date there are no crystallographic structures available for hA_3 and hA_1 ARs, we retrieved from the *Adenosiland* web-platform [43,44] previously developed by our research group, their homology models constructed using 4EIY structure as template. Those models were constructed in the presence of ZM-241385 as environment for induced fit, so the resulting structures consist in complexes between each AR subtype and the antagonist ZM-241385.

The residues are identified according to the generic Ballesteros Weinstein numbering system [45].

5.2.3 Molecular docking

Three-dimensional structures of ligands were built taking advantage of the MOE-Builder tool and ionization states were predicted using the MOE-Protonate-3D tool [46]. Ligand structures were subjected to MMFF94x energy minimization until the root mean square (rms) gradient fell below 0.05 kcal mol^{-1} Å^{-1}. GOLD docking tool [40] was selected as conformational search program and GoldScore as scoring function, thanks to a docking benchmark study previously carried out in our laboratory [38,47]. For each compound, 10 docking runs were performed on each receptor subtype, searching in a sphere of 20 Å radius centered on the coordinates of the center of mass of ZM-241385 in complex with the receptor. Along with the compounds under investigation, docking simulations were conducted also for ZM-241385 as a reference example.

After computing atomic partial charges both of ligand poses, using PM3/ESP method, and receptors, using Amber10EHT force field, electrostatic and van der Waals contributions to the binding energy were calculated with MOE.

5.2.4 Interaction energy fingerprints (IEFs)

Individual electrostatic and hydrophobic interactions, hereinafter identified as IEele and IEhyd, respectively, were computed between ligand poses and each protein residue involved in binding [37,38]. Both these contributions were computed using MOE and, in particular, IEele were calculated as non-bonded electrostatic interactions energy term of the force field, so they are expressed in kcal/mol. Instead, IEhyd were computed as contact hydrophobic surfaces and are associated to an adimensional score (the higher the better). The data obtained by this analysis were reported in a graphic, called Interaction Energy Fingerprints (IEFs), representing residues (x-axis) in the form of equally high rectangles rendered according to a colorimetric scale. As regards IEele, colors from blue to red represent energy values ranging from negative to positive values; for IEhyd, colors from white to dark green depict scores going from 0 to positive values. More precisely, we retrieved the coordinates of the center of mass of ZM-241385 in the structure of each AR subtype complex. Only residues within 10 Å from this point were retained as belonging to the binding site, and plotted in the IEFs.

5.2.5 Interaction Energy Fingerprints comparison (IEFs comparison)

A new method has been introduced to evaluate docking results, which rests on the observation that ligands able to bind the same site of a protein often share a similar interaction pattern, too. The new method consists in the comparison of the IEFs of the pose of a candidate ligand (hereinafter called "docked") with the IEFs of a ligand whose bound conformation is considered known (hereinafter called "reference").

A quantitative estimation of the similarity of IEFs is computed as root mean square deviation (RMSD) between per residue interaction energies of the docked and the reference poses, both for electrostatic and hydrophobic interactions. This would inform about the average divergence of the docked from the reference: in particular a high RMSD value corresponds to large differences.

So far, there is no information about the direction of the divergence thus, along with RMSD, another analysis, named RMSDtrend, has been proposed. This consists of the sum of differences between per residue interaction energies of the docked and the reference, weighted by the number of residues of the binding site. A more favorable interaction energy profile would correspond to a negative $\mathrm{RMSD}_{\mathrm{trend}}$ in the case of electrostatic interactions, while to a positive one in the case of hydrophobic interactions.

In summary, low RMSD values, along with negative electrostatic $\mathrm{RMSD}_{\mathrm{trend}}$ and high hydrophobic $\mathrm{RMSD}_{\mathrm{trend}}$ could be interpreted as an indication of a higher "stability" of the docked pose respect the reference in the orthosteric binding state.

Moreover, this approach could be expanded to compare the behavior of the same ligand on different receptor subtypes, in order to have a preliminary "selectivity" profile based on the stabilities of the docked poses in their corresponding orthosteric binding states. In that case, RMSD and $\mathrm{RMSD}_{\mathrm{trend}}$ are computed for a docked compound against a reference on each receptor subtype. The reference compound should be a known good binder for each subtype and, at best, the crystallographic structure of the complex should be known.

In our case, ZM-241385 was chosen as reference compound, since it is a ligand for all ARs, having a Ki of 774 nM for hA_1 AR, of 1.6 nM for hA_{2A} AR and of 743 nM for hA_3 AR. As regards the hA_{2A} receptor, 4EIY crystallographic complex could be employed, while, for hA_1 and hA_3 ARs, we used the homology models, that are receptor-ZM-241385 complexes, since they were constructed considering ZM-241385 as environment for induced fit.

An additional graph was added, which allows to compare electrostatic and hydrophobic IEFs RMSDs and $\mathrm{RMSD}_{\mathrm{trend}}$ for different ligands on the different AR subtypes. RMSD and $\mathrm{RMSD}_{\mathrm{trend}}$ for the ligands (y-axis) on the various receptors (x-axis) were reported on a heat map, where they are represented by a colorimetric scale going from red to blue from unfavorable to favorable values. Finally, if a ligand presents blue rectangles on all receptors, it is expected to be “non-selective”, otherwise red and blue rectangles should describe lower and higher stability values, respectively, among the different receptor subtypes.

5.2.6 MMsDocking video maker

To facilitate the visualization and analysis of data obtained from the docking simulations, we have implemented a in-house tool, named MMsDocking video maker, for the automated production of a video that shows the most relevant docking data, such as docking poses, per residue IEhyd and IEele data, experimental binding data and scoring values. Videos were mounted using MEncoder [48] starting from images obtained with the following procedure: the heat maps in the background were drawn with GNUPLOT 4.6 [49] starting from per residue IEhyd and IEele data computed with MOE. 2d depictions of compounds were generated using the open-source cheminformatics toolkit RDKit [50]. Representations of docking poses within the binding site were constructed using CHIMERA [51].

5.3 Pharmacological assays

5.3.1 Human cloned A_1, A_{2A} and A_3 AR binding assay

All synthesized compounds were tested to evaluate their affinity at human A_1, A_{2A} and A_3 ARs. Displacement experiments of $[^3H]$DPCPX (1 nM) to hA_1 CHO membranes (50 mg of protein/assay) and at least 6–8 different concentrations of antagonists for 120 min at 25°C in 50 mM Tris-HCl buffer pH 7.4 were performed [52]. Non-specific binding was determined in the presence 1 µM of DPCPX (≤10% of the total binding). Binding of $[^3$ H]ZM- 241385 (1 nM) to hA_{2A}CHO membranes (50 µg of protein/assay) was performed by using 50 mM Tris-HCl buffer, 10 mM MgCl2 pH 7.4 and at least 6–8 different concentrations of antagonists studied for an incubation time of 60 min at 4°C [53]. Non-specific binding was determined in the presence of 1 µM ZM-241385 and was about 20% of total binding. Competition binding experiments to hA_3 CHO membranes (50 µg of protein/assay) were performed incubating 0.5 nM $[^{125}I]$AB-MECA, 50 mM Tris-HCl buffer, 10 mM $MgCl_2$, 1 mM EDTA, pH 7.4 and at least 6–8 different concentrations of examined ligands for 60 min at 37°C [54]. Non-specific binding was defined as binding in the presence of 1 µM AB-MECA and was about 20% of total binding. Bound and free radioactivity were separated by filtering the assay mixture through Whatman GF/B glass fiber filters by using a Brandel cell harvester. The filter bound radioactivity was counted by Scintillation Counter Packard Tri Carb 2810 TR with an efficiency of 58%.

5.3.2 Measurement of cyclic AMP levels in CHO cells transfected with hA_{2B} AR

CHO cells transfected with hA_{2B} AR subtypes were washed with phosphate-buffered saline, diluted trypsin and centrifuged for 10 min at 200 *g*. The cells (1 X 106 cells/assay) were suspended in 0.5 ml of incubation mixture (mM): NaCl 15, KCl 0.27, NaH_2PO_4 0.037, $MgSO_4$ 0.1, $CaCl_2$ 0.1, Hepes 0.01, $MgCl_2$ 1, glucose 0.5, pH 7.4 at 37°C, 2 IU/ml adenosine deaminase and 4–(3-butoxy-4- methoxybenzyl)-2-imidazolidinone (Ro 20–

1724) as phosphodiesterase inhibitor and preincubated for 10 min in a shaking bath at 37°C. The potency of antagonists to the A_{2B} AR was determined by the inhibition of NECA (200 nM)-induced cyclic AMP production [55]. The reaction was terminated by the addition of cold 6% trichloroacetic acid (TCA). The TCA suspension was centrifuged at 2000 *g* for 10 min at 4°C and the supernatant was extracted four times with water saturated diethyl ether. The final aqueous solution was tested for cyclic AMP levels by a competition protein binding assay. Samples of cyclic AMP standard (0–10 pmoles) were added to each test tube containing [^{3}H] cyclic AMP and incubation buffer (trizma base 0.1 M, aminophylline 8.0 mM, 2-mercaptoethanol 6.0 mM, pH 7.4). The binding protein prepared from beef adrenals was added to the samples previously incubated at 4°C for 150 min, and, after the addition of charcoal, was centrifuged at 2000 *g* for 10 min. The clear supernatant was counted in a Scintillation Counter Packard Tri Carb 2810 TR with an efficiency of 58%.

5.3.3 Data analysis

The protein concentration was determined according to a Bio-Rad method [56] with bovine albumin as a standard reference. Inhibitory binding constant (Ki) values were calculated from those of IC_{50} according to Cheng & Prusoff equation $Ki=IC_{50}/(1 + [C^*]/K_D^*)$, where [C*] is the concentration of the radioligand and K_D* its dissociation constant [57]. A weighted non-linear least-squares curve fitting program LIGAND [58] was used for computer analysis of inhibition experiments. IC_{50} values obtained in cyclic AMP assay were calculated by non-linear regression analysis using the equation for a sigmoid concentration–response curve (Graph-PAD Prism, San Diego, CA).

References

1. Fredholm BB, IJzerman AP, Jacobson KA, Klotz KN, Linden J (2001) International Union of Pharmacology. XXV. Nomenclature and classification of adenosine receptors. Pharmacol Rev 53:527–552

2. Fredholm BB, IJzerman AP, Jacobson KA, Linden J, Müller CE (2011) International Union of Basic and Clinical Pharmacology. LXXXI. Nomenclature and classification of adenosine receptors--an update. Pharmacol Rev 63:1–34

3. Maemoto T, Tada M, Mihara T, et al (2004) Pharmacological characterization of FR194921, a new potent, selective, and orally active antagonist for central adenosine A1 receptors. J Pharmacol Sci 96:42–52

4. Mihara T, Iwashita A, Matsuoka N (2008) A novel adenosine A(1) and A(2A) receptor antagonist ASP5854 ameliorates motor impairment in MPTP-treated marmosets: comparison with existing anti-Parkinson's disease drugs. Behav Brain Res 194:152–161

5. Jacobson KA, Gao Z-G (2006) Adenosine receptors as therapeutic targets. Nat Rev Drug Discov 5:247–264

6. Navarro G, Borroto-Escuela DO, Fuxe K, Franco R (2016) Purinergic signaling in Parkinson's disease. Relevance for treatment. Neuropharmacology 104:161–168

7. Armentero MT, Pinna A, Ferré S, Lanciego JL, Müller CE, Franco R (2011) Past, present and future of A(2A) adenosine receptor antagonists in the therapy of Parkinson's disease. Pharmacol Ther 132:280–299

8. Chen J-F, Eltzschig HK, Fredholm BB (2013) Adenosine receptors as drug targets--what are the challenges? Nat Rev Drug Discov 12:265–286

9. Kyowa Hakko K. Approval for manufacturing and marketing of NOURIAST tablets 20 mg. A novel antiparkinsonian agent; 2013. Available from: http://www.kyowakirin.com/news releases/2013/e20130325_04.htlm.

10. Shook BC, Rassnick S, Wallace N, et al (2012) Design and characterization of optimized adenosine A_2A/A_1 receptor antagonists for the treatment of Parkinson's disease. J Med Chem 55:1402–1417

11. Atack JR, Shook BC, Rassnick S, et al (2014) JNJ-40255293, a novel adenosine A2A/A1 antagonist with efficacy in preclinical models of Parkinson's disease. ACS Chem Neurosci 5:1005–1019

12. Preti D, Baraldi PG, Moorman AR, Borea PA, Varani K (2015) History and perspectives of A2A adenosine receptor antagonists as potential therapeutic agents. Med Res Rev 35:790–848

13. Perez-Aso M, Chiriboga L, Cronstein BN (2012) Pharmacological blockade of adenosine A2A receptors diminishes scarring. FASEB J 26:4254–4263

14. Leone RD, Lo Y-C, Powell JD (2015) A2aR antagonists: Next generation checkpoint blockade for cancer immunotherapy. Comput Struct Biotechnol J 13:265–272

15. Catarzi D, Colotta V, Varano F, Lenzi O, Filacchioni G, Trincavelli L, Martini C, Montopoli C, Moro S (2005) 1,2,4-Triazolo[1,5-a]quinoxaline as a versatile tool for the design of selective human A3

adenosine receptor antagonists: synthesis, biological evaluation, and molecular modeling studies of 2-(hetero)aryl- and 2-carboxy-substituted derivatives. J Med Chem 48:7932–7945

16. Lenzi O, Colotta V, Catarzi D, et al (2006) 4-amido-2-aryl-1,2,4-triazolo[4,3-a]quinoxalin-1-ones as new potent and selective human A3 adenosine receptor antagonists. synthesis, pharmacological evaluation, and ligand-receptor modeling studies. J Med Chem 49:3916–3925

17. Morizzo E, Capelli F, Lenzi O, et al (2007) Scouting human A3 adenosine receptor antagonist binding mode using a molecular simplification approach: from triazoloquinoxaline to a pyrimidine skeleton as a key study. J Med Chem 50:6596–6606

18. Colotta V, Catarzi D, Varano F, et al (2008) Synthesis, ligand-receptor modeling studies and pharmacological evaluation of novel 4-modified-2-aryl-1,2,4-triazolo[4,3-a]quinoxalin-1-one derivatives as potent and selective human A3 adenosine receptor antagonists. Bioorg Med Chem 16:6086–6102

19. Colotta V, Lenzi O, Catarzi D, et al (2009) Pyrido[2,3-e]-1,2,4-triazolo[4,3-a]pyrazin-1-one as a new scaffold to develop potent and selective human A3 adenosine receptor antagonists. Synthesis, pharmacological evaluation, and ligand-receptor modeling studies. J Med Chem 52:2407–2419

20. Lenzi O, Colotta V, Catarzi D, et al (2009) 2-Phenylpyrazolo[4,3-d]pyrimidin-7-one as a new scaffold to obtain potent and selective human A3 adenosine receptor antagonists: new insights into the receptor-antagonist recognition. J Med Chem 52:7640–7652

21. Poli D, Catarzi D, Colotta V, Varano F, Filacchioni G, Daniele S, Trincavelli L, Martini C, Paoletta S, Moro S (2011) The identification of the 2-phenylphthalazin-1(2H)-one scaffold as a new decorable core skeleton for the design of potent and selective human A3 adenosine receptor antagonists. J Med Chem 54:2102–2113

22. Squarcialupi L, Colotta V, Catarzi D, et al (2013) 2-Arylpyrazolo[4,3-d]pyrimidin-7-amino derivatives as new potent and selective human A3 adenosine receptor antagonists. Molecular modeling studies and pharmacological evaluation. J Med Chem 56:2256–2269

23. Catarzi D, Colotta V, Varano F, et al (2013) Pyrazolo[1,5-c]quinazoline derivatives and their simplified analogues as adenosine receptor antagonists: synthesis, structure-affinity relationships and molecular modeling studies. Bioorg Med Chem 21:283–294

24. Squarcialupi L, Colotta V, Catarzi D, et al (2014) 7-Amino-2-phenylpyrazolo[4,3-d]pyrimidine derivatives: structural investigations at the 5-position to target human A_1 and A(2A) adenosine receptors. Molecular modeling and pharmacological studies. Eur J Med Chem 84:614–627

25. Varano F, Catarzi D, Squarcialupi L, et al (2015) Exploring the 7-oxo-thiazolo[5,4-d]pyrimidine core for the design of new human adenosine A3 receptor antagonists. Synthesis, molecular modeling studies and pharmacological evaluation. Eur J Med Chem 96:105–121

26. Squarcialupi L, Catarzi D, Varano F, et al (2016) Structural refinement of pyrazolo[4,3-d]pyrimidine derivatives to obtain highly potent and selective antagonists for the human A3 adenosine receptor. Eur J Med Chem 108:117–133

27. Federico S, Paoletta S, Cheong SL, et al (2011) Synthesis and biological evaluation of a new series of 1,2,4-triazolo[1,5-a]-1,3,5-triazines as human A(2A) adenosine receptor antagonists with improved water solubility. J Med Chem 54:877–889

28. Vu CB, Pan D, Peng B, et al (2005) Novel diamino derivatives of [1,2,4]triazolo[1,5-a][1,3,5]triazine as potent and selective adenosine A2a receptor antagonists. J Med Chem 48:2009–2018

29. Wong R, Dolman SJ (2007) Isothiocyanates from tosyl chloride mediated decomposition of in situ generated dithiocarbamic acid salts. J Org Chem 72:3969–3971

30. Gittos MW, Robinson MR, Verge JP, Davies RV, Iddon B, Suschitzky H (1976) Intramolecular cyclisation of arylalkyl isothiocyanates. Part I. Synthesis of 1-substituted 3,4-dihydroisoquinolines. Journal of the Chemical Society, Perkin Transactions 1 33

31. Antoš K, Nemec P, Hrdina M (1972) 4-Substituierte β-Phenyläthylisothiocyanate. Collection of Czechoslovak chemical communications 37:3339–3341

32. Brown G, Weliky V (1958) 2-Chloroadenine and 2-Chloroadenosine. J Org Chem 23:125–126

33. Oumata N, Bettayeb K, Ferandin Y, et al (2008) Roscovitine-derived, dual-specificity inhibitors of cyclin-dependent kinases and casein kinases 1. J Med Chem 51:5229–5242

34. Lee W, Ortwine DF, Bergeron P, et al (2013) A hit to lead discovery of novel N-methylated imidazolo-, pyrrolo-, and pyrazolo-pyrimidines as potent and selective mTOR inhibitors. Bioorg Med Chem Lett 23:5097–5104

35. Kanojia RM, Salata JJ, Kauffman J (2000) Synthesis and class III type antiarrhythmic activity of 4-aroyl (and aryl)-l-aralkylpiperazines. Bioorg Med Chem Lett 10:2819–2823

36. Meyer WE, Tomcufcik AS, Chan PS, Haug M (1989) 5-(1-piperazinyl)-1H-1,2,4-triazol-3-amines as antihypertensive agents. J Med Chem 32:593–597

37. Ciancetta A, Sabbadin D, Federico S, Spalluto G, Moro S (2015) Advances in Computational Techniques to Study GPCR-Ligand Recognition. Trends Pharmacol Sci 36:878–890

38. Ciancetta A, Cuzzolin A, Moro S (2014) Alternative quality assessment strategy to compare performances of GPCR-ligand docking protocols: the human adenosine A(2A) receptor as a case study. J Chem Inf Model 54:2243–2254

39. Chemical Computing Group (CCG) Inc. (2016) Molecular Operating Environment (MOE). http://www.chemcomp.com.

40. GOLD suite, version 5.2. Cambridge Crystallographic Data Centre: 12 Union Road, Cambridge CB2 1EZ, UK. http://www.ccdc.cam.ac.uk

41. Stewart JJP (2007) Optimization of parameters for semiempirical methods V: modification of NDDO approximations and application to 70 elements. J Mol Model 13:1173–1213

42. Liu W, Chun E, Thompson AA, et al (2012) Structural basis for allosteric regulation of GPCRs by sodium ions. Science 337:232–236

43. Floris M, Sabbadin D, Medda R, Bulfone A, Moro S (2012) Adenosiland: walking through adenosine receptors landscape. Eur J Med Chem 58:248–257

44. Floris M, Sabbadin D, Ciancetta A, Medda R, Cuzzolin A, Moro S (2013) Implementing the “Best Template Searching” tool into Adenosiland platform. In silico pharmacology 1:25

45. Ballesteros JA, Weinstein H (1995) Integrated methods for the construction of three-dimensional models and computational probing of structure-function relations in G protein-coupled receptors. Receptor Molecular Biology. Elsevier, pp 366–428

46. Labute P (2009) Protonate3D: assignment of ionization states and hydrogen coordinates to macromolecular structures. Proteins 75:187–205

47. Cuzzolin A, Sturlese M, Malvacio I, Ciancetta A, Moro S (2015) DockBench: An Integrated Informatic Platform Bridging the Gap between the Robust Validation of Docking Protocols and Virtual Screening Simulations. Molecules 20:9977–9993

48. MEncoder. http://www.mplayerhq.hu/design7/projects.html

49. Gnuplot. http://www.gnuplot.info/index.html

50. RDKit: Open-source cheminformatics. http://www.rdkit.org

51. Pettersen EF, Goddard TD, Huang CC, Couch GS, Greenblatt DM, Meng EC, Ferrin TE (2004) UCSF Chimera--a visualization system for exploratory research and analysis. J Comput Chem 25:1605–1612

52. Borea PA, Dalpiaz A, Varani K, Gessi S, Gilli G (1996) Binding thermodynamics at A1 and A2A adenosine receptors. Life Sci 59:1373–1388

53. Varani K, Rigamonti D, Sipione S, Camurri A, Borea PA, Cattabeni F, Abbracchio MP, Cattaneo E (2001) Aberrant amplification of A(2A) receptor signaling in striatal cells expressing mutant huntingtin. FASEB J 15:1245–1247

54. Varani K, Cacciari B, Baraldi PG, Dionisotti S, Ongini E, Borea PA (1998) Binding affinity of adenosine receptor agonists and antagonists at human cloned A3 adenosine receptors. Life Sci 63:PL 81–7

55. Varani K, Gessi S, Merighi S, et al (2005) Pharmacological characterization of novel adenosine ligands in recombinant and native human A2B receptors. Biochem Pharmacol 70:1601–1612

56. Bradford MM (1976) A rapid and sensitive method for the quantitation of microgram quantities of protein utilizing the principle of protein-dye binding. Anal Biochem 72:248–254

57. Cheng Y, Prusoff WH (1973) Relationship between the inhibition constant (K1) and the concentration of inhibitor which causes 50 per cent inhibition (I50) of an enzymatic reaction. Biochem Pharmacol 22:3099–3108

58. Munson PJ, Rodbard D (1980) Ligand: a versatile computerized approach for characterization of ligand-binding systems. Anal Biochem 107:220–239

Published: *J Enzyme Inhib Med Chem. 2017 Dec;32(1):248–263.*

Deciphering the Complexity of Ligand–Protein Recognition Pathways Using Supervised Molecular Dynamics (SuMD) Simulations

Alberto Cuzzolin, Mattia Sturlese, Giuseppe Deganutti, Veronica Salmaso, Davide Sabbadin, Antonella Ciancetta, and Stefano Moro

(2016) Deciphering the Complexity of Ligand-Protein Recognition Pathways Using Supervised Molecular Dynamics (SuMD) Simulations. J Chem Inf Model 56:687–705

Abstract

Molecular recognition is a crucial issue when aiming to interpret the mechanism of known active substances as well as to develop novel active candidates. Unfortunately, simulating the binding process is still a challenging task because it requires classical MD experiments in a long microsecond time scale that are affordable only with a high-level computational capacity. In order to overcome this limiting factor, we have recently implemented an alternative MD approach, named supervised molecular dynamics (SuMD), and successfully applied it to G protein-coupled receptors (GPCRs). SuMD enables the investigation of ligand–receptor binding events independently from the starting position, chemical structure of the ligand, and also from its receptor binding affinity. In this article, we present an extension of the SuMD application domain including different types of proteins in comparison with GPCRs. In particular, we have deeply analyzed the ligand–protein recognition pathways of six different case studies that we grouped into two different classes: globular and membrane proteins. Moreover, we introduce the SuMD-Analyzer tool that we have specifically implemented to help the user in the analysis of the SuMD trajectories. Finally, we emphasize the limit of the SuMD applicability domain as well as its strengths in analyzing the complexity of ligand–protein recognition pathways.

1. Introduction

The essential features of ligand–protein interaction are very often summarized under the expression “molecular recognition” incorporating both thermodynamic aspects (quantified by K_d, the equilibrium dissociation constant) and kinetic aspects (reflected by the rate constants k_{on} and k_{off}) of ligand binding. Consequently, molecular recognition is thus a crucial issue in interpreting the mechanism of known active substances as well as in the development of novel active candidates since both thermodynamic and kinetic aspects greatly affect the understanding of ligand-mediated signal transmission in living organisms or whether a chemical compound can be transformed in a drug candidate [1].

The physicochemical bases governing the optimization of thermodynamic aspects of ligand binding are relatively well acknowledged, but unluckily, they remain still poorly understood for binding kinetics. In fact, the K_d value depends on the free energy difference between the ligand–protein bound and unbound states, both of which are chemically stable and generally experimentally observable. On the contrary, k_{on} and k_{off} rate constants depend on the height of the free energy barrier separating those states, and in particular, the highest free energy barrier defined as a transition state is characterized only by a fleeting existence [2]. Consequently, the major challenge in the optimization of the kinetics parameters is the complexity in characterizing all plausible approaching pathways of the ligand to the target protein. In fact, different approaching pathways can be characterized by different metastable intermediate states (referred also as meta-binding sites) [3] connected to each other and to the final bound state by different transition states. Understanding the molecular interactions between ligand and protein during the approaching pathways is thus central to the deep understanding and to the rational control of ligand binding kinetics.

Even though experimental techniques for measuring the kinetic parameters of ligand binding have existed for decades, all of them only provide indirect evidence about transient structures visited along a ligand-binding pathway [2]. Alternatively, computational methods, and in particular molecular dynamics (MD) simulations, can provide detailed structural information on metastable intermediate states (meta-binding sites) and transition states at the atomistic level of detail [4]. Due to increases in computational power, it has recently become possible to simulate the full process of spontaneous ligand–protein association which typically occurs on the microsecond time scale, providing direct access to detailed information on binding mechanisms that have been difficult to access experimentally [4, 5]. Unfortunately, simulating this binding process is still a challenging task because it requires classical MD experiments in a long microsecond time scale that is affordable only with a high-level computational capacity. However, the probability of reproducing a ligand–protein binding or unbinding event on an accessible time scale can be enhanced through the introduction of biased potentials that facilitate the crossing of energy barriers or the application of external forces on the ligand, respectively [6]. An alternative strategy that does not require the introduction of biases or external forces and enables us to explore the ligand–protein approaching path in a nanosecond simulation time scale has been recently proposed by us specifically in the field of G protein-coupled receptors (GPCRs) [7, 8]. The “supervised molecular dynamics” (SuMD) approach exploits a tabu-like algorithm to monitor the distance between the center of masses of the ligand atoms and the protein binding site in standard short MD simulations (Figure 1, left panel). According to this strategy, an arbitrary number of distance points is collected “on the flight” at regular intervals and fitted into a linear function f(x) = *m*x. If the slope (*m*) is negative, the ligand–receptor distance is likely to be shortened, and the simulation is restarted from the last set of coordinates. Otherwise, the simulation is restored from the original set of coordinates and started over. The supervision is repeated until the ligand–receptor distance is less than 5 Å. The results of a SuMD simulation are displayed in a graph reporting the interaction energy toward the distance between the ligand and the binding site (Figure 1, right panel). We have recently applied the SuMD approach to interpret at the molecular level: (i) the binding of different antagonists at the human A_{2A} adenosine receptor (hA_{2A} AR) by detecting and characterizing a possible energetically stable meta-binding site [7], (ii) the binding of the natural agonist adenosine at the hA_{2A} AR by detecting and characterizing a possible energetically stable meta-binding site [9], (iii) the positive allosteric modulation mediated by LUF6000 toward the human A_3 adenosine receptor (hA_3 AR) by suggesting at least two possible mechanisms to explain the available experimental data [10], and (iv) the binding of different ligands at the human P2Y12 receptor by detecting and characterizing again possible energetically stable meta-binding site [11].

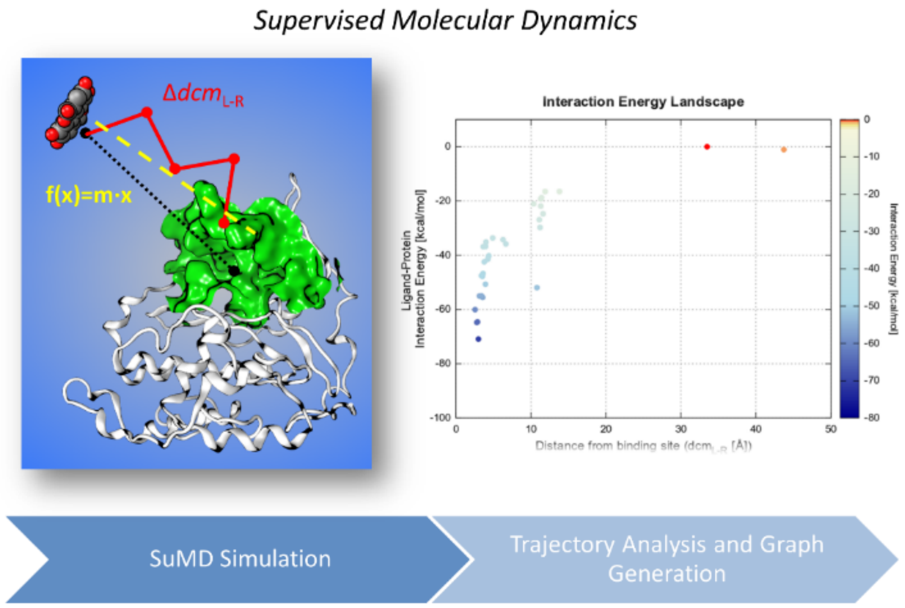
Supervised Molecular Dynamics
Δdcm L-R
f(x)=m·x
Interaction Energy Landscape
Ligand-Protein Interaction Energy [kcal/mol]
0
-20
-40
-60
-80
-100
0
10
20
30
40
50
Distance from binding site (dcm L-R [Å])
Interaction Energy [kcal/mol]
0
-10
-20
-30
-40
-50
-60
-70
-80
SuMD Simulation
Trajectory Analysis and Graph Generation

Fig. 1 Schematic representation of supervised molecular dynamics (SuMD) algorithm (left) and the outcoming ligand–protein interaction energy landscape (right). Interaction energy values: kcal/mol.

In the present work, we present an extension of the SuMD application domain to types of proteins beyond GPCRs. In particular, we deeply analyzed the ligand–protein recognition pathways of six different case studies that we grouped into two different classes: globular and membrane proteins (Table 1). Moreover, we introduce the SuMD-Analyzer tool that we have specifically implemented to help, also nonexpert users, in the analysis of the SuMD trajectories.

Table 1 Structural Summary of Selected Ligand–Protein Complexes[a].

globular systems						
PDB	protein	ligand	Resolution [Å]	affinity	Ligand MW	ref
2ZJW	CK2	Ellagic Acid	2.40	Ki = 0.04 µM	302.197	41
13GS	GSTP1-1	SASP	1.90	Ki = 24 µM	398.39	44
4K7I	PRDX5	Benzen-1,2-diol	2.25	KD = 1500 µM	110.11	45
2VDB	HSA	(S)-naproxen	2.52	Ka = 1.2-1.8 μM^{-1}	230.25	49,59
transmembrane systems						
PDB	protein	ligand	Resolution [Å]	affinity	Ligand MW	ref
3GWW	LeuT	(S)-fluoxetine	2.46	IC_{50} = 355 mM	345.79	51
2YDV	hA_{2A} AR	NECA	2.60	K_i = 13.8 nM	308.29	55

[a] In the affinity column, different constants were reported according the method by which they were inferred; K_i, K_d, and K_a correspond, respectively, to the inhibition, dissociation, and association constants. For the complex 3GWW, only the half maximal inhibitory concentration (IC_{50}) was experimentally available.

2. Materials and methods

2.1 General

All computations were performed on a hybrid CPU/GPU cluster. MD simulations were carried out with the ACEMD engine [12] on a GPU cluster equipped with four NVIDIA GTX 580, two NVIDIA GTX 680, three NVIDIA GTX 780, and four NVIDIA GTX 980. Before running SuMD simulations, the following preliminary phases were carried out: (i) protein–ligand system preparation, (ii) ligand parametrization, and (iii) solvated system setup and equilibration. Two different protocols based on AMBER12 [13] /general Amber force field (GAFF) [14] and the CHARMM27 [15] /CHARMM general force field (CGenFF) force fields combinations were adopted for globular and transmembrane systems, respectively [16, 17].

2.2 Systems Preparation

Protein–ligand complexes were retrieved from the RCSB PDB database [18]. Protein structures were prepared with the protein preparation tool as implemented in MOE: [19] Hydrogen atoms were added to the complex, and appropriate ionization states were assigned by means of the Protonate-3D tool [20]. Missing atoms in protein side chains were built according to either the AMBER12 [13] or the CHARMM27 [15] force field topology. Missing loops were modeled by the default homology modeling protocol implemented in the MOE protein preparation tool. Non-natural N-terminal and C-terminal were capped to mimic the previous residue. For each considered system, the conformer with highest occupancy was selected whenever available. To avoid protein–ligand long-range interactions in the starting geometry, the ligand was then moved at least 15 Å from any protein atoms.

2.3 Ligand Parametrization

2.3.1Globular Systems

For the MD simulations based on the AMBER12 force field [13], the ligands were subjected to two energy minimization steps with MOPAC2012 [21] using PM6 method [22] and Gaussian 09 [23] (HF/6-31G*). After geometry minimization, ligand parameters were derived with GAFF [14] as implemented in Ambertools2014 [13] by using antechamber and parmchk tools. RESP partial charges where calculated with Gaussian 09 [23] following the procedure suggested by antechamber.

2.3.2 Transmembrane Systems

For the MD simulation based on the CHARMM27 force field [24], initial parameters for the ligands were retrieved from the paramchem service and subsequently optimized consistently to CGenFF [16, 25] at the MP2/6-31G* level of theory [26] by using Gaussian 09 [23] and the Force Field Toolkit [27] implemented in the VMD engine [28].

2.4 Solvated System Setup and Equilibration

2.4.1Globular Systems

Protein–ligand complexes were assembled with the tleap tool using AMBER14SB [29] as the force field for the protein [29]. The systems were explicitly solvated by a cubic water box with cell borders placed at least 12 Å away from any protein or ligand atom using TIP3P as the water model [30]. To neutralize the total charge, Na^+/Cl^- counterions were added to a final salt concentration of 0.150 M. The systems were energy minimized by 2000 steps with the conjugate-gradient method and then 50,000 steps of NVE (100 ps) followed by 1 ns of NPT simulation, both using a 2 fs as the time step and applying a harmonic positional constrain on protein and ligand atoms gradually reduced with a scaling factor of 0.1. Pressure was maintained at 1 atm using a Berendsen barostat [31]. The Langevin thermostat was set with a low damping constant of 1 ps^{-1} [32]. Bond lengths involving hydrogen atoms were constrained using the M-SHAKE algorithm [33]. The MD productive runs were conducted in a NVT ensemble. Long-range Coulomb interactions were handled using the particle mesh Ewald summation method (PME) setting the mesh spacing to 1.0 Å [34]. A nonbonded cutoff distance of 9 Å with a switching distance of 7.5 Å was used.

2.4.2 Transmembrane Systems

Transmembrane proteins were embedded in a 1-palmitoyl-2-oleoyl-snglycero-3-phosphocholine (POPC) lipid bilayer according to the suggested orientation reported in the Orientations of Proteins in Membranes (OPM) database [35]. Initial POPC atoms were placed through the VMD [28] membrane builder plugin, and lipids within 0.6 Å from amino acid atoms were removed. The systems were solvated with TIP3P [30] water using the program Solvate 1.0 [36] and neutralized by Na^+/Cl^- counterions to a final concentration of 0.154 M. The systems were then equilibrated through a two-step procedure: In the first stage, after 2000 cycles of a conjugate-gradient minimization algorithm (in order to reduce steric clashes produced by the system manual setting), 10 ns of MD simulation were performed in the NPT ensemble, restraining ligand and protein atoms by a force constant of 1 kcal mol^{-1} $Å^{-2}$. The temperature was maintained at 310 K using a Langevin thermostat with a low damping constant of 1 ps^{-1} [32]. Pressure was maintained at 1 atm using a Berendsen barostat [31]; bond lengths involving hydrogen atoms were constrained using the M-SHAKE algorithm [33] with an integration time step of 2 fs. In the second stage, once water molecules diffused inside the protein cavity and the lipid bilayer reached equilibrium, the force constant was gradually reduced to 0.1 kcal mol^{-1} $Å^{-2}$ for the next 10 ns of MD simulation.

2.5 Supervised Molecular Dynamics (SuMD)

SuMD is a command line tool written in python, tcl, and bash that operates the supervision of MD trajectories according to the algorithm that has been previously described [7]. The program exploits visual molecular dynamics (VMD) and Gnuplot functionalities [28, 37]. In its current implementation, SuMD is interfaced with the ACEMD [12] engine and supports AMBER and CHARMM force fields.

2.5.1 SuMD Input Files

SuMD requires a configuration file (selection.dat, Figure S1A) organized in three major sections containing information about (i) the system, (ii) the supervision procedure, and (iii) the simulation settings. In the system settings section, the following details about the molecular system need to be provided: (i) the PDB file name containing the starting coordinates, (ii) the three-letter code name of the ligand, and (iii) the residues describing the target binding site. In the supervision settings section, the following values are declared: (i) the slope threshold (default value: 0) and (ii) the number of maximum consecutive failed steps (default value: 31) to stop the simulation. In the simulation settings section, the following details must be specified: (i) the force field to use, (ii) the parameter file, and (iii) the GPU device ID to which the calculation will be addressed. In this section, a Boolean operator manages the introduction of a randomization step that varies the position of the ligand through a 600 ps (Section 2.5.2) of nonsupervised MD simulation. In the same directory where SuMD is launched, a file containing the cell dimension as well as a parameter file (prmtop/psf with the same name of the PDB) must also be provided.

2.5.2 SuMD Main Code

The workflow of the SuMD main code is reported in Figure 2. As depicted, at the beginning of the simulation, SuMD detects the atoms that identify the ligand and the target binding site to define the distance between their mass centers $dcm_{(L-R)}$ that will be monitored. Then, a series of 600 ps classical MD simulations are performed. This is a crucial parameter that we have empirically set up to guarantee to a ligand to significantly translate its center of mass during this short time of conventional MD simulation. After each simulation, five $dcm_{(L\text{-}R)}$ distance points are collected at regular intervals of 75 ps. Using these points, the slope value (m) is derived by a linear fitting. As previously described, if the resulting slope m is negative or below the user selected threshold (i.e., the distance $dcm_{(L\text{-}R)}$ is decreasing), the next simulation step starts from the last set of coordinates produced, otherwise the simulation is restarted by randomly assigning the atomic velocities. To avoid problematic starting geometries (i.e., geometries prone to lead to dead-end pathway), in the first simulation step, SuMD supervises the distance $dcm_{(L\text{-}R)}$ with a maximum threshold of 31 failed attempts (preliminary run). In the case this threshold is reached, SuMD callbacks a randomization process on the set of coordinates supplied by the user by a classical 600 ps MD simulation. During the following steps, the simulations are perpetuated under the supervision rules. In particular, the first time a slope value below the threshold is recorded, the program enters the so-called "SuMD Run". When the distance $dcm_{(L\text{-}R)}$ drops below 5 Å, the supervision is disabled, and the simulation proceeds though a classical MD simulation. At the end of the simulation, only the productive steps are saved, chronologically numbered, and stored in a separate directory.

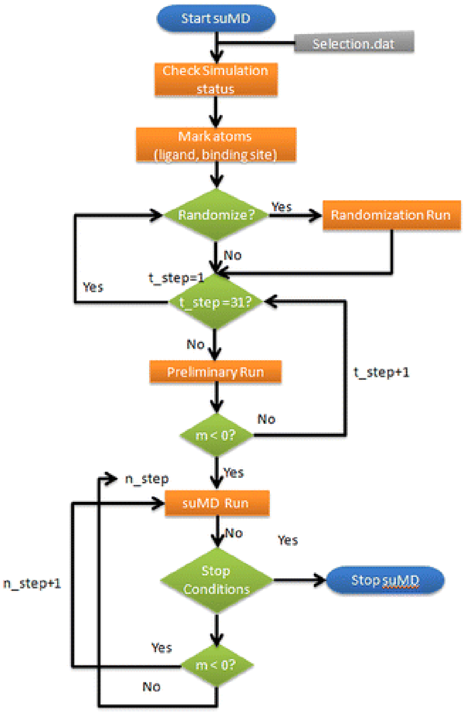

Fig. 2 Workflow of the SuMD main code.

2.5.3 SuMD Log File

At each SuMD simulation step, a log file (Figure S1B) is updated collecting information about (i) the step number, (ii) the $dcm_{(L\text{-}R)}$ distance, (iii) the slope value (m), and (iv) the electrostatic and van der Waals potential energy contributions of the ligand–receptor interaction energy (IE). A counter keeps track of how many times each SuMD step has been attempted. Furthermore, three counters corresponding to the dcm$_{(L-R)}$ distance ranges 0–2, 2–5, and 5–9 Å are reported. These distances monitor how many times the binding site is approached, i.e., how often the dcm$_{(L-R)}$ distance lies below the long-range interaction cutoff. These counters determine the program termination criteria (see following section), and according to the binding site definition supplied by the user, they might represent the target binding site, its neighbors, and putative allosteric/meta-binding sites, respectively.

2.5.4 SuMD Termination Criteria

A SuMD simulation is stopped when one of the following four counters reaches the default maximum value: (i) Counter 1 is incremented when the step is not productive, otherwise it is restored to zero (default maximum value: 17 steps correspond to 10.2 consecutive ns). (ii) Counter 2 monitors the dcm$_{(L-R)}$, and its value is incremented when the distance is between 9 and 5 Å (default maximum value: 19 corresponding to 11.4 nonconsecutive ns). (iii) Counter 3 monitors the dcm$_{(L-R)}$, and its value is incremented when the distance is between 5 and 2 Å (default maximum value: 19 corresponding to 11.4 nonconsecutive ns). (iv) Counter 4 monitors the dcm$_{(L-R)}$, and its value is incremented when the distance is lower than 2 Å (default maximum value: 19 corresponding to 11.4 nonconsecutive ns).

2.6 SuMD-Analyzer Tool

The SuMD-Analyzer is a plugin written in python, tcl, and bash to analyze the SuMD trajectories (Figure 3). The tool is integrated with VMD [28] and UCSF Chimera [38] for the graphical visualization and exploits Wordom [39] and Gnuplot [37] functionalities. The provided analyses cross over four different aspects: (i) the ligand position, (ii) the IE, (iii) the per residue interactions, and (iv) the replicas comparison.

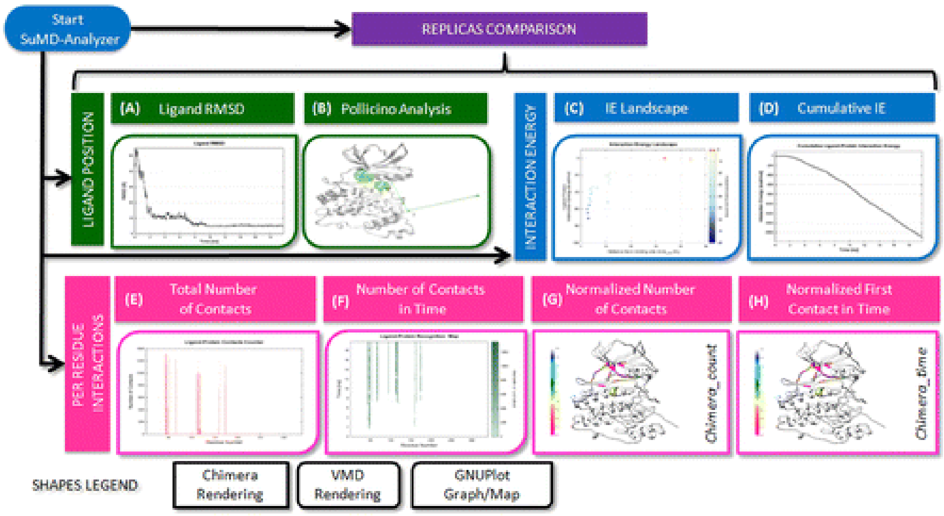

Fig. 3 Overview of the analyses provided by SuMD-Analyzer. The analysis are colored based on the class they belong to. Green: ligand position analysis. Blue: interaction energy analysis. Magenta: per residue interaction. Violet: per replicas analysis.

When the SuMD-Analyzer is launched, the trajectories produced by SuMD are merged and aligned to the starting reference structure using the RMSD tool in VMD by using alpha-carbon atoms for the superposition. The merged trajectory is subjected to a striding procedure picking one frame every fivr through the VMD *animate* module.

2.6.1 Ligand Position

Two analyses follow the coordinates explored by the ligand during the SuMD trajectory (Figure 3, green boxes): (i) the root mean square deviation (RMSD) and (ii) the so-called "Pollicino analysis". If a reference complex structure is available, the RMSD between the ligand and the reference coordinates supplied is computed along the trajectory. The calculation is performed on the heavy atoms of the ligand using the *measure rmsd* function implemented in VMD, and the data obtained are plotted against the time using Gnuplot [37] (Figure 3A). The Pollicino analysis is a simplified representation of the trajectory, highlighting only the most relevant phases of the recognition pathway explored by the ligand. The analysis collects the last frame of each SuMD simulation step (one point each 600 ps) and clusters the coordinates of the ligand mass center according to the corresponding $dcm_{(L\text{-}R)}$ using a threshold value of 2 Å. The coordinates belonging to the same cluster are averaged and represented by a sphere which radius depends on the population of the cluster. According to this procedure, each sphere can collect states arisen from different moments of the trajectory. Arrows indicate the chronological order onto which the regions where the sphere reside are approached by the ligand mass center (Figure 3B).

2.6.2 Interaction Energy

The ligand–protein interaction is analyzed by means of the *mdenergy* function embedded into VMD. The electrostatic and van der Waals contributions to the potential energy are calculated for each frame and summed to obtain the total IE. With this value, two graphs are derived (Figure 3, blue boxes): (i) the "Interaction Energy Landscape" and (ii) the "Cumulative Interaction Energy". The former chart displays the total IE profile with respect to the $dcm_{(L\text{-}R)}$ through a colorimetric scale representing the IE value. Each point displayed in the chart represents the last position of the corresponding SuMD step (Figure 3C). The latter plot shows the cumulative sum of the total IE values for each frame against the time. Therefore, each point is the sum of all previous IE values. Changes in the observed trend highlight how the variation of ligand conformation/position affects the IE (Figure 3D).

2.6.3 Per Residue Interactions

A further set of analyses was developed to highlight the most important residues involved in the ligand recognition pathway (Figure 3, magenta boxes): (i) the "protein–ligand contacts count" and (ii) the "ligand–protein recognition map". In the first graph (Figure 3E), the residues more frequently approached by the ligand during the trajectory are reported, and for each residue, the total number of established contacts is rendered as histograms. In this representation, at each SuMD frame, only the residues lying within a distance of 4 Å from any ligand atoms are considered. In the second graph (Figure 3F), the residues approached by the ligand are depicted with respect to the simulation time. In particular, each dot in the map represents a trajectory frame colored according to the total number of contacts the ligand has established with a particular residue. White dots means that, at the considered frame, the residue atoms are farther than 4 Å from ligand atoms, while green dots correspond to a contact event. The sum of the contact is coded by the light-green to dark-green scale.

To support the user in the topological localization of the residues mainly interacting with the ligand during the trajectory, molecular 3D representations of the protein are automatically set using UCSF Chimera [38] (Figure 3G,H). In particular, the number of ligand–protein contacts is normalized and stored into the B-factor field of the involved residue in the protein PDB file. In the protein 3D representation “chimera_count” (Figure 3G), the ribbons are colored according the so-derived B-factor values. A similar representation, “chimera_time” (Figure 3H), is available with the color code (blue to violet) reflecting the chronological order onto which the residues have been approached by the ligand for the first time.

2.6.4 Replicas Analysis

The replica analysis (Figure 3, violet box) tool integrated in the SuMD-Analyzer was developed taking advantage of VMD and Chimera as graphical visualization tools. The tool collects the raw data from all the simulated replicas and merges the data for the above-described plots and graphical representations.

3. Results and Discussion

3.1 Case Studies Selection

As already anticipated, in this work, the SuMD applicability domain has been extended using six different case studies, grouped into two major protein classes: (i) globular systems and (ii) transmembrane systems (as summarized in Table 1). Specifically, considering the globular proteins we selected (a) the human caseine kinase 2 (CK2) in complex with ellagic acid, (b) the P1-1 isoform of glutathione S-transferase (GSTP1-1) in complex with sulphasalazine (2-hydroxy-(5-{[4-(2-pyridinylamino)sulfonyl]phenyl}azo) benzoic acid, SASP), (c) the human peroxiredoxin 5 (PRDX5) in complex with a benzen-1,2-diol, and (d) the human serum albumin (HSA) in complex with (*S*)-naproxen. Considering the membrane proteins, we selected (a) the leucine transporter (LeuT) from *Aquifex aeolicus* in complex with (*S*)-fluoxetine and (b) the human adenosine A_{2A}receptor (hA_{2A} AR) in complex with the synthetic agonist 5’-N-ethylcarboxamidoadenosine (NECA). An overview of the structural features of the considered ligand–protein complex is reported in Figure 4 and briefly described in the following.

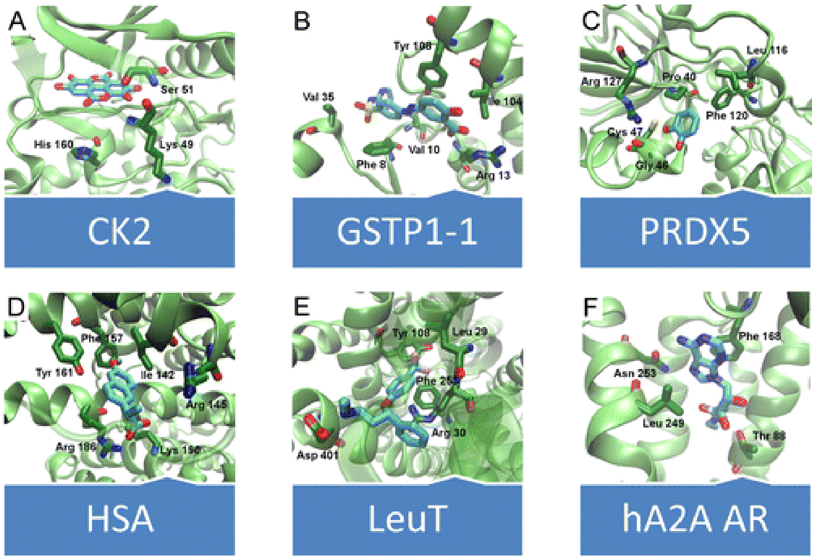

Fig. 4 Overview of the X-ray protein–ligand complexes used as validation cases: (A) acid ellagic–CK2, (B) SASP–GSTP1-1, (C) benzen-1,2-diol–PRDX5, (D) (S)-naproxen–HAS, (E) (S)-fluoxetine–LeuT, and (F) NECA–hA2A AR.

CK2 is a ubiquitous and constitutively active serine/threonine kinase (PK) that phosphorylates more than 300 substrates. It is involved in the regulation of numerous cellular processes such as cycle progression, apoptosis, transcription, and viral infection [40]. The catalytic alpha subunit is composed by two lobes connected by a small loop called the "hinge region". The N-terminal lobe presents five β-strands, and the α-helix C is involved in the substrate recognition, whereas the C-terminal lobe is composed of α-helices. All PKs present a glycine-rich loop (Ploop), an activation loop, and a catalytic loop [40]. The X-ray complex highlights that the inhibitor binds to Lys49, Ser51, and His160 as shown in Figure 4A [41].

Glutathione S-transferases (GSTs) are homodimeric phase II detoxification enzymes, active in the bioconjugation of glutathione (GSH) to a wide range of both endogenous and exogenous molecules. The catalytic region of GSTs is topologically subdivided in two different site: (i) the G-site, selective for GSH recognition and highly conserved crosswise GSTs isoforms and (ii) the H-site, less conserved and responsible for the binding of electrophilic molecules [42]. Isoform P1-1 probably represents the most studied GST and has been related to the development of tumors resistance toward numerous anticancer drugs [43]. SASP, which is able to inhibit GSTs without acting as a cosubstrate for the conjugation reaction with GSH, has been cocrystallized with GSTP1-1 and represents a starting point for structure-based design of new anticancer drugs [44]. The X-ray complex (Figure 4B) highlights that the inhibitor binds to a hydrophobic pocket formed by Phe8, Val10, Val35, Ile10,4 and Tyr108 side-chains. The SASP phenyl ring and salicylic acid moiety are engaged in π–π stacking interactions with the aromatic side chain of Phe8 and Tyr108, respectively, while the carboxylate group of the ligand is involved in an electrostatic interaction with the Arg13 side chain.

To extend the SuMD capabilities on low affinity ligand, we selected the recently solved structure of PRDX5 in complex with a benzen-1,2-diol [45]. PRDX5 belongs to the ubiquitary peroxiredoxin family whose role relies on the hydrogen peroxide and alkyl hydroperoxides reduction. PRDX5 plays a remarkable role in postischemic inflammations in the brain [46, 47]. The catechol was identified by a fragment-based screening, and the dissociation constant was estimated in the millimolar range (K_d = 1.5 ± 0.5 mM). More interestingly, the system was extensively characterized by NMR spectroscopy both with structure-based experiments and ligand-based experiments, resulting in a solid model system for a low-affinity binding event [45]. In the X-ray complex (Figure 4C), the catechol ring is localized to the N-terminus of the second helix establishing a hydrogen bond network with the backbone nitrogen of Gly46 and Cys47 residues. The side chain of Arg127 is oriented toward the hydroxyl moiety and contributes to the binding with an additional hydrogen bond. Similarly, the thiol group of Cys47 is faced to the catechol. Pro40, Leu116, and Phe120 establish hydrophobic interactions with the aromatic ring.

Human serum albumin (HSA) is a deeply investigated protein for its ability to bind a wide range of different molecules in human plasma. (*S*)-naproxen strongly binds HSA and more interestingly in different sites depending on the presence of other small molecules (e.g., hormones, xenobiotic, fatty acids) [48, 49]. The only structure available for this complex was obtained in the presence of decanoic acid driving the accommodation of the naproxen molecule in the IB site, a vast and hydrophobic pocket where a multitude of different ligands can be hosted [49]. In the IB site, (*S*)-naproxen inserts its naphthalene scaffold within the hydrophobic pocket and interacts directly with the aliphatic tail of decanoic acid and the residues Ile142, Phe157, and Tyr161 (Figure 4D). The carboxylic group is partially exposed to the solvent but is surrounded by several charged residues forming the entrance of the pocket: Arg145, Lys 190, and in particular, Arg186.

The neurotransmitter sodium symporter (NSS) family includes the human serotonin transporter (SERT), norepinephrine transporter (NET), and dopamine transporter (DAT) [50]. To date, there is a lack of focused information about the structure of these important therapeutic targets. In the recent past, the crystallographic structure of the LeuT from *Aquifex aeolicus* (a NSS family member) has been disclosed with the aim of better understanding the basis of selective serotonin reuptake inhibitors (SSRIs) activity toward serotonin transporters [51]. The LeuT-(*S*)-fluoxetine X-ray complex (Figure 4E) highlights hydrophobic contacts between the inhibitor and Leu29, Arg30, Tyr108, and Phe253 side chains. The (*S*)-fluoxetine secondary amino group points toward the extracellular space and engages Asp401 in an electrostatic interaction, while the extracellular gate is locked by the salt bridge between Asp404 and Arg30.

Moving to the last key study, adenosine receptors (ARs) belong to the GPCRs superfamily. The known four subtypes, termed adenosine A_1, A_{2A}, A_{2B}, and A_3 receptors, are widely distributed in the human body, involved in several physio-pathological processes, and represent potential targets for the treatment of several diseases [52]. In the past decade, X-ray structures of the $hA_{2A}AR$ in complex with agonists and antagonists have been released, thus offering the basis for molecular modeling investigation [53] including also SuMD simulations [7, 54, 10]. Here, we focus on the complex with NECA [55] (Figure 4F) that features a strong polar interaction between the exocyclic amine group of NECA and the side chain of the conserved Asn253 residue; a hydrogen bond with the nitrogen atom of NECA acetamide moiety and the Thr88 side chain; and an aromatic π–π stacking with the conserved Phe168, located in the second extracellular loop (EL2), and hydrophobic contacts with, among others, the Leu249 side chain.

A summary of the SuMD simulation performed on the selected case studies is reported in Table 2. For each replica, the productive simulation time is reported, and for the simulation in which the ligand reached the binding site ($dcm_{(L-R)} < 5$ Å), a brief statistical analysis about the comparison with the final state and the experimentally solved structure is reported.

Table 2 SuMD Results Summary[a]

			Distance $dcm_{(L-R)} < 5$ Å		
System	**Replica**	**Time [ns]**	**RMSDmin [Å]**	**RMSDmax [Å]**	**RMSDave [Å]**
		Globular Systems			
Ellagic Acid–CK2	1	25.21	4.85	6.1	5.39
Ellagic Acid –CK2	2	19.81	4.62	6.55	5.25
Ellagic Acid –CK2	3	24.01	-	-	-
SASP –GSTP1-1	1	21.01	10.08	13.87	11.76
SASP –GSTP1-1	2	27.01	2.04	7.98	5.74
SASP –GSTP1-1	3	19.21	2.07	7.55	5.3
Benzen-1,2-diol –PRDX5	1	17.41	1.25	5.88	3.04
Benzen-1,2-diol –PRDX5	2	31.21	1.12	7.35	2.99
Benzen-1,2-diol –PRDX5	3	18.01	0.69	5.95	2.98
(S)-naproxen –HSA	1	13.21	4.77	11.99	7.54
(S)-naproxen –HSA	2	26.41	-	-	-
(S)-naproxen –HSA	3	27.01	-	-	-
		Transmembrane Systems			
(S)-fluoxetin –LeuT	1	19.21	7.65	8.46	8.13
(S)-fluoxetin –LeuT	2	18.61	-	-	-
(S)-fluoxetin –LeuT	3	12.01	-	-	-
NECA–hA2A AR	1	27.61	4.41	7.59	5.98
NECA–hA2A AR	2	22.21	4.35	7.67	5.59
NECA–hA2A AR	3	27.01	4.44	6.44	5.34

[a]For each system, the result of three replicas are reported within their simulation time. The RMSD minimum, maximum, and average are computed considering only the frames that present a dcm(L-R) lower than 5 Å.

3.2 Globular Systems

3.2.1 Ellagic Acid–CK2 Recognition Pathway

In the starting geometry, the ligand was placed at a distance of 50 Å from the binding site. After the initial randomization step, the distance reduced to 43 Å. As depicted in Figure 5A and shown in Video S1, the first interaction between the ligand and the protein is established after 2 ns of productive trajectory and is mediated by Lys49 that directs the ligand to the P-loop of the kinase. As shown by the Pollicino analysis (Figure 5B), the ellagic acid approaches the region of the P-loop and mostly interacts with the Arg47, Lys49, Glu53, and the Lys71 (Figure 5A). These residues describe an interaction site at 10.5 Å where the ligand resides for about 6 ns. In fact, the ligand RMSD plot (Figure 5C) records stable values in the 2–8 ns time lapse. The IE with the protein in this site is about −20 kcal/mol (Figure 4D at $dcm_{(L-R)}$ = 10 Å). The per residue contacts count graph (Figure 5E) highlights that the above-mentioned residues are those establishing the greatest number of contacts, whereas the corresponding 3D models helps in identifying their location (Figure 5F) and the chronological order at which they have been approached by the ligand (Figure 6A). Approximately after 7 ns of simulation, the ligand moves toward the orthosteric site, where Leu45 stabilizes its conformation and the side-chain of His160 hampers its passage. Through an interaction mediated by Arg43, the ligand overcomes the His160 gate and reaches a new interaction site described by Asp120, Arg47, and Met163. The permanency in this site is about of 2 ns with an IE of −51 kcal/mol (Figure 5C,D). Consistently, the RMSD plot presents another plateau in the time range of 8–10 ns (Figure 5C) that corresponds to the swarm of dots in the IE Landscape at $dcm_{(L-R)}$ = 11 Å (Figure 5D). A further stabilizing interaction with the Asn118 induces a shift in the ligand position that places the ring system parallel to the β7−β8 strands (Video S1). As shown in the cumulative ligand–protein IE (Figure 6B) and its corresponding decomposition into electrostatic and van de Waal contributions (Figure 6C and D, respectively), the change in the slope indicates that new conformation has a lower interaction energy than the previous one. In particular, as highlighted by the comparison of the graphs relative to the electrostatic and van der Waals contributions (Figure 6C and D, respectively), the stabilization can be ascribed by the establishment of an electrostatic interaction with Asp175. As result of the new interaction, the ligand moves into the orthosteric site (Figure 6E) and interacts with Lys159, Val66, Val116, Val53, His115, and Lys68 by maintaining the same position until the end of the SuMD simulation. The RMSD plot shows another plateau from 10 ns to the end, whereas the IE landscape indicates that in this time lapse the ligand is at a distance around 2.5 Å with an IE between −40 ando −70 kcal/mol.

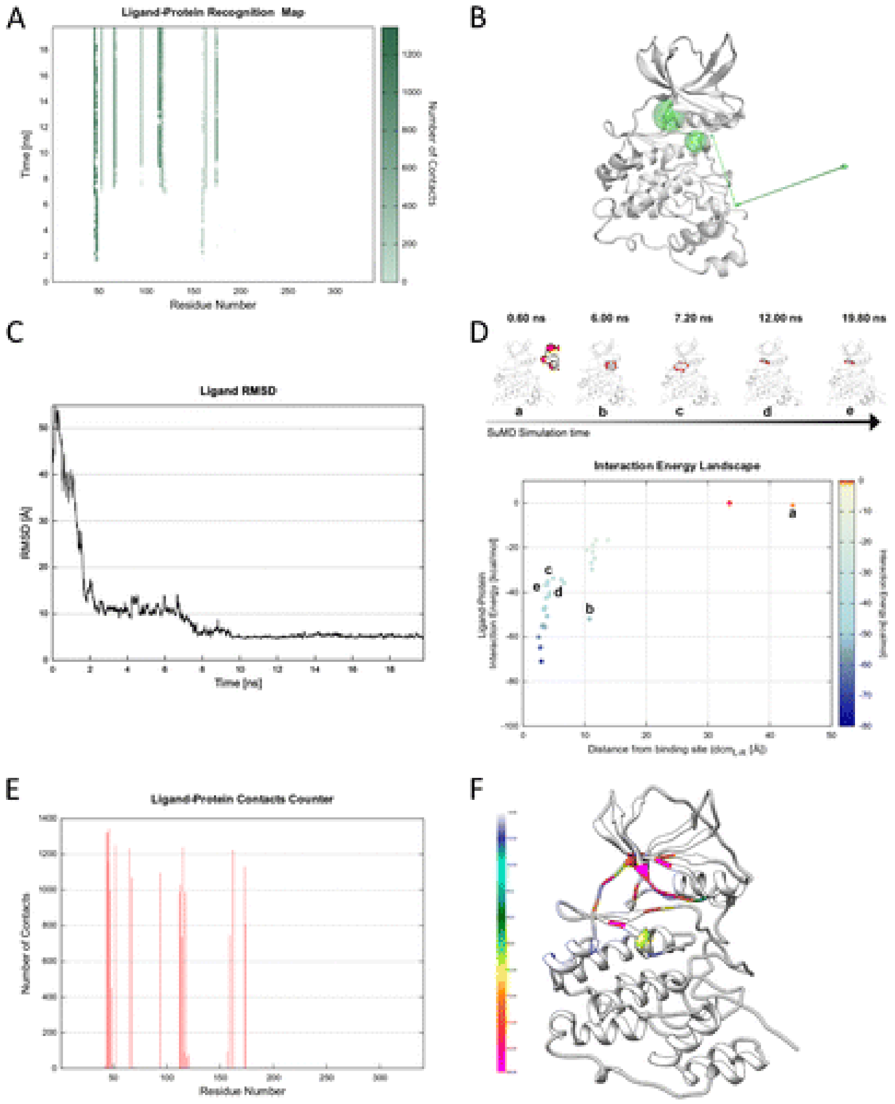

Fig. 5 Ellagic acid–CK2 recognition pathway: (A) ligand–protein recognition map, (B) Pollicino analysis, (C) ligand–RMSD, and (D) IE landscape, (E) ligand–protein contacts count, and (F) chimera contacts.

The simulation was replicated three times, and the replicas analysis results are reported in Figure 7. In particular, the RMSD plot indicates that one replica does not reach the orthosteric site (Figure 7A, green line), whereas the others reach the same final RMSD value. The same conclusion arises from the investigation of the Pollicino analysis where the ligand pathway of the two replicas converge in the proximity of the protein (Figure 7B, red and blue spheres). The per replica IE landscape helps in explaining why the third replica does not reach the orthosteric site; as indicated by the green dots in Figure 7C, the ligand reaches a different interaction site with an IE of −60 kcal/mol, a value close to the IE of the replicas that converges into in the orthosteric site (Figure 7C, red and blue dots). This consideration is confirmed by the trend of the per replica cumulative IE that highlights a more negative slope for the third replica (Figure 7D, green line), indicating a very strong interaction.

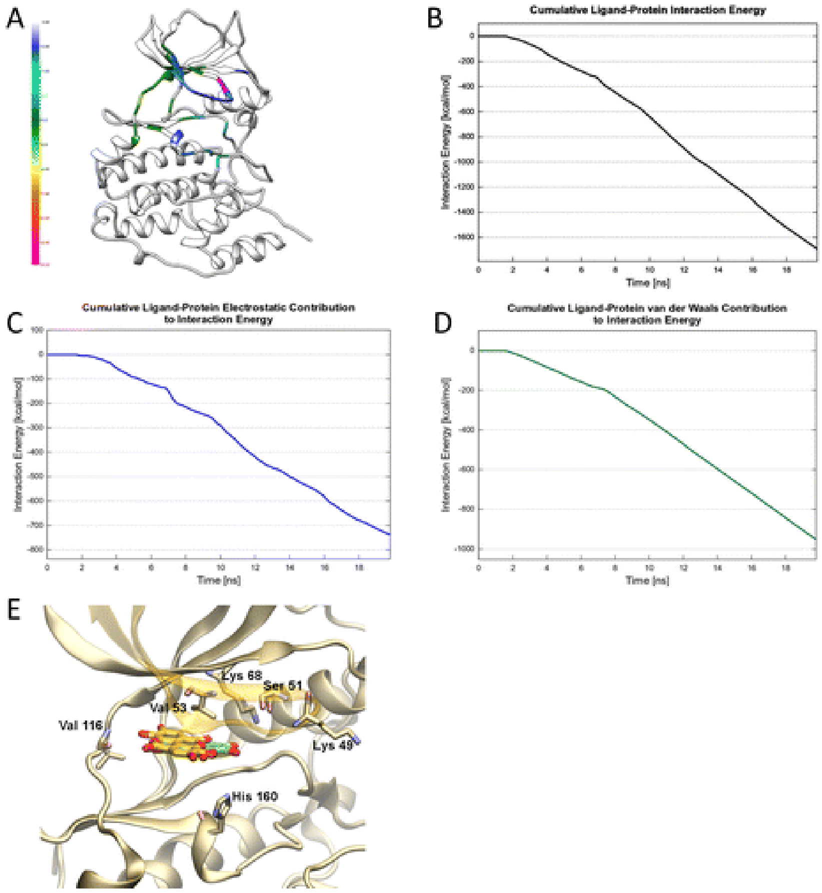

Fig. 6 Ellagic acid–CK2 recognition pathway: (A) chimera time, B) cumulative IE, (C) cumulative IE electrostatic contribution, (D) cumulative IE van der Waals contribution, and (E) superimposition between SuMD endpoint conformation (gold) and the X-ray binding mode (green). The residues interacting with the ligand are labeled in black, except the ones detected only in the X-ray complex that are labeled in green.

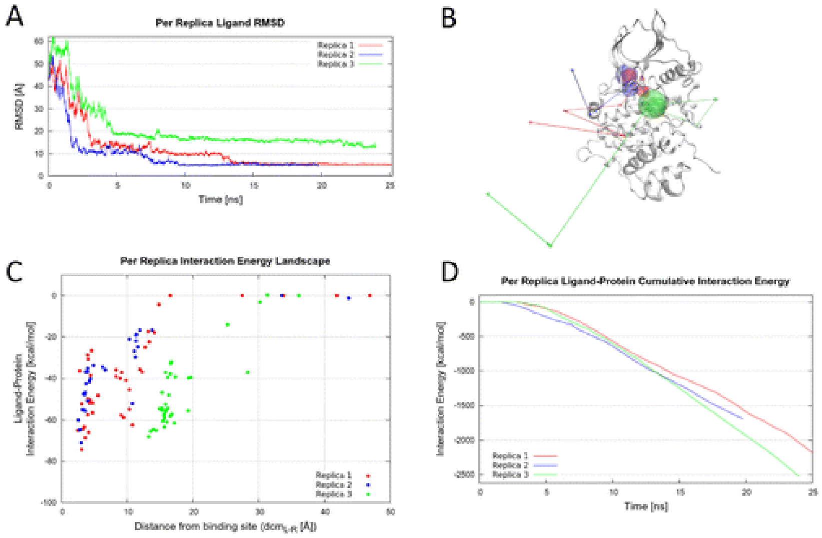

Fig. 7 Ellagic acid–CK2 recognition pathway: (A) per replica ligand RMSD, (B) per replica Pollicino analysis, (C) per replica IE landscape, and (D) per replica cumulative IE.

In order to compare the role of the supervision in reducing the computation time, we performed 1 µs of classical MD simulation using the same starting geometry of the SuMD simulation (Video S7) in which the ligand was placed at a distance of 50 Å from the binding site. As expected, during the classical simulation, the ligand did not approach the protein in agreement with the results previously obtained also for other systems [7].

3.2.2 SASP–GSTP1-1 Recognition Pathway

During the SuMD simulation, the SASP reaches the GSTP1-1 catalytic H site in less than 6 ns (Video S2). The IE landscape highlights the formation of the first protein–ligand stabilizing interaction when the ligand and protein H site distance is 15 Å (point a, Figure 8A,B). In this preliminary complex, SASP engages the Gly205 backbone oxygen in a hydrogen bond interaction through its sulfamide nitrogen atom and establishes an aromatic π–π stacking interaction between the salicylic moiety and Tyr108 (interactions corresponding to the first continues lines in the protein–ligand recognition map, Figure 8C).

This situation anticipates a ligand positional shift that allows the SASP salicylic carboxylate to approach the positively charged Arg13 side chain, while the benzene ring replaces the salicylic aromatic moiety in the π–π stacking interaction with Tyr108 (point b, Figure 8A).

The energy stabilization of the complex increases, and after 8 ns of simulation, SASP proceeds toward a farther conformation, able to gain a more favorable interaction geometry with Arg13 side chain, after the displacement of two water molecules from the solvation sphere of the positively charged residue. This new pose (point c, Figure 8A,B) is retained until the end of SuMD simulation, with the exception of conformational changes occurring to the pyridylsulfamoyl moiety, able to fit in the hydrophobic pocket delimited by Phe8, Val35, and Trp38. During the SASP–GSTP1-1 recognition event, GSH remains in the catalytic G site of the enzyme, not interacting with the inhibitor.

Figure 8D highlights all the residues involved in the interaction with SASP during the SuMD simulations; the selective contacts toward only one enzymatic subunit, as well as the topologically restricted area interested, are well defined by the ribbon colorations. Considering the SASP crystallographic conformation as a geometrical reference, the ligand RMSD analysis (Figure 8E) reaches a minimum after 15 ns of simulation (Figure 8F) before stabilizing around a value of about 5 Å. Figure S2 reports other ligand–protein IE analyses. The replicas analysis (Figure S3) depicts a recognition event with no metastable binding sites, characterized by almost a univocal pathway. Nevertheless, in one replica, in the final complex SASP is rotated by 180° (as highlighted by the higher RMSD value) and loses the electrostatic stabilization between its salicylic moiety and Arg13 side chain.

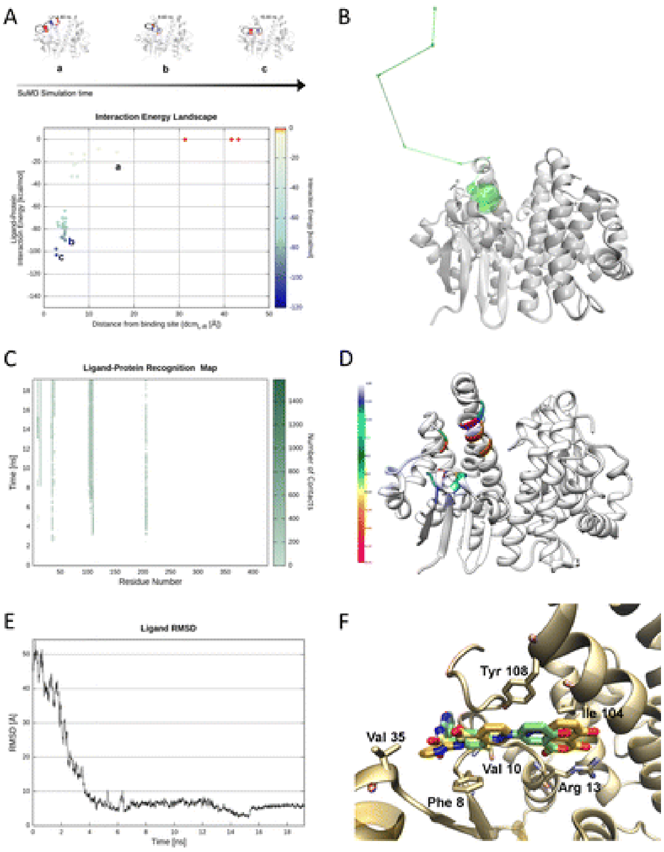

Fig. 8 SASP–GSTP1-1 recognition pathway: (A) landscape, (B) Pollicino analysis, (C) ligand–protein recognition map, (D) chimera, (E) ligand–RMSD, and (F) superimposition between SuMD endpoint conformation (gold) and the X-ray binding mode (green). The residues interacting with the ligand are reported.

3.2.3 Benzen-1,2-diol–PRDX5 Recognition Pathway

The simulations were repeated on both the monomeric and dimeric forms yielding similar results. However, here we focus on the dimeric form according to solution NMR studies, in which the authors stated the protein as dimer [56]. At the beginning of randomization step, the fragment was placed at 78 Å from PRDX5 binding site ($dcm_{(L\text{-}R)}$ = 78 Å). As reported in Figure 9A (point b), B, and C, after nearly 3 ns, the fragment approaches the protein in a region located at around 30 Å from the primary binding site (Video S3). This meta-binding site lies in the opposite monomeric subunit with respect to the primary binding site, and it is defined by residues Leu62, Lys63, Val69, and Val70. As shown by the IE landscape and the Pollicino analysis (Figure 9A and B, respectively), this site engages the ligand in favorable interactions for a couple of nanoseconds. In particular, the formation of a hydrogen bond between the hydroxyl groups of catechol and the carbonyl moiety of the backbone amide of residue Lys95 stabilizes this conformation. After nearly 6 ns, the fragment is released by this site and fluctuates to finally reach the primary binding site through a series of molecular interactions, including residues (chronologically sorted) Glu91, Glu16, Glu18, and Phe79 belonging to the first monomer unit (Figure S4). Finally, the fragment accesses the binding site where it fluctuates experimenting different conformations in accordance with its affinity in the millimolar range. The fluctuations of the fragment in the binding site are also evident in the protein–ligand energy profiles, in which the energy wavers around the value of −20 kcal/mol (Figure S4). During the fluctuation, the catechol contacts most of the residue forming the site, in particular (sorted by number of molecular contacts during the trajectory) Thr147, Thr44, Arg127, Phe120, Leu116, Gly46, and Cys47 (Figure 9C,D). The main conformation observed corresponds to the crystallographic one, as reported in Figure 9E and F where the RMSD reaches a minimum value 0.69 Å at 17.3 ns.

The simulation was repeated in thriplicate randomizing the position of the ligand. The replicas analysis is reported in Figure S5. Briefly, in each replica, the fragment reached the primary binding site experiencing the conformation reported in the crystallographic data with the best RMSD of 1.12 and 1.24 Å for replica 2 and 3, respectively.

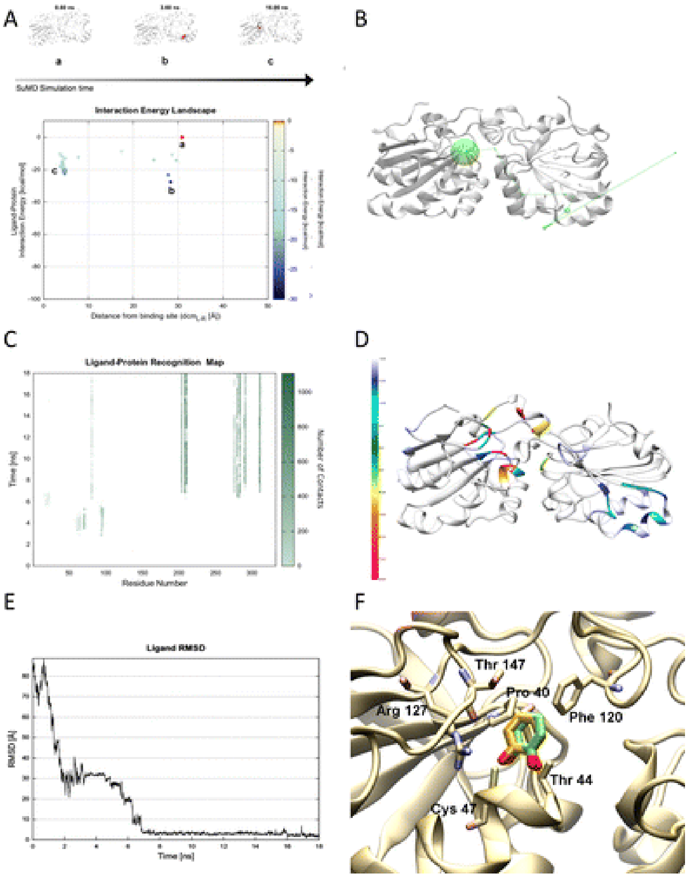

Fig. 9 Benzen-1,2-diol–PRDX5 recognition pathway: (A) landscape, (B) Pollicino analysis, (C) ligand–protein recognition map, (D) chimera, (E) ligand–RMSD, and (F) superimposition between SuMD endpoint conformation (gold) and the X-ray binding mode (green). The residues interacting with the ligand are reported.

3.2.4 (S)-Naproxen–HAS Recognition Pathway

The SuMD simulation was performed maintaining decanoic ligand in the IB site according the crystallographic geometries. (*S*)-Naproxen was separated from the HSA-decanoid acid complex by placing it 32 Å far from the IB site (point a, Figure 10A,B). In the first SuMD step, the ligand fluctuates until 50 Å from the IB site. As reported in Figure 10C, after a couple of nanoseconds, the ligand approaches the first protein site by engaging Lys510 and Thr564 (Video S4). Shortly after, the ligand establishes a network of interaction for 1 ns (from 2.3 to 3.2 ns) in a site located at around $\mathrm{dcm}_{(\mathrm{L\text{-}R})}$ = 20 Å (point b, Figure 10A), defined by residues Val116, Pro118, Val122, Thr133, and Phe134. Then, the molecule approaches a second site, where it fluctuates for about 3 ns by establishing strong interaction with residues Leu115, Pro118, Lys137, and Ile142 (as also evident from protein–ligand interaction energy in Figure S6). This meta-binding site is located in front of the principal binding site to which is separated by the presence of a long extended loop (residue 106 to 119) that acts as a gate for the IB site. Finally, after 6 ns, (*S*)-naproxen is able to pass behind the extended loop and reach the IB site (residues Leu115, Ile142, Phe157, and Tyr161) as shown by Figure 10B and E. Within the primary site, the ligand is able to place the methyl ether group in the proximity of Phe157 with an orientation very similarly to the one observed in the crystal structure. On the other hand, the naphthalene core and, in particular, the carboxylic group adopts a different position due to the presence of the extended loop. This different orientation abolishes the ionic interaction between the carboxyl group and the Arg117 observed in the crystallographic structure (Figure 10F). At the end of the simulation, the RMSD fluctuates around 5 Å, reaching the lowest value of 4.76 at 12.70 ns (Figure 10E,F).

Interestingly, in the other replicas (Figure S7), the ligand reaches the IB site by approaching the extended loop from a different position and occupies a slightly different location in the vast IB site. This suggests that the loop might have a crucial role in the recognition process (Figure S7).

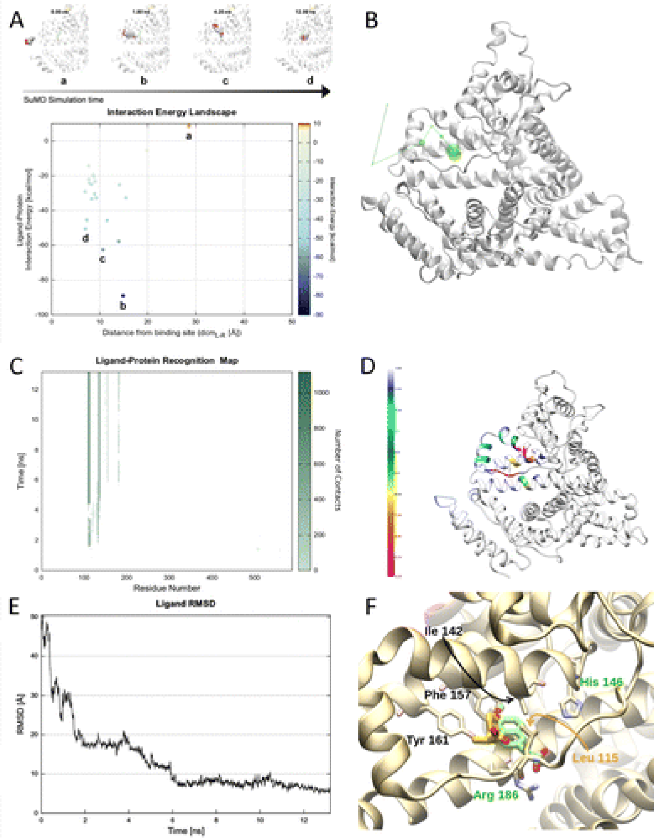

Fig. 10 (S)-Naproxen–HAS recognition pathway: (A) landscape, (B) Pollicino analysis, (C) ligand–protein recognition map, (D) chimera, (E) ligand–RMSD, and (F) superimposition between SuMD end point conformation (gold) and the X-ray binding mode (green). The residues interacting only with the cocrystallized ligand are labeled in green, whereas the ones interacting in SuMD are labeled in gold. The labels of the residues present in both cases are colored in black.

3.3 Transmembrane Systems

3.3.1 (S)-Fluoxetine–LeuT Recognition Pathway

The (*S*)-fluoxetine recognition pathway highlights, after 1 ns of SuMD simulation, a first electrostatic interaction between the Asp 158 side chain and the charged secondary amine group of the ligand (Video S5). The energetic stabilization characterizing this complex corresponds to the IE landscape minimum reported in Figure 11A (point a) and B. This preliminary complex is able to favor the ligand approach toward an inner pocket of LeuT, topologically defined by Tyr471 and the aliphatic chains of Lys474 and Glu478, reciprocally involved in an ionic interaction. Hydrophobic contacts stabilize this intermolecular complex for about 2 ns, before a conformational change allows (*S*)-fluoxetine to establish a more favorable electrostatic interaction with the Glu402 side chain.

This scenario anticipates the ligand repositioning inside an inner hydrophobic site, where the ligand engages for almost 7 ns Tyr471, Trp406, Ile475, and Phe405 side chains in lipophilic interactions through its phenyl ring (point b, Figure 11A,B).

During the remaining simulation time, the inhibitor makes contacts with Ala319 (EL4) and the side chains of the key residues Asp404 and Arg30 (point c, Figure 11A,B, and continuous lines corresponding to the last 4 ns of SuMD simulation, Figure 11C), both located at the protein extracellular gate and involved in a ionic lock that sterically obstructs the SSRIs binding site disclosed by the LeuT crystallographic structure. Figure 11D summarizes all the amino acids involved in the (*S*)-fluoxetine recognition event during the SuMD simulation.

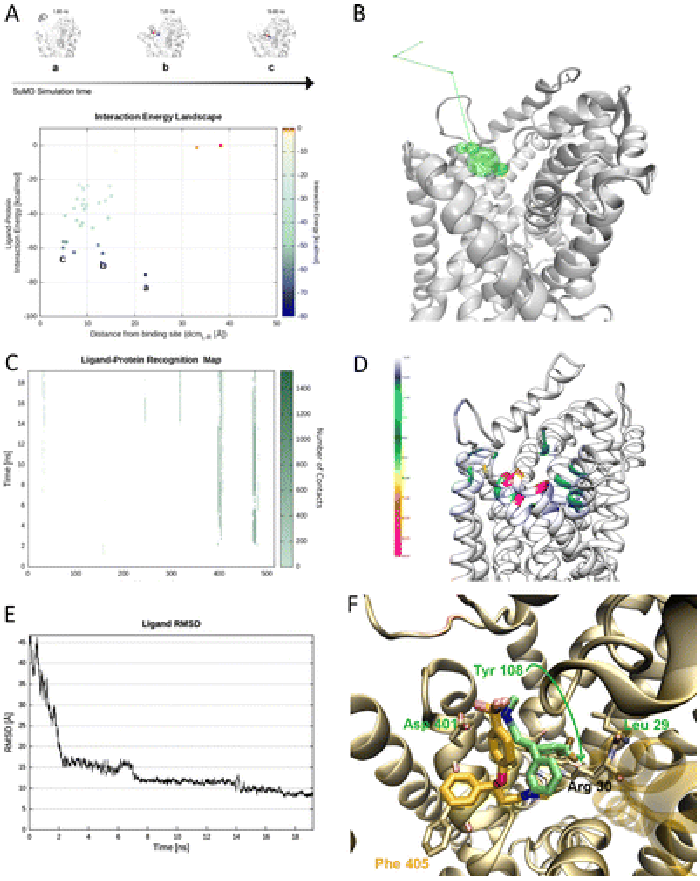

Fig. 11 (S)-Fluoxetine–LeuT recognition pathway: (A) landscape, (B) Pollicino analysis, (C) ligand–protein recognition map, (D) chimera, (E) ligand–RMSD, and (F) superimposition between SuMD endpoint conformation (gold) and the X-ray binding mode (green). The residues interacting only with the cocrystallized ligand are labeled in green, whereas the ones interacting in SuMD are labeled in gold. The labels of the residues present in both the cases are colored in black.

The RMSD plot (Figure 11E) outlines the inhibitor difficulty in reproducing the experimental pose (Figure 11F). Investigation of the LeuT crystal structure without a cocrystallized inhibitor reveals an alternative conformation of the Arg30 side chain and the absence of the ionic lock (Figure S12) [57]; it is possible to speculate that the extracellular gate in LeuT, during the SuMD simulation time scale, is able to remain in a stable conformation, previously induced by the inhibitor binding and retained even after the removal of the ligand during the preparation of the system for SuMD simulations.

Replicas analysis (Figure S9) highlights two alternative recognition pathways through the extracellular vestibule that do not reproduce the binding mode observed in the crystallographic complex and are characterized by accentuated energy variations in proximity of the extracellular transporter gate.

3.3.2 NECA–hA$_{2A}$ AR Recognition Pathway

NECA establishes the first stabilizing contacts with the hA$_{2A}$ AR after about 4 ns of SuMD simulation (Video S6). During this initial scenario (point a, Figure 12A,B), the ligand approaches the protein topological structure defined by ECL2, the N-terminus, and the residues located at top of TM5 and TM6. More precisely, NECA engages the Phe257 (TM6) side chain in a π–π stacking interaction through its purine scaffold and locates the N-ethylcarboxamido moiety toward a pocket delimited by Trp143 (ECL2), Pro173 (ECL2), and Asn175 (TM5) side chains, as highlighted by the first stripes in Figure 12C and the yellow and violet ribbons in Figure 12D.

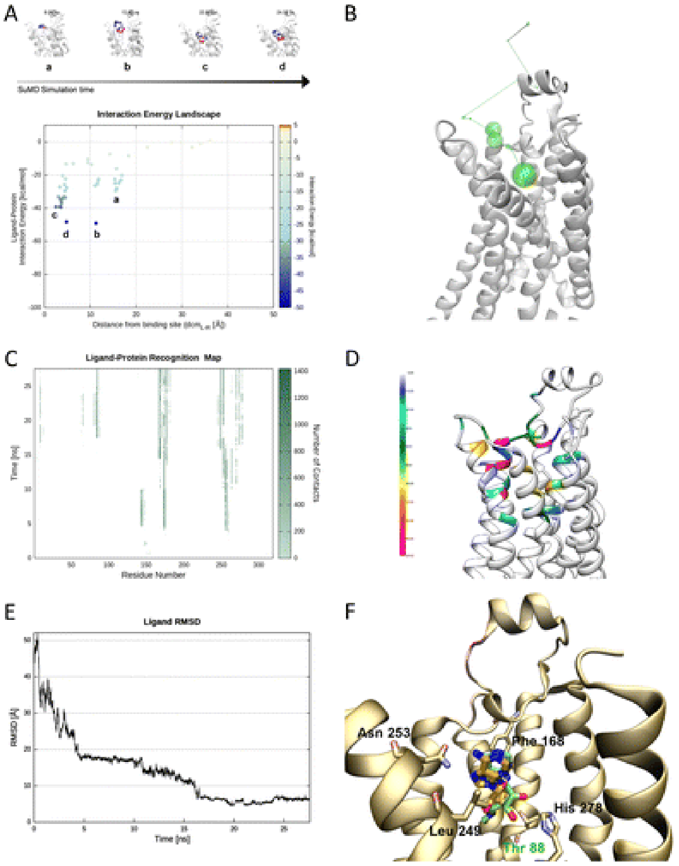

Fig. 12 NECA–hA2A AR recognition pathway: (A) landscape, (B) Pollicino analysis, (C) ligand–protein recognition map, (D) chimera, (E) ligand–RMSD, and (F) superimposition between SuMD endpoint conformation (gold) and X-ray binding mode (green). The residues interacting with the ligand are labeled in black, except the ones detected only in the X-ray complex that are labeled in green.

This complex anticipates a repositioning that allows the ligand to reach a meta-stabile binding site, mainly characterized by a π–π stacking interaction with His264 (EL3) side chain, an hydrophobic contact in the direction of Met174 (TM5) side chain, and a hydrogen bond interaction between its C2′ hydroxide group and Asn253 (TM6) (point b, Figure 12A,B).

During the time slot rising from 14 to 20 ns of SuMD simulation, the agonist reaches a deeper position inside the orthosteric binding site and explores different conformations (included a temporary *anti*–*syn* transition about the glycoside linkage), until it engages the Phe168 (ECL2) side chain in a π–π stacking interaction and an Asn253 (TM6) side chain in hydrogen bond interactions through its exocyclic amine and the N7 position of the purine scaffold (point c, Figures 12A,B). This complex orientation (associated with the minimum RMSD value in Figure 12E, with respect to the NECA crystallographic conformation) is followed by an alternative stabilized conformation (point d, Figure 12A,B) which involves also hydrophobic interactions with Leu249 (TM6), Leu85 (TM3), and Val84 (TM3). Data from mutagenesis experiments confirm the involvement of some residues highlighted by the SuMD simulations. More precisely, there is strong evidence about the recruitment of Phe257, Asn253, and Phe168 side chains during agonists recognition [58].

During the remaining SuMD simulation time, the protein–ligand complex geometry remains almost unaltered, with the exception of a reorientation of the N-ethylcarboxamidoribose moiety, pointing toward TM4, and the loss of the aromatic π–π interaction due to a conformational change occurring to Phe168 (EL2) side chain. In Figure S10, other ligand–protein energy interaction analyses are reported.

At the minimum RMSD value, NECA pyrimidine scaffold coincides with the crystallographic orientation, while the ribose moiety is oriented in an alternative conformation (Figure 12F).

Replicas analysis (Figure S11) highlights also a different NECA recognition pathway, which involves residues located at the ECL2 and characterized by comparable energetic stabilizations.

4. Conclusions

In the present work, we have demonstrated the general applicability of SuMD simulations using different types of targets, including both globular and membrane proteins. Moreover, we have presented the SuMD-Analyzer tool that helps, also a nonexpert user, in the analysis of the SuMD trajectories. Even if various other MD methods have also been used to characterize binding pathways, SuMD has the great advantage of being able to explore the ligand–protein approaching path in the nanosecond simulation time scale. Furthermore, SuMD simulations enable the investigation of ligand–protein binding events independently from the starting position and chemical structure of the ligand, and also from its target binding affinity. As described for each key study, SuMD simulations are able to characterize multiple ligand–protein binding pathways identifying a variety of metastable intermediate states (meta-binding sites). This information may be an interesting starting point for further argumentations regarding the pharmacological consequences of that specific ligand–protein recognition process. Moreover, it is worthy to underline that, contrary to the expectations, not all SuMD trajectories converge to the structure of the complex obtained by X-ray crystallography. Indeed, there are several plausible reasons that may be argued to describe this particular unexpected behavior: (a) The crystallographically pose of the ligand is not the only minimum of the potential energy surface described by the force field during the SuMD simulations. (b) The crystallographically conformation of the protein in its bound state is remarkably different with respect to its apo-form. This could be interpreted as the sign of an important induce-fit process during the ligand recognition. (c) The boundary conditions that led to the formation of the crystallographically ligand–protein complex (solvent and cosolvent, pH, ionic strength, or temperature just as a few examples) are not well described during the SuMD simulations. This must always be kept in mind when making any conjecture from the analysis of SuMD trajectories. Currently, a major effort is underway to estimate, from SuMD simulations, binding kinetics properties (in particular on-rate values) in approximate agreement with experimental measurements.

One of the key aspects is the notably reduction of the time needed to obtain a SuMD trajectory in comparison to classical MD; the computation time is in the range from a few hours to tens of hours for the presented case studies. Thanks to these performances, a second effort will be addressed to extend the number of replicas with the aim to investigate the convergence of the pathway in sampling a bigger number of states. Hopefully, the future of drug design will involve detailed characterization of not only the bound state but also the whole ligand–protein network of recognition pathways, including all metastable intermediate states (meta-binding sites). With such a complete understanding, we hope to expand our perspectives in several scientific areas from molecular pharmacology to drug discovery.

References

1. Böhm H-J, Schneider G, Mannhold R (2003) Protein-Ligand Interactions: From Molecular Recognition to Drug Design. Wiley-VCH Verlag GmbH & Co. KGaA:Weinheim, Germany

2. Pan AC, Borhani DW, Dror RO, Shaw DE (2013) Molecular determinants of drug-receptor binding kinetics. Drug Discov Today 18:667–673

3. Moro S, Hoffmann C, Jacobson KA (1999) Role of the extracellular loops of G protein-coupled receptors in ligand recognition: a molecular modeling study of the human P2Y1 receptor. Biochemistry 38:3498–3507

4. Dror RO, Jensen MØ, Borhani DW, Shaw DE (2010) Exploring atomic resolution physiology on a femtosecond to millisecond timescale using molecular dynamics simulations. J Gen Physiol 135:555–562

5. Buch I, Giorgino T, De Fabritiis G (2011) Complete reconstruction of an enzyme-inhibitor binding process by molecular dynamics simulations. Proc Natl Acad Sci U S A 108:10184–10189

6. Johnston JM, Filizola M (2014) Beyond standard molecular dynamics: investigating the molecular mechanisms of G protein-coupled receptors with enhanced molecular dynamics methods. Adv Exp Med Biol 796:95–125

7. Sabbadin D, Moro S (2014) Supervised molecular dynamics (SuMD) as a helpful tool to depict GPCR-ligand recognition pathway in a nanosecond time scale. J Chem Inf Model 54:372–376

8. Ciancetta A, Sabbadin D, Federico S, Spalluto G, Moro S (2015) Advances in Computational Techniques to Study GPCR-Ligand Recognition. Trends Pharmacol Sci 36:878–890

9. Sabbadin D, Ciancetta A, Deganutti G, Cuzzolin A, Moro S (2015) Exploring the recognition pathway at the human A2A adenosine receptor of the endogenous agonist adenosine using supervised molecular dynamics simulations. Medchemcomm 6:1081–1085

10. Deganutti G, Cuzzolin A, Ciancetta A, Moro S (2015) Understanding allosteric interactions in G protein-coupled receptors using Supervised Molecular Dynamics: A prototype study analysing the human A3 adenosine receptor positive allosteric modulator LUF6000. Bioorg Med Chem 23:4065–4071

11. Paoletta S, Sabbadin D, von Kügelgen I, et al (2015) Modeling ligand recognition at the P2Y12 receptor in light of X-ray structural information. J Comput Aided Mol Des 29:737–756

12. Harvey MJ, Giupponi G, Fabritiis GD (2009) ACEMD: Accelerating Biomolecular Dynamics in the Microsecond Time Scale. J Chem Theory Comput 5:1632–1639

13. D.A. Case, V. Babin, J.T. Berryman, R.M. Betz, Q. Cai, D.S. Cerutti, T.E. Cheatham, III, T.A. Darden, R.E.Duke, H. Gohlke, A.W. Goetz, S. Gusarov, N. Homeyer, P. Janowski, J. Kaus, I. Kolossváry, A. Kovalenko,T.S. Lee, S. LeGrand, T. Luchko, R. Luo, B. Madej, K.M. Merz, F. Paesani, D.R. Roe, A. Roitberg, C. Sagui,R. Salomon-Ferrer, G. Seabra, C.L. Simmerling, W. Smith, J. Swails, R.C. Walker, J. Wang, R.M. Wolf, X.Wu and P.A. Kollman (2014) AMBER 14.

14. Wang J, Wolf RM, Caldwell JW, Kollman PA, Case DA (2004) Development and testing of a general amber force field. J Comput Chem 25:1157–1174

15. MacKerell AD, Banavali N, Foloppe N Development and current status of the CHARMM force field for nucleic acids. Biopolymers 56:257–265

16. Vanommeslaeghe K, Raman EP, MacKerell AD (2012) Automation of the CHARMM General Force Field (CGenFF) II: assignment of bonded parameters and partial atomic charges. J Chem Inf Model 52:3155–3168

17. Vanommeslaeghe K, MacKerell AD (2012) Automation of the CHARMM General Force Field (CGenFF) I: bond perception and atom typing. J Chem Inf Model 52:3144–3154

18. Berman HM, Westbrook J, Feng Z, Gilliland G, Bhat TN, Weissig H, Shindyalov IN, Bourne PE (2000) The protein data bank. Nucleic Acids Res 28:235–242

19. Chemical Computing Group (CCG) Inc. (2014.09) Molecular Operating Environment (MOE). http://www.chemcomp.com

20. Labute P (2009) Protonate3D: assignment of ionization states and hydrogen coordinates to macromolecular structures. Proteins 75:187–205

21. Stewart J J P MOPAC2012, Version 2012. http://OpenMOPAC.net

22. Stewart JJP (2007) Optimization of parameters for semiempirical methods V: modification of NDDO approximations and application to 70 elements. J Mol Model 13:1173–1213

23. Frisch M J, Trucks G W, Schlegel H B, Scuseria G E, Robb M A, Cheeseman J R, Scalmani G, Barone V, Mennucci B, Petersson G A, Nakatsuji H, Caricato M, Li X, Hratchian H P, Izmaylov A F, Bloino J, Zheng G, Sonnenberg J L, Hada M, Ehara M, Toyota K, Fukuda R, Hasegawa J, Ishida M, Nakajima T, Honda Y, Kitao O, Nakai H, Vreven T, Montgomery J A, Peralta J E, Ogliaro F, Bearpark M, Heyd J J, Brothers E, Kudin K N, Staroverov V N, Kobayashi R, Normand J, Raghavachari K, Rendell A, Burant J C, Iyengar S S, Tomasi J, Cossi M, Rega N, Millam J M, Klene M, Knox J E, Cross J B, Bakken V, Adamo C, Jaramillo J, Gomperts R, Stratmann R E, Yazyev O, Austin A J, Cammi R, Pomelli C, Ochterski J W, Martin R L, Morokuma K, Zakrzewski V G, Voth G A, Salvador P, Dannenberg J J, Dapprich S, Daniels A D, Farkas, Foresman J B, Ortiz J V, Cioslowski J, Fox D J - Gaussian 09, Revision B.01; Gaussian, Inc.: Wallingford, CT, 2009. http://gaussian.com/

24. MacKerell AD, Bashford D, Bellott M, et al (1998) All-atom empirical potential for molecular modeling and dynamics studies of proteins. J Phys Chem B 102:3586–3616

25. Vanommeslaeghe K, MacKerell AD (2012) Automation of the CHARMM General Force Field (CGenFF) I: bond perception and atom typing. J Chem Inf Model 52:3144–3154

26. Head-Gordon M, Pople JA, Frisch MJ (1988) MP2 energy evaluation by direct methods. Chem Phys Lett 153:503–506

27. Mayne CG, Saam J, Schulten K, Tajkhorshid E, Gumbart JC (2013) Rapid parameterization of small molecules using the Force Field Toolkit. J Comput Chem 34:2757–2770

28. Humphrey W, Dalke A, Schulten K (1996) VMD: visual molecular dynamics. J Mol Graph 14:33–8, 27

29. Hornak V, Abel R, Okur A, Strockbine B, Roitberg A, Simmerling C (2006) Comparison of multiple Amber force fields and development of improved protein backbone parameters. Proteins 65:712–725

30. Jorgensen WL, Chandrasekhar J, Madura JD, Impey RW, Klein ML (1983) Comparison of simple potential functions for simulating liquid water. J Chem Phys 79:926

31. Berendsen HJC, Postma JPM, van Gunsteren WF, DiNola A, Haak JR (1984) Molecular dynamics with coupling to an external bath. J Chem Phys 81:3684

32. Loncharich RJ, Brooks BR, Pastor RW (1992) Langevin dynamics of peptides: the frictional dependence of isomerization rates of N-acetylalanyl-N'-methylamide. Biopolymers 32:523–535

33. Kräutler V, van Gunsteren, Wilfred F., Hünenberger PH (2001) A fast SHAKE algorithm to solve distance constraint equations for small molecules in molecular dynamics simulations. J Comput Chem

34. Essmann U, Perera L, Berkowitz ML, Darden T, Lee H, Pedersen LG (1995) A smooth particle mesh Ewald method. J Chem Phys 103:8577

35. Lomize MA, Lomize AL, Pogozheva ID, Mosberg HI (2006) OPM: orientations of proteins in membranes database. Bioinformatics 22:623–625

36. Grubmüller H, Groll V - Solvate, Version1.0.1, 1996. http://www.mpibpc.mpg.de/grubmueller/solvate

37. Williams T, Kelley C Gnuplot 4.5: an interactive plotting program, version 4.5; http://gnuplot.info.

38. Pettersen EF, Goddard TD, Huang CC, Couch GS, Greenblatt DM, Meng EC, Ferrin TE (2004) UCSF Chimera--a visualization system for exploratory research and analysis. J Comput Chem 25:1605–1612

39. Seeber M, Felline A, Raimondi F, Muff S, Friedman R, Rao F, Caflisch A, Fanelli F (2011) Wordom: a user-friendly program for the analysis of molecular structures, trajectories, and free energy surfaces. J Comput Chem 32:1183–1194

40. Cozza G, Bortolato A, Moro S (2010) How druggable is protein kinase CK2? Med Res Rev 30:419–462

41. Sekiguchi Y, Nakaniwa T, Kinoshita T, Nakanishi I, Kitaura K, Hirasawa A, Tsujimoto G, Tada T (2009) Structural insight into human CK2alpha in complex with the potent inhibitor ellagic acid. Bioorg Med Chem Lett 19:2920–2923

42. Wilce MCJ, Parker MW (1994) Structure and function of glutathione S-transferases. Biochimica et Biophysica Acta (BBA) - Protein Structure and Molecular Enzymology 1205:1–18

43. Laborde E (2010) Glutathione transferases as mediators of signaling pathways involved in cell proliferation and cell death. Cell Death Differ 17:1373–1380

44. Oakley AJ, Lo Bello M, Nuccetelli M, Mazzetti AP, Parker MW (1999) The ligandin (non-substrate) binding site of human Pi class glutathione transferase is located in the electrophile binding site (H-site). J Mol Biol 291:913–926

45. Aguirre C, ten Brink T, Guichou J-F, Cala O, Krimm I (2014) Comparing binding modes of analogous fragments using NMR in fragment-based drug design: application to PRDX5. PLoS ONE 9:e102300

46. Declercq JP, Evrard C, Clippe A, Stricht DV, Bernard A, Knoops B (2001) Crystal structure of human peroxiredoxin 5, a novel type of mammalian peroxiredoxin at 1.5 A resolution. J Mol Biol 311:751–759

47. Shichita T, Hasegawa E, Kimura A, et al (2012) Peroxiredoxin family proteins are key initiators of post-ischemic inflammation in the brain. Nat Med 18:911–917

48. Sjöholm I, Ekman B, Kober A, Ljungstedt-Påhlman I, Seiving B, Sjödin T (1979) Binding of drugs to human serum albumin:XI. The specificity of three binding sites as studied with albumin immobilized in microparticles. Mol Pharmacol 16:767–777

49. Lejon S, Cramer JF, Nordberg P (2008) Structural basis for the binding of naproxen to human serum albumin in the presence of fatty acids and the GA module. Acta Crystallogr Sect F Struct Biol Cryst Commun 64:64–69

50. Kanner BI, Zomot E (2008) Sodium-coupled neurotransmitter transporters. Chem Rev 108:1654–1668

51. Zhou Z, Zhen J, Karpowich NK, Law CJ, Reith MEA, Wang D-N (2009) Antidepressant specificity of serotonin transporter suggested by three LeuT-SSRI structures. Nat Struct Mol Biol 16:652–657

52. Jacobson KA, Gao Z-G (2006) Adenosine receptors as therapeutic targets. Nat Rev Drug Discov 5:247–264

53. Cooke RM, Brown AJH, Marshall FH, Mason JS (2015) Structures of G protein-coupled receptors reveal new opportunities for drug discovery. Drug Discov Today 20:1355–1364

54. Sabbadin D, Ciancetta A, Moro S (2014) Bridging molecular docking to membrane molecular dynamics to investigate GPCR-ligand recognition: the human A_2A adenosine receptor as a key study. J Chem Inf Model 54:169–183

55. Lebon G, Warne T, Edwards PC, Bennett K, Langmead CJ, Leslie AGW, Tate CG (2011) Agonist-bound adenosine A2A receptor structures reveal common features of GPCR activation. Nature 474:521–525

56. Barelier S, Linard D, Pons J, Clippe A, Knoops B, Lancelin J-M, Krimm I (2010) Discovery of fragment molecules that bind the human peroxiredoxin 5 active site. PLoS ONE 5:e9744

57. Krishnamurthy H, Gouaux E (2012) X-ray structures of LeuT in substrate-free outward-open and apo inward-open states. Nature 481:469–474

58. Keränen H, Gutiérrez-de-Terán H, Åqvist J (2014) Structural and energetic effects of A2A adenosine receptor mutations on agonist and antagonist binding. PLoS ONE 9:e108492

59. Kober A, Sjöholm I (1980) The binding sites on human serum albumin for some nonsteroidal antiinflammatory drugs. Mol Pharmacol 18:421–426

Exploring Protein-Peptide Recognition Pathways Using a Supervised Molecular Dynamics Approach

Veronica Salmaso, Mattia Sturlese, Alberto Cuzzolin, and Stefano Moro

(2017) Combining self- and cross-docking as benchmark tools: the performance of DockBench in the D3R Grand Challenge 2. J Comput Aided Mol Des. doi: 10.1007/s10822-017-0051-4

Abstract

Peptides have gained increased interest as therapeutic agents during recent years. The high specificity and relatively low toxicity of peptide drugs derive from their extremely tight binding to their targets. Indeed, understanding the molecular mechanism of protein-peptide recognition has important implications in the fields of biology, medicine, and pharmaceutical sciences. Even if crystallography and nuclear magnetic resonance are offering valuable atomic insights into the assembling of the protein-peptide complexes, the mechanism of their recognition and binding events remains largely unclear. In this work we report, for the first time, the use of a supervised molecular dynamics approach to explore the possible protein-peptide binding pathways within a timescale reduced up to three orders of magnitude compared with classical molecular dynamics. The better and faster understating of the protein-peptide recognition pathways could be very beneficial in enlarging the applicability of peptidebased drug design approaches in several biotechnological and pharmaceutical fields.

1. Introduction

Protein-peptide recognition has a crucial role in various fundamental aspects of cellular homeostasis, such as signal transduction, protein-trafficking, and immune response. Moreover, protein-peptide recognition has an important impact on various biotechnological and pharmaceutical applications, such as peptide-based therapeutics, biosensors, biomarkers, and functional modulators of proteins. In particular, nowadays peptide-based drug discovery could be a serious option for addressing new therapeutic challenges [1-3]. In fact, novel chemical strategies for limiting metabolism and alternative routes of administration have emerged in recent years and resulted in an increasing number of peptide-based drugs that are now being marketed [1-3].

Understanding the molecular mechanism of protein-peptide recognition has, and surely will have even more in the future, important applications in the fields of biology, medicine, and pharmaceutical sciences. High-resolution structure determination methods, such as X-ray crystallography and nuclear magnetic resonance, are offering valuable atomic insights into the assembling of the protein-peptide complexes. However, the molecular mechanism of the recognition and binding events that occur between the bound and unbound

Published: *Structure. 2017 Apr 4;25(4):655–662.e2*

states remains largely unclear. Computational modeling offers the opportunity to directly inspect the binding event and understand the key features of protein-peptide recognition. Molecular docking and molecular dynamic (MD) simulations have already been proposed as suitable strategies to explore protein-peptide interactions [4-15]. Unfortunately, the whole recognition process from the unbound to the bound state is a very rare event to describe at the molecular level, and even with the recent GPU-based computing resources, it is necessary to carry out classical molecular dynamics simulation in a long microsecond timescale. Recently, we have overcome this limiting factor by implementing an alternative MD approach, named supervised molecular dynamics (SuMD), that notably speeds up the complete simulation of a protein-ligand recognition process compared with classical MD [16-17]. As described previously, SuMD enables the investigation of ligand-receptor binding events independently from the starting position, from the chemical structure of the ligand, and also from its receptor binding affinity.

Starting from the original implementation of SuMD, for the first time, we have extended the applicability domain of SuMD toward the exploration of the protein-peptide recognition pathway (pepSuMD) within a timescale reduced up to three orders of magnitude compared with classical MD. In particular, to evaluate the performance and robustness of pepSuMD, three well-renowned complexes were selected from a subset of characterized protein-protein interaction targets [18], as pilot key studies: two of them containing natural peptides (Bcl-X_L/BAD and MDM2/p53) [19, 20] and one containing a stapled peptidomimetic (MDM2/SAH-p53-8) [21], as summarized in Table 1. Both Bcl-XL/BAD and MDM2/p53 complexes play a key role in the regulation of the apoptotic pathway. In fact, one of the ways that cancer cells can evade physiological cellular regulation and chemotherapeutic-induced cell death is by overexpression of pro-survival proteins, such as Bcl-XL and MDM2, or by amplification of their genes. The BAD protein disrupts the heterodimer normally formed by Bcl-XL with specific pro-apoptotic proteins such as BAK and BAX [22]. Similarly, MDM2 exerts its oncogenic effects primarily by interacting with the p53 tumor suppressor protein [23].

Table 1. Summary of Structural Information and Results of the Selected Peptide-Target Complexes.

Complex	Peptide length	PDB ID	Method	Affinity and Referece.	RMSDMIN (Å)
Bcl-XL - BAD	25	1G5J	Solution NMR	(Kd=0.6 nM)[19]	4.72
MDM2 - p53	17	1YCQ	X-Ray diffraction	(Kd≈1 µM) [20]	4.15
MDM2 - SAH-p53-8	10 (stapled)	3V3B	X-Ray diffraction	(Kd=55 nM) [21]	1.87

The preliminary results collected in this pilot key study are very encouraging. In fact, pepSuMD methodology allows the simulation of the whole process of protein-peptide recognition (from the unbound to the bound state) in a nanosecond timescale, with an appreciable capability to reproduce the crystallographic structures of the native complexes. The better and faster understating of the protein-peptide recognition pathways could be very beneficial in enlarging the applicability of peptide-based drug design approaches in several biotechnological and pharmaceutical fields.

2. Results

From a computational point of view, pepSuMD is based on the same supervision approach used in the previously published SuMD methodology [16, 17]. In brief, a pepSuMD simulation is composed of a number of consecutive short unbiased MD simulations (600 ps) in which a supervision strategy, based on a tabu search-like strategy, is applied at the end of each simulation. The supervised variable is the distance between the center of mass of the peptide and the center of mass of its binding site on the protein. In a nutshell, if this distance is likely to be shortened during the simulation, the MD simulation is prolonged, otherwise, it is stopped, and the simulation is restarted from the previous set of coordinates. The supervision is maintained until the protein-peptide distance reaches a preset threshold value, then the simulation proceeds as a conventional unbiased MD simulation. This threshold is user-definable and in this pilot key study has been set at 10 Å. A completely automated set of tools has been developed to analyze a pepSuMD trajectory from a geometric and energetic point of view, including a self-production video recorder to reproduce the whole pepSuMD trajectory.

The most remarkable results for each of the three key studies will be briefly described below.

2.1 Test Case 1: Bcl-XL/BAD Complex

In this case, as well as for all other described herein, to avoid any bias in reproducing the protein-peptide bound state, the initial unbound state was prepared randomly distancing the peptide very far from its protein recognition site and, as well, very far from the long-range interaction cutoff (i.e., 9 Å). In the case of the Bcl-X_L/BAD complex, the BH3 domain of BAD (Asn103- Lys127) was positioned 72 Å away from the binding cleft of Bcl-X_L ($d_{cm(P-T)}$ = 72 Å). As reported previously, the unbound state was hydrated, neutralized, and equilibrated before running the pepSuMD protocol [16, 17].

As shown in Movie S1, in the first part of the simulation (0–7 ns) the peptide tumbles in solution before approaching the cutoff threshold for the attractive interactions with Bcl-X_L. The evolution of the distance between the centers of mass (peptide-protein) is reported in Figure S1.

The flexibility of the BH3 α helix of BAD is evident between 2.4 and 3.4 ns when it temporarily bends at about 90° with respect to the helix axis; at 2.82 ns the peptide highly deviates from the reference conformation, with a Cα-root-mean-square deviation (Cα-RMSD) value of 6.27 Å (Figure S5).

The first peptide-protein interaction occurs at around 7 ns and is mediated by the peptide N terminus and the loop connecting the α3 and α4 helices of Bcl-X_L, involving residues Gln111- Gln121 (Figure 1D).

After 2 ns, BAD establishes a greater contact with the α2 and α3 helices of Bcl-X$_L$, in particular through the interactions of Glu113 (BAD) with Arg102/103 (Bcl-XL) and of Asn103 (BAD) with Asp107 (Bcl-XL) (Figures 1E and 1F). A series of hydrophobic contacts are established between Tyr101 (α3 helix of Bcl-X$_L$) and Tyr110 and Leu114 (BAD) leading to the reorientation of the BAD peptide with the helix axis parallel to the Bcl-X$_L$ cleft.

Up to 10 ns, the C-terminal helix of Bcl-X$_L$ explores a wide pool of conformations (Figure S4C). The Cα-RMSD of Bcl-X$_L$ reaches the maximum value of 6.24 Å at 5.42 ns (Figure S4A), with the greater contribution provided by the C-terminal portion, as indicated by per-residue RMSD analysis (Figure S4B). After 10 ns, the C-terminal portion of Bcl-X$_L$ makes contacts with BAD, driving it toward the binding site, and this enhances the stabilization of the Bcl-X$_L$ C terminus close to the bound reference to the end of the simulation (Figures S4D–S4F).

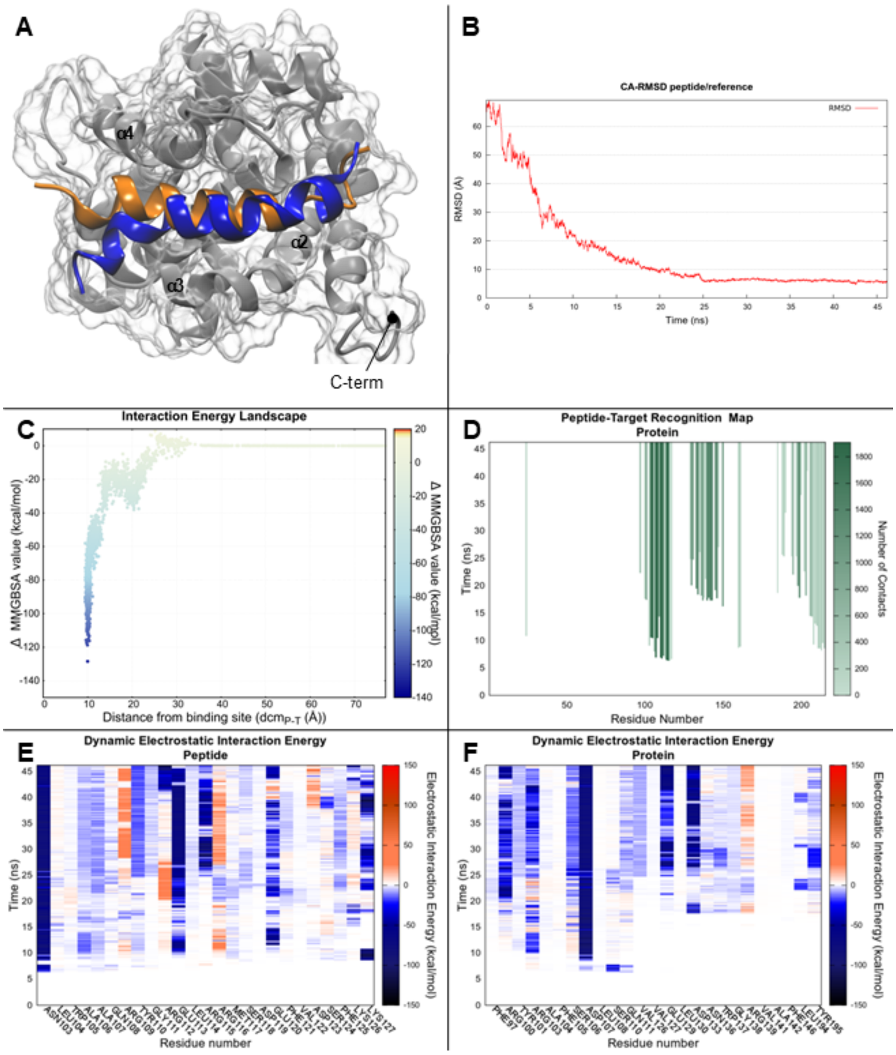

Fig. 1 Bcl-XL-BAD Recognition Pathway (A) Superimposition between the experimental nuclear magnetic resonance complex (PDB:1G5J) (orange-colored BAD peptide) and the pepSuMD conformation with lowest RMSD along the trajectory (blue-colored BAD peptide). The superposition was performed considering only the target protein residues. The peptide is shown using a ribbon style, while the protein is represented using both ribbon (gray) and surface (white, transparent rendering). The nomenclature of the most relevant Bcl-X$_L$ helices is reported on the corresponding α helix segment. (B) RMSD of simulated BAD peptide Cα carbon atoms against PDB references. (C) Interaction energy landscape. (D) Peptide-target recognition map. (E and F) Dynamic electrostatic interaction energy, on the peptide and protein side, respectively.

Between 12 ns and 18 ns, the peptide does not undergo significant movement; the whole peptide is involved in contacts with α2, α3, and C-terminal helices of Bcl-X_L, with a strong electrostatic interaction between Glu120 (BAD) and Arg100 (Bcl-X_L). The protein region involved in this prolonged interaction may be defined as a metastable binding site, as revealed by the stability of MMGBSA energy values (Movie S1, lower left). A metastable binding site is a sort of stopover with a sufficient residence time, that breaks the progressive and continual approach of the peptide.

The molecular mechanism leading BAD to reach the final binding site is the interaction between Arg115 and Glu129 of BAD and Asp133 at the C terminus of α4 helix of Bcl-X_L (Figures 1E and 1F). A dynamic qualitative and quantitative analysis of the target residues mainly involved in BAD binding is reported in Movie S1, lower right, in which the cumulative electrostatic interactions highlight residues Asp107, Asp133, Glu129, Arg100, and Arg103 as important in the binding process.

Finally, at 25 ns the pattern of interactions found in the experimental structure is achieved: the hydrophobic residues Tyr110, Leu114, Phe121, and Phe125 of BAD are inserted into a series of hydrophobic pockets within the binding cleft.

In the final 20 ns the peptide fluctuates without changing its orientation, as can be observed by the RMSD profile (Figure 1B; Movie S1, upper right). The fluctuations are restricted to side chains, which lead to the optimization of intermolecular peptide-protein interactions, as shown in the MMGBSA energy profile (Movie S1, lower left). Moreover, the estimated MMGBSA energy values that can be associated to the bound state are in accordance with the extended surface involved in binding and are compatible with the sub-nanomolar value of the experimental Bcl-XL/BAD complex dissociation constant [19].

Summarizing, the recognition pathway of BAD with Bcl-XL depicted by the analysis of SuMD trajectories is compatible with a two-step mechanism of binding: a first intermediate binding state that anticipates the final bound state, as shown by the interaction energy landscape in which the profile clearly shows a nonmonotonic trend (Figure 1C).

2.2 Test Case 2: MDM2/p53 Complex

In this second key study, the p53 peptide was positioned 28 Å away from the MDM2 binding cleft away ($d_{cm(P-T)}$ = 28 Å).

The whole recognition pathway can also be appreciated in this case by browsing Movie S2. The peptide-protein centers of mass distance decreases from the initial 28 Å to about 10 Å during the first 15 ns of SuMD simulation. After that, it is stabilized at about 8 Å , with a 7.7 Å value in the last frame (Figure S2). The first significant contacts between p53 and MDM2 occur after the first 1.5 ns, involving the loop connecting α1 and α2 (Gln40-Thr45) and the peptide C terminus (Movie S2, upper left, and Figure 2D). At around 3 ns of simulation, the peptide gets closer to helix α2 due to the interactions of Ser20, Asp21, Trp23, and Lys 24 with Tyr51 and Gln55 of MDM2 (Figures 2E and 2F). These interactions lead to a peptide reorientation assuming a parallel position to helix α2 of MDM2.

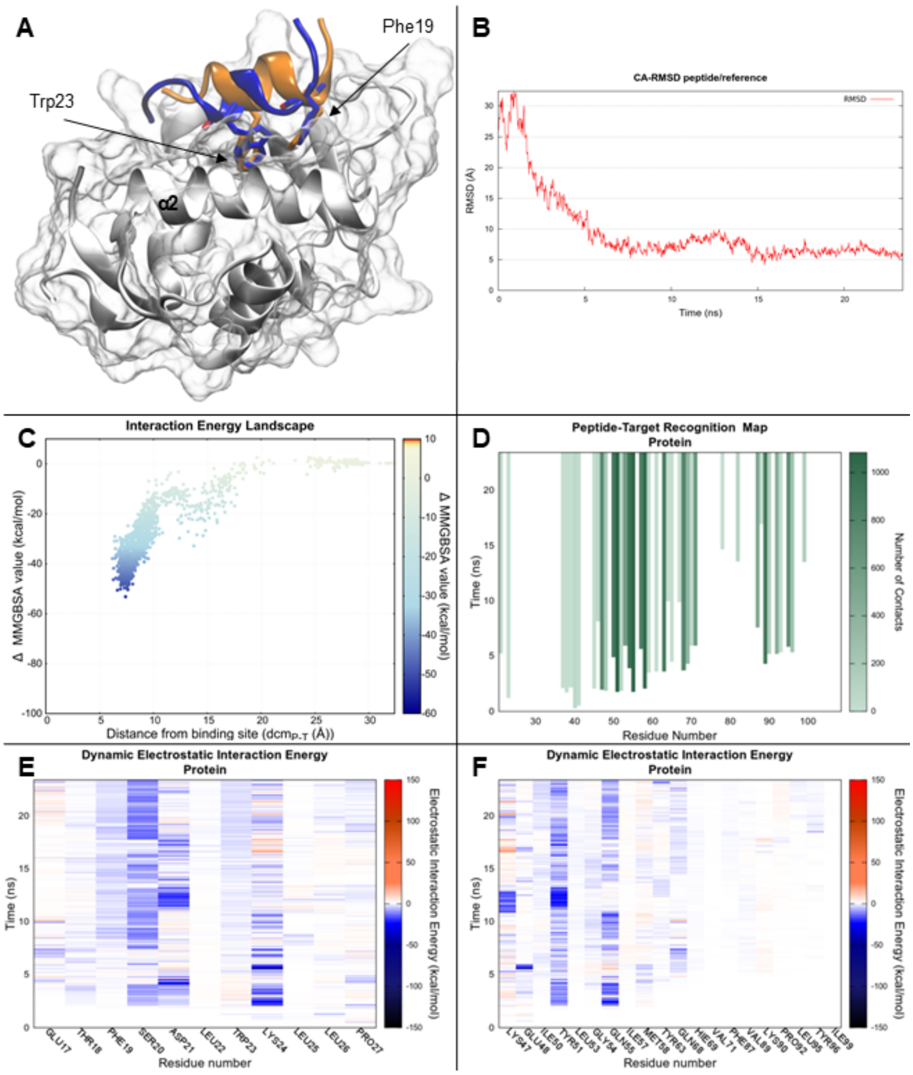

Fig. 2 MDM2/p53 Recognition Pathway (A) Superimposition between the experimental crystallographic complex (PDB: 1YCQ) (orange-colored p53 peptide) and the pepSuMD conformation with lowest RMSD along the trajectory (blue-colored p53 peptide). The superposition was performed considering only the target protein residues. The protein structure is represented using both ribbon (gray) and surface (white, transparent rendering). The peptide is represented using the ribbon style and the most relevant residues for the interaction, Phe19, and Thr23, are also rendered by heavy atoms, the carbon atoms of which are colored according to the corresponding ribbon. (B) RMSD of simulated p53 peptide Cα carbon atoms against PDB references. (C) Interaction energy landscape. (D) Peptide-target recognition map. (E and F) Dynamic electrostatic interaction energy, on the peptide and protein side, respectively.

At this point, p53 needs to roll over the surface of helix α2 to finally reach the binding cleft. This recognition mechanism is nicely described by the MMGBSA energy plot (Movie S2, lower left) in which the two minima at 4 and 8 ns are separated by an energetic barrier (5.5 ns).

Finally, at 13 ns the p53 peptide joins the orientation found in the crystallographic structure, with Phe19 and Trp23 inserted in the binding cleft of MDM2, and the RMSD drops at around 5 Å. In the next 10 ns, the position of the peptide maintains the same orientation as highlighted by the RMSD profile (Figure 2B; Movie S2, upper right), while the side chains of both protein and peptide continue in an induced-fit recognition mechanism that can be evinced by the MMGBSA profile (Movie S2, lower left) and, in a phenomenological manner, by the molecular trajectory (Movie S2, upper left).

Although the orientation of the helix of p53 is nicely reproduced in the last part of the simulation, the helix axis is slightly shifted and the characteristic hydrogen bond between the indolic nitrogen of Trp23 and the backbone of Ile50 of MDM2 is not observed, due to a flipping by 180° of the indole ring (Figure 2A).

From these preliminary simulations, the p53-MDM2 recognition pathway extracted by the analysis of SuMD trajectories is again compatible with a two-step mechanism of binding, as supported by the non-monotonic trend of the energy interaction landscape (Figure 2C). In particular, the preliminary binding to the a2 helix could be considered as an intermediate binding site.

2.3 Test Case 3: MDM2/SAH-p53-8 Complex

The last key study has been chosen in order to evaluate the capability of the pepSuMD approach to appropriately deal with simulations in which a peptide is replaced by a peptidomimetic. Specifically, in this case we have explored the recognition of MDM2 by a stapled p53 peptide, named SAH-p53-8 [21]. This peculiar peptidomimetic has been designed to stabilize the helical conformation, crucial for the interaction with MDM2, through the introduction of an olefinic crosslinking moiety placed before Asn20 and after Leu26 in the native p53 sequence numbering.

In these simulations, the SAH-p53-8 p53 mimetic was positioned 27 Å away from the MDM2 binding cleft ($d_{cm(P-T)}$ = 27 Å), and the possible recognition pathway is summarized in Movie S3. The evolution of the distance between the centers of mass (peptide-protein) supervised by pepSuMD is reported in Figure S3. In the first part of the trajectory, the peptide randomly tumbles in the water box and requires 2 ns of pepSuMD simulation to approach the protein. A preliminary stable recognition occurs at around 1.6 ns (Movie S3, upper left) and involves the two loops surrounding the binding site (Val93-Arg97, earlier, and Gln71-His73) with the C terminus of the peptidomimetic (Figure 3D). Immediately thereafter, helix α2 of MDM2 (Ly51-Gln59) is also engaged in the interaction and the peptide assumes an orientation parallel to the binding cleft, compatible with the native interaction. At 3.7 ns, a well-known induced-fit mechanism occurs [24, 25]: the side chain of Tyr67 (MDM2) rotates enlarging the binding pocket to accommodate Phe19 (SAH-p53-8) and the consecutive settlement of the peptide. Here, SAH-p53-8 reaches a stable conformation almost identical to the crystal structure (Figure 3A): Phe19, Trp23, and Leu26 side chains are oriented in the hydrophobic cleft of MDM2 and the olefinic chain interacts with helix α2 of MDM2. The coordinates of the indolic nitrogen atom of Trp23 and the backbone carbonyl group of Leu54 are compatible with the hydrogen bond formation found in the crystallographic structure. Gln72 is relevant in the complex stabilization for the formation of a hydrogen bond with the N-terminal portion of SAH-p53-8, which emerges especially between about 8 and 10 ns (Figure 3E; Movie S3, lower right).

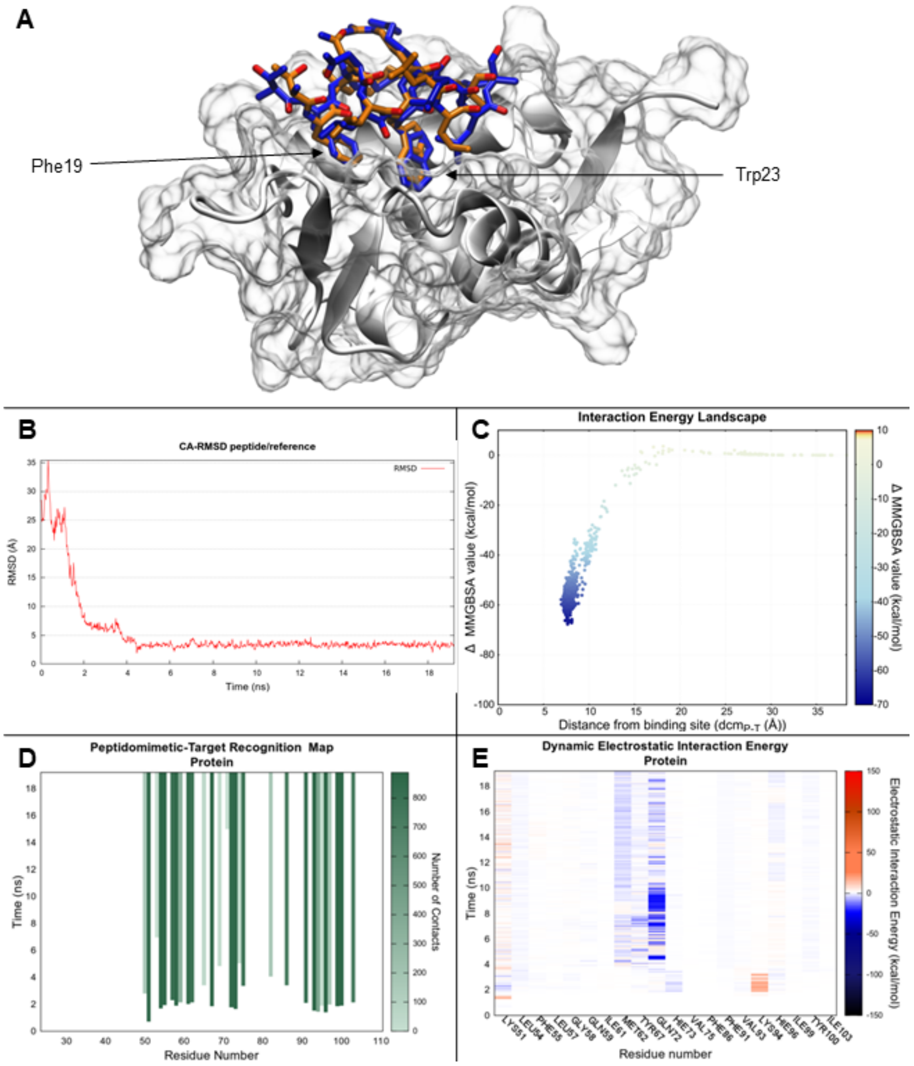

Fig. 3 MDM2/SAH-p53-8 Recognition Pathway (A) Superimposition between the experimental crystallographic complex (PDB: 3V3B) (orange-colored peptidomimetic) and the pepSuMD conformation with lowest RMSD along the trajectory (blue-colored peptidomimetic). The superposition was performed considering only the target protein residues. The protein is represented using both ribbon (gray) and surface (white, transparent rendering). The peptidomimetic is represented using full heavy-atom style. The position of the most relevant residues for the interaction, Phe19 and Thr23, are indicated by black arrows. (B) RMSD of simulated SAH-p53-8 ligand heavy atoms against PDB references. (C) Interaction energy landscape. (D) Peptidomimetic-target recognition map. (E) Dynamic electrostatic interaction energy, on the protein side.

The RMSD reaches the minimum value of 1.9 Å, at 4.5 ns (Figure 3B; Movie S3, upper right) when computed on all the peptide heavy atoms in the peptide, while it drops to 0.7 Å considering only the side chains of Phe19 and Trp23. The strength of the interaction is evident in the MMGBSA profile (Movie S3, lower left), which reaches values close to 60 kcal/mol.

In this trajectory, the absence of stable metastable binding sites is evident from the interaction energy landscape (Figure 3C), in which the profile can be approximated by a monotonic function differently to the p53 peptide of the previous test case. In addition, the modest dispersion of the energy values emphasizes the stability of the complex.

The effect of the introduction of the olefinic bridge is clear when the energetic profiles are compared with the natural peptide p53: it results in a greater stability of the complex (less dispersed points) and a stronger interaction (more negative values) that perfectly fits with experimental evidence.

3. Discussion

The preliminary results obtained from pepSuMD simulations are promising. Although we are aware that, in this first pilot study, the number of protein-peptide complexes taken into account is limited, in all the key studies analyzed, the pepSuMD approach succeeded in reproducing the native binding mode, even when starting from a random and very distant position of the peptide from its binding site. Considering the preliminary reproducibility analysis of SuMD trajectories, the distance between the centers of mass of the simulated peptide in the final bound state and the center of mass of the experimental peptide fell below 5 Å in all the examples, as reported in Figures S1–S3. A summary of the preliminary statistical analysis is reported in Table S1 and Movies S4, S5, and S6. However, even if encouraging, a robust statistical analysis based on a large campaign of pepSuMD simulations is in progress to appropriately analyze the strengths and weakness of the approach and to explore the limits of the applicability domain of this new technique. Moreover, the final conformations of simulated peptides are comparable with those observed in the experimental bound state, as demonstrated by Cα-RMSD values lower than 6 Å in all cases (Figures 1B, 2B, and 3B).

In addition, pepSuMD trajectories were able to reveal the presence of multiple intermediate states (metabinding sites) that chronologically anticipate the native bound site, as observed, for example, for Bcl-X_L/BAD and MDM2/p53 systems. Finally, the energetic profiles extracted from pepSuMD trajectories are very useful to analyze the localization, the nature and the intensity of the most crucial peptide-protein interactions (hotspots).

Another crucial aspect that must be carefully taken into account is related to those intrinsically disordered peptides that fold upon binding. In fact, in our pilot study, all peptides in their unbound states are pre-folded and they are recognized by pre-folded proteins through a conformational selection mechanism. In particular, the pepSuMD approach is particularly efficient in dealing with conformational constrained peptides and peptidomimetics. However, minor induced-fit phenomena can be observed during pepSuMD trajectories, as can be seen from the Cα-RMSD profiles in Figures S4 and S5. As already noted, for example, the C-terminal portion of Bcl-X_L explores multiple conformations when unbound, while it is stabilized, close to the native conformation in the bound state (Figures S4C–S4F). Indeed, considerable induced-fit and folding-upon-binding mechanisms have not been extensively explored and, in principle, it could be quite difficult to observe relevant folding phenomena within the short timescale of our supervised binding process. However, further implementations of the pepSuMD approach dealing specifically with the induced-fit phenomena are under development.

Understanding the intimate protein-peptide recognition process remains a charming challenge for structural biology and peptide-based drug discovery.

For the first time, we reported the application of a pepSuMD approach on three different peptide-protein key studies with the aim of verifying the effectiveness and robustness of this method in depicting their possible binding pathways leading to the final bound state as described by the corresponding experimental high-resolution structures. pepSuMD was able to reproduce experimental peptide-protein complexes and to reduce the timescale of a peptide-protein binding event by up to three orders of magnitude in comparison with classical MD.

Insights from pepSuMD simulations can be helpful to explain the mechanistic evidence of recognition processes and they could be very beneficial in enlarging the challenges of peptidebased drug discovery.

4. Method details

4.1 General

All simulations were carried out on a hybrid CPU/GPU cluster. MD simulations were performed with the ACEMD engine [26] on a GPU cluster equipped with 20 NVIDIA GTX graphics cards. Prior to run pepSuMD simulations, the following preliminary steps were accomplished: (i) protein-peptide system preparation; (ii) peptidomimetic parameterization, if necessary; (iii) solvated system setup and equilibration.

4.2 Protein-Peptide Systems Preparation

Protein-peptide complexes were retrieved from the RCSB PDB database [27] and processed with the protein preparation tool as implemented in MOE [28]: hydrogen atoms were added to X-ray derived complexes and appropriate ionization states were assigned by Protonate-3D tool [29]. Missing atoms in protein side chains were built according to AMBER12 [30] force field topology. Non-natural N-terminal and C-terminal were capped to mimic the previous residue. To avoid protein-ligand long range interactions in the starting geometry, the peptide was then moved far from the protein at a distance bigger than the electrostatic cut-off term used in the simulation (9 Å with Amber force field).

4.3 Peptidomimetic Parameterization

The non-natural portion of the peptidomimetic ligand was parametrized with GAFF [31] as implemented in ambertools2014 [32] by using antechamber and parmchk tools. RESP partial charges were calculated with Gaussian 09 [33] following the procedure suggested by Antechamber [34].

4.4 Solvated System Setup and Equilibration

Complexes were assembled with tleap tool using AMBER14SB [32] as force field for the protein. The systems were explicitly solvated by a cubic water box with cell borders placed at least 12 Å away from any protein or ligand atom using TIP3P as water model. To neutralize the total charge, Na+ /Cl- counterions were added to a final salt concentration of 0.150 M. The systems were energy minimized by 2000 steps with conjugate-gradient method, then 50000 steps of NVE (100 ps) followed by 1 ns of NPT simulations were carried out, both using 2 fs as time step and applying harmonic positional constraints on protein and peptide/peptidomimetic heavy atoms by a force constant of 1 kcal mol^{-1} Å^{-2}, gradually reduced with a scaling factor of 0.1. During this step, the temperature was maintained at 310 K by a Langevin thermostat and the pressure at 1 atm by a Berendsen barostat.

4.5 Peptidic Supervised Molecular Dynamics (pepSuMD)

pepSuMD ensues from SuMD code recently developed [17], in order to be applicable to peptides and peptidomimetics. The entire protocol is written in Python and bash and operates the supervision of MD trajectories according to the algorithm that has been previously described. Similarly to the original implementation, also in this protocol the supervision algorithm monitors the distance between the mass centers of the peptide and the target ($d_{cm(P-T)}$).

The program exploits ProDy Python package [35] and Gnuplot functionalities [36]. In its current implementation, pepSuMD is interfaced with the ACEMD [26] engine and supports AMBER and CHARMM force fields. Differently from the previous SuMD code, here more input parameters are user-editable, such as: the MD timestep (here, 2 fs), the number of MD steps within a pepSuMD step (here, 300000), an eventual substructure of the peptide used for mass centers computation (here, the entire peptide).

Three simulations were carried out for each system starting from the same initial geometry. The more significant replica for each test case is described in the Results section.

4.6 Analysis of pepSuMD Trajectories

All the trajectories generated by pepSuMD were analyzed by an in-house script written in tcl and python, that makes use of Numpy [37] and ProDy modules [35].

The single pepSuMD step trajectories were stridden (by a user defined value, here 10), superposed on the first frame Cα carbon atoms of the target protein, wrapped and merged. The following analyses were then performed on the whole trajectories. The peptide RMSD of Cα carbon atoms was computed with respect to the reference PDB structure, after superposing the target protein structure to its corresponding PDB one. The RMSD values were plotted over time and reported on the upper-right side of the Movies S1, S2, and S3 and in Figures 1B, 2B, and 3B. The RMSD graphic depicts the peptide conformation variation along the trajectory in comparison to the experimental conformation within the target binding site.

A peptide-target interaction energy estimation during the recognition process was calculated using an MMGBSA protocol with Amber2014 [32], adopting for non-polar and polar solvation energy calculations LCPO [38] and GB^{OBC}model II [39], respectively. MMGBSA values were plotted over time and reported in the lower-left side of the Movies S1, S2, and S3.

The MMGBSA values were also arranged according to the distances between peptide and target mass centers ($d_{cm(P-T)}$) in the Interaction Energy Landscape plots (Figures 1C, 2C, and 3C). Here, the distances between mass centers are reported on the x-axis, while the MMGBSA values on the y-axis, and are rendered by a colorimetric scale going from blue to red for negative to positive values. These graphs allow evaluating the variation of the interaction energy profile at different peptide-target distances, helping to individuate meta-stable binding states during the binding process.

In order to have a rapid indication about the residues mostly involved in the binding process, for each target residue, the total number of contacts with the peptide was computed along the trajectory. A target residue within a distance of 4 Å from any peptide atoms was considered as in contact with the peptide. On the basis of these data, the Peptide-Target Recognition Maps (Figures 1D, 2D, and 3D) were constructed, resuming the chronological evolution of the molecular contacts in a quantitative manner: here, for each residue (x-axis) the total number of contacts is reported with respect to the simulation time (y-axis) and rendered by a colorimetric scale going from white to dark green from 0 to higher numbers.

The most contacted residues were selected both for protein target and peptide to compute the per-residue electrostatic interaction energy with the peptide and target, respectively. NAMD was used for post-processing computation of electrostatic interactions, using AMBER14SB force field. The Dynamic Electrostatic Interaction Energy plots (Figures 1E, 2E, and 3E (protein), F (peptide)) depict for each selected residue (x-axis) the evolution of the electrostatic interaction energy along time (y-axis), using a colorimetric scale going from blue to red for negative to positive values.

The cumulative electrostatic interactions were computed for the same target residues by summing the energy values frame by frame along the trajectory, and the resulting graphs were reported at the lower-right of Movies S1, S2, and S3.

Representations of the molecular structures were prepared with VMD [40].

4.7 Data and software availability

pepSuMD code was writted in python language starting from the previously developed SuMD code. The algorithm is described at the beginning of the Results section. An in-house script written in python and tcl was used to automate analyses of the pepSuMD trajectories. An explanation of the analyses is reported in the Method Details section. All software used are reported in the Method Details section, together with the Key Resources Table.

Key Resources Table

Software and Algorithms	Source	Identifier
ACEMD 3212u2	Acellera Ltd, Harvey et al., 2009	http://www.acellera.com
MOE suite	(Chemical Computing Group (CCG) Inc., 2016	https://www.chemcomp.com
Gaussian 09	Frisch et al., 2009	http://gaussian.com
Ambertools2014	Case et al., 2014	http://ambermd.org
pepSuMD	This paper	http://mms.dsfarm.unipd.it

References:

1. Ahrens VM, Bellmann-Sickert K, Beck-Sickinger AG (2012) Peptides and peptide conjugates: therapeutics on the upward path. Future Med Chem 4:1567–1586

2. Craik DJ, Fairlie DP, Liras S, Price D (2013) The future of peptide-based drugs. Chem Biol Drug Des 81:136–147

3. Fosgerau K, Hoffmann T (2015) Peptide therapeutics: current status and future directions. Drug Discov Today 20:122–128

4. Trellet M, Melquiond ASJ, Bonvin AMJJ (2013) A unified conformational selection and induced fit approach to protein-peptide docking. PLoS ONE 8:e58769

5. Raveh B, London N, Zimmerman L, Schueler-Furman O (2011) Rosetta FlexPepDock ab-initio: simultaneous folding, docking and refinement of peptides onto their receptors. PLoS ONE 6:e18934

6. Kurcinski M, Jamroz M, Blaszczyk M, Kolinski A, Kmiecik S (2015) CABS-dock web server for the flexible docking of peptides to proteins without prior knowledge of the binding site. Nucleic Acids Res 43:W419–24

7. Antes I (2010) DynaDock: A new molecular dynamics-based algorithm for protein-peptide docking including receptor flexibility. Proteins 78:1084–1104

8. London N, Raveh B, Schueler-Furman O (2013) Peptide docking and structure-based characterization of peptide binding: from knowledge to know-how. Curr Opin Struct Biol 23:894–902

9. Aita T, Nishigaki K, Husimi Y (2010) Toward the fast blind docking of a peptide to a target protein by using a four-body statistical pseudo-potential. Comput Biol Chem 34:53–62

10. Russo A, Scognamiglio PL, Hong Enriquez RP, Santambrogio C, Grandori R, Marasco D, Giordano A, Scoles G, Fortuna S (2015) In Silico Generation of Peptides by Replica Exchange Monte Carlo: Docking-Based Optimization of Maltose-Binding-Protein Ligands. PLoS ONE 10:e0133571

11. Capra JA, Laskowski RA, Thornton JM, Singh M, Funkhouser TA (2009) Predicting protein ligand binding sites by combining evolutionary sequence conservation and 3D structure. PLoS Comput Biol 5:e1000585

12. Zaidman D, Wolfson HJ (2016) PinaColada: peptide-inhibitor ant colony ad-hoc design algorithm. Bioinformatics 32:2289–2296

13. Shan Y, Kim ET, Eastwood MP, Dror RO, Seeliger MA, Shaw DE (2011) How does a drug molecule find its target binding site? J Am Chem Soc 133:9181–9183

14. Dagliyan O, Proctor EA, D'Auria KM, Ding F, Dokholyan NV (2011) Structural and dynamic determinants of protein-peptide recognition. Structure 19:1837–1845

15. Lee H, Heo L, Lee MS, Seok C (2015) GalaxyPepDock: a protein-peptide docking tool based on interaction similarity and energy optimization. Nucleic Acids Res 43:W431–5

16. Sabbadin D, Moro S (2014) Supervised molecular dynamics (SuMD) as a helpful tool to depict GPCR-ligand recognition pathway in a nanosecond time scale. J Chem Inf Model 54:372–376

17. Cuzzolin A, Sturlese M, Deganutti G, Salmaso V, Sabbadin D, Ciancetta A, Moro S (2016) Deciphering the Complexity of Ligand-Protein Recognition Pathways Using Supervised Molecular Dynamics (SuMD) Simulations. J Chem Inf Model 56:687–705

18. Scott DE, Bayly AR, Abell C, Skidmore J (2016) Small molecules, big targets: drug discovery faces the protein-protein interaction challenge. Nat Rev Drug Discov 15:533–550

19. Petros AM, Nettesheim DG, Wang Y, et al (2000) Rationale for Bcl-xL/Bad peptide complex formation from structure, mutagenesis, and biophysical studies. Protein Sci 9:2528–2534

20. Kussie PH, Gorina S, Marechal V, Elenbaas B, Moreau J, Levine AJ, Pavletich NP (1996) Structure of the MDM2 oncoprotein bound to the p53 tumor suppressor transactivation domain. Science 274:948–953

21. Baek S, Kutchukian PS, Verdine GL, Huber R, Holak TA, Lee KW, Popowicz GM (2012) Structure of the stapled p53 peptide bound to Mdm2. J Am Chem Soc 134:103–106

22. Delbridge ARD, Grabow S, Strasser A, Vaux DL (2016) Thirty years of BCL-2: translating cell death discoveries into novel cancer therapies. Nat Rev Cancer 16:99–109

23. Wade M, Li Y-C, Wahl GM (2013) MDM2, MDMX and p53 in oncogenesis and cancer therapy. Nat Rev Cancer 13:83–96

24. Popowicz GM, Dömling A, Holak TA (2011) The structure-based design of Mdm2/Mdmx-p53 inhibitors gets serious. Angew Chem Int Ed Engl 50:2680–2688

25. Carry J-C, Garcia-Echeverria C (2013) Inhibitors of the p53/hdm2 protein-protein interaction-path to the clinic. Bioorg Med Chem Lett 23:2480–2485

26. Harvey MJ, Giupponi G, Fabritiis GD (2009) ACEMD: Accelerating Biomolecular Dynamics in the Microsecond Time Scale. J Chem Theory Comput 5:1632–1639

27. Berman HM, Westbrook J, Feng Z, Gilliland G, Bhat TN, Weissig H, Shindyalov IN, Bourne PE (2000) The protein data bank. Nucleic Acids Res 28:235–242

28. Chemical Computing Group (CCG) Inc. (2016) Molecular Operating Environment (MOE). Chemical Computing Group, 1010 Sherbooke St. West, Suite #910, Montreal, QC, Canada, H3A 2R7

29. Labute P (2009) Protonate3D: assignment of ionization states and hydrogen coordinates to macromolecular structures. Proteins 75:187–205

30. Hornak V, Abel R, Okur A, Strockbine B, Roitberg A, Simmerling C (2006) Comparison of multiple Amber force fields and development of improved protein backbone parameters. Proteins 65:712–725

31. Wang J, Wolf RM, Caldwell JW, Kollman PA, Case DA (2004) Development and testing of a general amber force field. J Comput Chem 25:1157–1174

32. Case D, Babin V, Berryman J, et al (2014) Amber14, version AMBER14; http://ambermd.org/. University of California, San Francisco

33. Frisch MJ, Trucks GW, Schlegel HB, et al (2009) Gaussian 09, Revision B.01; http://gaussian.com/ . Gaussian, Inc.: Wallingford, CT

34. Wang J, Wang W, Kollman PA, Case DA (2006) Automatic atom type and bond type perception in molecular mechanical calculations. J Mol Graph Model 25:247–260

35. Bakan A, Meireles LM, Bahar I (2011) ProDy: protein dynamics inferred from theory and experiments. Bioinformatics 27:1575–1577

36. Williams T, Kelley C Gnuplot 4.5: an interactive plotting program, version 4.5; http://gnuplot.info (accessed October 2015).

37. Van der Walt S, Colbert SC, Varoquaux G (2011) The NumPy Array: A Structure for Efficient Numerical Computation. Comput Sci Eng 13:22–30

38. Weiser J, Shenkin PS, Still CW (1999) Approximate atomic surfaces from linear combinations of pairwise overlaps (LCPO). J Comput Chem

39. Onufriev A, Bashford D, Case DA (2004) Exploring protein native states and large-scale conformational changes with a modified generalized born model. Proteins 55:383–394

40. Humphrey W, Dalke A, Schulten K (1996) VMD: visual molecular dynamics. J Mol Graph 14:33–8, 27

New Trends in Inspecting GPCR-ligand Recognition Process: the Contribution of the Molecular Modeling Section (MMS) at the University of Padova

Antonella Ciancetta, Alberto Cuzzolin, Giuseppe Deganutti, Mattia Sturlese, Veronica Salmaso, Andrea Cristiani, Davide Sabbadin, Stefano Moro

(2016) New Trends in Inspecting GPCR-ligand Recognition Process: the Contribution of the Molecular Modeling Section (MMS) at the University of Padova. Mol Inform 35:440–448

Abstract

In this review, we present a survey of the recent advances carried out by our research groups in the field of ligand-GPCRs recognition process simulations recently implemented at the Molecular Modeling Section (MMS) of the University of Padova. We briefly describe a platform of tools we have tuned to aid the identification of novel GPCRs binders and the better understanding of their binding mechanisms, based on two extensively used computational techniques such as molecular docking and MD simulations. The developed methodologies encompass: *(i)* the selection of suitable protocols for docking studies, *(ii)*the exploration of the dynamical evolution of ligand-protein interaction networks, *(iii)* the detailed investigation of the role of water molecules upon ligand binding, and *(iv)* a glance at the way the ligand might go through prior reaching the binding site.

2. Introduction

Today, it is largely recognized that G protein-coupled receptors (GPCRs) represent the largest family of surface receptors with more than 800 members in humans.[1] They respond to different extracellular stimuli ranging from small molecules to lipids, peptides, proteins, and even light.[2] The binding event triggers the activation of cytoplasmic heterotrimeric GTP binding proteins (G proteins) and mediates the signal transduction through the modulation of several downstream effectors. The participation of GPCRs in numerous physio-pathological processes entails a potential role for their modulation by agonist, antagonists and inverse agonists in the treatment of several diseases, including cardiovascular and mental disorders,[3] cancer,[4] and viral infections.[5] Nowadays, about more than 50 % of the drugs in clinical use targets a GPCR.[6]

According to the GRAFS classification,[7] human GPCRs are commonly grouped into five main classes: Glutamate (Class C), Rhodopsin (Class A), Adhesion (Class B), Secretin (Class B), and Frizzled/Taste2 (Class F). From a structural point of view, all members share a common architecture represented by seven membranespanning helices connected by three intracellular and three extracellular loops with the N-Term domain exposed toward the extracellular side.

The insertion into the cell membrane along with receptors dynamism have hampered for long time the structural determination of GPCRs by X-ray crystallography. To overcome these limitations, several techniques have been developed: the use of fusion proteins such as T4 lysozyme or apocytochrome,[8],[9] complexation with antibody fragments,[10] and the receptor thermostabilization through systematic scanning mutagenesis.[11] The advances in protein engineering and crystallography have represented a breakthrough for the research focused on GPCRs and yielded numerous X-ray structures.[12] The availability of ligand-bound three-dimensional structures provides invaluable insights to understand GPCRs function and pharmacology and enables the application of structure-based drug design approaches to aid the discovery of novel candidates with improved pharmacological profiles.[13] In particular, molecular dynamics (MD) simulations have become a helpful complement for the study of GPCRs biophysics and molecular pharmacology, by enriching our understanding of, among other aspects, ligand-receptor interaction and ligand-subtype selectivity.[14],[15]

In addition, the recent exploitation of the commodity, graphics processing units (GPUs), a technology firstly designed to improve video game performances, in the molecular modeling field represents an important step forward for the simulation of GPCRs in explicit lipid-water environments within a reasonable computation time.[16] In this paper, we briefly survey the recent advances carried out by our research groups in the field of ligand-GPCRs recognition process simulations.[17] Following the description of the tools we have developed to aid the identification of novel binders of GPCRs binders and the better understanding of their binding mechanisms, we will discuss their use in a case study: the comparison between ZM 241385 (4-(2-(7-Amino-2-(furan-2-yl)-[1],[2],[4]triazolo[2,3-a][1,5-a][1],[3],[5]triazin-5-yl-amino)ethyl) phenol) and caffeine, a strong and weak human Adenosine 2A Receptor (hA2A AR) antagonists, respectively.

2. Methods

2.1 Docking Protocols Validation: the “Quality Descriptors”

The availability of ligand-bound crystal structures enables to perform docking simulations to rationalize structure-activity relationships of known binders or to conduct virtual screening campaigns to identify novel candidates. It is highly recommended to assess the performances of a docking protocol in reproducing the available experimental data prior to applying it. This procedure is best known as benchmark study. We have recently developed a pipeline that allows a fast graphical evaluation of different docking protocols, based on two newly defined quality descriptors: the “Protocol Score” and the “Interaction Energy Map” (IEM).[18],[19] The “Protocol Score” is a RMSD based descriptor that assigns a 0–3 score to each docking protocol according to the following criteria: (i) if the protocol returns either a RMSDave value lower than the crystal structure resolution (R) or generates at least 10 (out of 20) conformations having RMSD<R, a score 1 is assigned; (ii) if a protocol satisfies both the above mentioned requirements, a score 2 is assigned; (iii) if a protocol satisfies none of the above mentioned requirements, a score 0 is assigned. Moreover, a score 3 is conferred to the best protocols, i.e. those returning at the same time the lowest RMSDave value and the highest number of conformers with a RMSD<R. The scores are then converted in a color code and the data visualized as a colored map (Figure 1A): protocols corresponding to white and light green spots are not suitable for the system under consideration, dark green spots highlight good protocols, whereas blue spots identify the best among the tested ones.

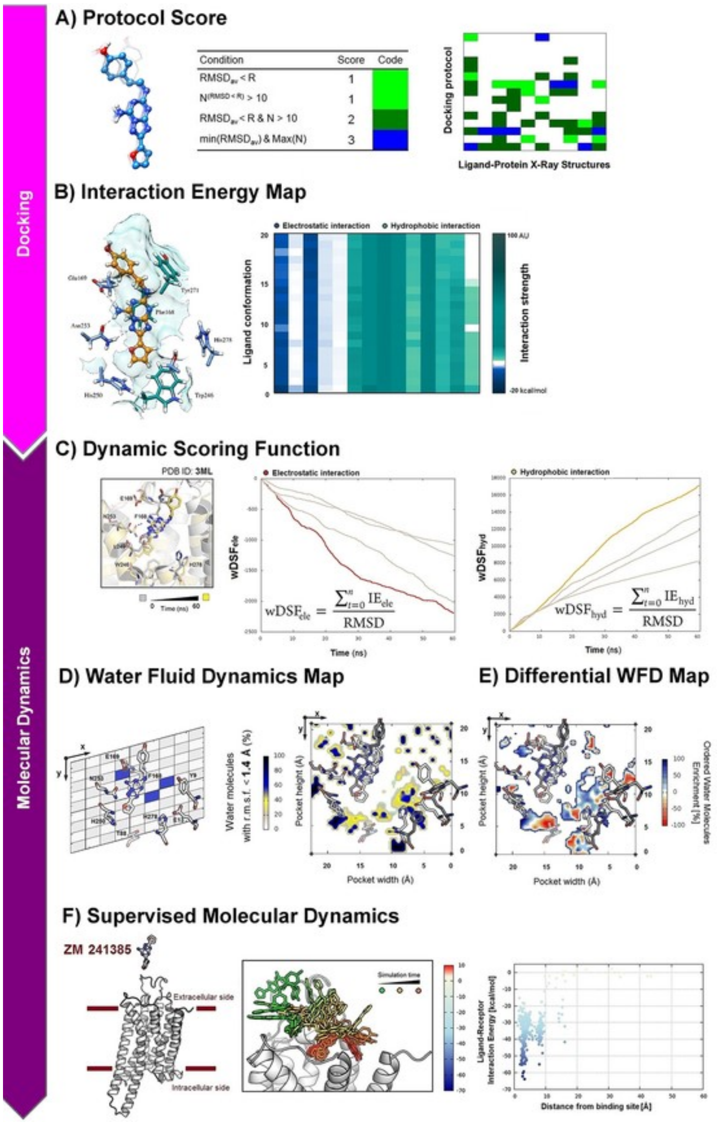

Fig. 1 Schematic representation of the developed tools: A) Protocol Score; B) Interaction Energy Maps (IEMs); C) RMSD weighted Dynamic Scoring Function (wDSF); D) Water Fluid Dynamics (WFD) maps; E) Differential WFD maps; F) Ligand-receptor interaction energy landscape from supervised MD (SuMD) simulations. The figures were adapted from the original papers.[18],[21],[27],[35]

The IEMs are based on the analysis of ligand-protein interactions and are derived as follows. Firstly, *per residue* electrostatic and hydrophobic contributions to the interaction energy (denoted IEele and IEhyd, respectively) are computed for residues surrounding the binding site or known to play a role in the binding. The analysis is performed for both the crystallographic binding modes and the docking poses. These pieces of information are then graphically transferred into heat-like maps reporting the key residues involved in the binding with the considered ligands along with a color code reflecting the quantitative estimate of the occurring interactions (the more intense the color, the stronger the interaction). The comparison is therefore based on the quality of the interactions – in terms of number of established interactions and their relative strength – among the X-Ray binding mode and the generated docking poses (Figure 1B).

The main advantage of the proposed pipeline resides in the full automation of the benchmark procedure: the user is provided with pre-compiled input files for several docking programs, thus minimizing the required expertise to carry out the benchmark study. To this aim, the results are presented as easy to interpret colored maps enabling a fast graphical inspection of large amount of data. The results are analyzed on the basis of the above described quality descriptors.

2.2 Binding Modes Inspection: the Dynamic Scoring Function (DSF)

The docking approach suffers from several limitations.[20] Although is a valuable method to get insights on the final stage of ligand-protein recognition, it lacks the description of two fundamental aspects that might play a significant role in ligand binding: water molecules mediated interactions and protein flexibility. To complete the description provided by the docking method with such contributions, we have recently developed the "dynamic scoring function" (DSF), an approach that enables to follow the dynamical evolution of a docking pose in a realistic environment, *i.e*. the solvated membrane embedded ligand-protein complex.[21] The DSF provides a dynamic estimate of both the ligand position and the strength of the interaction network while accounting for the interplay of water molecules and protein side-chains flexibility. The procedure envisages the dynamic selection of residues within a range of 4.5 Å from the ligand during the MD simulation, starting from a previously obtained docking pose. The DSF is the cumulative sum of electrostatic and hydrophobic contributions to ligand-protein interaction (DSF_{ele} and DSF_{hyd}, respectively) and is calculated at frames extracted every 100 ps as follows:

$$DSF_{ele} = \sum_{t=0}^{n} IE_{ele} \tag{1}$$

$$DSF_{hyd} = \sum_{t=0}^{n} IE_{hyd} \tag{2}$$

The DSF value corrected for the ligand fluctuation (RMSD) with respect to the starting position yields the weighted DSF (wDSF), a number that highlights differences between stable and unstable poses. The corresponding weighted electrostatic and hydrophobic DSFs (denoted as $wDSF_{ele}$ and DSF_{hyd}, respectively) are therefore obtained as reported below:

$$wDSF_{ele} = \frac{\sum_{t=0}^{n} IE_{ele}}{RMSD} \tag{3}$$

$$wDSF_{hyd} = \frac{\sum_{t=0}^{n} IE_{hyd}}{RMSD} \tag{4}$$

The DSFs can be computed during the MD simulations or performed as a post-processing procedure, so that in principle any trajectory that has been previously produced can be re-analyzed with this approach. It can be regarded as an alternative to conventional scoring functions, as it is able to take into account both the complex flexibility in the membrane environment as well as water-driven interactions. The resulting graphs (Figure 1C) obtained by plotting the DSFs against the simulation time enable a graphical comparison of the relative stability of docking poses. This representation can help in detecting and validating the feasibility of alternative binding conformations proposed by the docking algorithm. We have recently exploited this feature to support an apparently less plausible binding mode of a series of 5-alkylaminopyrazolo[4,3-*e*]1,2,4-triazolo[1,5-*c*]pyrimidine at the hA_3 AR.[22] Moreover, we tested the applicability of our approach by taking part in the community-wide 2013 GPCR Dock Assessment.[23] Among the proposed targets, we focused on the $5HT_{2B}$/ergotamine complex, whose X-Ray structure has been released after the predictions were submitted. Therefore we tested the applicability of our tool to homology models of a system on which our laboratory did not hold expertise. We submitted several alternative ligand-protein complexes suggested by the docking protocol to membrane MD simulations and selected the best final poses according to the outcomes of the DSFs analysis. Our predictions ranked 8th among 254, suggesting the portability of our approach to homology models as well as to other GPCRs.[23]

2.3 A Closer Look at Water Molecules: Water Fluid Dynamics (WFD) Maps

It is generally recognized that water molecules contribute to protein-ligand binding in at least two ways: they either stabilize the complex by forming hydrogen bond networks,[24] or are replaced by the ligand once the complex is formed.[25],[26] It is therefore crucial in a drug design process to be able to distinguish between water molecules that mediate protein-ligand interactions and those that can be targeted for being displaced. To this aim, we have very recently tuned a tool that inspects the time-dependent variation of fluid dynamics properties of water molecules as a consequence of the binding event by means of MD simulations.[27] Our approach detects structural water molecules inside the orthosteric binding site of the receptor and collects these pieces of information in a bi-dimensional graph, that we called water fluid dynamics (WFD) map. Unlike other existing MD based methodologies,[28],[29] our approach is aimed at localizing protein "hot-spots" – *i.e.* regions where water molecules playing a key role in ligand binding mostly reside – rather than estimating their binding affinity. The WFD maps have been therefore mainly conceived as qualitative tool to drive ligand design to avoid substituents disrupting key water molecules' networks.

The WFD maps are derived as follows: residues within a range of 5 Å from the ligand are selected and a box surrounding the binding site is created and split into a three-dimensional grid. During the MD simulations the diffusion of water molecules in each grid cell is followed. The data are acquired by saving the MD trajectories at regular intervals (every 10 ps) and by projecting the averaged position of water molecules showing a RMSF value below 1.4 Å into a bi-dimensional grid. The overlap of these grids yields a map (Figure 1D) with cell colored according to the residence time of water molecules on a 0–100 % scale. White zones (0 %) are occupied by water molecules with a residence time equivalent to bulk, whereas blue regions (100 %) are occupied by trapped water molecules showing the maximum residence time of the considered trajectory. The maps allow a fast graphical identification of water distribution inside the orthosteric binding pocket. Moreover, "differential" WFD maps representing by a color code the enrichment or displacement of water molecules as a consequence of ligand binding (Figure 1E) are derived by comparing the WFD maps of the receptor in the apo and bound states.

2.4 Exploring the Ligand-Receptor Recognition Process: the Supervised Molecular Dynamics (SuMD) Approach

One of the most challenging tasks for ligand-GPCRs modeling is the prediction of the recognition pathway, an event which knowledge would ease the development of drug candidates with better pharmacodynamic profiles. Unfortunately, the recognition of a ligand by a receptor is a process hard to simulate as it requires classical MD experiments in a long microsecond time scale.[14],[30],[31] To overcome this technical limitation, enhanced sampling methods that facilitate the crossing of energy barriers through the introduction of biased potentials have been developed.[32],[33] Another approach,[34] induces ligand unbinding by applying external forces to the system, thus requiring knowledge of the ligand-receptor complex final state. Within this framework, we have recently proposed an alternative strategy – the "supervised molecular dynamics" (SuMD)[35] – that enables to follow the ligand-GPCR approaching path by considerably reducing the simulation time scale and without introducing bias. SuMD performs standard simulations in which the distance between the center of masses of the ligand atoms and the receptor binding site is monitored by a tabu-like algorithm. If the location of the binding site is unknown, several simulations are run by setting the centers of previously detected cavities. An arbitrary number of distance points is collected "on the flight" and fitted into a linear function $f(x)=mx$. The tabu-like algorithm is applied to increase the probability to produce ligand-receptor binding events as follows: If the slope (m) is negative, the ligand-receptor distance is likely to be shortened and a classic MD simulation is restarted from the last set of coordinates. Otherwise, the simulation is restored from the original set of coordinates and random velocities are reassigned to each atom. The supervision is repeated until the ligand-receptor distance is less than 5 Å.

The results of a SuMD simulation are displayed in a graph reporting the interaction energy toward the distance between the ligand and the binding site (Figure 1F). This approach can be exploited to analyze binding events to both orthosteric and allosteric sites and to assist the design of site-directed mutagenesis experiments in order to infer the role of specific residues on the molecular recognition process.

3. Application to Drug Design

To explain the applicability of the described tools, we discuss here as case study the comparison between ZM 241385 and caffeine, a strong and a weak hA_{2A} AR binder with pK_D values 9.18±0.23 and 5.31±0.44, respectively.[36] Among the hA_{2A} AR available crystal structures we have selected the two co-crystallized with the ligands of interest identified by the following PDB IDs: 3EML and 3RFM.[36],[37] The starting point of the study is the evaluation of the reproducibility of the X-Ray binding modes through docking calculations. To accomplish this task we compare the IEMs computed for the best performing docking protocols. We then proceed by evaluating the dynamic evolution of alternative binding modes proposed by the docking algorithm, thus imaging the common case where X-Ray structures are not available for comparison. As anticipated, MD simulations allow taking into account the flexibility of the receptor and the role of water molecules in the binding. A more careful inspection of water dynamics is then performed by deriving differential WFD maps from the computed trajectories of a selected docking pose for each structure. Finally, we move outside the receptor and try to reproduce the binding pathways from the extracellular side through SuMD experiments.

3.1 Assessing the Reproducibility of a Binding Mode: IEMs Comparison

We start our case study by assessing the performance of a previously selected docking algorithm through IEMs inspection.[18] Figure 2 displays the comparison between the computed IEMs for the two considered structures. As shown, the binding mode of ZM 241385 (3EML, Figure 2A) encompasses a tight interaction network that is correctly reproduced by the majority of the 20 generated poses. On the other hand, the caffeine binding mode (3RFM, Figure 2B) is more challenging to be reproduced and implies a lower number of less intense interactions with the binding site residues. The comparison of IEMs therefore helps evaluating in a fast graphical fashion both the docking protocols performances and the reproducibility of X-Ray observed binding modes. Interaction patterns without interruptions are clue of binding modes easy to reproduce and indicate good protocol performances, whereas discontinuous patterns suggest binding modes challenging to be predicted and unsatisfactory protocol performances.

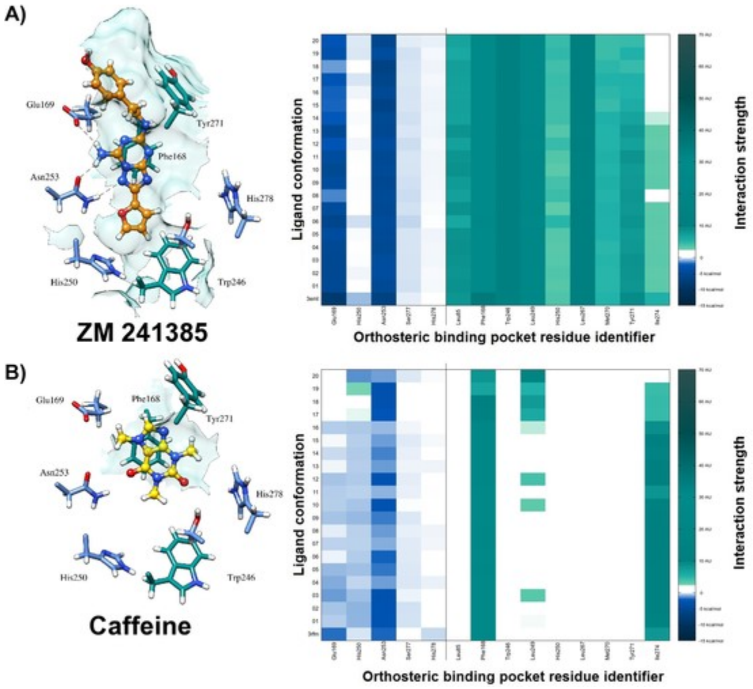

Fig. 2 Comparison of IEMs for two hA_{2A} AR ligands: ZM 241385 (A) and caffeine (B). While ZM 241385 establishes a strong interaction network conserved among the 20 generated poses, caffeine finds lower number and less intense interactions. IEele values: kcal $Å^{-1}$ mol^{-1}, IEhyd values: arbitrary units. The figures were adapted from the original papers.[18]

3.2 Following the Dynamics of Ligand-receptor Interactions: wDSFs Profiles

When the X-ray structures of the ligand-protein complex of interest are not available, usually a modeler is asked to select among several feasible binding modes suggested by the docking protocol slightly differing for the assigned scores. How to recognize the solution best approaching the “real” binding mode? Figure 3 displays the exercise we have conducted to address this issue: in order to identify as many different as possible binding modes, we forced the docking protocol to return ten poses that differed in terms of RMSD for at least 1.75 Å.[27] Nevertheless, the protocol assigned to the generated conformations scores differing at most for ten units. We subjected each docking pose to MD simulation and evaluated the wDSFs. Figure 3A–B displays the results for the two considered structures: the different values of both the cumulative electrostatic and the hydrophobic contributions reflect the different affinities of the two binders. In particular, ZM 241385 exhibits higher absolute values for both contribution types consistently with its higher affinity for the receptor. Moreover, for both structures, the wDSFs trends enable to graphically recognize the pose that best reproduces the X-ray observed binding mode, *i.e*. the one showing the slope with the highest absolute value.

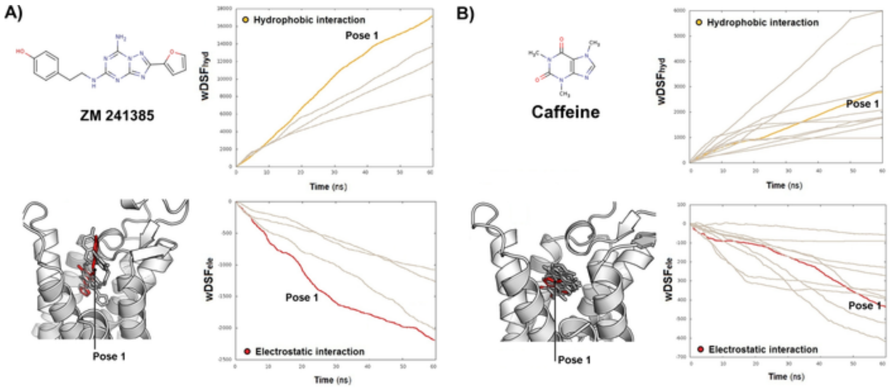

Fig. 3 wDSFs comparison: A) ZM 241385 $wDSF_{hyd}$ (top) and $wDSF_{ele}$ (down); B) caffeine $wDSF_{hyd}$ (top) and $wDSF_{ele}$ (down). IEele values: kcal $Å^{-1}$ mol^{-1}, IEhyd values: arbitrary units. For both ligands the boundle of poses subjected to MD are rendered coloring pose number 1 in red. The same color scheme is used in the plots to identify pose 1 among the others. The figures were adapted from the original paper.[21]

3.3 What About the Role of Water Molecules? WFD Maps Inspection

A detailed inspection of the WFD maps of the two considered compounds further contributes to explain their different binding affinities to the hA_{2A} AR. The WFD map for the ZM 241385 complex (Figure 4A) highlights the presence of water molecules bridging the aromatic scaffold to key residues in the binding site, namely Tyr9, Glu13, His278, Asn253, and Glu169.[27] The interactions with some of those residues were already detected from the docking pose, whereas other ones arose from MD simulations. The differential WFD map (Figure 4B) highlights that the ligand displaces water molecules close to Thr88 while binding. The WFD map corresponding to the caffeine complex (Figure 4C), instead, shows a high propensity of bulk water molecules to solvate the fragment-like compound.[27] This is a direct consequence of the lack of strong interactions with the residues of the binding site detected during the MD simulation and aid explaining the lower affinity of the compound.

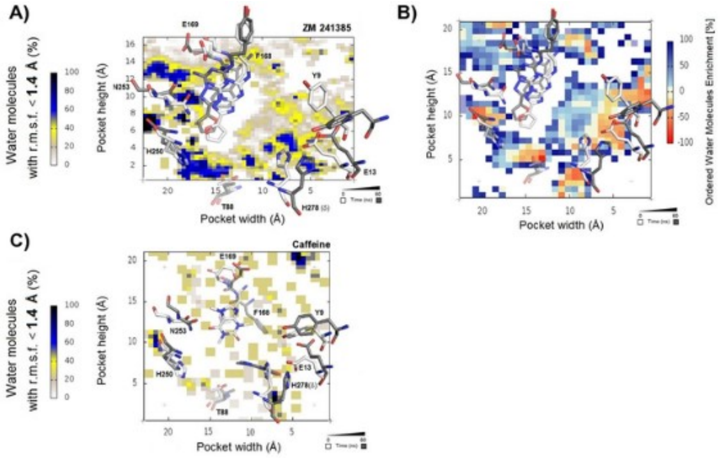

Fig. 4 WFD maps comparison: A) position of water molecules experimentally determined for ZM 241385 complex structure; B) differential WFD for ZM 241385 in comparison to the apo-state of hA_{2A} AR; C) differential WFD for caffeine in comparison to the apo-state of hA_{2A} AR. Receptors are viewed from the membrane side facing TM6 and TM7. Side chains of key residues are displayed as gray sticks. Hydrogen atoms are not displayed. The figures were adapted from the original paper.[27]

3.4 On the Extracellular Side of hA_{2A} AR: the SuMD Approach

On its way to the orthosteric binding site, the ligand might interact with the so-called meta-binding sites,[38] which in some cases, may coincide with possible allosteric sites. The SuMD path we have computed for ZM 241385 highlights two major interaction sites: the second and third extracellular loop (EL2 and EL3, respectively, Figure 5A).[35] As depicted in the diagram in Figure 5B, although a higher interaction (less favorable) energy is associated to these meta-binding sites, they seem to play a role in tuning the correct orientation of the ligand scaffold while approaching the orthosteric site. The EL3 also takes part in the caffeine recognition pathway (Figure 5C),[35] which, however, lacks strong interactions with the orthosteric site (Figure 5D). The SuMD simulations thus recognize the critical role of the hA_{2A} AR extracellular loops in the ligand recognition process, role that has been postulated in the past by using site-directed mutagenesis.[39],[40] We have recently applied the SuMD approach to interpret the binding of two challenging ligands: *(i)* the natural agonist and a *(ii)* imidazoquinolinamine derivative acting as positive modulator (LUF6000). The binding of the natural agonist adenosine at the hA_2 AR revealed a possible energetically stable meta-binding site.[41] The SuMD simulations suggested at least two possible mechanisms to explain the available experimental data for the positive allosteric modulation mediated by LUF6000 toward the hA_3 AR.[42]

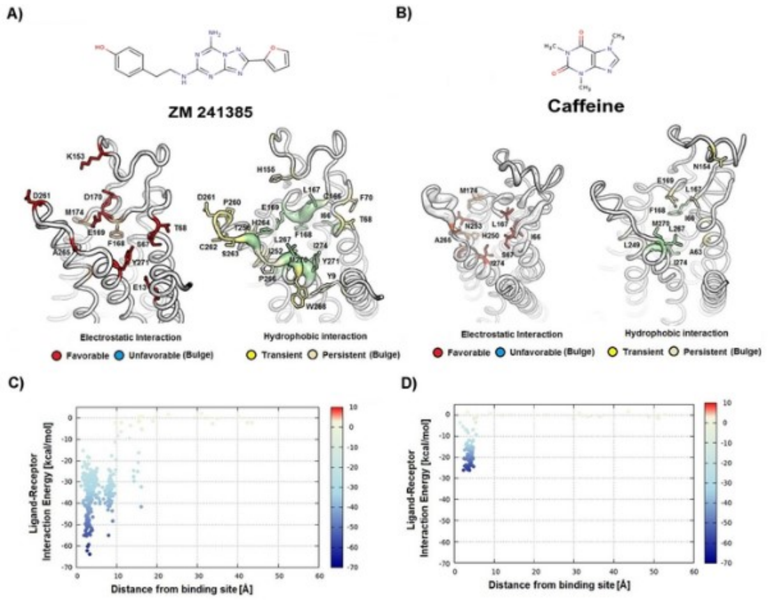

Fig. 5 SuMD experiments on hA_{2A} AR. Top: electrostatic and hydrophobic contributions to the interaction energy of each receptor residue involved in the binding with A) ZM 241385 and B) caffeine. Down: SuMD ligand-receptor interaction energy landscape for C) ZM 241385 and D) caffeine. Interaction Energy values: kcal mol^{-1}. The figures were adapted from the original paper.[35]

4. Summary and Outlook

Through this paper, we have surveyed the recent advances carried out by our research groups in modeling the ligand-GPCRs recognition process. The crystallographic revolution of the last decade, on one side, and the advent of graphics processing units (GPUs) in the molecular modeling field, on the other side, allowed us to tune several tools to assist the drug design procedure.

The proposed approaches enrich the pool of molecular modeling techniques currently available to disclose the factors influencing the ligand-GPCRs recognition process and exploit two computational methodologies extensively used by modelers such as molecular docking and membrane MD simulations. The majority of the methods herein presented are conceived as post-processing procedures, so that in principle any docking output or MD trajectory previously obtained can be rapidly re-analyzed using these tools. Moreover, the full automation of the procedures as well as the presentation of the results as easy to interpret colored maps are aimed at broadening their applicability within the scientific community encouraging non-expert users to approach them. A different philosophy is instead at the basis of the SuMD approach, which introduces a supervision of the MD trajectory through a tabu-like algorithm to speed up the computation time required to inspect the ligand-GPCRs recognition event. The comparison between ZM 241385 and caffeine, a strong and a weak hA_{2A} AR antagonists, has been presented as case study to explain the usefulness and potentiality of our approaches.

As a future perspective we foresee to extend and improve the applicability of these computational tools to address other fascinating open questions in GPCRs field. We would like to summarize some of the hottest topics in the area: a) clarify at the molecular level the orthosteric and the allosteric control mediated by different binders on GPCR functionality; b) elucidate the implication of phosphorylation and glycosylation in both ligand binding and receptor activation; c) understanding the physio-pathological meaning of monomer-oligomer (homo and/or hetero) receptor equilibrium; d) identification of novel second messengers involved in G protein-alternative signaling pathways; e) explore the possibility to perform high-throughput SuMD (HTSuMD) simulations for virtual screening applications as well as for real-time interpretations of mutagenesis data.

Concluding, we hope that these computational approaches carefully integrated with all other experimental GPCRs competencies will broaden our perspectives in several scientific areas from molecular pharmacology to drug discovery.

References

1. Pierce KL, Premont RT, Lefkowitz RJ (2002) Seven-transmembrane receptors. Nat Rev Mol Cell Biol 3:639–650

2. Kristiansen K (2004) Molecular mechanisms of ligand binding, signaling, and regulation within the superfamily of G-protein-coupled receptors: molecular modeling and mutagenesis approaches to receptor structure and function. Pharmacol Ther 103:21–80

3. Moreno JL, Holloway T, González-Maeso J (2013) G protein-coupled receptor heterocomplexes in neuropsychiatric disorders. Prog Mol Biol Transl Sci 117:187–205

4. O'Hayre M, Degese MS, Gutkind JS (2014) Novel insights into G protein and G protein-coupled receptor signaling in cancer. Curr Opin Cell Biol 27:126–135

5. Sodhi A, Montaner S, Gutkind JS (2004) Viral hijacking of G-protein-coupled-receptor signalling networks. Nat Rev Mol Cell Biol 5:998–1012

6. Lundstrom K (2006) Latest development in drug discovery on G protein-coupled receptors. Curr Protein Pept Sci 7:465–470

7. Fredriksson R, Lagerström MC, Lundin L-G, Schiöth HB (2003) The G-protein-coupled receptors in the human genome form five main families. Phylogenetic analysis, paralogon groups, and fingerprints. Mol Pharmacol 63:1256–1272

8. Rosenbaum DM, Cherezov V, Hanson MA, et al (2007) GPCR engineering yields high-resolution structural insights into beta2-adrenergic receptor function. Science 318:1266–1273

9. Thompson AA, Liu W, Chun E, et al (2012) Structure of the nociceptin/orphanin FQ receptor in complex with a peptide mimetic. Nature 485:395–399

10. Hino T, Arakawa T, Iwanari H, et al (2012) G-protein-coupled receptor inactivation by an allosteric inverse-agonist antibody. Nature 482:237–240

11. Warne T, Serrano-Vega MJ, Baker JG, Moukhametzianov R, Edwards PC, Henderson R, Leslie AGW, Tate CG, Schertler GFX (2008) Structure of a beta1-adrenergic G-protein-coupled receptor. Nature 454:486–491

12. Stevens RC, Cherezov V, Katritch V, Abagyan R, Kuhn P, Rosen H, Wüthrich K (2013) The GPCR Network: a large-scale collaboration to determine human GPCR structure and function. Nat Rev Drug Discov 12:25–34

13. Jacobson KA, Costanzi S (2012) New insights for drug design from the X-ray crystallographic structures of G-protein-coupled receptors. Mol Pharmacol 82:361–371

14. Dror RO, Pan AC, Arlow DH, Borhani DW, Maragakis P, Shan Y, Xu H, Shaw DE (2011) Pathway and mechanism of drug binding to G-protein-coupled receptors. Proc Natl Acad Sci U S A 108:13118–13123

15. Selvam B, Wereszczynski J, Tikhonova IG (2012) Comparison of dynamics of extracellular accesses to the β(1) and β(2) adrenoceptors binding sites uncovers the potential of kinetic basis of antagonist selectivity. Chem Biol Drug Des 80:215–226

16. Buch I, Harvey MJ, Giorgino T, Anderson DP, De Fabritiis G (2010) High-throughput all-atom molecular dynamics simulations using distributed computing. J Chem Inf Model 50:397–403

17. Ciancetta A, Sabbadin D, Federico S, Spalluto G, Moro S (2015) Advances in Computational Techniques to Study GPCR-Ligand Recognition. Trends Pharmacol Sci 36:878–890

18. Ciancetta A, Cuzzolin A, Moro S (2014) Alternative quality assessment strategy to compare performances of GPCR-ligand docking protocols: the human adenosine A(2A) receptor as a case study. J Chem Inf Model 54:2243–2254

19. Cuzzolin A, Sturlese M, Malvacio I, Ciancetta A, Moro S (2015) DockBench: An Integrated Informatic Platform Bridging the Gap between the Robust Validation of Docking Protocols and Virtual Screening Simulations. Molecules 20:9977–9993

20. Warren GL, Andrews CW, Capelli A-M, et al (2006) A critical assessment of docking programs and scoring functions. J Med Chem 49:5912–5931

21. Sabbadin D, Ciancetta A, Moro S (2014) Perturbation of fluid dynamics properties of water molecules during G protein-coupled receptor-ligand recognition: the human A2A adenosine receptor as a key study. J Chem Inf Model 54:2846–2855

22. Sabbadin D, Ciancetta A, Moro S (2014) Bridging molecular docking to membrane molecular dynamics to investigate GPCR-ligand recognition: the human A_2A adenosine receptor as a key study. J Chem Inf Model 54:169–183

23. Kufareva I, Katritch V, Participants of GPCR Dock 2013, Stevens RC, Abagyan R (2014) Advances in GPCR modeling evaluated by the GPCR Dock 2013 assessment: meeting new challenges. Structure 22:1120–1139

24. Lu Y, Wang R, Yang C-Y, Wang S (2007) Analysis of ligand-bound water molecules in high-resolution crystal structures of protein-ligand complexes. J Chem Inf Model 47:668–675

25. Snyder PW, Mecinovic J, Moustakas DT, Thomas SW, Harder M, Mack ET, Lockett MR, Héroux A, Sherman W, Whitesides GM (2011) Mechanism of the hydrophobic effect in the biomolecular recognition of arylsulfonamides by carbonic anhydrase. Proc Natl Acad Sci U S A 108:17889–17894

26. De Lucca GV, Jadhav PK, Waltermire RE, Aungst BJ, Erickson-Viitanen S, Lam PY (1998) De novo design and discovery of cyclic HIV protease inhibitors capable of displacing the active-site structural water molecule. Pharm Biotechnol 11:257–284

27. Young T, Abel R, Kim B, Berne BJ, Friesner RA (2007) Motifs for molecular recognition exploiting hydrophobic enclosure in protein-ligand binding. Proc Natl Acad Sci U S A 104:808–813

28. Michel J, Tirado-Rives J, Jorgensen WL (2009) Prediction of the water content in protein binding sites. J Phys Chem B 113:13337–13346

29. Buch I, Giorgino T, De Fabritiis G (2011) Complete reconstruction of an enzyme-inhibitor binding process by molecular dynamics simulations. Proc Natl Acad Sci U S A 108:10184–10189

30. Dror RO, Green HF, Valant C, et al (2013) Structural basis for modulation of a G-protein-coupled receptor by allosteric drugs. Nature 503:295–299

31. Laio A, Parrinello M (2002) Escaping free-energy minima. Proc Natl Acad Sci U S A 99:12562–12566

32. Hamelberg D, Mongan J, McCammon JA (2004) Accelerated molecular dynamics: a promising and efficient simulation method for biomolecules. J Chem Phys 120:11919–11929

33. Park S, Schulten K (2004) Calculating potentials of mean force from steered molecular dynamics simulations. J Chem Phys 120:5946–5961

34. Sabbadin D, Moro S (2014) Supervised molecular dynamics (SuMD) as a helpful tool to depict GPCR-ligand recognition pathway in a nanosecond time scale. J Chem Inf Model 54:372–376

35. Doré AS, Robertson N, Errey JC, et al (2011) Structure of the adenosine A(2A) receptor in complex with ZM241385 and the xanthines XAC and caffeine. Structure 19:1283–1293

36. Jaakola V-P, Griffith MT, Hanson MA, Cherezov V, Chien EYT, Lane JR, Ijzerman AP, Stevens RC (2008) The 2.6 angstrom crystal structure of a human A2A adenosine receptor bound to an antagonist. Science 322:1211–1217

37. Moro S, Hoffmann C, Jacobson KA (1999) Role of the extracellular loops of G protein-coupled receptors in ligand recognition: a molecular modeling study of the human P2Y1 receptor. Biochemistry 38:3498–3507

38. Kim J, Jiang Q, Glashofer M, Yehle S, Wess J, Jacobson KA (1996) Glutamate residues in the second extracellular loop of the human A2a adenosine receptor are required for ligand recognition. Mol Pharmacol 49:683–691

39. Kim J, Wess J, van Rhee AM, Schöneberg T, Jacobson KA (1995) Site-directed mutagenesis identifies residues involved in ligand recognition in the human A2a adenosine receptor. J Biol Chem 270:13987–13997

40. Sabbadin D, Ciancetta A, Deganutti G, Cuzzolin A, Moro S (2015) Exploring the recognition pathway at the human A2A adenosine receptor of the endogenous agonist adenosine using supervised molecular dynamics simulations. Medchemcomm 6:1081–1085

41. Deganutti G, Cuzzolin A, Ciancetta A, Moro S (2015) Understanding allosteric interactions in G protein-coupled receptors using Supervised Molecular Dynamics: A prototype study analysing the human A3 adenosine receptor positive allosteric modulator LUF6000. Bioorg Med Chem 23:4065–4071

Published: *Mol Inform 2016 Sep;35(8-9):440–448.*

Conclusions
And
Future Perspectives

The present work has focused on the role of protein flexibility in binding processes and on the importance of considering this element in computer-aided drug design. Methods neglecting protein flexibility could be exploited more easily for high throughput virtual screening campaign because of their speed. Otherwise, such an approximation could result both in the identification of false positives, since the kinetic component of binding is omitted, and false negative, since possible alternative conformations of the protein and binding pockets are not considered.

During this work, the flexibility issue has been afforded in mainly two strategies, one belonging to the field of traditional molecular docking methods, and the other to the field of molecular dynamics.

As regards molecular docking, a docking benchmark pipeline has been introduced, merging ligand-based and structure-based strategies to assess the best protein structure for each ligand of a database. In particular, each compound is associated to an ensemble of protein structures by similarity with the co-crystallized ligands. Then, a cross-docking job is used to select the best protein of the ensemble for that ligand. Subsequently, docking is performed for each compound of the database with its tailored protein structure. This method is based on the assumption that similar compounds bind similar conformations of the protein, either by inducing that conformation (induced-fit) or by selecting it (conformational selection). Thus, in our approach, protein flexibility is addressed by associating to each ligand the protein that, having memory of a similar compound, most likely will host it properly. The great advantage of the proposed method is that it is completely automatic, with a consequent convenience in terms of speed. Work is in progress to implement the ligand-similarity filter and the cross-docking engine into the previously developed DockBench software, with the idea to make the proposed benchmark strategy available to the scientific community.

In the field of molecular dynamics, the Supervised Molecular Dynamics tool has been developed. The SuMD algorithm can be considered a fully flexible docking method, which explores the approach of a ligand towards the target binding site along time. The difficulties related to the simulation of this event with classical molecular dynamics simulations are related to the long timescale of the process. SuMD has been observed to accelerate this event of at least 2 orders of magnitude, giving the possibility to do a flexible docking experiment to anyone is equipped with a low-cost GPU machine. The strength of this approach is the possibility to individuate metastable binding sites along the recognition pathway and to analyze the role of waters during the recognition.

The domain of applicability of SuMD is under investigation, but a precious implementation has been developed to study peptide-protein binding. At the moment, the test cases have included rigid peptides (well-structured peptides and cyclic peptidomimetics), while more flexible structures are still challenging. Currently SuMD is still in development, with the aim to broaden its application to a wider pool of test cases.